Sheffield Hallam University

A Sheffield Hallam University thesis

Mid-IR Imaging and Multivariate Analysis of Dynamic Processes in Pharmaceutically Relevant Microparticles

Hakan Keles

A thesis submitted in partial fulfilment of the requirements of

Sheffield Hallam University

for the degree of Doctor of Philosophy
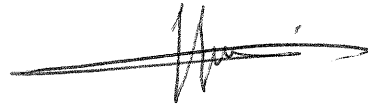
February 2014

Declaration

The work described in this thesis was carried out by the author in the Materials and Engineering Research Institute at Sheffield Hallam University, Sheffield, United Kingdom, between October 2010 and February 2014. The author declares that this work has not been submitted for any other degree. The work is original except where acknowledged by reference.

Author:

(Hakan Keles)

Director of Studies:

(Dr. Christopher Sammon)

Acknowledgements

Contents

List of Abbreviations

API	Active pharmaceutical ingredient
ATR	Attenuated total reflection
B	Hydrated layer size
BSA	Bovine serum albumin
cm^{-1}	Wavenumber
CPL	Critical Pharmaceuticals Limited
CPU	Central processing unit
D_2O	Heavy water
DSC	Differential scanning calorimetry
FDA	U.S.A Food and Drug Administration
FoV	Field of view
FPA	Focal plane array
FTIR	Fourier transform infrared
FWHM	Full width at half maximum
GA	Glycolic acid
Ge	Germanium
GPC	Gel permeation chromatography
GRAS	Generally recognised as safe
h	Hour
H_2O	Water
HEPES	4-(2-hydroxyethyl)-1-piperazineethanesulfonic acid
hGH	Human growth hormone
HPLC	High-performance liquid chromatography

IR	Infrared
k	Degradation rate
K	Kelvin
kGy	Kilo Gray
LA	Lactic acid
m	Minute
MCR	Multivariate curve resolution
MCR-ALS	Multivariate curve resolution-alternating least squares
MCT	Mercury-cadmium-telluride
Mid-IR	Medium-infrared
mm	Millimetre
M_n	Average molecular weight
M_w	Molecular weight
NA	Numerical aperture
NLCF	Non-linear curve fitting
nm	Nanometre
PBS	Phosphate buffer saline
PCA	Principal component analysis
PDI	Polydispersity index
PH	Peak height
PLA	Poly(lactic acid) or Polylactide
PLGA	Poly(lactic-co-glycolic acid)
PGSS	Particles from gas saturated solutions
Poloxamer 407	Ethylene oxide and propylene oxide blocks

RAM	Random-access memory
ROI	Region of interest
$ScCO_2$	Supercritical carbon dioxide
sd	Spray dried
SEC	Size-exclusion chromatography
SEM	Scanning electron microscopy
t	Time
T_c	Crystallisation temperature
T_g	Glass transition temperature
T_m	Melting temperature
UV	Ultraviolet
UV-Vis	Ultraviolet-Visible
2D	2 Dimensional
3D	3 Dimensional
γ	Gamma
λ	Wavelength
°C	Degree Celsius
μm	Micrometre

Abstract

Sustained release microparticles used for parenteral drug delivery must be well characterized in terms of their size range, morphology and function. It is widely understood that the chemistry and morphology of microparticles have a degree of interdependence which strongly affects drug release behaviour from microparticles.

This thesis investigates, for the first time, the use of mid-IR imaging along with the development and optimisation of relevant multivariate image analysis methods for studying the real-time degradation of pharmaceutically relevant biodegradable polymer microparticles and the real-time release of protein based drugs from such microparticle systems.

The application of attenuated total reflection - Fourier transform infrared spectroscopic (ATR-FTIR) imaging and analysis to monitor the degradation of a single microparticle is optimised and the developed methodology is detailed. A series of time resolved images of a PLGA microparticle undergoing hydrolysis at 70 °C are obtained using ATR-FTIR imaging for the first time. A novel partially supervised non-linear curve fitting (NLCF) tool is developed and the output from the NLCF is evaluated by direct quantitative comparison with a traditional peak height (PH) data analysis approach and multivariate curve resolution alternating least squares (MCR-ALS) analysis for the same images, in order to develop an image analysis strategy. The NLCF method is shown to facilitate the calculation of hydrolysis rate constants for both the glycolic (kG) and lactic (kL) segments of the PLGA copolymer. This results in improved spatial resolution on time-resolved microparticle images, so providing better insight into the dimensions of hydration layers and particle dimension changes during hydrolysis when compared to images derived from both PH measurements and MCR-ALS. The MCR-ALS routine is shown to be faster than NLCF and its images are found to provide sufficient contrast to be used for qualitative comparison.

The optimised mid-IR-ATR procedures are then applied to investigate several factors influencing the hydrolytic degradation of a family of PLGA microparticles. Degradation rate constants for glycolic and lactic units are shown to increase (whilst maintaining a ~1.3 ratio between each other) with increasing initial glycolic content of the copolymer, temperature or γ-radiation exposure. Differential scanning calorimetry (DSC) and gel permeation chromatography (GPC) results indicate a chain scission based degradation in PLGA upon γ exposure. The distribution of lactic acid is probed with IR during the hydrolysis of a PLA microparticle for the first time, showing a diffusional pathway from the degrading microparticle outwards into surrounding water.

Utilising the chemical selectivity of the infrared methodology, ATR-FTIR imaging is applied for the first time to monitor the redistribution and release of human growth hormone (hGH) from a range of CriticalMix^{TM} processed PLGA/PLA microparticles during a set of dissolution experiments at 37 °C in D_2O. Increasing the γ dose is shown to have a profound influence on the release mechanism, with higher γ doses leading to a dramatic increase in the initial burst release followed by retardation in the sustained release and a lower total level of hGH release over the dissolution experiment. These changes are shown to be the result of: (i) protein aggregation as a function of applied γ-dose as studied by size exclusion chromatography; (ii) decrease in overall porosity as studied by SEM; (iii) decrease in M_w of all of the component polymers post γ irradiation indicating a chain scission mechanism as studied by GPC and DSC; and (iv) the increase in the number of oxygenated components in the Poloxamer 407 excipient, thereby increasing the strength of interaction between the microparticle and the entrapped hGH. These findings suggest that any γ sterilisation dose should be less than 25 kGy and that other sterilisation methods may need to be considered, due to the stability of the studied formulations.

1 Introduction

This thesis investigates the use of Mid-IR spectroscopic imaging and relevant multivariate data analysis techniques to characterise the degradation kinetics of biodegradable polymer microparticles and the release of protein drugs from such matrices.

The work presented within this thesis was conducted at Sheffield Hallam University in collaboration with Critical Pharmaceuticals Ltd. This chapter provides a brief introduction into the drug delivery systems investigated within this thesis. It includes information about polymers, proteins and controlled release drug delivery systems along with production methods for such systems with particular attention to supercritical CO_2 based processes among which a modified particles from gas saturated solutions (PGSS) method (CriticalMix^{TM}) was used to produce the samples studied here by the collaborating company.

In this chapter a very brief initial insight is given for Mid-IR spectroscopic imaging, including its relevance for studying polymer degradation and drug release before the aims of this work are discussed in detail.

In Chapter 2, the theory of the main method of study, FTIR spectroscopy and imaging, is detailed and relevant data analysis techniques are discussed. Other characterisation methods including scanning electron microscopy, chromatography, differential scanning calorimetry, UV-Vis dissolution testing and microscopic sample preparation method (ultra-microtomy) are also detailed including information regarding the parameters and methods used.

Chapter 3 demostrates the optimisation of ATR imaging method coupled with relevant image analysis techniques for studying degradation in single polymeric microparticles. A direct numerical comparison of three data analysis methods: peak height measurements, soft and hard modelling, is studied using the same IR image set of a PLGA 75/25 microparticle undergoing hydrolysis at 70 °C.

In Chapter 4, a range of single PLGA microparticles are studied using the ATR imaging methodology developed in Chapter 3. Effect of CriticalMix^{TM} process, copolymer ratio (LA:GA), morphology and gamma irradiation (a typical sterilisation method used for

PLGA based microparticle systems) on hydrolytic degradation behaviour of individual PLGA microparticles is investigated and results are discussed.

In Chapter 5, a lead controlled release formulation that consists of PLGA/PLA polymers, an excipient (Poloxamer 407) and human growth hormone (hGH) is initially investigated in terms of its components' spatial distributions in dry form in order to validate the formulation model. The release of hGH from scuh complex formulation is monitored using ATR-FTIR imaging. Finally the effect of γ- irradiation on the stability of PLGA microparticles and on the release of the hGH protein from the microparticles is investigated using FTIR imaging, SEM analyses and using a combination of conventional bulk methods including; differential scanning calorimetry (DSC) to understand thermal properties of irradiated and un-irradiated pure polymers, gel permeation chromatography (GPC) to monitor effect of irradiation on the molecular weight of the polymers, UV-Vis spectrophotometry to monitor *in vitro* API release from the microparticles and size exclusion chromatography (SEC) to determine protein aggregation and stability.

The overall conclusions and possible further work are summarised in Chapter 6.

1.1 Drug Delivery

The concept of drug delivery is the administration of active pharmaceutical ingredients (APIs) to patients, in sufficient amounts that they reach and treat the targeted region of body without causing any adverse effect(s). Although this can be achieved by several routes including parenteral (which is achieved thorugh injection; into a vein, under the skin or into a muscle, or through inhalation or through absorption by intact skin), oral, pulmonary or nasal application, the administration of proteins are limited to the parenteral (often subcutaneous) type as their high molecular weight or poor stability blocks their transdermal, nasal or oral delivery.

Another problem in the delivery of proteins and peptides is their short half-life in the human body. Therefore their unfavourable pharmacokinetics means that they are usually administered by frequent injections, for example for human growth hormone deficiency every 3 days, which is inconvenient for patients and can affect patient compliance. However, the development of sustained release formulations can overcome these issues as controlled release drug delivery is used to delay the release of drugs within the body.

1.2 Controlled Release Drug Delivery

The use of biodegradable polymers is one of the fundamental ways of controlling release systems. There are three different types of micro-scale controlled release systems; (1) reservoir devices, where the drug is released upon degradation of a biopolymer that is used to encapsulate it avoiding immediate release, (2) diffusion devices, where the drug is released through pores of the biopolymer matrix and (3) erosion, where the drug release is based up on degradation of the biopolymer matrix. However for porous biopolymer matrices it is often the case that combination of last two hypotheses occurs as initially the surface attached drug molecules will be released upon contact with aqueous media by diffusion through pores and finally the degradation of biopolymer will result in release of the drug molecules entrapped deeper in the biopolymer matrix (Figure 1.1).
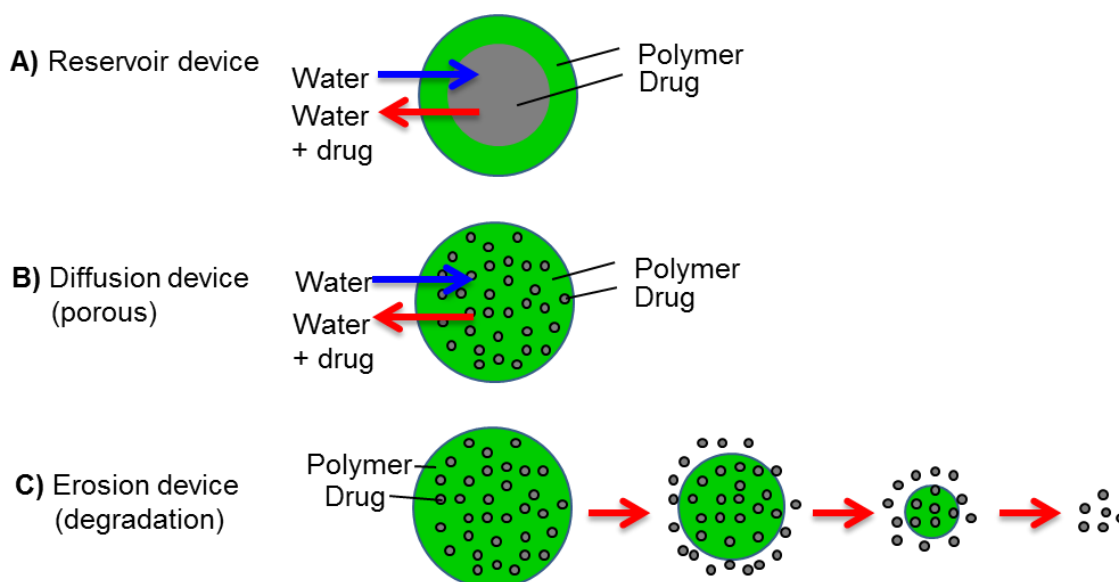
Figure 1.1 Controlled release scenarios for polymer microparticles; (a) reservoir devices, (b) diffusion of drug from porous polymer matrix and (c) erosion mechanism where the drug molecules are released as they become free from degrading polymer.

In recent years research in molecular and cell biology to meet clinical needs has intensified the interest in biologics, a variety of therapeutics such as vaccines, recombinant proteins and peptides, genes, viruses and synthetic tissues, ensuing a strong market growth [1]. As a result, currently hundreds of recombinant proteins and peptides are in the pipeline for the U.S. Food and Drug Administration (FDA) approval.

There are numerous candidate biodegradable polymers for carrying and releasing biologics as shown in Figure 1.1 however concerning biocompatibility to human body, the FDA approved ones are few [2,3].

Poly (lactide-*co*-glycolide) (PLGA) is a FDA approved biodegradable synthetic polyester that is physically strong and highly processable [4]. Hence PLGA has been the most studied carrier matrix for macromolecules such as proteins, DNA, RNA, vaccines and peptides for treatment of important diseases such as cancer, human growth deficiency and multiple sclerosis [3].

Another advantage of PLGA is that its degradation *in vivo* is controllable by choice of polymer molecular weight and copolymer ratio (lactide to glycolide (*L/G*)) and yields lactic and glycolic acids, which are biocompatible and rapidly cleared from the body via the renal system [2].

The number of PLGA based formulations that are readily administered through a syringe, has been researched increasingly resulting in many formulations that are marketed today including ones given in Table 1.1.

Table 1.1 PLGA based microparticle formulations available in the market [1,3].

Product name	API	Company	Application
Lupron Depot®	Leuprolide	TAP	Prostate cancer, endometriosis
Enantone Depot®	Leuprolide	Takeda	Prostate cancer, endometriosis
Trenantone	Leuprolide	Takeda	Prostate cancer, endometriosis
Nutropin Depot®	Growth hormone	Genetech	Pediatric growth hormone deficiency
Suprecur® MP	Buserelin acetate	Aventis	Prostate cancer
Decapeptyl®	Triptorelin pamoate	Ferring	Prostate cancer
Sandostatin LAR® Depot	Octreotide acetate	Novartis	Acromegaly
Somatuline® LA	Lanreotide	Ipsen	Acromegaly
Decapeptyl SR	Triptorelin	Ipsen	Prostate cancer
Trelstar™ Depot	Triptorelin pamoate	Pfizer	Prostate cancer
Arestin®	Minocycline	Orapharma	Periodontal disease
Risperidal® Consta™	Risperidone	Johnson & Johnson	Antipsychotic
Parlodel® LAR	Bromocriptine	Novartis	Parkinsonism

From the pharmaceutical manufacturing technology perspective, the key goal; controlling the release of the drug for longer periods without causing any degradation of the drug at production stage, can be achieved by obtaining a homogenous distribution of the drug within the matrix. The following sections will give relevant details of the polymers, proteins and the manufacturing methods that are widely used for making

protein loaded polymer microparticle systems, with a focus on relation to the novel microparticle systems characterised in this thesis.

1.3 Polymers

The self-definition of 'polymers' can be derived from the Greek words 'poly' meaning 'many' and 'mono' meaning 'one', as polymers are macromolecules built up from monomers covalently bonded together forming a chain type structure. Repeating monomer units connected together may form linear, branched or 3D structured (cross-linked polymers in which one chain is bonded with monomers of another chain) types as illustrated in Figure 1.2.
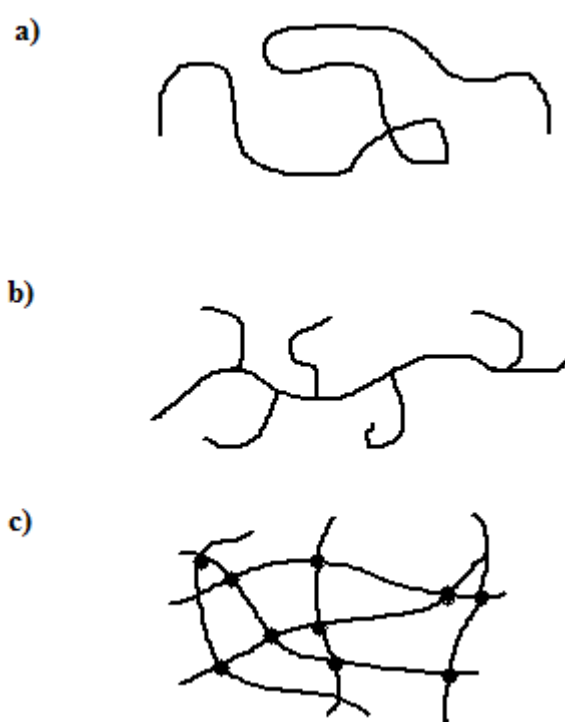
Figure 1.2 Linear (a), branched (b) and 3-dimensional (c) structures of polymers.

Since the initial understanding of their structure by Hermann Staudinger [5], polymers became the most versatile material type in our daily lives ranging from the simplest form as a recyclable carrier bag, to arguably more complicated and important forms such as long life batteries used in mobile electronic devices or biodegradable matrices for carrying drugs.

Polymers can be grouped most generally in to two; biopolymers (polymers with natural origin) such as chitosan and proteins, or synthetic polymers including biodegradables such as polyesters (i.e. poly(lactic acid), poly(glycolic acid), poly(ε-caprolactone),

poly(β-malic acid)) and non-biodegradables such as silicones and some acrylic polymers [6]. Step growth polymerisation and chain growth polymerisation are the two principal methods for synthesising man-made polymers [7]. Step growth polymerisation occurs as multifunctional monomers react to form dimers, trimers longer oligomers and long chain polymers at the end of the reactions. Chain growth polymerisation occurs as the unsaturated monomers continuously add onto the growing polymeric chains.

Polymers exhibit two types of morphology; crystalline in which molecules are packed in regular arrays and amorphous in which molecules are oriented randomly and are entangled and most polymers contain both crystalline and amorphous regions (semicrystalline). At low temperatures the molecules of an amorphous polymer vibrate at low frequency, exhibiting solid state properties, this is termed as the 'glassy state'. Upon heating an amorphous polymer, due to the increase in molecular energy, a transition occurs from the glassy state to a rubbery state and the inflection temperature at which this effect occurs is called the glass transition temperature (T_g). Crystalline polymers show a clear phase transition upon heating; melting. The temperature at which this thermodynamic effect occurs is called melting temperature (T_m).

Differential scanning calorimetry (DSC) which is discussed in Chapter 2 can be used to determine the melting temperature and the glass transition temperature of polymers. Thermal properties of polymers are often dependent on their molecular weight which can be given as;

$$M_w = \frac{\sum_i N_i M_i^2}{\sum_i N_i M_i}$$
<div align="right">**Equation 1.1**</div>

or their molecular number which can be given as;

$$M_n = \frac{\sum_i N_i M_i}{\sum_i N_i}$$
<div align="right">**Equation 1.2**</div>

where N_i is the number of molecules with length i and M_i is the mass of polymer chain with length i, both define the size of a molecule and can both be measured using gel permeation chromatography (GPC) [8] as discussed in Chapter 2.

Most polymers vary in their chain lengths. Their distribution in the length of the chains is defined as polydispersity index (*PDI*) which is molecular number per molecular weight. The decrease in molecular weight due to degradation, measured with GPC, can be used to calculate and compare the degradation rate of polymers.

Copolymers are substances that are usually produced by step polymerisation from chains in which two or more different monomers are connected through covalent bonds. Copolymers are useful in that thermodynamic and physicochemical properties of polymers therein can be improved and modified. Considering their form, copolymers can be grouped as; 'random' in which two or more different repeating units are distributed randomly, in which sequences of the different monomers alternate without any regular pattern and block in which long sequences of monomers are followed by another of the same or graft in which one type of monomer chain is connected to another as branches at different points. The formation of copolymers results in a combination of the properties of the original homopolymers and this can improve the properties of the individual polymers such as tensile strength, reactivity and thermodynamic properties [9].

Two or more polymers or co-polymers can be mixed, typically; by heating and/or stirring or by dissolving each in a co-solvent adding together and letting solvent evaporate or using one monomer as a solvent for another, resulting in a 'blend' in which polymers are connected by intermolecular forces, but not covalent bonds. Depending on their homogeneity at a molecular level, polymer blends are classed as miscible (very homogenous) or immiscible (phase separated) showing single or multiple T_g in DSC analysis, respectively.

1.3.1 Polymers in Sustained Release Drug Delivery

The use of biodegradable and biocompatible (i.e. that can degrade in to molecules that are not toxic to human body and therefore are ejected without causing any damage) polymers enables the extended release of drugs.

During this project, two polymers have been used as the drug carrier matrix, poly(lactic acid) (PLA) and poly (lactide-*co*-glycolide) (PLGA). Poloxamer407, accepted as a GRAS (generally regarded as safe) has also been used as a processing aid in the production of these microparticles as it enhances the drug release [10].

1.3.1.1 Poly(lactic acid) (PLA)

PLA has 3 stereoisomers that are the crystalline l-PLA and d-PLA forms and the amorphous DL-PLA [11]. The most common synthetic route to produce PLA is via the ring opening polymerisation of lactide which is catalysed by stannous octanoate (Figure 1.3).
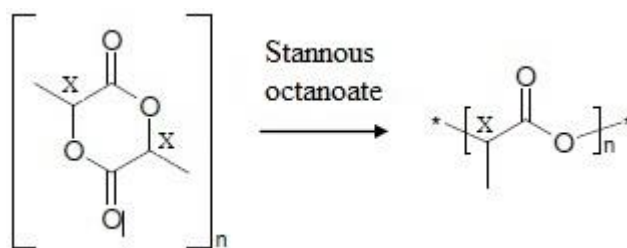
Figure 1.3 Synthesis of PLA where chiral centres are indicated with X.

PLA are more suited as implants than controlled release delivery devices as their crystalline nature retards their water uptake causing long degradation times (typically more than a year depending on molecular weight). Upon contact with aqueous media, PLA undergoes hydrolysis and breaks down to lactic acid fragments. PLA has a T_g of about 60-65 ºC and a melting temperature of about 173-178 ºC [11].

1.3.1.2 *Poly(lactide-co-glycolide) (PLGA)*

PLGA is synthesised by the ring opening polymerisation of the cyclic diesters of lactic acid and glycolic acid, catalysed by stannous octanoate (Figure 1.4) [12].
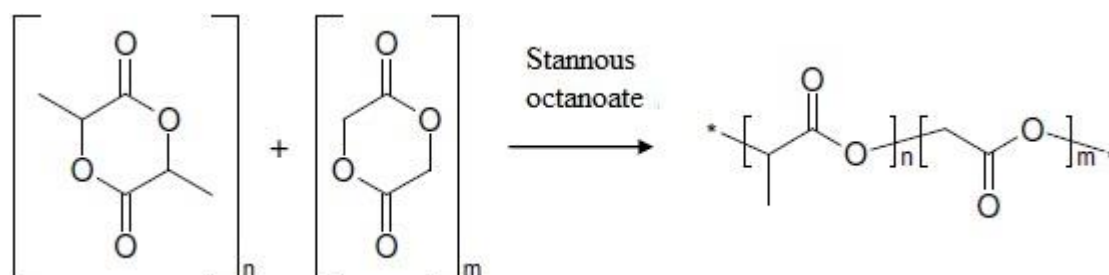
Figure 1.4 Synthesis of PLGA.

Although PGA is not useful as a drug delivery device due to its high crystallinity and high melting temperature, as mentioned earlier in this chapter, PLGA, a copolymer of glycolic acid (GA) and lactic acid (LA), is the most used biodegradable polymer in delivery of biologics [13]. Depending on the ratio of lactide to glycolide used for the polymerization, different forms of PLGA can be obtained. These are usually identified by the monomer ratio used. For example PLGA 75:25 identifies a copolymer composition of 75% lactic acid and 25% glycolic acid. All PLGAs are amorphous rather than crystalline and show a glass transition temperature in the range of 40-60 °C [12]. Unlike the homopolymers of lactic acid (polylactide) and glycolic acid (polyglycolide), which show poor solubilities, PLGA has the property of hydrophobicity and therefore can be dissolved by a wide range of common solvents, including acetone and ethyl

acetate. The production of a 50:50 mixture of these two polymers also reduces the degradation time of PLA from several months to few weeks.
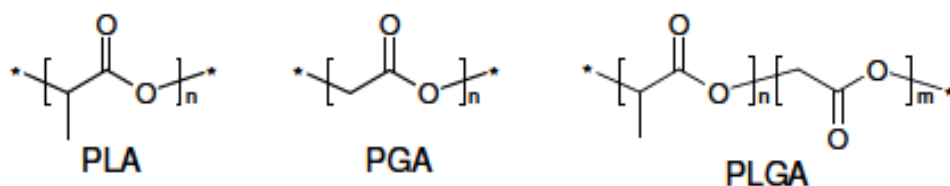
Figure 1.5 Structures of PLA, PGA and PLGA.

As shown in Figure 1.5, PLA contains an additional methyl group over PGA which creates the amorphous nature by making chain packing more difficult whereas the absence of this group allows PGA to be crystalline. As PLGA is a copolymer of these two monomers it is less crystalline compared to PGA, due to the addition of the methyl group. And this provides the observed differences in the degradation rates. Degradation rates of bulk PLGAs can be calculated using Raman and IR spectroscopies [14]. PLGA can degrade via hydrolysis of the ester linkage into small, water soluble fragments.

1.3.1.2.1 PLGA Hydrolysis

When PLGA is exposed to an aqueous solution or vapour, the ester carbonyl is subject to nucleophilic attack by water, as shown in Figure 1.6 [15]. The ester group in these polymers will be hydrolysed via a tetrahedral intermediate to give primary OH and carboxyl end groups, resulting in chain cleavage. Esters are vulnerable to hydrolysis because the electron withdrawing effects of the attached oxygen atoms result in a partially positive ester carbon. The accumulation of carboxylic acid hydrolysis products in PLGA matrices results in autocatalysis of the hydrolysis reaction which is followed by addition of a proton to carbonyl oxygen, which facilitates the reaction by stabilizing the tetrahedral intermediate.
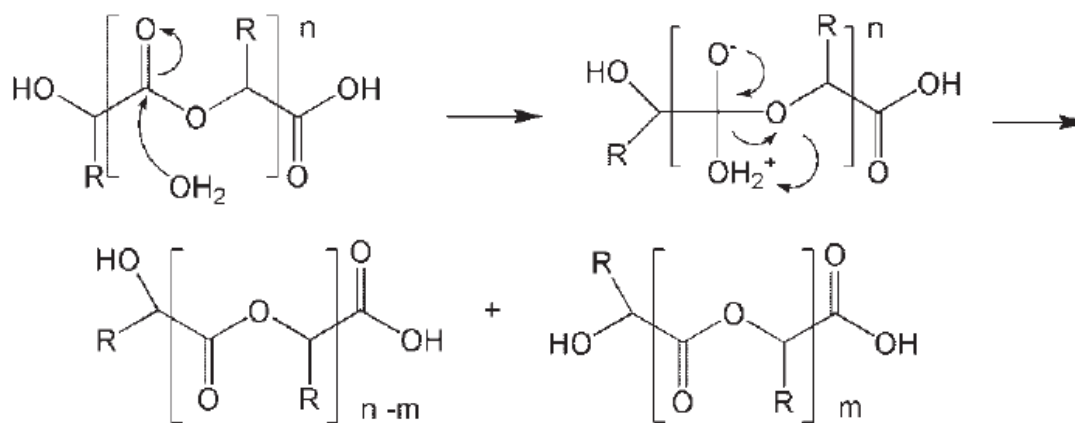
Figure 1.6 PLGA hydrolysis mechanism via ester links. R groups represent CH$_3$ for lactide and H for glycolide. The resulting alcohol can abstract a proton from the carboxylic acid during the chain cleavage step as shown, or a proton addition to alcohol and removal from carboxylic acid can be provided by water (from [15]).

Alteration of either the PLA:PGA ratio, molecular weight or PDI can change the degradation rate of PLGA. Glycolic acid is slightly more hydrophilic than lactic acid, therefore increased glycolic acid content may lead to an increase in the hydrolysis rate for the same morphology and size of particles [13]. Typical ratios of lactide to glycolide range from 50:50 to 100:0 with molecular weights typically ranging from 10 to 100 kDa (or 10^3 unified atomic mass units). The hydrolysis rate of PLGA also depends on its end groups which may be carboxylic acid, making the polymer more hydrophilic or ester-capped, decreasing the rate.

1.3.1.3 *Poloxamer 407*

Poloxamer 407 (also known as Lutrol or Pluronic F127), poly(ethylene oxide)/poly(propylene oxide)/poly(ethylene oxide) (PEO–PPO–PEO) triblock copolymers, is a hydrophilic surfactant and best known for its use in mouthwash and contact lens solutions where its function is to help remove organic molecules such as lipids by increasing their solubility in aqueous media.
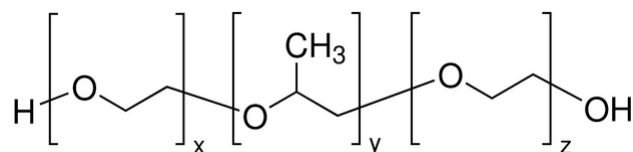
Figure 1.7 Structure of Poloxamer407.

Surfactants are often used to increase the water solubility of poorly soluble drugs, in pharmaceutical formulations.

In controlled release drug delivery, poloxamer 407 is shown to enhance solubilisation of biologics and also prolong their release [16].

1.4 Proteins

Like other bio-macromolecules such as nucleic acids, proteins are essential parts of organisms and participate in many processes within cells. With varying sizes and molecular weights, proteins have a range of functions as they are able to bind to other biomolecules, nucleic acids and metal ions [17]

Linkage between amino acids result in long polymer chains called proteins. Proteins consist of carbon, hydrogen, nitrogen, oxygen and sulphur atoms, for example, $C_{990}H_{1532}N_{262}O_{300}S_7$, namely human growth hormone.
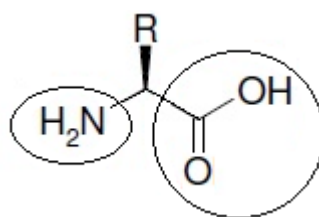
Figure 1.8 Structure of an amino acid showing the amine in the left hanside and carboxyl group in the right hand side circles, respectively.

There are twenty common types of aminoacids that vary in their R groups (Figure 1.8). Aminoacids can be grouped as non-polar, uncharged polar and charged polar [17]. Non polar amino acids tend to be unreactive. Uncharged polar amino acids contain either hydroxyl or amine groups, which are capable of hydrogen bonding to other residues and the third group can bind to metal ions and which is important in biology [17].

The primary structure of a protein is the sequence of aminoacids of this backbone. The secondary protein structure is the specific geometric shape caused by intramolecular and intermolecular hydrogen bonding of amide groups. Proteins have three common secondary structures, α-helix, β-sheet and turn [17]. The secondary structure of proteins can readily be characterised by FTIR spectroscopy [18]. The tertiary structure of proteins is the bending and twisting of the polypeptide backbone into a compact structure. Several polypeptide chains may exhibit weak interactions forming large molecules; the so called quaternary structure. UV-Vis spectrophotometry can be used to

detect proteins when dissolved in a solution as proteins absorb UV light at 200nm (peptide bonds) and ~280 nm (aminoacids with aromatic rings, Tyrosine and Tryptophan) [19].

1.4.1   Bovine Serum Albumin (BSA)

With its 582 amino acids and 66267 Da total molecular weight, BSA is a large and widely used model protein as it is not only cheap but also stable at 60 ℃ up to 10 hours [20]. BSA has a total charge of -18 (at pH 7) which is high due to its charged amino acids such as arginine and aspartic acid. BSA has been used as a model protein in this project for the preliminary investigations of a single polymer formulation.
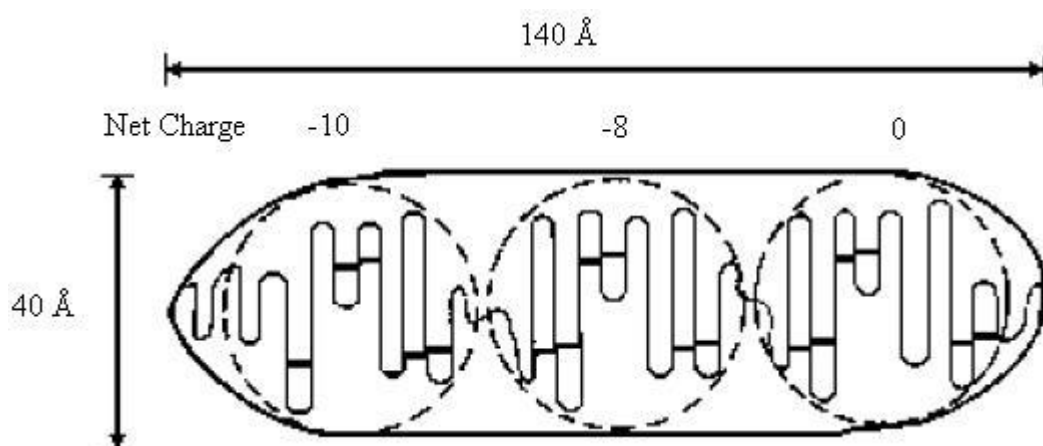
Figure 1.9 BSA structure showing the three charge domains.

1.4.2   Human growth hormone (hGH)

Human growth hormone (hGH) has been used to treat various diseases including children with growth hormone deficiency (paediatric hypopituitary dwarfism), muscle-wasting disease associated with HIV, Turner's syndrome for girls and chronic kidney failure [21]. For children's growth deficiency treatment it is delivered via a painful injection ~3 times a week, consuming valuable hospital resources and resulting in poor patient compliance.

hGH contains 191 amino acid residues and is a single chain peptide with a molecular weight of ~22.13 kDa and melting point of 76 ℃ [22]. Its secondary structure, shown in Figure 1.10, contains four helices connected with random loops and chains and internally cross linked by two disulfide bonds that provide stability and enable interaction with the growth hormone receptor [22].
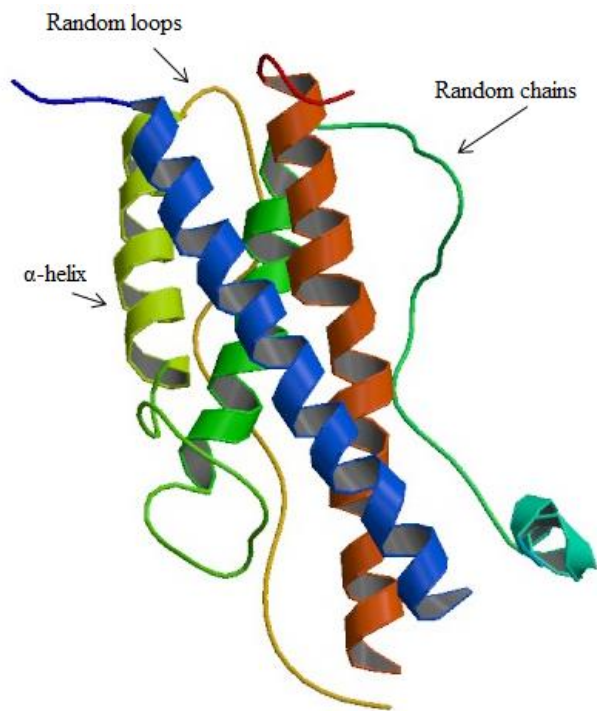
Figure 1.10 hGH secondary structure (from [22]).

1.5 Methods of Producing Controlled Release Drug Delivery Systems

In order to produce microparticles that follow one or both of the hypothesised scenarios shown in Figure 1.1b and Figure 1.1c, the drug needs to be mixed with the polymer(s) homogenously and this is mainly dependent on liquefication of the polymer(s) during the formation of the particles. Common methods for producing sustained release drug delivery systems differ mainly in how they are liquefied, as outlined in this section.

1.5.1 Spray Drying

Spray drying is an established method in the food industry for producing a range of dry powder form products including coffee and milk powder [23]. The use of spray drying is also common in micronisation (the process of reducing particles to a size of less than typically 10 μm) of drug-polymer formulations in the pharmaceutical industry. During a typical micronisation process a solvent such as dichloromethane (DCM), in which the polymer of interest is dissolved initially, is mixed with the drug, forming a solvated mixture. This mixture is then induced to atomise and forms droplets as it is forced through a nozzle as shown in Figure 1.11. The spray is dried by applying a hot (~65 °C) gas as the droplets emerge, resulting in solidified particles.
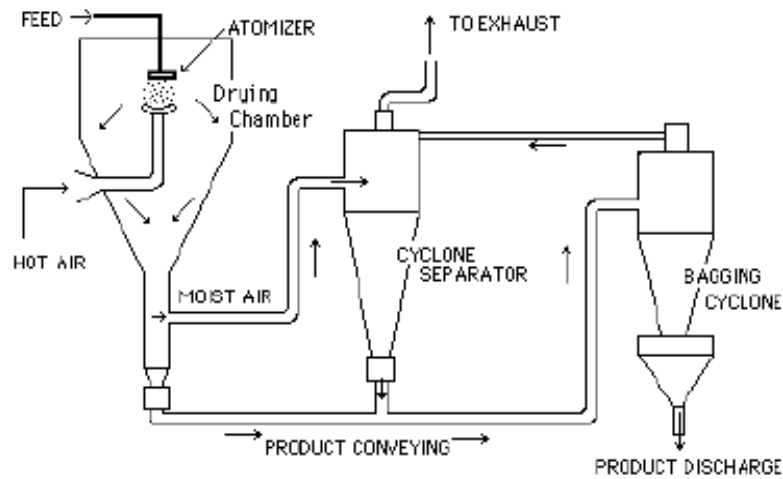
Figure 1.11 Schematic diagram of spray dryer (from [24]).

The spray drying method has been studied widely for producing PLGA based sustained release devices as carriers for various biologics and has been shown to be successful in producing <100 μm microspheres with encapsulation efficiencies up to ~80% [3,25,26].

However, considering the efficacy of proteins that are very sensitive to temperature and the biocompatibility of the produced formulation, the high process temperatures (beyond 60 ℃) and the possible existence of toxic solvent residues within microparticles caused by insufficient drying, exist as critical drawbacks.

1.5.2 Emulsion

Emulsification processes can be grouped into two; single and double [3]. The former involves two main steps; firstly, dissolving the polymer in an organic solvent such as chloroform and adding the drug molecules to this solution and secondly, adding this mixture into a water- emulsifier mixture and stirring. Upon evaporation of the solvent, the drug loaded polymer solidifies in the aqueous phase. As one can expect by the description of the method, single emulsification is not suitable for water soluble drugs [4].

The double emulsion method is similar to the single emulsion one, the only difference being that the drug molecules are dissolved in water before being added to the polymer solution, such that a primary emulsion is formed on mixing. The rest of the procedure follows as in single emulsification. A stabilizer such as polyvinyl alcohol (PVA) may also be added to the water.

14

Since the solvents used can cause degradation, emulsification is not suitable for the encapsulation of sensitive drugs such as proteins into biodegradable polymers such as PLGA. Requiring the use of large amounts of solvents, this method is also expensive and has potential environmental hazards.

1.5.3   Supercritical Fluid Technologies

Substances become supercritical fluids (SCF) when placed above their critical point (i.e. above their critical temperature and critical pressure) exhibiting the flow properties of a gas (i.e. showing low viscosity) and the dissolving power of a liquid, thus becoming ideal solvents [27].

SCF, first observed by Cagniard de la Tour in 1822 [28], can easily penetrate through materials because they do not exhibit significant surface tension, and their solvent power can be controlled by altering temperature and/or pressure as it is related to their density [29].

Among many other molecules including propane, ethane, ammonia and water, carbon dioxide has become the fluid of choice in SC processes because it is cheap, non-flammable, has GRAS (generally regarded as safe) status, is environmentally acceptable and may be recycled. $ScCO_2$ is best known for its 'famous' application of caffeine extraction from coffee beans, but perhaps more importantly, its easily achievable critical point (31.1ºC and 73.8 bar) also makes it ideal for processing biologics without causing denaturation [30].

During the last decade, drug encapsulation of polymer microparticles using supercritical fluid technology has been reported using a number of methods. These include expansion of supercritical solutions (RESS), gas anti-solvent techniques (GAS), supercritical anti-solvent technique (SAS) and particles from gas saturated solutions (PGSS) [31]. One disadvantage of $scCO_2$ considering applicability for wide use is that only non-polar and some low polar molecular substances can dissolve in $scCO_2$. However for the latter method, PGSS, this is not a concern, particularly for biodegradable polymers and most biologics as they do not need to be dissolved in CO_2 as detailed in section 1.5.3.4.

1.5.3.1   *Rapid Expansion of Supercritical Solutions (RESS)*

This process requires both the polymer and drug to be dissolved in $scCO_2$, before being mixed and then forced through a nozzle (typically <150 µm) into a lower pressure zone. Tom *et al.* [32] first demonstrated the encapsulation of microparticles using the RESS

process however since only a few polymers are soluable in $scCO_2$ this method has not been widely applied. In the case of having to use a poor $scCO_2$ soluble polymer, organic co-solvents can be added to improve solubility; however this may cause protein degradation. Also, the processes may have to be performed at temperatures over 100 °C and 200 bar, to improve polymer solubility, which makes it impossible to process biologics without damaging them [31].

1.5.3.2 Gas Antisolvent Technique (GAS)

In this process, $scCO_2$ acts as an anti-solvent (a solvent in which the product is insoluble) therefore the polymer and drug are not required to dissolve in $scCO_2$. A solution of the drug and polymer in an organic solvent is produced beforehand and $scCO_2$ is then gradually added. As the polymer and drug are insoluble in the $scCO_2$ they come out as microparticles.

This process has been used to prepare insulin and insulin/PEG loaded P*L*LA nanoparticles with ~94% encapsulation efficiency and very low residual content ~300 ppm) [33]. However, solvent residue issues cannot be overcome with this technique.

1.5.3.3 Supercritical Antisolvent Technique (SAS)

Although this is a similar process to GAS, based on $scCO_2$ being used as an antisolvent, it is different in that the polymer-drug solution is forced through a nozzle or capillary into the $scCO_2$ phase. The solvent then evaporates forming encapsulated polymer microparticles. Using this process Duarte *et al.* produced naproxen-loaded microspheres from ethylcellulose/methylcellulose blends for oral delivery that showed a sustained release of the drug [34].

1.5.3.4 Particles from Gas Saturated Solution (PGSS)

This process, first developed for the coatings industry [35], is simply analogous to painting with a spray coater using small particles. After its reported suitability for micronisation of nifedipine [36], a small molecule drug, more recent developments have focused on production of drug particles entrapped within polymers in microparticle [37], implant [38] or scaffold [39] form. Unlike the aforementioned methods, PGSS has the advantage in that it works in the absence of organic solvents and the polymer and drugs do not need to be soluble in $scCO_2$. However the polymer needs to be sufficiently plasticised by $scCO_2$. This is achievable at moderate temperatures (typically <40 °C) and pressures (<150 bar) which have been shown to have no adverse effect on the protein stability within controlled release PLGA/PLA formulations [30]. The use of the

16

PGSS procedure for producing a protein encapsulated polymer formulation is illustrated in Figure 1.12. The polymer and drug are initially added to a high pressure vessel (Figure 1.12-step1). CO_2 is added and the temperature and pressure are set to the critical conditions of CO_2 (Figure 1.12-step2). Then as a result, as shown in Figure 1.12-step3, the polymer liquefies. The plasticised mixture is then stirred with a helical impeller (Figure 1.12-step4) to mix the drug molecules with liquefied polymer until a homogenous mixture is formed as depicted in Figure 1.12-step5. This polymer/drug mixture is then let through a nozzle generating particles as shown in Figure 1.12-step6. Upon spraying, the CO_2 evaporates setting the shape of the particles as the polymer solidifies [31]. Using different nozzles, the particle shape and size can be controlled.

An important complication of this process may be that the escaping CO_2 can influence polymer morphology, for example generating macroporosity [40]. Further this process requires high precision equipment which is expensive both to modify for drug encapsulation and to maintain.
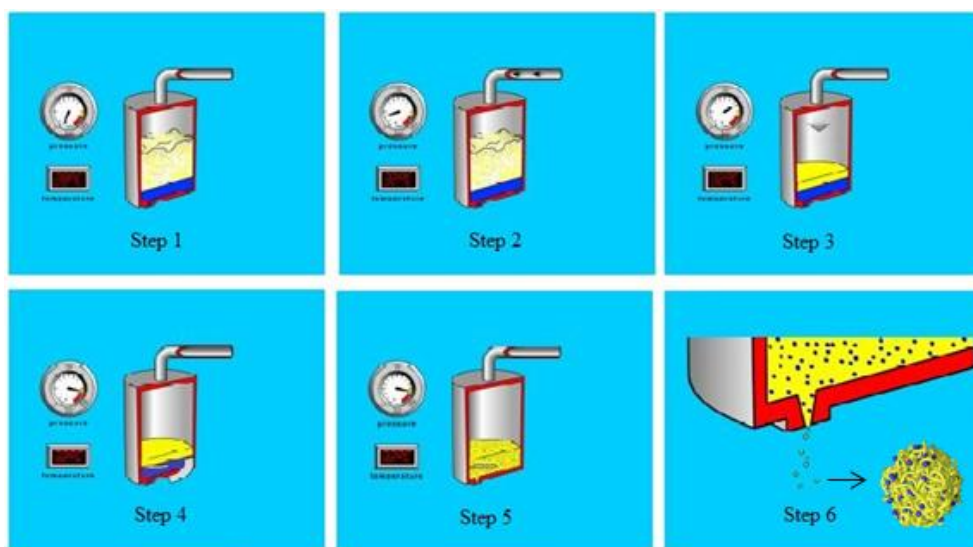
Figure 1.12 Schematic diagram of the processing steps of PGSS method (from [41]).

1.5.3.4.1 A Custom Built PGSS Apparatus-CriticalMix^TM

A high pressure particle rig was developed at University of Nottingham implementing the PGSS process to encapsulate drugs within polymer microparticles [42].

The CriticalMix^TM method is a novel PGSS approach developed using this rig, and was used to produce the microparticles characterised in this thesis as a simple, one-step

process with 100% encapsulation efficiency [37]. The workings of the method are briefly outlined below.

When suitable polymers, such as PLGA, PLA and protein particles, such as BSA, hGH, are exposed to scCO$_2$ in a pressure vessel, the polymer is liquefied, thereby allowing the protein to be mixed efficiently with the polymer. Following mixing, the mixture is depressurised through a nozzle whereby the CO$_2$ returns to a gaseous state and evaporates whilst the polymer solidifies around the protein, resulting in the production of microparticles with the protein distributed throughout.

For the formulations investigated in this thesis, a typical batch was prepared by adding 2.1 g of a pre-weighed combination of polymer, protein and excipients such as Poloxamer407 to the PGSS apparatus. The apparatus was sealed, pressurised with CO$_2$ to 700 psi (48 bar) and heated to 40 °C. Once at temperature, the pressure was increased to 2030 psi (140 bar). The liquefied protein/polymer mixture was then stirred at 150 rpm for 1 hour, after which time stirring was stopped and the mixture was depressurised through a nozzle generating microparticles. These were collected in a cyclone and recovered as a free flowing white powder.

1.6 Mid-IR Spectroscopic Imaging and Analysis Concept

The subject of this thesis is the development of mid-IR spectroscopic imaging and multivariate analysis applied to controlled release polymer microparticles to investigate kinetic processes, including degradation, drug release and particle morphology, 'visually' and 'quantitatively'.

A brief introduction is given here particularly to introduce the subject area for readers unfamiliar with chemical imaging and analysis concepts and to help better define the aims of the project.

Natural contrast arises from molecular vibrations in vibrational spectroscopy, magnetic effects in nuclear magnetic resonance imaging, electronic transitions in electron and x-ray microscopy, from chemical labels in near field optical microscopy, auto or enhanced fluorescence in fluorescence microscopy or surface topography (mechanically) in scanning probe microscopy (Figure 1.13). For polymers and proteins, chemical information is richest at mid-IR wavelengths, without the need of any dyes, complicated specimen preparation or radiation damage concerns. Also obtaining spatiotemporal images of samples under kinetic conditions raises few practical difficulties. MRI has

been 'the' other non-invasive and non-destructive imaging modality that facilitates internal and surface images (2D and 3D) of pharmaceuticals and living organisms on both micro and macro scale [43]. Figure 1.13 demonstrates that SEM is also well suited to the study of morphology and it requires relatively simple sample preparation.
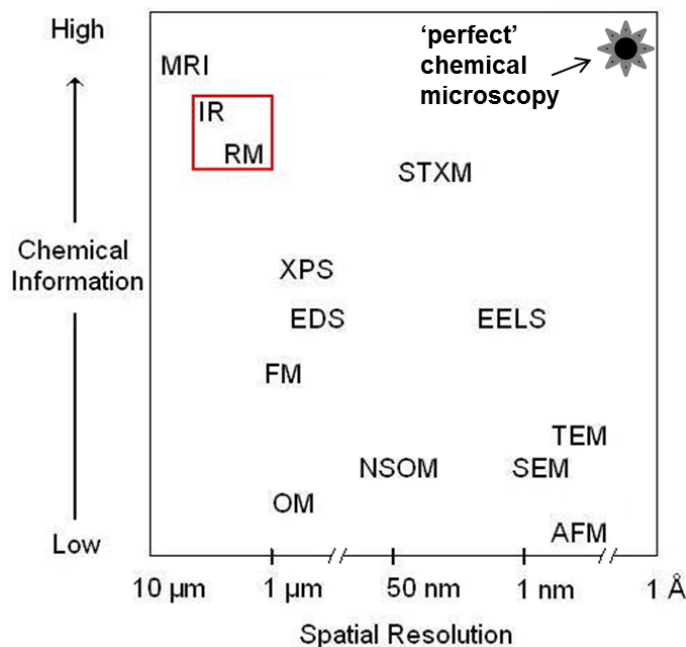
Figure 1.13 A comparison plot of well-established microscopy methods that particle systems can be studied with micron scale or better spatial resolution versus chemical information. Magnetic resonance imaging (MRI), vibrational chemical imaging (Raman and Infrared microscopic imaging, RM and IR, respectively), x-ray photoelectron spectroscopy (XPS), energy dispersive x-ray spectroscopy (EDS), scanning transmission x-ray microscopy (STXM), electron energy loss spectroscopy (EELS), transmission electron microscopy (TEM), scanning electron microscopy (SEM), fluorescence microscopy (FM), optical microscopy (OM), nearfield scanning optical microscopy (NSOM) and atomic force microscopy (AFM) (adapted from [44]).

Mid-IR imaging facilitates the generation of chemical images using an FPA detector where each of the pixels of the focal plane array (FPA) detector acts as an individual detector, allowing the collection of thousands of IR spectra simultaneously. A stack of 2D images can be collected within a few minutes, proving good temporal resolution in slow processes with a spatial resolution down to 5 µm depending on the sampling method used (Figure 1.14). However regardless of the sampling method (transmission, reflection etc.) or wavelength range used (IR, X-rays etc.), particularly for kinetic

experiments that last longer than a few hours, hyperspectral images often require detailed analysis once collected.
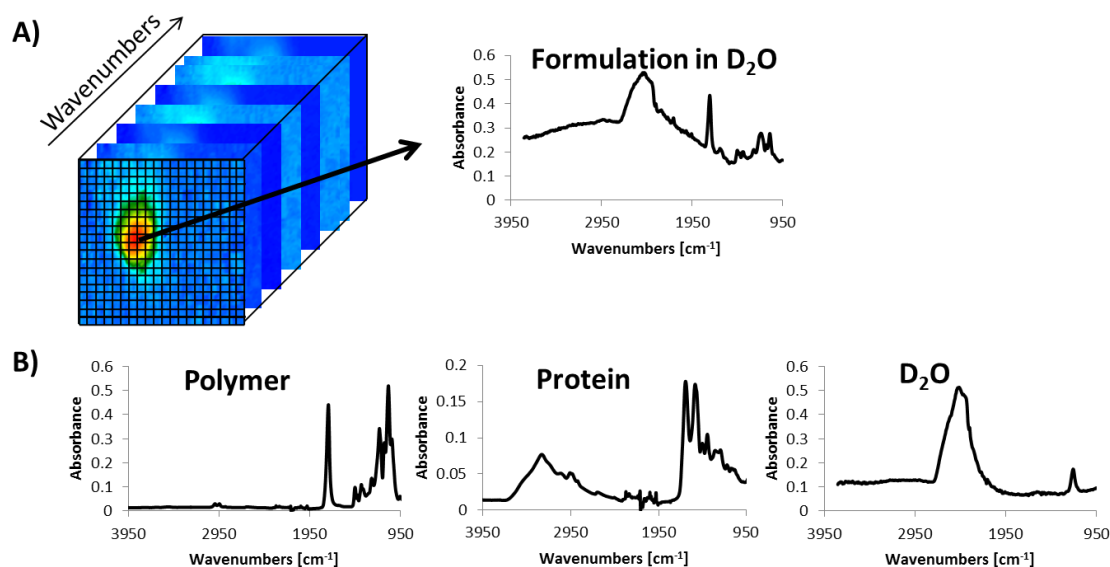
Figure 1.14 Mid-infrared spectroscopic image stack of a protein loaded polymer microparticle in water, showing a pixel spectrum on the right (A) and pure component spectra (B) therein to be extracted from formulation spectra for each pixel.

1.7 Project Aims

The preliminary aim of this project has been to investigate and fine-tune the application of mid-IR imaging to characterise $scCO_2$ processed 'dry' microparticle formulations as received. This is based on determining their changing components' distributions, particularly the drug distribution throughout individual microparticles using available sampling methods (described in Chapter 2) and relevant multivariate data analysis methods (described in Chapter 3).

Following dry state characterisation of model drug loaded PLGA microparticles, the next objective was to optimise the experimental conditions such that the first kinetic imaging study on real-time hydrolysis of a single PLGA microparticle was conducted. Further objectives related to this novel experiment were to improve this temporal hyperspectral data set which had decreasing SNR over time, in terms of spatial resolution and SNR, using soft multivariate methods and developing a hard modelling method to obtain and compare the most important information of such experiment, degradation rate. Visual and quantitative evidence on particle's morphology exhibiting

physicochemical phenomena such as swelling, shrinking and eroding was also investigated using soft and hard modelling approaches.

Developing this proof of concept, a further objective, emerging immediately, was to study PLGA copolymer microparticles with *L/G* molar compositions of 100/0, 75/25 and 50/50 at 50 ºC and 70 ºC to investigate and compare effects on their degradation rates, again for the first time utilising mid-IR imaging and multivariate analysis.

ATR-FTIR imaging has been a fast progressing method used to study drug release in semisolid formulations, drug penetration, and the influence of penetration modifiers *in situ* commonly at sample-solution interfaces. However there has been lack of literature in studying evolution of single microparticles during dissolution. Hence it was of interest to see and monitor drug redistribution and release in such systems and to correlate such data to conventional drug dissolution methods.

Consequently an aim was set to demonstrate the feasibility of the ATR geometry for monitoring drug release *in situ* from PLGA microparticles and to utilise data analysis methods to extract associated drug release profiles.

Pharmaceuticals often need to be sterilised before use. Finally mid-IR imaging and analysis were used for visualising and rationalising the effect of gamma irradiation (a common sterilisation method for biodegradable polymer based drugs) on a pipeline product of the collaborating company that has shown successful *in vivo* and *in vitro* sustained release for the delivery of hGH.

The overall aim of this project can be summarised as the development of mid-IR imaging and analysis as a standalone toolbox for studying kinetic processes in biopolymeric microparticles. This was assisted mainly by verification of morphology using SEM, thermal properties using DSC, dissolution testing using UV-spectrophotometry and molecular weight using GPC.

1.8 References

[1] C.F. van der Walle, O. Olejnik, Chapter 1 - An Overview of the Field of Peptide and Protein Delivery, in: C.F. van der Walle (Ed.), Peptide and Protein Delivery, 1st ed., Academic Press, Boston, 2011, pp. 1-22.

[2] S.S. Davis, L. Illum, S. Stolnik, Polymers in drug delivery, Current Opinion in Colloid & Interface Science. 1 (1996) 660-666.

[3] R.C. Mundargi, V.R. Babu, V. Rangaswamy, P. Patel, T.M. Aminabhavi, Nano/micro technologies for delivering macromolecular therapeutics using poly(d,l-lactide-co-glycolide) and its derivatives, Journal of Controlled Release. 125 (2008) 193-209.

[4] C. Wischke, S.P. Schwendeman, Principles of encapsulating hydrophobic drugs in PLA/PLGA microparticles, Int. J. Pharm. 364 (2008) 298-327.

[5] H. Staudinger, Ketene, eine neue Körperklasse, Berichte der deutschen chemischen Gesellschaft. 38 (1905) 1735-1739.

[6] O. Pillai, R. Panchagnula, Polymers in drug delivery, Curr. Opin. Chem. Biol. 5 (2001) 447-451.

[7] Walton D , Lorimer P, Polymers, Oxford University Press, New York, 2000.

[8] J. M. G. Cowie, V. Arrighi, Polymers: Chemistry and Physics of Modern Materials, 3rg ed., CRC Press, UK, 2008.

[9] P.L. D. Walton, Polymers, Oxford University Press, New York, 2000.

[10] G. Dumortier, J. L.Grossiord, F. Agnely, J. C. Chaumeil, A Review of Poloxamer 407 Pharmaceutical and Pharmacological Characteristics, Pharmaceutical Research. 23 (2006) 2709-2728.

[11] S. Inkinen, M. Hakkarainen, A. Albertsson, A. Sodergard, From Lactic Acid to Poly(lactic acid) (PLA): Characterization and Analysis of PLA and Its Precursors, Biomacromolecules. 12 (2011) 523-532.

[12] C.E. Astete, C.M. Sabliov, Synthesis and characterization of PLGA nanoparticles, Journal of Biomaterials Science, Polymer Edition. 17 (2006) 247-289.

[13] J. M. Anderson , M. S. Shive, Biodegradation and biocompatibility of PLA and PLGA microspheres, Advanced Drug Delivery Reviews. 28 (1997) 5-24.

[14] E. Vey, C. Rodger, J. Booth, M. Claybourn, A.F. Miller, A. Saiani, Degradation kinetics of poly(lactic-co-glycolic) acid block copolymer cast films in phosphate buffer solution as revealed by infrared and Raman spectroscopies, Polym. Degrad. Stab. 96 (2011) 1882-1889.

[15] M.L. Houchin, E.M. Topp, Chemical degradation of peptides and proteins in PLGA: a review of reactions and mechanisms, Journal of pharmaceutical sciences. 97 (2008) 2395-2404.

[16] G. Dumortier, Grossiord J.L., F. Agnely, J.C. Chaumeil, A review of poloxamer 407 pharmaceutical and pharmacological characteristics, Pharmaceutical Research. 23 (2006) 2709-2728.

[17] J.M. Berg, J.L. Tymoczko, L. Stryer , Protein Structure and Function, in: J.M. Berg (Ed.), Biochemistry, 5th ed., W.H. Freeman, New York, 2002, pp. Chapter 3.

[18] K. Fu, K. Griebenow, L. Hsieh, A.M. Klibanov, R. Langera, FTIR characterization of the secondary structure of proteins encapsulated within PLGA microspheres, J. Controlled Release. 58 (1999) 357-366.

[19] A. Aitken, M. Learmonth, Protein Determination by UV Absorption, in: J. Walker (Ed.), Humana Press, 2002, pp. 3-6.

[20] X.M. He, J.X. Carter, Structure of human serum albumin, Science. 249 (1990) 302-303.

[21] J. M. Tanner, R. H. Whitehouse, P. C. R. Hughes and F. P. Vince, Effect of Human Growth Hormone Treatment for 1 to 7 Years on Growth of 100 Children, with Growth Hormone Deficiency, Low Birthweight, Inherited Smallness, Turner's Syndrome, and Other Complaints, Archives of Disease in Childhood. 46 (1971) 745.

[22] I. Gomez-Orellana, B. Varinano, J. Miura-Fraboni, S. Milstein, D.R. Paton, Thermodynamic characterization of an intermediate state of human growth hormone, Protein Science. 7 (1998) 1352-1358.

[23] http://www.niro.com/NIRO/cmsdoc.nsf/WebDoc/webb8ckjc8, December 2013.

[24] http://www.malvern.de/ProcessEng/processes/spraydrying/overview.htm, December 2013.

[25] S. Guerrero, E. Muñíz, C. Teijón, R. Olmo, J.M. Teijón, M.D. Blanco, Ketotifen-loaded microspheres prepared by spray-drying poly(D,L-lactide) and poly(D,L-lactide-co-glycolide) polymers: Characterization and in vivo evaluation, J. Pharm. Sci. 97 (2008) 3153-3169.

[26] P.A. Rivera, M. Martinez-Oharriz, M. Rubio, J.M. Irache, S. Espuelas, Fluconazole encapsulation in PLGA microspheres by spray-drying, J. Microencapsul. 21 (2004) 203-211.

[27] S.C. Tucker, Solvent Density Inhomogeneities in Supercritical Fluids, Chem. Rev. 99 (1999) 391-418.

[28] C. de la Tour , C., Annales des Chimie et des Physique. 22 (1822) 127-132.

[29] J. Williams, A. Clifford, S. Al-Saidi, Supercritical fluids and their applications in biotechnology and related areas, Mol. Biotechnol. 22 (2002) 263-286.

[30] C.A. Kelly, S.M. Howdle, A. Naylor, G. Coxhill, L.C. Tye, L. Illum, A.L. Lewis, Stability of human growth hormone in supercritical carbon dioxide, J. Pharm. Sci. 101 (2012) 56-67.

[31] O.R. Davies, A.L. Lewis, M.J. Whitaker, H. Tai, K.M. Shakesheff, S.M. Howdle, Applications of supercritical CO2 in the fabrication of polymer systems for drug delivery and tissue engineering, Adv. Drug Deliv. Rev. 60 (2008) 373-387.

[32] J.W. Tom, Lim Gio-Bin, P.G. Debenedetti, R.K. Prud'homme, Applications of Supercritical Fluids in the Controlled Release of Drugs, in: Anonymous American Chemical Society, 1992, pp. 238-257.

[33] N. Elvassore, A. Bertucco, P. Caliceti, Production of insulin-loaded poly(ethylene glycol)/poly(l-lactide) (PEG/PLA) nanoparticles by gas antisolvent techniques, J. Pharm. Sci. 90 (2001) 1628-1636.

[34] A.R.C. Duarte, M.S. Costa, A.L. Simplício, M.M. Cardoso, C.M.M. Duarte, Preparation of controlled release microspheres using supercritical fluid technology for delivery of anti-inflammatory drugs, International journal of pharmaceutics. 308 (2006) 168-174.

[35] M.D. Donohue, J.L. Geiger, A.A. Kiamos, K.A. Nielsen, Reduction of Volatile Organic Compound Emissions During Spray Painting, in: Anonymous American Chemical Society, 1996, pp. 152-167.

[36] J. Kerč, S. Srčič, Ž Knez, P. Senčar-Božič, Micronization of drugs using supercritical carbon dioxide, Int. J. Pharm. 182 (1999) 33-39.

[37] M.J. Whitaker, J. Hao, O.R. Davies, G. Serhatkulu, S. Stolnik-Trenkic, S.M. Howdle, K.M. Shakesheff, The production of protein-loaded microparticles by supercritical fluid enhanced mixing and spraying, J. Controlled Release. 101 (2005) 85-92.

[38] V.K. Popov, A.V. Evseev, E.N. Antonov, V.N. Bagratashvili, A.N. Konovalov, V.Y. Panchenko, J.J.A. Barry, M.J. Whitaker, S.M. Howdle, Laser technologies for fabricating individual implants and matrices for tissue engineering, J. Opt. Technol. 74 (2007) 636-640.

[39] H. Tai, M.L. Mather, D. Howard, W. Wang, L.J. White, J.A. Crowe, S.P. Morgan, A. Chandra, D.J. Williams, S.M. Howdle, K.M. Shakesheff, Control of pore size and structure of tissue engineering scaffolds produced by supercritical fluid processeing, European Cells and Materials. 14 (2007) 64-77.

[40] J. Hao, M.J. Whitaker, B. Wong, G. Serhatkulu, K.M. Shakesheff, S.M. Howdle, Plasticization and spraying of poly (DL-lactic acid) using supercritical carbon dioxide: control of particle size, J. Pharm. Sci. 93 (2004) 1083-1090.

[41] http://www.criticalpharmaceuticals.com, November 2011.

[42] J. Hao, M.J. Whitaker, G. Serhatkulu, K.M. Shakesheff, S.M. Howdle, Supercritical fluid assisted melting of poly(ethylene glycol): a new solvent-free route to microparticles, J. Mater. Chem. 15 (2005) 1148-1153.

[43] J.C. Richardson, R.W. Bowtell, K. Mäder, C.D. Melia, Pharmaceutical applications of magnetic resonance imaging (MRI), Adv. Drug Deliv. Rev. 57 (2005) 1191-1209.

[44] http://www.lightsource.ca/files/download.php?id=2707&view=1, December 2013.

2 Experimental Methods and Data Analysis

2.1 Fourier Transform Infrared Spectroscopy

2.1.1 Infrared Theory

2.1.1.1 *Infrared (IR) Radiation*

Light is an electromagnetic wave. Electromagnetic waves 'radiate' from electrically charged particles as the particles move in a magnetic field, thus light is also called electromagnetic 'radiation'. Electromagnetic radiation occurs, as electric and magnetic waves undulate in planes perpendicular to each other, in the direction of the third Cartesian coordinate that is perpendicular to the first two. Motion of electromagnetic waves can fundamentally be described as an oscillation following simple harmonic motion and therefore the amplitude of the electric vector is often illustrated by a sine function as shown in Figure 2.1. Distance that a wave can travel during time that takes to complete a repeating period (T), or a cycle, is its wavelength (λ).

In vibrational spectroscopy commonly the number of waves per unit length called wavenumber in 1/cm is used instead of wavelength as it is proportional to energy therefore easier to interpret.
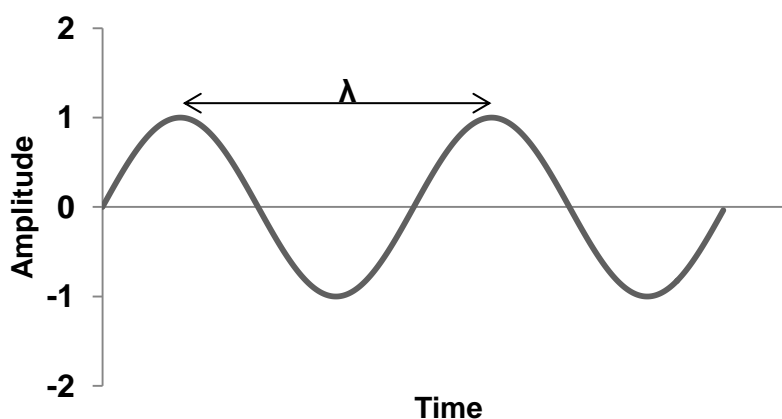
Figure 2.1 Electric vector amplitude of a light wave.

Electromagnetic radiation can also be defined as a stream of particles (photons), travelling at the speed of light ($c=3\text{x}10^8$ m/s), that have no mass but energy (E) that is related to their frequency (v) according to Planck's equation;

$$E = h v = h\frac{c}{\lambda}$$

Equation 2.1

where h=6.626 x 10^{-34} Js is the Planck's constant.

The full range of photon energies are listed in a chart, so-called electromagnetic spectrum (Figure 2.2a). The IR region of the electromagnetic spectrum includes near-infrared (NIR), mid-infrared (MIR) and far-infrared (FIR) (Figure 2.2b). In this thesis the terms 'infrared' or 'IR' are used to indicate the mid-IR region, that is wavelengths between 25 and 2.5 μm (or wavenumbers from 4000 cm^{-1} to 400 cm^{-1}).
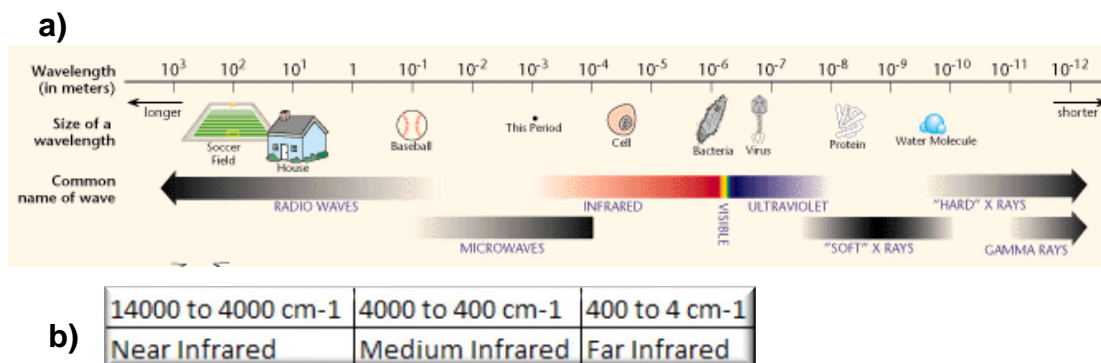
Figure 2.2 (a) Electromagnetic spectrum (adapted from [1]) and (b) The part of EM spectrum, in wavenumbers, that FTIR spectroscopy is related to.

2.1.1.2 Molecular Vibrations

The total energy of a molecule consists of its electronic, vibrational, rotational and translational energy levels. Unlike shorter wavelength radiation, IR radiation cannot excite electrons but can cause a change in a molecule's net dipole moment inducing transitions between quantized vibrational energy levels. An electronic energy level of a molecule can be divided in to a number of vibrational states and each vibrational state includes multiple rotational states. FIR and microwave radiation, having lower energy than rest of the IR region, can induce rotational energy level transitions that match energy levels of molecules made of heavy atoms and/or weak bonds. The theory of vibration-rotation spectroscopy and near infrared spectroscopy will not be discussed because they are beyond the scope of this thesis.

A non-linear molecule with N atoms can exhibit translational motion and rotational motion in 3 orthogonal directions, x, y and z, excluding these; a molecule has 3N-6 degrees of freedom that is the number of ways that the atoms of the molecule can vibrate. For a linear molecule the number vibrational modes is 3N-5 as it has 2 rotational modes instead of 3. As one can imagine, these vibrations result either a periodic change in bond length (stretching) or a periodic change in bond angle

28

(bending). For multiple bonds, the stretching mode can be symmetric or antisymmetric and four types of bending modes are possible, namely; scissoring, rocking, wagging and twisting. Visual illustration of these modes is demonstrated in many web sites including [2].

Vibration of a diatomic molecule, that is confined to stretching only as explained above, can be approximated to simple harmonic oscillation of 2 masses connected with a spring in space following Hook's law and their motion is determined by the causing force as;

$$F = -kx \hspace{4cm} \textbf{Equation 2.2}$$

where k is the spring constant and x is displacement. Potential energy of this system is;

$$E = \frac{1}{2}kx^2 \hspace{4cm} \textbf{Equation 2.3}$$

Since vibrational energies are quantised vibrational energy of the modes that approximated to simple harmonic motion, or Hooke's law, can be calculated from the Schrodinger equation to reflect this as;

$$E_v = hv\left(n + \frac{1}{2}\right) \hspace{3cm} \textbf{Equation 2.4}$$

where n=0, 1, 2, 3, … is the vibrational quantum number.
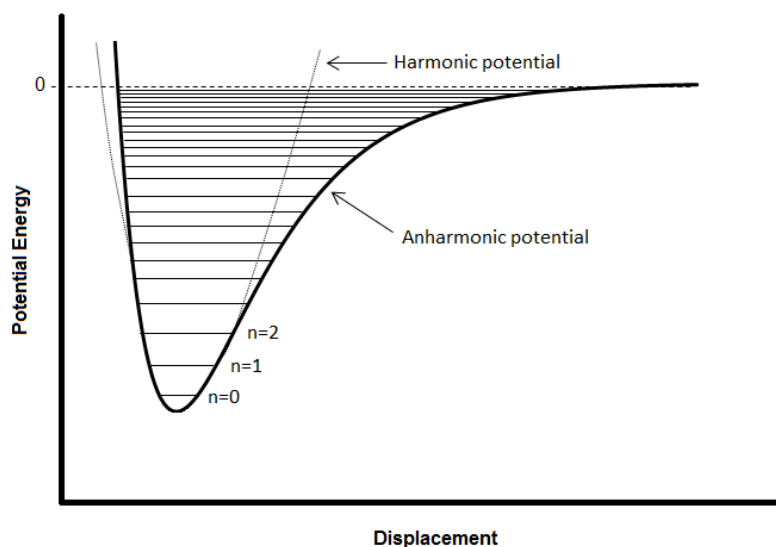
Figure 2.3 Potential energy of a diatomic molecule following Hooke's law and an anharmonic oscillator (adapted from [3]).

In practice Equation 2.4 should be derived from a Morse-type or anharmonic potential function because real molecular vibrations are not harmonic, i.e. bonds do not obey

Hooke's law, therefore potential energy of real molecules deviate from simple harmonic oscillator approximation as anharmonicity arises (Figure 2.3).

The energy levels including anharmonicity effect can be approximated as;

$$E_v = hv\left(n + \frac{1}{2}\right) + hv\alpha\left(n + \frac{1}{2}\right)^2 \qquad \textbf{Equation 2.5}$$

where is α is the anharmonicity constant.

To move a molecule from one energy level to another (i.e. from E=0 to E=1), in order to induce IR bands, molecular vibrations must cause a change in the dipole moment of the molecule. This is called 'the selection rule' and for example O_2 and N_2 do not reveal IR bands because their stretch vibration does not cause a change in their dipole moments. Commonly observed transitions postulated by Equation 2.5 are; n=1←0 (fundamental), n=2←0 (1st overtone) and n=3←0 (2nd overtone).

2.1.1.3 Beer's Law

The Bouguer-Lambert-Beer law (or Beer's law for short) is the foundation for all quantitative absorption spectroscopy relating number of molecules sampled to incident (I_0) and transmitted (I) beam intensity as;

$$I = I_0 \exp(-\epsilon cl) \qquad \textbf{Equation 2.6}$$

where c is the concentration, ε is the frequency dependent extinction coefficient and l is the cell thickness.

2.1.2 Fourier Transform Infrared Spectrometry

FT instruments dominate the infrared spectrometry market as they are advantageous to dispersive instruments, in that; firstly there is no slit therefore higher throughput can be achieved from source to detector (Jacquinot advantage), secondly all frequencies are simultaneously detected (the multiplex or Fellgett's advantage), thirdly better frequency accuracy is obtained employing a superimposed laser beam to compare and correct spectra (Connes advantage). And FT computation takes almost no time with today's conventional computers therefore it is never a handicap. However, FT instruments use a single beam therefore unlike dispersive instruments, a channel ratio correction cannot be applied and as a result atmospheric components (water vapour, CO_2) will be detected. To circumvent this, instruments are purged with dry N_2 or air and a background spectrum is ratioed against each spectrum collected. Since the background and sample

cannot be measured simultaneously and the possibility of background mis-match is permanent due to variations in atmosphere of the experimental environment, this drawback can never be totally overcome but may be minimised by efficient post processing. The other major practical difficulty in infrared spectroscopy has been the analysis of mixtures. Although some mixtures can be purified and therefore their components can be measured separately, the interest in infrared spectroscopy rises from its ability to measure 'as is' particularly in pharmaceutical and biological research. Therefore post processing of spectroscopic data has been developing in parallel to IR spectrometry.

2.1.2.1 *Instrumentation*

Conventional FTIR instruments consist of a spectrometer including an IR source, a Michelson interferometer and a laser following the IR beam, and a detector.

Unlike most short wavelength spectroscopy techniques, such as x-ray microscopy, that are confined to synchrotrons due to the necessity of a bright source that is yet unavailable at laboratory scale, producing an IR beam has been the easiest technical part of table top IR spectrometry as an air-cooled, heated ceramic source can produce an intense IR beam for several years. Brighter and much more consistent sources than incandescent ones are available at free electron laser (FEL) facilities and at synchrotrons however at the expense of long waiting times (typically less than a year) and user fees.

Since its invention in late 19th century, same design of the Michelson's interferometer still forms the basis of almost all interferometers today. In the Michelson interferometer a beam of radiation is split into two paths and then recombined after a path difference has been introduced (Figure 2.4) [4].
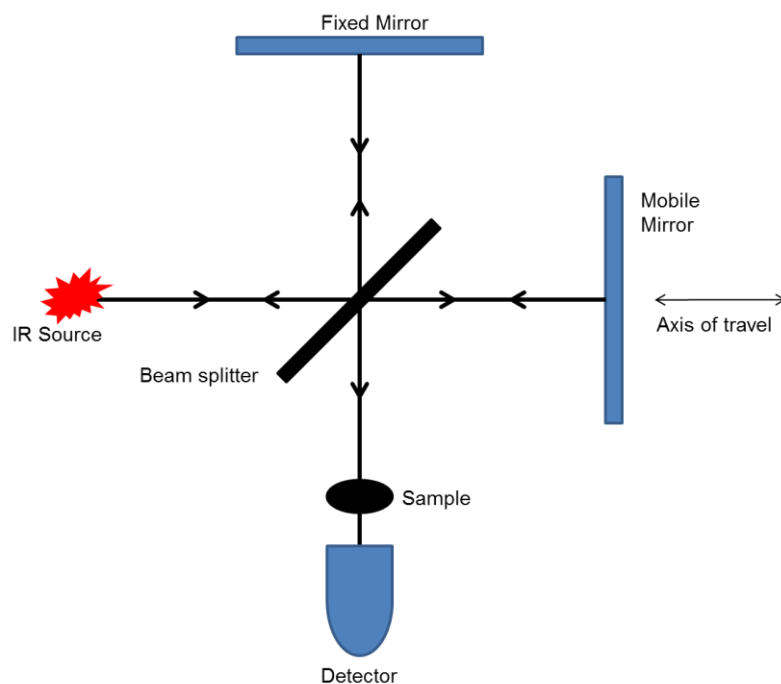
Figure 2.4 Layout of the Michelson interferometer.

A non-absorbing beam splitter reflects one part of the beam to a fixed mirror and transmits the other part to a moving mirror that is mutually perpendicular to the fixed mirror. Reflected beams interfere back again at the beam splitter where they are partially reflected and partially transmitted towards the detector. Therefore a relation of the variation in the intensity of the beam reaching the detector and the path difference can be established. In order to yield the spectral information, the data from the interferometer in time domain need to be converted in to data in frequency domain using a Fourier Transform (FT) given as;

$$I(v) = \int_{-\infty}^{\infty} f(t)e^{-2\pi ivt}dt \qquad \textbf{Equation 2.7}$$

where *I(v)* and *f(t)* are the frequency domain and time domain points, respectively.

Depending on the movement of the mobile mirror there are two modes of interferometers; step-scan mode in which the mirror is held equally at spaced points and continuous-scan mode (or rapid-scan) in which the mirror is stepped rapidly between these points. Most FT-IR spectrometers currently in use work in latter mode where signal to noise ratio (SNR) of the spectrum is improved by repeated measurement and co-addition of the interferograms such that;

$$SNR \; \alpha \; \sqrt{number \; of \; scans} \qquad \textbf{Equation 2.8}$$

Every FTIR instrument contains a laser, usually helium-neon (He-Ne) that measures the optical path difference of the interferometer.

An infrared detector is effectively a transducer, transforming light into electrical signal. Pyroelectric materials whose properties change with temperature, or photoconductive materials whose electrons can be excited by IR photons are the two main types used in producing IR detector elements. An IR transparent window is also used to protect the detector elements from environment. A common type of thermal detector element is deuterated triglycine sulphate (DTGS). The electrical polarization of DTGS fluctuates with temperature, triggering a current flow which is then measured and calibrated in order to trace the amount of IR light. A typical DTGS detector is 1mm square and with a KBr window it can cover the whole Mid-IR region. However, although cheap and self-cooling, DTGS detectors are rather slow and noisy compared to photodetectors. An alloy of Mercury, Cadmium and Telluride (MCT) is the most common photoconductor material. In MCT detectors the speed of response and sensitivity are about an order of magnitude better than DTGS detectors however they are relatively expensive, their lower energy end cut off is ~700 cm^{-1} and operating temperatures are low (~75 K) therefore MCTs need to be cooled with liquid N_2. Single point MCT detector elements are typically 250 µm square.

2.1.2.2 Sampling Techniques

When a beam of light is focused on a sample, up on interaction, it may be reflected, refracted, transmitted or absorbed. All of these modes may facilitate to probe vibrational characteristics of a sample however among these, transmission and reflection have been most popular due to relatively simple sample preparation and ease of experiments [4].

The transmission method requires relatively thin samples (<~10µm for IR), therefore microtomy or some other form of preparation may be necessary. Among common IR reflectance techniques, specular reflectance, diffuse reflectance, and attenuated total reflectance (ATR), the latter is the most common particularly in pharmaceutical research as it requires no sample preparation and allows *in situ* characterisation under changing conditions.

2.1.2.2.1 ATR-FTIR

Attenuated total reflection has been the most widely practiced technique in IR spectroscopy [4] because unlike transmission sampling where samples may require grinding, microtoming, melting, use of KBr discs, cast films or mineral oils mulls, disks

or another form of sample preparation that cause morphological changes on the sample, ATR sampling does not require any sample preparation because the IR light is not transmitted therefore even powders or fabrics can be studied as long as a 'good contact' with the ATR crystal is achieved [5]. The definition of a good contact for the samples studied in this thesis (polymer microparticles) is discussed in detail in Chapter 2, Section 2.1.2.2.1. However it is necessary to note here that contact for samples with non-uniform morphology will be difficult to reproduce, therefore quantitative analysis may be difficult in single point analysis as the ratio of signal from good contact regions to signal from poor contact regions will be different for different experiments, causing inconsistent peak intensities when the two are averaged due to having 1 pixel, even though the sample is the same.

The use of ATR sampling in infrared spectroscopy is based upon the fact that, when a crystal of a material with high refractive index n_1 (the ATR crystal), such as diamond (n=2.4), zinc selenide (n=2.4), silicon (n=3.4), or germanium (n=4.0) is brought into contact with the sample with a lower refractive index n_2 (for polymers n=~ 1.5) although total internal reflection occurs at the sample–crystal interface, radiation does in fact penetrate a short distance into the sample, this is known as the evanescent field. The distance that the evanescent field can travel within a sample in direct contact with the ATR crystal is defined as the depth of penetration (d_p). Harrick and DuPre [6] defined dp as the value at which the initial electric field strength (E_o) decays to a value of $E_o exp^{-1}$ and can be given as;

$$d_p = \frac{\lambda}{2\pi n_1 \sqrt{sin^2\theta - (n_1/n_2)^2}}$$ **Equation 2.9**

where θ is the angle of incidence that is greater than the critical angle ($\theta_c = sin^{-1}(n_1/n_2)$) (Figure 2.5).
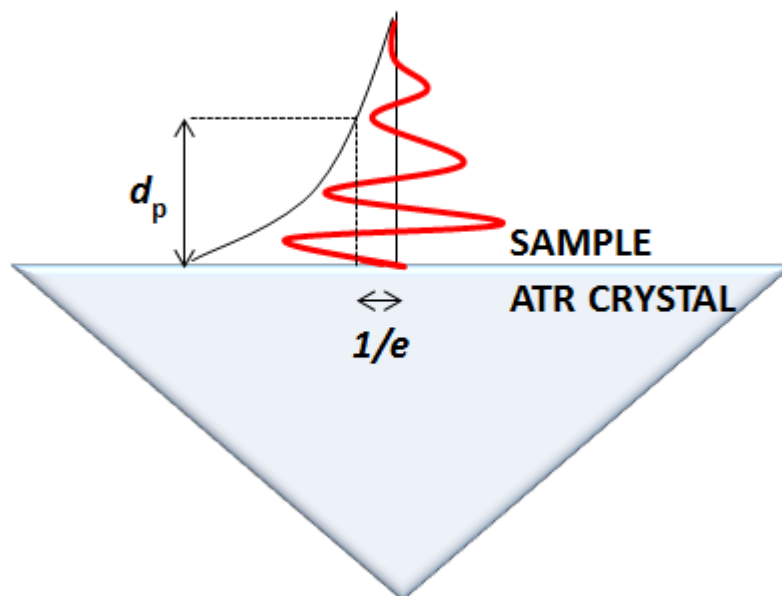
Figure 2.5 Schematic representation of attenuated total reflection (reproduced from [7]).

In practice, shown by Mirabella, the true depth of penetration is ~3 times more than the calculated d_p value [8]. Clearly, ATR only probes the near-surface of a sample but this permits the study of 'difficult samples' such as samples in aqueous media (n_2= ~1.33), strongly absorbing and/or thick solids which can be very challenging using traditional approaches such as transmission.

2.1.3 FTIR Imaging with Focal Plane Array Detectors

Hyperspectral imaging by probing molecular vibrations can be achieved through the measurement of either the infrared or Raman spectrum. Coupling the speed and chemical selectivity of table top mid-infrared spectrometer, with or without a microscope, with the regional selectivity of a focal plane array (FPA) IR detector, replacing the aforementioned single point detector, allows fast (typically a few minutes) global imaging facilitating remarkable insight into a wide range of processes in the mid-infrared region where the most of vibrational chemical information is hidden.

Using a microscope and moving stage, Harthcock and Atkin obtained the first chemical MIR map [9]. Since the first demonstration of use of FPA in mid-IR spectrometry [10], the advancements in the imaging technology peaked such that over the last two decades Fourier transform infrared (FTIR) spectroscopic imaging has become routine, facilitating chemical characterization of multicomponent systems under both static and kinetic conditions [11].

In comparison to microspectroscopy where an image is obtained by point or line mapping using a single point or 1D array detector, respectively, global imaging can be considered to be advantageous, at least practically, since generating same number of pixels with same spectral resolution and number of scans, point or line mapping will take at least 10 times longer than that of global imaging. However since SNR and spectral resolution of mapping systems are better than global imaging systems, IR microscopes are often equipped with both a single point and FPA detector where the former is used when point specific information is more valuable than widefield IR spectral data.

The detection of IR light has probably been the most expensive and challenging part of IR instrumentation during the leap from single point detection to line mapping and finally imaging which has been purely dependant on detector development. MCT plane array detectors are the most commonly used mid-IR detector due to wide spectral sensitivity (from 2 μm to 20 μm), depending on the mercury/cadmium concentration ratio. A 64x64 pixel MCT FPA detector (Santa Barbara Focal plane) on which the physical size of each FPA pixel is 40 μm x 40 μm was used in this project. Depending on the magnification of optical setup used in each sampling method, the image pixel size varies as outlined below.

An Agilent 680-IR spectrometer with an achievable spectral resolution of 2 cm^{-1} was used in rapid-scan mode for this thesis.

In an IR microscope Cassegrainian objectives are used for focusing the beam instead of glass lenses (which are impenetrable for IR radiation). The objective illuminates the sample, and after passing through (transmission mode (Figure 2.6a)) or reflecting off (micro-ATR mode) or passing and reflecting off (transflection) the specimen, the infrared light is collected by the condenser. An optical image can also be obtained beforehand using the objectives (15x or 4x for the instrument used here). For defining the area of interest on the optical image, in most cases rectangular apertures are used, usually located in a remote image plane. In the microscope (Agilent Technologies' UMA620) used in this project a field of view of 350 μm x 350 μm can be imaged. A larger field of view for transmission mode with no magnification (2.56 x 2.56 mm) is also possible when the microscope is eliminated and the IR beam is diverted straight to the detector, however this comes with worse spatial resolution of ~40 μm and the

sample needs to be in between two IR transparent (i.e. CaF$_2$, KBr) slides or held on its own vertically, although difficult to reproduce, in the spectrometer compartment.

In infrared absorption-reflection or transmission-reflection, often referred to as transflection, mode in which IR beam passes through a sample, reflects back from a reflective surface behind and passes back through the sample again, samples need to be relatively thin (<10 μm) and laid upon very smooth metal surfaces, preferably gold deposited thin films (Figure 2.6b). In the microscope the IR beam from the FTIR spectrometer is diverted with Cassegrain type objectives on to the sample and the transmitted signal, collected by the same objective lenses, is focused on to the MCT-FPA.

The ATR sampling can be achieved in two modes, micro and macro.

Micro ATR imaging is performed with an infrared microscope similar to transflection but a Ge hemispherical internal reflection element that acts like an oil immersion lens is used for internally reflecting the incident beam therefore a better spatial resolution is achieved without requiring the sample to be thin (Figure 2.6c). However this comes at the expense of a smaller field of view (64 μm x 64 μm) that can be obtained through 64x64 pixels of the FPA detector.

The macro ATR (Specac Golden Gate^{TM}, diamond) imaging setup does not include a microscope and the IR beam from the spectrometer is directly detected with the MCT-FPA after reflecting through the sample on the diamond crystal (Figure 2.6d). Although this results in worse spatial resolution due to lower magnification, the imaging field of view is increased (640 μm x 640 μm). The hardness of the diamond allows compaction to be performed directly on the surface of the ATR crystal and enables temperature control. Therefore *in situ* studies are facilitated well in macro-ATR mode.

Equation 2.9 also shows that a good optical contact between the sample and ATR crystal is critical for obtaining a uniform absorbance profile avoiding artefacts within the field of view. The Golden Gate^{TM} Imaging Single Reflection Diamond ATR Accessory (Specac Ltd.) has corrective optics that adjust the plane of best focus to be situated on the crystal surface thus minimising any distortion and an auto-levelling sapphire anvil that ensures a uniform contact between the crystal and sample [12].
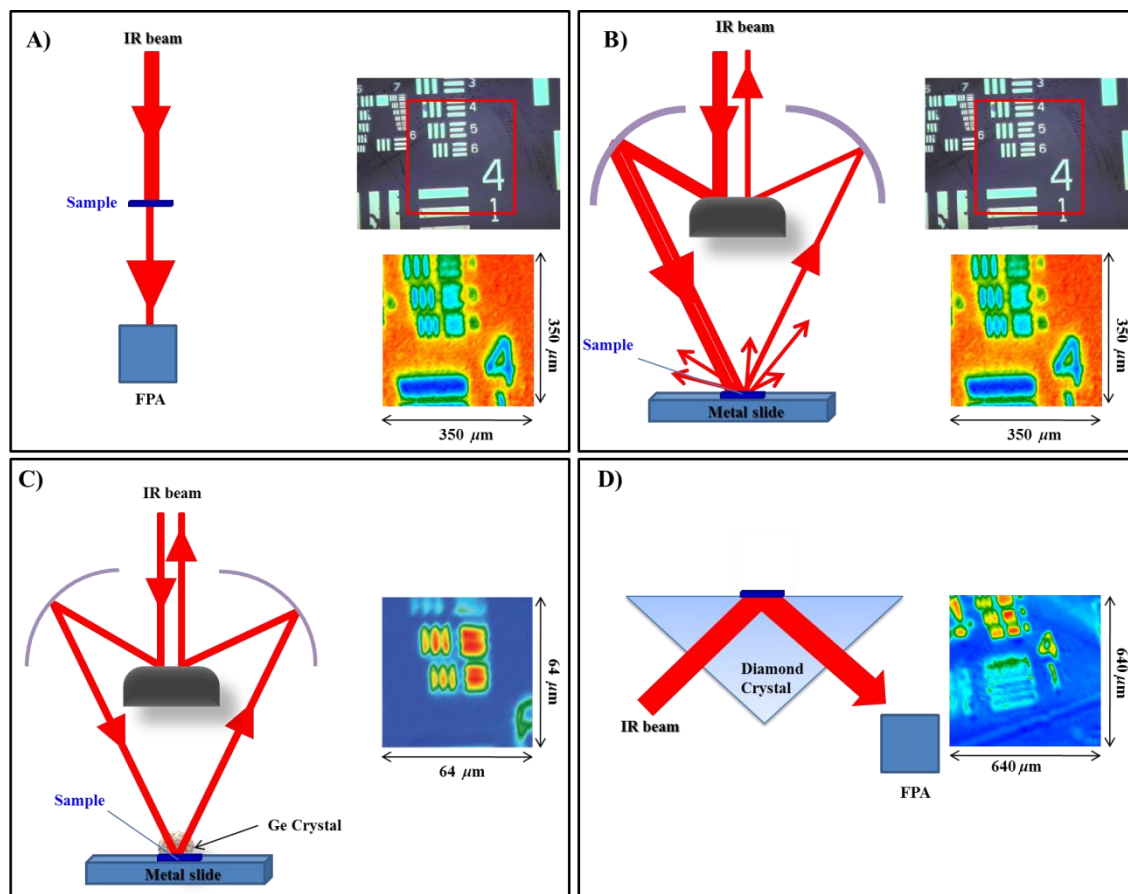
Figure 2.6 FTIR imaging sampling techniques; a) Transmission, b) Transflection, c) Micro-ATR and d) Macro-ATR, where a false colour USAF 1951 1X 38257 target image is given on the right at 2000 cm^{-1} wavenumbers (below a white light image in (a) and (b)) showing the smallest features that can be resolved in each method respectively (adapted from [7]).

2.1.3.1 Spatial Resolution

The spatial resolution of a microscope is theoretically determined by the diffraction of radiation i.e. the Rayleigh criterion, which is defined in Equation 2.10 as

$$r = 0.61 \frac{\lambda}{NA} \qquad \textbf{Equation 2.10}$$

where λ is the wavelength and *NA* is the numerical aperture (the refractive index of the medium between sample and objective, multiplied by half the opening angle of the objective). This implies that two objects are totally resolved if they are separated by 2r. Under these conditions, 2r is the definition of spatial resolution. However in an infrared imaging system, FPA detector pixels are not points and have a finite size that is greater than the wavelength of the IR light, therefore this relation is never observed. Therefore for FPA imaging systems it has been shown to be more appropriate to determine the spatial resolution based on real measurements. The smallest features resolved in each

sampling method by using a test sample, USAF 1951 1X 38257 target, which has grouped rectangular features of Chromium deposited on a soda glass, are listed in Table 2.1. Spatial resolution of FTIR imaging instruments is discussed in more detail, including the application of a numerical method for measuring it, in Chapter 3.

Table 2.1 List of achievable spatial resolution and field of view for common sampling methods in table-top FTIR imaging.

MODE	Transflection	Transmission (micro)	Micro-ATR (Ge)	Macro-ATR (Diamond)	Transmission (macro)
Spatial Resolution (μm)	~13	~15	~5	~18	~40
FoV (μmxμm)	350x350	350x350	64x64	640x640	2560x2560

2.1.3.2 Data Analysis

Hyperspectral images require a range of initial corrections and preferably chemometric means due to speed and certainty in processing (including the widest range of wavelengths possible that contains all specie specific peaks) to extract relevant information from the huge volume of data. All of the raw images in this thesis were collected using the Agilent Technologies' ResolutionsPro FTIR Spectroscopy software version 5.2.0(CD846). The processing workflow and methods used and developed are summarised below.

2.1.3.2.1 Pre-processing

Instrumental factors such as fluctuations caused by the changes in the IR source intensity or temperature or detector sensitivity and optical artefacts caused by mismatch of the refractive index of species being imaged are known to cause a slope in the baseline in FTIR spectroscopy. In order to eliminate this slope; a first order baseline correction between the two end points of a previously cropped spectral range was found useful for some data sets for elimination of the baseline drift when collecting an image. A second derivative can be applied, however caution is advised if there are very weak infrared bands of interest as a second derivative will magnify the noise and some low intensity peaks may be lost in the noise.

In order to remove systematic discrepancies such as variations in detector sensitivity or contact non-uniformity, all raw IR images were vector normalised to minimise

absorbance variance. Vector normalisation works such that each spectrum is divided by the vector length which is square root of the sum of all absorbance values squared.

2.1.3.2.2 Univariate Analysis

Univariate analysis, or functional group imaging, only considers the peak height of, or the integrated absorbance under, a peak of interest, therefore chemical information can be obtained based on the association of the peak position with certain functional groups. Although it is useful in providing a quick overview of the species in the raw image data, a peak height image usually convolutes the underlying chemical information from the overlapping peaks in the intensity map. Integrating the absorbance for a particular peak over a spectral region of interest may provide a better distribution map by increasing the SNR. However, as in most cases, a complex heterogeneous mixture will not include an isolated band of interest therefore the integrated values will not represent the amounts present at different locations in the image with the required certainty. Another draw-back of functional group imaging is that a homogeneous object may be shown to be in a different location in the image when univariate images are created based on the integration of infrared bands observed in different parts of the spectrum. This occurs because the diffraction limited spatial resolution of the generated images strongly depend on the chosen part of the MIR spectral region. These disadvantages can be overcome by using multivariate approaches, which allow all of the species to be searched in the same spectral range thus allowing a contribution from all the peaks of the same species (or factor). Another advantage of multivariate approaches is that the interferences such as water vapour can be detected as a factor, and may therefore be eliminated.

2.1.3.2.3 Multivariate Analysis

Multivariate analysis, based on the statistical principle of multivariate statistics, involves observation and analysis of more than one statistical variable, in our case chemical species, at a time. A few statistical approaches that were found useful (i.e. in agreement with respect to each other) therefore relevant in this project are summarised here.

2.1.3.2.3.1 Principal Component Analysis (PCA)

Principal component analysis (PCA) is the most common decomposition method used in image analysis. PCA is a mathematical procedure based on reducing the matrix dimensionality by removing correlation between variables as first described by

Hotelling [13]. The principal components (PCs) are iteratively computed, the first showing the most variance, the second being constrained to be orthogonal to the first and explaining the residual variance not taken into account by the first, and so on (Figure 2.7).
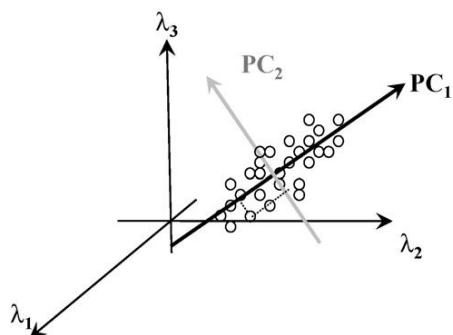
Figure 2.7 Geometric visualization of principal component analysis (from [14]).

However, whilst useful in explaining variance, PCA will not provide chemical meaning but a qualitative image, therefore not all principal components are significant but a subset of them will be. The noise will also be extracted as a component which may be easily interpreted. The contributions of each PC to the total calibration data set are known as the eigenvalues. A test algorithm can be used to find the significant number of components, as the remaining principal components would be simply noise. Then those most meaningful principal components and scores calculated from the principal components and the calibration set spectra are stored to represent the absorbance spectra. This can be represented in vector notation as,

$$A = S \cdot F + E_A$$ **Equation 2.11**

where **A** is the absorbance matrix (the calibration spectra), **S** the scores matrix, **F** is the matrix of the PCs, and **E$_A$** is the error matrix or so called the matrix of residual spectra.

As each calculated PC represents less variance than the previous one, the number of PCs will always be less than number variables, including different types of noise(s). Therefore usually up to first 12 PCs are considered in PCA analysis. For a thorough discussion of PCA results and score images reader is referred to work by Sasic *et al.* [15].

2.1.3.2.3.2 Multivariate Curve Resolution Alternating Least Squares (MCR-ALS)

Multivariate curve resolution (MCR) methods are soft modelling tools that require not prior knowledge of the components in the mixtures to be deconvoluted [16]. MCR

methods are mainly grouped into two, non-iterative and iterative. Non-iterative MCR algorithms are unconstrained therefore may find unique profiles within the mixture being studied. However although these mathematically obtained unique profiles may be close to real chemical profiles that need to be resolved from the mixture data set, non-iterative methods often suffer from ambiguities that arise due to strong overlapping or low SNR of species and noise. On the other hand, in the iterative MCR algorithms soft constraints such as non-negativity and unimodality or hard constraints such as the use of pure component profiles to be compared with extracted profiles to modify them accordingly are implemented minimise ambiguities [17].

Multivariate Curve Resolution–Alternating Least Squares (MCR-ALS) is an iterative resolution method valid for data sets formed by one or more data matrices [18]. It can be described by a bi-linear model as,

$$\mathbf{D} = \mathbf{C} \cdot \mathbf{S}^{\mathbf{T}} + \mathbf{E} \qquad\qquad \textbf{Equation 2.12}$$

where $\mathbf{D}$ is the original raw data matrix with the mixed experimental information, the columns in $\mathbf{C}$ and the rows in $\mathbf{S}^{\mathbf{T}}$ contain the pure response profiles of the n mixture components associated with the row direction and the column direction of $\mathbf{D}$, respectively, and $\mathbf{E}$ is the error-related matrix.

At each iterative step, matrices $\mathbf{C}$ and $\mathbf{S}^{\mathbf{T}}$ are calculated under constraints such that the error in the reproduction of the original data set, $\mathbf{D}$ is minimised. This process can be summarised as below,

i.   Estimating the number of components in $\mathbf{D}$.
ii.   Construction of non-random initial estimates of spectra, $\mathbf{S}^{\mathbf{T}}$ or concentration profiles, $\mathbf{C}$, using chemometric methods.
iii. Given $\mathbf{D}$ and $\mathbf{S}^{\mathbf{T}}$, least-squares calculation of $\mathbf{C}$ under the suitable constraints.
iv.   Given $\mathbf{D}$ and $\mathbf{C}$, least-squares calculation of $\mathbf{S}^{\mathbf{T}}$ under the suitable constraints.
v.   Reproduction of $\mathbf{D}$, using $\mathbf{C}$ and $\mathbf{S}^{\mathbf{T}}$. If the convergence criterion is fulfilled, the process is finished. If not, go to iii.

By definition, MCR-ALS is a soft-modelling method that can extract component information from the raw measurement data alone, as long as this data contains some variance; spatially as one might anticipate in an image or as a function of time when monitoring a reaction.

Compared to other multivariate methods, this approach is particularly useful for studying large, temporal data sets. However difficulties in estimating **S** (due to ambiguities) and colinearity phenomena, which is lack of separation when two components are changing linearly are the two main draw-backs.

2.1.3.2.3.3 Non-linear Curve Fitting (NLCF)

The strategy behind curve fitting or hard modelling is to generate a model spectrum based on the sum of the component peaks that it contains. If the components within a spectrum and by extension an image are known, then an estimate of the relative amount of each component can be used as a starting point in the application of hard modelling. Here we have developed an efficient curve-fitting algorithm to optimise the parameters (lineshape, peak height, peak width) for infrared absorption bands and the percentage contribution of each fitted curve to the overall spectrum was used as the initial loading value.

In order to use curve-fitting procedures, analytical functions must be used which describe the lineshapes of the peaks. Typical lineshapes encountered in spectroscopic studies are the Gaussian

$$I(k) = I(k_0)\exp[-2.773\ (k - k_0)/\Delta^2]$$
Equation 2.13

and the Lorentzian

$$I(k) = I(k_0)\ /\ [1 + (2(k - k_0)/\Delta)^2]$$
Equation 2.14

where $I(k)$ is the intensity at wavenumber k, k_0 is the wavenumber at the peak centre and Δ is the full width at half maximum (FWHM). The Lorentzian peak shape is often used to fit infrared absorption bands. However in real infrared spectra, effects including hydrogen bonding, rotational fine structure and, in FTIR-ATR, anomalous dispersion effects might affect the shape of the infrared band thus a true Lorentzian shape does not always occur. In ATR-FTIR, dispersion effects can lead to asymmetry in observed infrared bands, therefore in this thesis it was considered to use a family of peak curves called the Pearson profiles, specifically the Pearson IV profile which is asymmetric and is related to the Pearson VII,

$$I(k) = I(k_0)\big[1 + P^2\big]^{-M}$$
Equation 2.15

where $P = [2(k - k_0)\sqrt{2^{1/M} - 1}]/\Delta$ and M is known as the Pearson parameter. Equation 2.15 reduces to the Lorentzian function when M=1, approaches the Gaussian function when M becomes large and can approximate the Voigt function for intermediate M [19]. Modifying Equation 2.15 with an exponential term provides the required asymmetry and for M<1 the distribution has very broad wings. The Pearson IV function is given in terms of this by

$$I(k) = I(k_0)\left[1 + P^2\right]^{-M} \exp[-\nu \tan^{-1} P]$$ **Equation 2.16**

The exponential term has been shown to affect peak shapes when M is close to 1 (i.e. Lorentzian) more than it does for those where M is close to 10 (i.e. Gaussian).

A routine in MATLAB Version 7.10 (R2010a) was developed to create fits for the each pixel within an IR imaging data set consisting of 4096 spectra individually. An automated peak detection algorithm was implemented and the height and width of the peaks in the raw spectra at detected or selected positions were used as initial guesses for the iterative loop. More detail about this method including its development and application in comparison to other conventional analysis tools above is given in Chapter 3.

2.2   Raman Microspectroscopy

Raman spectroscopy, another common vibrational spectroscopy method which is often complimentary to FTIR spectroscopy, measures changes in the scattered light frequencies, or vibrational energy differences, between the ground and excited vibrational states of molecules when they are subject to laser photons (Figure 2.8) [20].

The intensity of bands in the Raman spectrum of a compound are governed by the change in polarizability (α), and can be given as,

$$I_{Raman} = KP(\vartheta_0 - \vartheta_i)^4 \left(\frac{d\alpha}{dQ}\right)^2$$ **Equation 2.17**

where P is the laser power at the sample (~300 mW in the setup used in this thesis), $\vartheta_0 - \vartheta_i$ is the wavenumber at which the band is measured, $d\alpha/dQ$ is the change in polarisability with the normal coordinate of the vibration and K is a constant dependent on the optical geometry, collection efficiency, detector sensitivity and amplification [4].
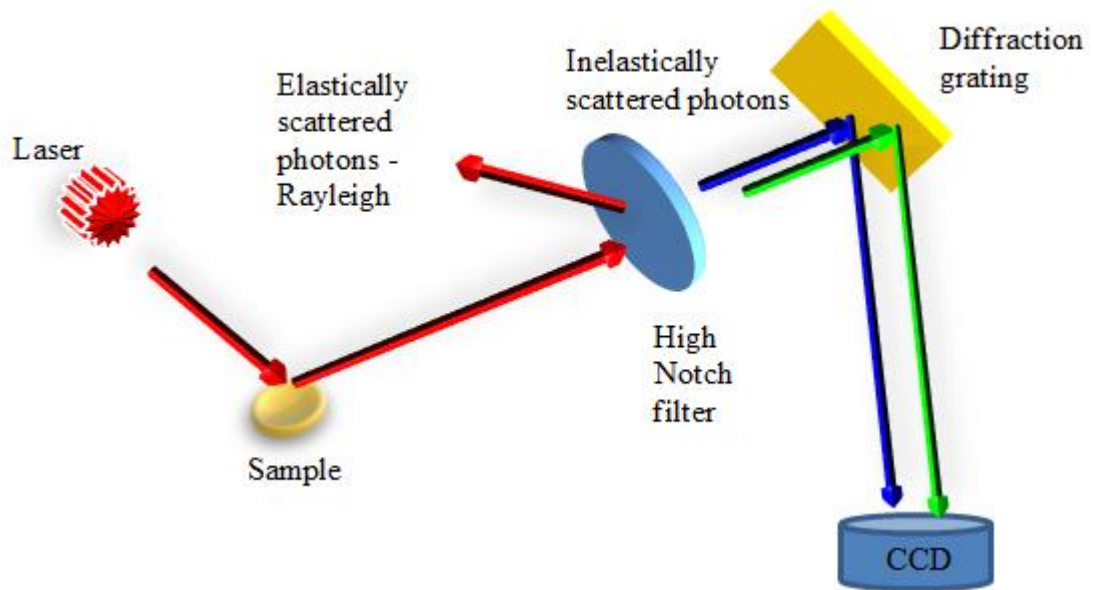
Figure 2.8 Illustration of a typical Raman spectroscopic measurement showing the sample being illuminated with an intense, single frequency light source and the relative frequency shift of the inelastically scattered light which is what is left after filtering, being measured with a cooled CCD detector.

In Figure 2.8 when the laser excites the sample at a single spot, a Raman spectrum is acquired. Raster scanning the sample in two dimensions by moving the stage enables one to create a 2D map (Figure 2.9a). However the beam can be deconvoluted along a line that is imaged through the slit, and this facilitates the collection of multiple spectra (up to 41 with the instrument used here, Renishaw inVia Raman microscope) along the line. Therefore, line illumination only requires scanning along one axis, allowing faster imaging (Figure 2.9b) [21].

The length of the laser line on the sample is inversely proportional to the magnification of the objective lens. In our configuration using a x50 objective (with *NA*=0.8) can yield a 37.9 μm line which can be decreased by adjusting the CCD area if needed. Therefore the excited sample region can be divided into *N* spatial zones, which might be as small as 1 μm at a spectral resolution of 1.05 cm^{-1}, each of which corresponds to a specific pixel along the *y* dimension of the CCD.
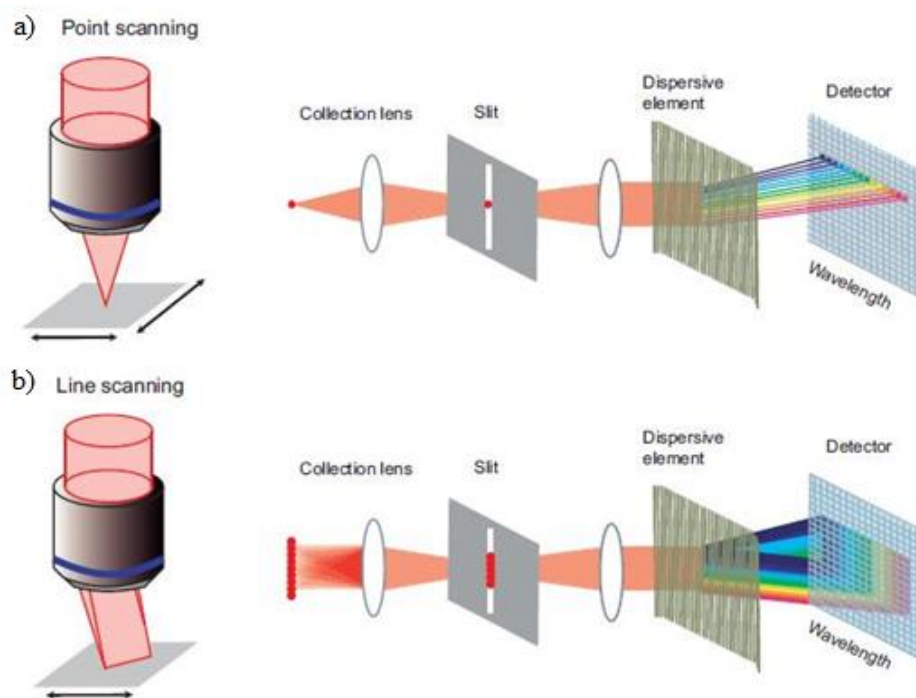
Figure 2.9 Comparison of the point (a) and line-scanning (b) methods for Raman microspectroscopy (adapted from [21]).

Using the wavelength of the most common laser (785 nm) used in pharmaceutical research, in Equation 2.10, calculated spatial resolution of the Raman microscope for different objectives is listed in Table 2.2

Table 2.2 Theoretical spatial resolution of the Raman microscope used (Renishaw InVia) for common lenses.

Objective	5x	10x	20x	20x (wide)	50x	100x
NA	0.1	0.3	0.46	0.4	0.8	0.95
Spatial Resolution (µm)	9.6	3.2	2.1	2.4	1.2	1.0

In order to verify these, copper grids on a flat Si surface were scanned, with the x20 objective in Figure 2.10a and with the x50 objective in Figure 2.10b. The Raman images are peak height observations at 520 cm^{-1}, where Si peaks and 15 µm bar width in Figure 2.10a and 6.5 µm hole width Figure 2.10b are observed.
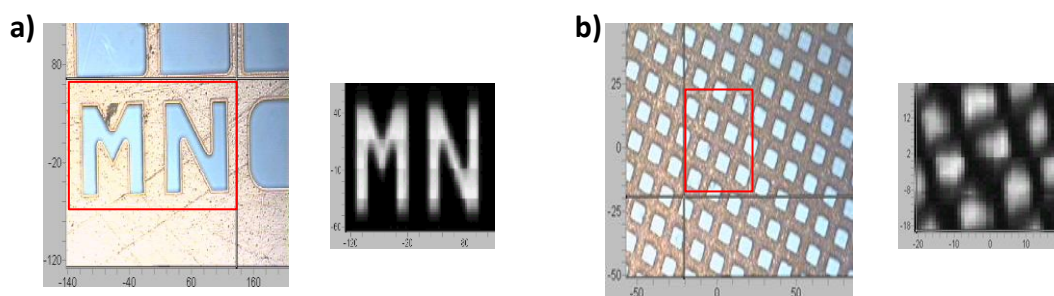
Figure 2.10 (a) A copper grid (Agar Scientific F4 finder grid) laying on a Si surface, white light image on the left and Raman image obtained with line scanning on the right. (b) White light image of a copper mesh (Agar Scientific 2000 mesh) floated on Si surface on the left and Raman line image of the red box area on the right.

Raman spectroscopy was shown to provide the unique opportunity to non-destructively analyse chemical concentrations in individual cells on the submicron spatial resolution scale without the need for optical labels [21]. Unlike IR spectroscopy which probes absorbance, Raman spectroscopy measures scattered light and Raman data are often used to compliment IR data with better spatial resolution and without the use of purging as a result of water and CO_2 being weak scatterers of light. Another advantage of Raman spectroscopy in comparison to FTIR is that the laser light can be focused on to different layers of a sample, therefore using so-called 'confocal mode' 3D Raman images can be obtained without the need of sectioning or any other form of sample preparation.

However for the purpose of study conducted in this project, considering the relatively long experiment time (line scanning) and the lower SNR from proteins in comparison to IR imaging with FPA detectors, Raman spectroscopic mapping could not be fitted in to the timescale of this project, therefore no detailed study was conducted.

2.3 Scanning Electron Microscopy (SEM)

SEM is a tool that is readily applied to the microscopic characterisation of particles and other polymer surfaces [22]. Conventional scanning electron microscopy is based on raster scanning a focused beam of high-energy electrons on the surface of solid samples under vacuum and detecting secondary or backscattered electrons, SE or BSE respectively, to generate 2D images that display spatial distribution of species based on their electronic properties with a typical magnification of up to 30,000 X and a spatial resolution of down to 2 nm.

Essential components of a typical SEM instrument include an electron gun, focusing and scanning coils, electron and x-ray detectors, IR camera and sample stage (Figure 2.11).
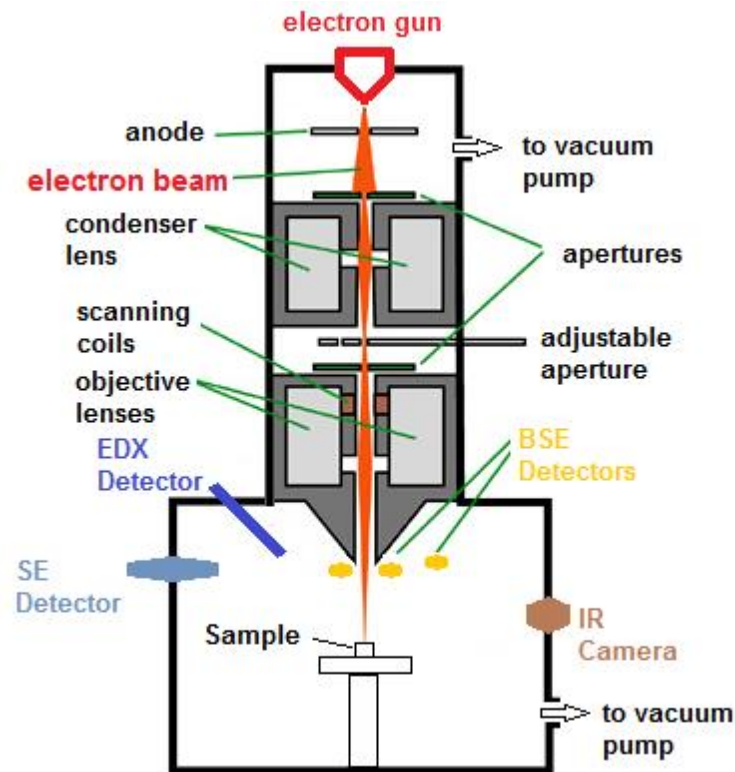
Figure 2.11 Illustration of a SEM instrument showing the main components (adapted from [23]).

Primary electrons are produced by thermionic emission from a heated filament in the electron gun where the beam brightness is dependent on selection of the filament material. Electrons are then deflected by radial and axial components of the magnetic lenses to a helical path, and focused on to the sample with energy of 0.5-30 keV covering a typical spot size of ~2-50 nm. The objective lens includes a pinhole that reduces the aberration. The instrument operates under vacuum as electrons cannot travel required long distances in air due to collisions.

Primary electrons that have scattered from the sample with high kinetic energies, backscattered electrons (BSE), and electrons that are escaped from the sample with an energy <50 eV, secondary electrons (SE), and x-rays that are emitted, due to relaxing of ionised atoms by shell to shell electron transitions, are detected by relevant detectors shown in Figure 2.11 and converted in to a signal at every point of the scanned area to generate a 2D image [24]

To obtain topographic contrast of the polymer microparticles, scanning electron microscopy was performed using a FEI NOVA 200 NanoSEM throughout this thesis. Images were formed using the secondary electron signal with a spatial resolution of ~2 nm. The samples were sprinkled onto an adhesive carbon tab on an aluminium stub and as the polymers are poor electron conductors, samples were sputter coated with gold (~ 20 nm) in an Argon atmosphere to enhance secondary electron emission.

2.4 Ultraviolet-Visible (UV-Vis) Dissolution Testing

In vitro protein release from the microparticles was monitored using UV-Vis spectroscopy that measures the amount of monochromatic light absorbed due to specific electronic transitions in the molecule according to the Beer's law. A Synergy HT plate reader (Bio-tek), facilitating analysis of 96 samples simultaneously, was used at 280 nm to measure both the absorbance of microparticles in solution and the release medium, in triplicate, thus allowing removal of any response from the buffer with reduced error.

Formulations were weighed out in triplicate (10 mg) and dissolved in 1.2 ml of 2:1 (v/v) dichloromethane (DCM)/acetone solution. Samples were centrifuged (8000 rpm for 5 min at RT) and 1 ml of supernatant discarded. Fresh DCM/acetone solution (1 ml) was added to each sample and the above step repeated 3 times. At the last step, all of the supernatant was removed and the protein pellets dried at RT for 1 h. Samples containing the protein were reconstituted in 1 ml of 0.025 M phosphate buffer (pH ~ 7.4), centrifuged 8000 rpm for 5 min and the supernatant analyzed by UV-Vis. A spike (polymer spiked with 1 mg of spray dried protein) and placebo (polymer only) were used as positive and negative controls.

2.5 Sieving

Sieving of the microparticles was undertaken using a 100 μm sieve (Fisher Scientific) on a Retch AS200 Sieve Shaker using an oscillatory amplitude of 1.5 mm for 30 minutes.

2.6 Ultra-Microtomy

Microtomy is a method for the preparation of thin sections of samples for further microscopic examination. An ultra-microtome is a mechanism in which, under an attached microscope, a mounted sample moves towards a knife at predetermined distance steps. After the first contact with knife, the specimen moves vertically past the cutting surface and a sample section that has equal thickness to the cutting step size (down to ~200 nm) is obtained. Finding a suitable resin for ultra-microtoming the

samples may become an important issue as the resin spectrum should not overlap with any of the components whilst it has to cure in ambient conditions due to temperature sensitivity of samples and also its density should be more than but close to that of the sample. For example widely available resins such as LR-White[TM] and Araldite (Huntsman LLC) were not useful for considering these constraints (too brittle) for the microparticles investigated here. However a hydroxyethyl methacrylate based resin, Technovit 7100 (soft and has a unique IR band that is not overlapping with samples investigated), satisfied the above conditions.

A Reichert-Jung Ultracut E ambient ultramicrotome was used with a fresh cut glass knife to obtain ~4 μm thick sections of microparticles that were embedded in Technovit 7100 resin for assessing the protein distribution within polymer matrices using FTIR imaging.

2.7   Gamma Irradiation

Raw polymers and scSO$_2$ produced microparticle formulations were irradiated by using ^{60}Co as irradiation source (Synergy Health PLC, Swindon, UK) at a few kGy/h dose rates ensuring a targeted total dose in accordance with the ISO 11137 standard. The sample temperature was kept at near room temperature during irradiation using thermometric controls. 30 mg of the polymer samples were sealed in a glass container and irradiated at 25 and 100 kGy total dose in air.

2.8   Differential Scanning Calorimetry (DSC)

DSC is used to identify the thermodynamic properties by measuring the difference in heat flow rate between a sample and a reference as a function of time and temperature. Phase transition temperatures of melting (T_m), crystallisation (T_c) and glass transition (T_g) can be observed in a typical DSC plot of heat flow (mW) versus temperature (°C) (Figure 2.12).

A TA instruments Q2000 DSC, calibrated with an Indium standard, using Tzero alu pans (TA instruments) under N$_2$ at a heating rate of 10 °C/min., was used to analyse raw polymers and polymer blends.

2 mg of sample was placed into the Tzero pan that is then pressed with a Tzero lid (TA instruments).
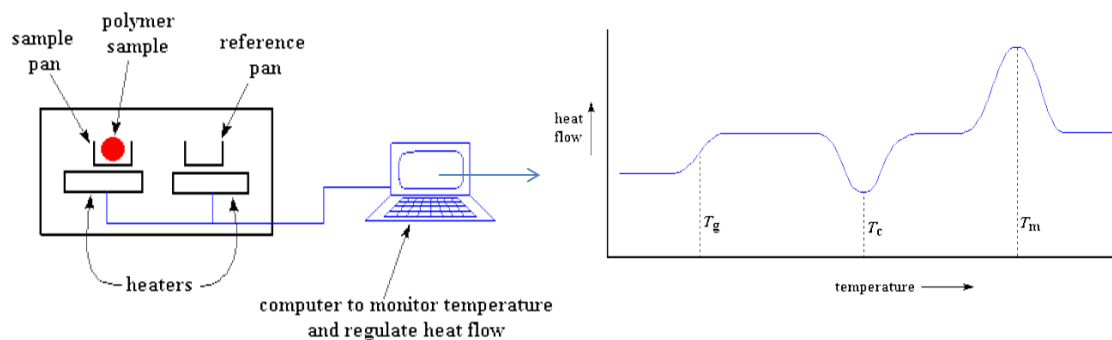
Figure 2.12 Schematic diagram of a DSC instrument and typical data on the right showing transition points (from [25]).

2.9 High Performance Liquid Chromatography (HPLC)

HPLC is a very sensitive (~200pg detection limit) separation technique that can be used to determine the number of components, the amount of each component present and degree of purity of each component based on their affinity for a column [26].
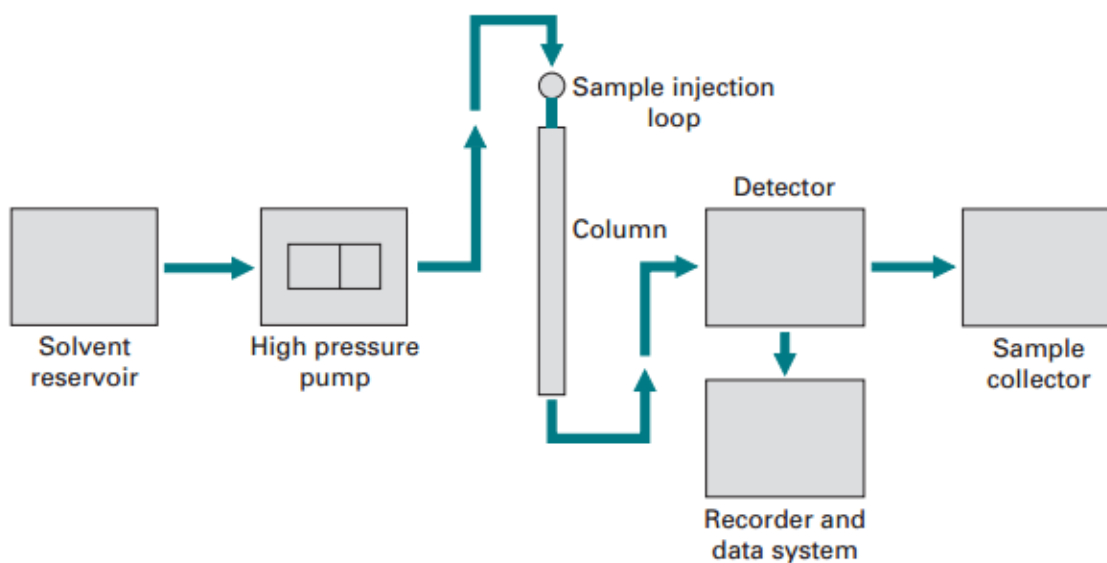
Figure 2.13 Schematic diagram of a HPLC system [3].

Figure 2.13 shows the layout of a typical HPLC system. The column, filled with a porous matrix (often called the stationary phase), is pumped with an aqueous buffer solution of the sample (often called the mobile phase as it moves) to be analysed. The mixture will exit from the column separated in to its components based on chemical or physical interactions with the column medium. Following its elution each component is quantified using a UV-absorption detector. The graphical representation of such separation is called a chromatogram. In this thesis, HPLC-SEC was employed to investigate protein efficacy and stability with in polymer matrices.

51

2.9.1 Size Exclusion Chromatography (SEC)

SEC or often also known as Gel Permeation Chromatography (GPC) is a well-established method of separating mixtures based on their size and obtaining their molecular-weight distributions. Any polymer dissolved in a solvent can be characterised. The separation occurs in the column (Figure 2.13) filled with porous polymer beads or 'gels', where small molecules are captured in the holes and large molecules are passed through rapidly thus the different molecular species are eluted from the column; largest molecular weight first and so on [3].

2.9.1.1 Evaluation of hGH stability and integrity

The un-irradiated and γ-irradiated hGH samples were analysed using HPLC-SEC in order to evaluate the effect of the γ-irradiation process.

Efficacy of the hGH was determined using an Agilent 1100 series HPLC-SEC system. hGH was assayed and soluble aggregate formation quantitated using size exclusion chromatography as described in the European Pharmacopoeia. A TSK2000SWXL (Toso-Haas) column was fitted to an Agilent 1100 HPLC and equilibrated with a mobile phase consisting of 97 % 0.063 M phosphate buffer pH 7.4 and 3 % 1-propanol at a flow rate of 1 ml/min. 20 µl of each sample was injected onto the column and protein peak detection performed at 280 nm. The relative peak area of monomeric hGH and soluble aggregates was measured and compared to control hGH samples of known concentration.

2.9.1.2 Determination of Molecular Weight of the Raw Polymers

A GPC PL-120 (Polymer Labs) with a differential refractive detector was used to analyse the molecular weight of the raw and γ-irradiated polymer samples. After drying, THF (1.2 ml) was added to each Eppendorf tube and the samples were placed on a vibrating plate for 1 hour to aid dissolution. Once dissolved, the mixture was filtered through a 0.2 µm filter. For GPC analysis, columns (two 30 cm Polar-gel Mixed-C columns in series) were eluted by THF and calibrated with narrow poly(styrene) standards. The calibration and analyses were performed at 40 °C with a THF flow rate of 1 ml/min. The GPC data were analysed by Cirrus software (version 2.0, Polymer Laboratories). The amount of protein in a formulation was calculated comparing the peak area at 214 nm to the literature value (European Pharmacopoeia standard).

2.10 References

[1] http://www.lbl.gov/MicroWorlds/ALSTool/EMSpec/EMSpec2.html, November 2013.

[2] http://chemwiki.ucdavis.edu/Physical_Chemistry/Spectroscopy/Vibrational_Spectros copy/Vibrational_Modes/Number_of_vibrational_modes_for_a_molecule, November 2013.

[3] K. Wilson and J. Walker, Principles and Techniques of Biochemistry and Molecular Biology, 7th ed., Cambridge University Press, Cambridge, 2010.

[4] P. R. Griffiths, J. A. de Haseth, Fourier Transform Infrared Spectrometry, 2nd ed., John Wiley & Sons Inc., Hoboken, New Jersey, 2007.

[5] C. Sammon, PhD Thesis: Vibrational Spectroscopic Studies of Degradation and Diffusion Processes in Poly(ethylene terephthalate), Sheffield Hallam University. (1997).

[6] N.J. Harrick and F.K. duPre, Applied Optics. 5 (1966) 1739.

[7] S.G. Kazarian, K.L.A. Chan, Micro- and Macro-Attenuated Total Reflection Fourier Transform Infrared Spectroscopic Imaging, Applied Spectroscopy. 64 (2010) 135A-152A.

[8] F.M. Mirabella, Strength of interaction and penetration of infrared radiation for polymer films in internal reflection spectroscopy, Journal of Polymer Science: Polymer Physics Edition. 21 (1983) 2403-2417.

[9] M.A. Harthcock, S.C. Atkin, Imaging with Functional Group Maps Using Infrared Microspectroscopy, Applied Spectroscopy. 42 (1988) 449-455.

[10] E. N. Lewis, P. J. Treado, R.C. Reeder, G. M. Story, A. E. Dowrey, C. Marcott, I. W. Levin, Fourier Transform Spectroscopic Imaging Using an Infrared Focal-Plane Array Detector, Analytical Chemistry. 67 (1995) 3377-3381.

[11] R. Bhargava, I.W. Levin, Fourier Transform Mid-Infrared Spectroscopic Imaging, Blackwell Publishing Ltd, Oxford, 2005.

[12] G. Thomson and G. Poulter, US20060261274 A1, US Patent. (2006).

[13] H. Hotelling, Analysis of a complex of statistical variables into principal components, Journal of Educational Psychology. 24 (1933) 417-441.

[14] C. Gendrin, Y. Roggo, C. Collet, Pharmaceutical applications of vibrational chemical imaging and chemometrics: A review, J. Pharm. Biomed. Anal. 48 (2008) 533-553.

[15] S. Sasic, An in-depth analysis of Raman and near-infrared chemical images of common pharmaceutical tablets, Applied Spectroscopy. 61 (2007) 239-250.

[16] J.M. Prats-Montalbán, A. de Juan, A. Ferrer, Multivariate image analysis: A review with applications, Chemometrics Intellig. Lab. Syst. 107 (2011) 1-23.

[17] M. De Luca, S. Mas, G. Ioele, F. Oliverio, G. Ragno, R. Tauler, Kinetic studies of nitrofurazone photodegradation by multivariate curve resolution applied to UV-spectral data, Int. J. Pharm. 386 (2010) 99-107.

[18] A. de Juan, R. Tauler, Chemometrics applied to unravel multicomponent processes and mixtures Revisiting latest trends in multivariate resolution, Analytica Chimica Acta. 500 (2003) 195-210.

[19] A.G. Michette and S.J. Pfauntsch, J. Phys. D: Appl. Phys. 33 (2000) 1186-1190.

[20] R.S. Krishnan, R.K. Shankar, Raman effect: History of the discovery, J. Raman Spectrosc. 10 (1981) 1-8.

[21] J. Chan, S. Fore, S. Wachsmann-Hogiu, T. Huser, Raman spectroscopy and microscopy of individual cells and cellular components, Laser & Photonics Reviews. 2 (2008) 325-349.

[22] V. Klang, C. Valenta, N.B. Matsko, Electron microscopy of pharmaceutical systems, Micron. 44 (2013) 45-74.

[23] http://www4.nau.edu/microanalysis/Microprobe-SEM/Instrumentation.html, November 2013.

[24] C. Lyman, D. Newbury, J. Goldstein, D. Williams, A. Romig, J. Armstrong, P. Echlin, C. Fiori, D. Joy, Lifshin, E and Peters, K., Scanning Electron Microscopy, X-Ray Microanalysis and Analytical Electron Microscopy: A Laboratory Workbook, 1st ed., Springer, New York, 1990.

[25] http://pslc.ws/macrog/dsc.htm, November 2013.

[26] B.A. Bidlingmeyer, Practical HPLC Methodology and Applications, John Wiley and Sons Inc., New York, USA, 1992.

3 Evaluation of Relevant Image Analysis Tools and Development of NLCF Methodology- A Direct Numerical Comparison on Mid-infrared Images Obtained from A Degrading Single Microparticle

3.1 Introduction

As detailed in Chapter 2, since the first use of a focal plane array IR detector coupled with an FTIR spectrometer to obtain chemical images in 1995 by Lewis and co-workers [1], Fourier transform infrared (FTIR) spectroscopic imaging has become routine, facilitating chemical characterization of multicomponent systems under both static and kinetic conditions [2,3].

Micro-ATR-FTIR imaging with a Ge objective provides a higher spatial resolution compared to transmission and transflection due to the effective magnification imparted by the high refractive index of the ATR crystal material. Conveniently, ATR-FTIR imaging in macro mode, i.e. without the use of a microscope, provides a temperature controlled environment for studying dynamic systems with a larger field of view still without the need of any sample preparation. FTIR imaging facilitates probing kinetic processes with IR light as a stack of 2D images at a range of IR wavelengths can be collected within a few minutes, providing good temporal resolution for relatively slow processes [4,5].

However, despite wide use of ATR-single point sampling on bulk polymers for studying chemical composition, reactions and adsorption [6], water diffusion and polymer swelling [7] or hydrolytic degradation [8] and ATR-FTIR imaging for monitoring drug release [5] and tablet dissolution [9] at micron scale there is still a lack of literature in the use of ATR-imaging and analysis for studying kinetic processes in individual biodegradable microparticles; generating quantitative chemical information with morphological visualization.

Therefore the first motivation behind the work reported in this chapter was the application of real-time ATR-FTIR imaging to obtain visual evidence of hydrolysis of a single microparticle. The practical design of such an experiment and its reproducibility in terms of quality of data to extract quantitative information using chemical information provided within the pixels of the spatiotemporal image cubes, has been assessed.

Since hyperspectral images that provide spatial and spectral information at the same time in an array of pixels and an individual pixel, respectively, can be obtained not only at IR wavelengths but also by a number of other techniques including, x-ray tomography [10], x-ray fluorescence [11], Raman microscopy [12] and Near infrared (NIR) imaging [13], multivariate analysis of hyperspectral imaging data has become a rapidly developing research field and has received considerable attention over the last decade [14].

When used to monitor slow kinetic processes that continue for tens of hours, fast Fourier transform infrared imaging with its relatively short image acquisition times (<5 minutes) yields huge volumes of spatiotemporal spectra that form raw images allowing morphological visualization of micron scale systems qualitatively at various wavelengths. However with varying noise and baseline distortions in each pixel due to hardware limitations (discussed in the following sections), FTIR imaging data need to be pre-processed (i.e. filtered and corrected by using transformations to somewhat minimize noise and correct the baseline that is different in each pixel) [15]. Following pre-processing, 'experiment specific' further analysis must be performed if the aim is to obtain higher resolution images to investigate morphology quantitatively from this large data and to be able to calculate key information such as reaction rate [16].

Therefore being able to couple *in situ* hyperspectral imaging and robust data analysis methods to obtain high resolution images facilitating direct extraction of quantitative information from pixel(s) representing regions of interest within the images, generates a global benefit not only for studying the systems considered in this thesis, but also many other microparticle systems where high resolution microscopic evidence is crucial to interpret chemical processes occurring. Hence, currently more than 80% of all pharmaceutical formulations are delivered in a powder format [17] and attenuated total reflection (ATR) FTIR has proved advantageous, particularly for pharmaceutically relevant systems, because the sample can be in any phase, form or shape and therefore can be analysed 'as is' [18].

The second objective of this chapter was to quantitatively compare the performances of the univariate and most common multivariate image analysis techniques. This comprised hard (curve fitting) and soft (MCR-ALS) modelling of imaging data in order to map and monitor the chemistry and morphology of a PLGA microparticle undergoing hydrolytic degradation.

Although several MCR-ALS packages compiled in MATLAB, including als2004 developed by Tauler *et al.* [19] and MCRv1.6 developed by Andrew and Hancewicz [20], and multiple spectra curve fitting tools such as PyMCA (a non-linear least-squares fitting application developed for x-ray imaging data [21]), were readily available, there was not an available peak-detecting non-linear optimisation algorithm, able to deconvolute temporal ATR-FTIR imaging data. Widely used data analysis and graphing software such as OriginPRO^{TM}, WiRE^{TM} and GRAMS^{TM} support curve fitting using a number of functions for a limited number of peaks. However, peak detection and fitting thousands of spectra in a relatively large spectral region (i.e. finger print region for mid-IR data) forming an image is not implemented in any of them.

The application of non-linear curve-fitting to large two-dimensional experimental infrared spectroscopic arrays [22] and a combination of non-linear curve-fitting and self-modelling curve resolution (SMCR) [23] have been demonstrated but for a limited data size and without considering mid-IR ATR microparticle imaging related SNR.
Therefore a novel, partially supervised non-linear curve fitting (NLCF) tool was developed to identify and fit peaks to the infrared spectrum obtained from each pixel within the 64x64 array. The output from the NLCF was compared directly and numerically with the traditional peak height (PH) data analysis approach and multivariate curve resolution alternating least squares (MCR-ALS) analysis for the same images, in order to understand and demonstrate the limitations and advantages of the NLCF methodology.

3.2 Experimental

3.2.1 Materials

PLGA RG752H (75/25 lactide/glycolide, I.V. 0.16-0.24, Bohringer-Ingleheim) was CriticalMix^{TM} processed (see 3.2.2). Pharmaceutical grade CO_2 (BOC Special Gasses) were used as received at Critical Pharmacueticals Limited (CPL) for the process. Water used in the experiments was purified with the ELGA Purelab option-R water distillation apparatus (Up to 15 MΩ-cm, Type II water) and degassed using a Fisherbrand FB11004 ultrasonic bath at 70 °C and 100% ultrasound power for 15 minutes.

3.2.2 CriticalMix^{TM} Process

The PLGA batch used in this study was prepared by adding 2.1 g of pre-weighed PLGA75/25, to a novel Particles from Gas Saturated Solutions (PGSS) apparatus developed at University of Nottingham, as described in Section 1.5.3.4.1 in Chapter 1.

3.2.3 Macro ATR-FTIR imaging of reactions with the Golden Gate^{TM} Sampling Accessory

Infrared images were collected using an Agilent 680-IR FT-IR spectrometer coupled with a liquid nitrogen cooled mercury cadmium telluride focal plane array detector MCT-FPA (64x64 pixels), capable of simultaneously collecting 4096 spectra from an image area of 640 µm x 640 µm using the Golden Gate^{TM} Imaging Single Reflection ATR Accessory (Specac Ltd). This accessory has a Diamond internal reflection element with corrective optics that adjusts the plane of best focus to sit on the crystal surface, eliminating any distortion, so that a symmetrical point spread function can be assumed. The angle of incidence of the infrared beam was 45° and the numerical aperture (*NA*) of the system was 0.32. Images were recorded in rapid scan mode and typical collection times were ~5 minutes. The detector was mounted on a Large Sample (LS) external sample compartment and the infrared beam from the spectrometer was projected directly on to the FPA after passing through the ATR sampling accessory. The physical size of each FPA pixel is 40 µm x 40 µm and with 4x magnification, where each pixel represents a 10 µm x 10 µm square in the image.

3.2.4 Real-time ATR-FTIR Imaging of Reactions

To set up the hydrolysis experiment, a single PLGA microparticle was placed in direct contact with the ATR crystal using a 40x microscope standing on top of the ATR accessory and sufficient pressure was applied using the sapphire anvil to ensure good contact between the particle and the crystal resulting in some deformation of the spherical particle. The images collected were not circular, most likely showing some evidence of anamorphism despite the use of corrective optics and this issue when using such collection optics has been observed previously by Everall *et al.* [24] and Chan *et al.* [25]. Once a satisfactory 'dry' image was collected water was introduced into the chamber in such a way that access to the particle was limited to the sides only as depicted in Figure 3.1.
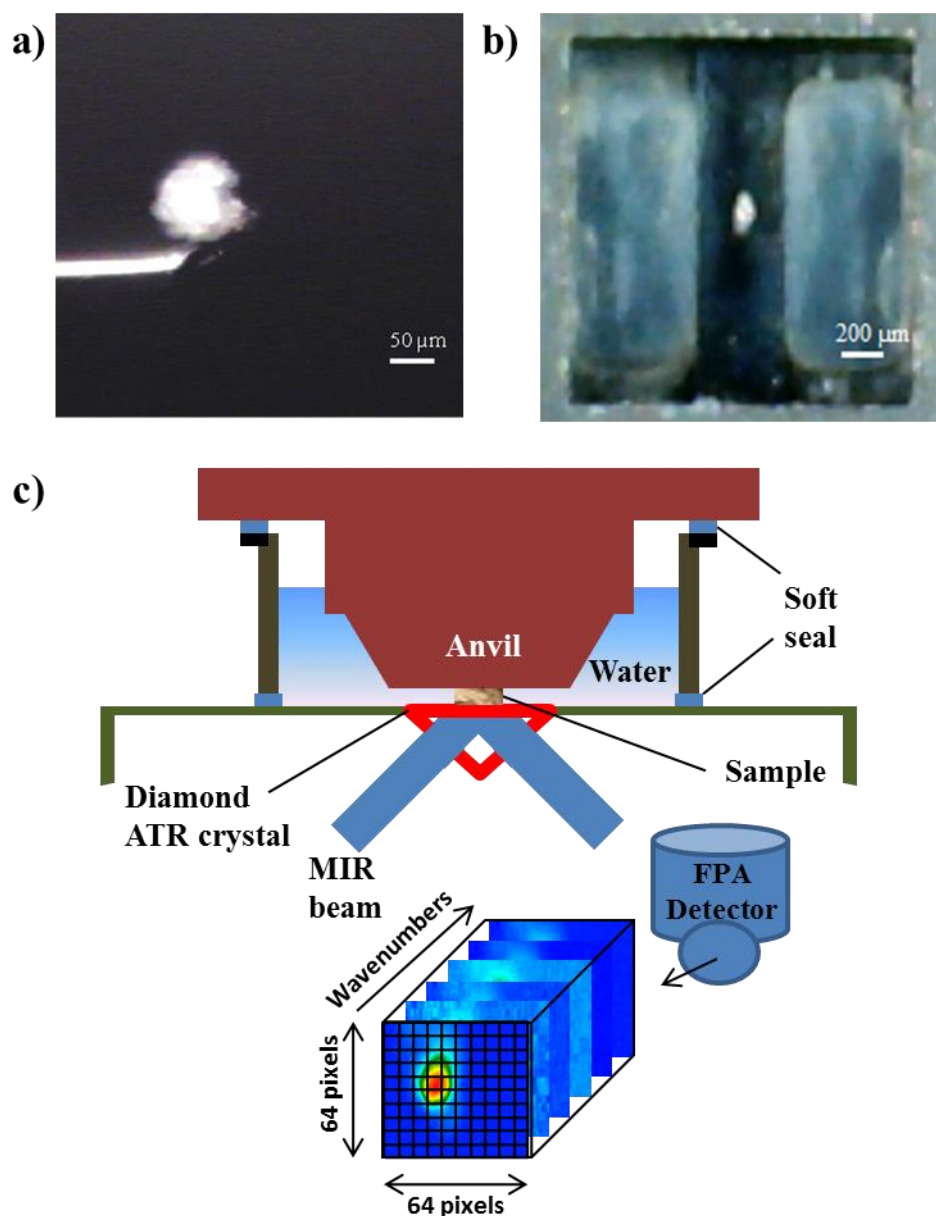
Figure 3.1 (a) White light image of a microparticle on the Agar microtool straight needle T5340 before being placed on the ATR crystal. (b) A microparticle placed on the ATR crystal before the anvil was brought into contact with it. (c) Schematic of the experiment setup after the particle was placed, anvil was in contact and water was added.

Images were collected using the Agilent Technologies' ResolutionsPro FTIR Spectroscopy software version 5.2.0 (CD846) at pre-determined time intervals and the collection parameters used were 128 co-added scans at a 4 cm^{-1} spectral resolution, in the mid-infrared (MIR) range (3800 to 950 cm^{-1}). The raw processed images were obtained by ratioing against a background of the blank ATR crystal comprising of 256 co-added scans.

60

3.3 Raw Data and Pre-processing

As mentioned in Chapter 2, absorbance spectra enables quantitative studies to be undertaken provided the analysis is sufficiently detailed. In FTIR imaging, single beam images are ratioed against a uniform background that is collected under the same experimental conditions but without the sample. For images obtained with an FPA detector, as each of the thousands of detector elements receives a different signal from the sample, the ratioing process often result in different baselines and offsets being applied in different detector pixels. Having to use the same background in a changing atmospheric environment also decreases the effective SNR mainly due to changes in the H_2O and CO_2 levels and detector drift. Therefore, as mentioned in Chapter 2, data pre-processing is vital, particularly for long lasting (more than a few hours) experiments, in the generation of infrared images.

Here raw processed image files were initially cropped between 1820 and 1000 cm^{-1} which provided a number of characteristic bands associated with PLGA and also included the water $\delta(OH)$ peak ~1635 cm^{-1}. Sunsequent pre-processing steps used in this work were 1st order baseline correction between the two ends of the cropped spectra and vector normalisation of the result. The effect of these processes on both the spectra and the resultant peak height images is outlined in Figure 3.2.

Figure 3.2a shows typical raw spectra taken from the interface highlighted by the grey arrow in the PLGA image next to the graph. The images shown in Figure 3.2b and Figure 3.2c were obtained by plotting the peak height of the 1745 cm^{-1} PLGA carbonyl peak (upper image) and the 1635 cm^{-1} peak (water bending mode) respectively. The contrast between the polymer particle and the water is quite poor in Figure 3.2c, due in part to baseline effects and although the instrument was purged using dried air difficulties arised due to fluctuating water vapour levels over the course of an experiment lasting tens of hours. Applying a 1st order baseline correction to the data (Figure 3.2d) improved the contrast significantly. This is especially noticeable in the water distribution image (Figure 3.2f), where the lack of contrast is more likely the result of a variation in the response of each pixel within the image. Vector normalisation (Chapter 2, Section 2.1.3.2.1) as shown in Figure 3.2g reduces the effect of variation in the pixel response, resulting in images with a good contrast for both the PLGA (Figure 3.2h) and water distribution (Figure 3.2i). Data pre-processing significantly improves the quality of the generated images; compare Figure 3.2b and Figure 3.2c with the data shown in Figure 3.2h and Figure 3.2i, respectively.
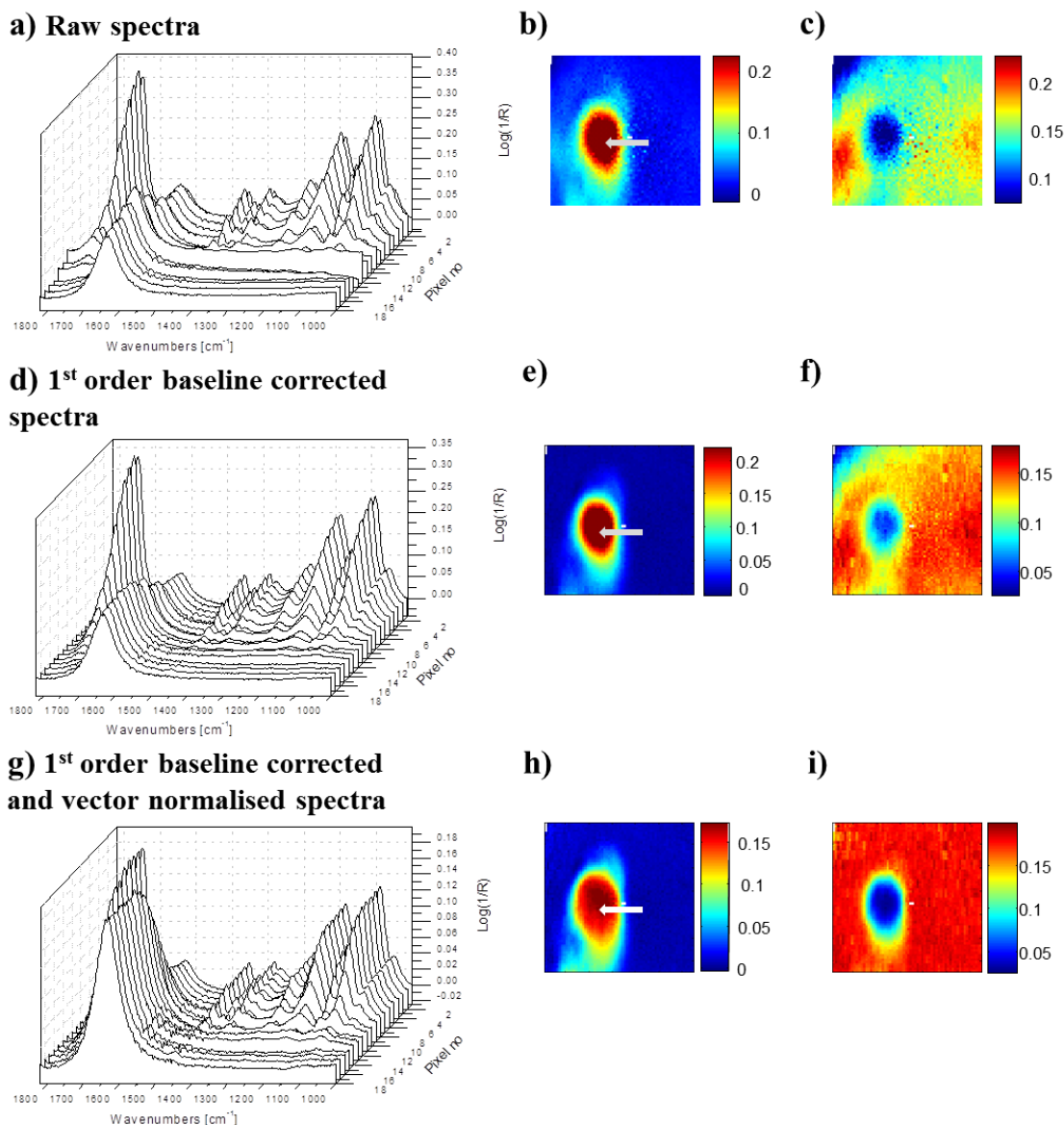
Figure 3.2 (a) Typical raw spectra and the resulting PLGA (b) and water (c) images, (d) the effect of 1st order baseline correction on the same data and the resulting PLGA (e) and water (f) images and (c) the effect of vector normalisation on the 1st order baseline corrected data and the resulting PLGA (h) and water (i) images.

3.4 Univariate Analysis

As detailed in Chapter 2, the most used and simplest approach for producing chemical images is the univariate method, in which the spatial distribution of each component is determined by its wavelength specific absorbance, within the mixture image. Univariate analysis requires prior knowledge of the sample, i.e. at what wavelength each component absorbs incident IR radiation and is rapid and convenient. However, for the

reasons given in Chapter 2, it only allows qualitative analysis and provides a quick overview of the data, with limited detail of the images.

3.5 Multivariate Analysis

The advantage in multivariate analysis arises from its multi-wavelength nature: multivariate analysis allows all species to be searched for over a given spectral range thus allowing contributions from all the peaks of the selected species (or factor) at all wavelengths. Another key advantage of multivariate approaches, in comparison to univariate analysis, is that interferences such as water vapour can be detected as a factor, and may therefore be eliminated.

3.5.1 MCR-ALS- a Soft Modelling Tool

As described in Chapter 2, multivariate curve resolution-alternating least squares (MCR-ALS) is a tool that facilitates the extraction of information from various spectroscopic and imaging techniques and is widely used in physical and biological sciences [26].

The MCR-ALS algorithm used in this thesis (MCRv1.6) [20] has been developed for two-way data. To use this approach, the 3D hyperspectral data cube must be unfolded into a two-dimensional matrix and refolded after analysis as shown in Figure 3.3.
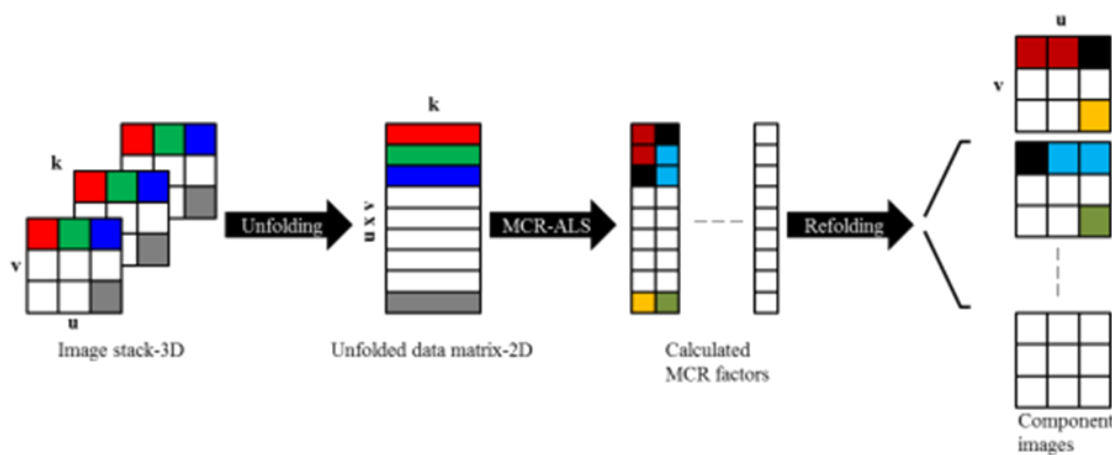
Figure 3.3 Unfolding and re-folding spectroscopic imaging data to generate factor distribution images using MCR-ALS.

FTIR images have a bilinear structure and it is assumed that some form of Beer's relationship exists between spectral intensity and concentration [27]. Therefore a bilinear model representing a spectroscopic image can be given as,

$$\mathbf{D}_{uxv} = \mathbf{A}_{uxz}\mathbf{B}_{zxv} \qquad \textbf{Equation 3.1}$$

where **D** is the measured data matrix, **A** is the matrix of normalised spectra of pure chemical components and **B** is the related intensity matrix for each component. The matrix size indices, u, v and z represent the number of spectroscopic resolution elements (wavenumbers), total number of spectra and number of resolvable components, respectively. Rearranging Equation 3.1 for the least squares estimation of **A** and **B** yields:

$$\mathbf{A} = (\mathbf{X}\mathbf{B^T})(\mathbf{B}\mathbf{B^T})^{-1} \qquad\qquad \textbf{Equation 3.2}$$

$$\mathbf{B} = (\mathbf{A^T}\mathbf{A})^{-1}(\mathbf{A^T}\mathbf{D}) \qquad\qquad \textbf{Equation 3.3}$$

The initial values of **A** and **B**, need to be estimated and this can be done by several methods. In the software used here, this was achieved by using a non-linear iterative partial least squares (NIPALS) decomposition method, the merits of which, when compared to using random numbers, eigenvalue decomposition, or dissimilarity criterion, is discussed in detail elsewhere [27]. This is followed by the selection of the optimal number of factors to calculate. This is achieved by considering the appropriateness of the initial estimate of the number of components. The final step, factor rotation, is a refining process in which alternating least squares is used to determine the optimal loadings and abstract factor matrices such that once recombined they most closely resemble the hyperspectral data matrix. Although ALS is the most common method for decomposing Equation 3.1 iteratively, a modified alternating least squares method (MALS) proposed by Wang *et al.* [28], which has been shown to overcome unstable convergence properties giving a non-optimum least squares solution, has been used for decomposition for all the MCR images generated here.

The MCRALSv1.6 software was run from its graphical user interface that allowed the user to input the number of factors (or components) to be estimated, number of iterations (used 500), and an ALS non negativity constraint (in this instance MALS-2D was used).

3.5.2   NLCF - A Hard Modelling Tool

A supervised non-linear curve fitting tool has been developed during the project to improve the spatial resolution of time resolved images and to monitor kinetic processes quantitatively, even from single pixels of the images. Therefore this work is demonstrating a peak detecting non-linear optimisation algorithm applied to temporal

ATR-FTIR imaging data for the first time. The advantages from which the novelty of the approach is originated are given in the results section.

A routine in MATLAB Version 7.10 (R2010a) was developed to obtain a set of Pearson IV lineshape fitted peaks (Equation 2.16, Chapter 2) for each spectrum in each image. Peaks were detected using the algorithm described elsewhere [29] and the height and width of the peaks in the raw spectra at detected positions were used as initial guesses for the iterative loop for each pixel. The key steps involved in the algorithm, to be applied to an IR image of a microparticle degrading in water can be summarised as follows;

1. For each pixel (i.e. each individual spectrum), the first task was to detect the peaks and for each detected peak store the peak centre ($k0$), maximum intensity $I(k0)$ and calculate and store the full width values at half maximum intensity ($I(k0)/2$). This was achieved by firstly smoothing the pre-processed data by employing a Savitzky-Golay filter [30] with a polynomial order of 3 and filter length of 13, in order to improve SNR and therefore avoid detecting noise as a peak. The imaging pixel data was sifted and the pixel with the highest intensity between 1820 and 1700 cm^{-1} (the ester carbonyl) was identified and assumed to be from the 'core' of the particle. 18 spectra in sequence as a line from the core of the particle towards the water region in the image were selected based on their position; 6 from the water rich regions, 6 from the PLGA rich regions and 6 from the interface. Peak detection for all 18 pixels was performed by visually assessing whether the expected PLGA peaks and water peak were detected in smoothed spectra of pixels from the core of the particle, the water rich region and interface regions using the same detection criteria. Peak detection was optimised such that all expected peaks in these 3 types of spectra could be detected using the same detection criteria and the peak detection algorithm was then performed. Using these criteria the output was visually assessed by checking the peak detection output (examples shown in Figure 3.4), and validated to ensure that each peak present had been detected. We expected to detect 11 peaks for spectra from wet samples and 10 peaks for spectra from dry samples. If the algorithm failed to detect all the peaks then the parameter 'Delta' (or peak threshold and related to height difference between peak and its surrounding) were adjusted to help the code identify peak maxima and minima. The calculated variables were stored and used later as the starting point when

running the gradient search algorithm to fit peaks to the spectrum obtained from each pixel.
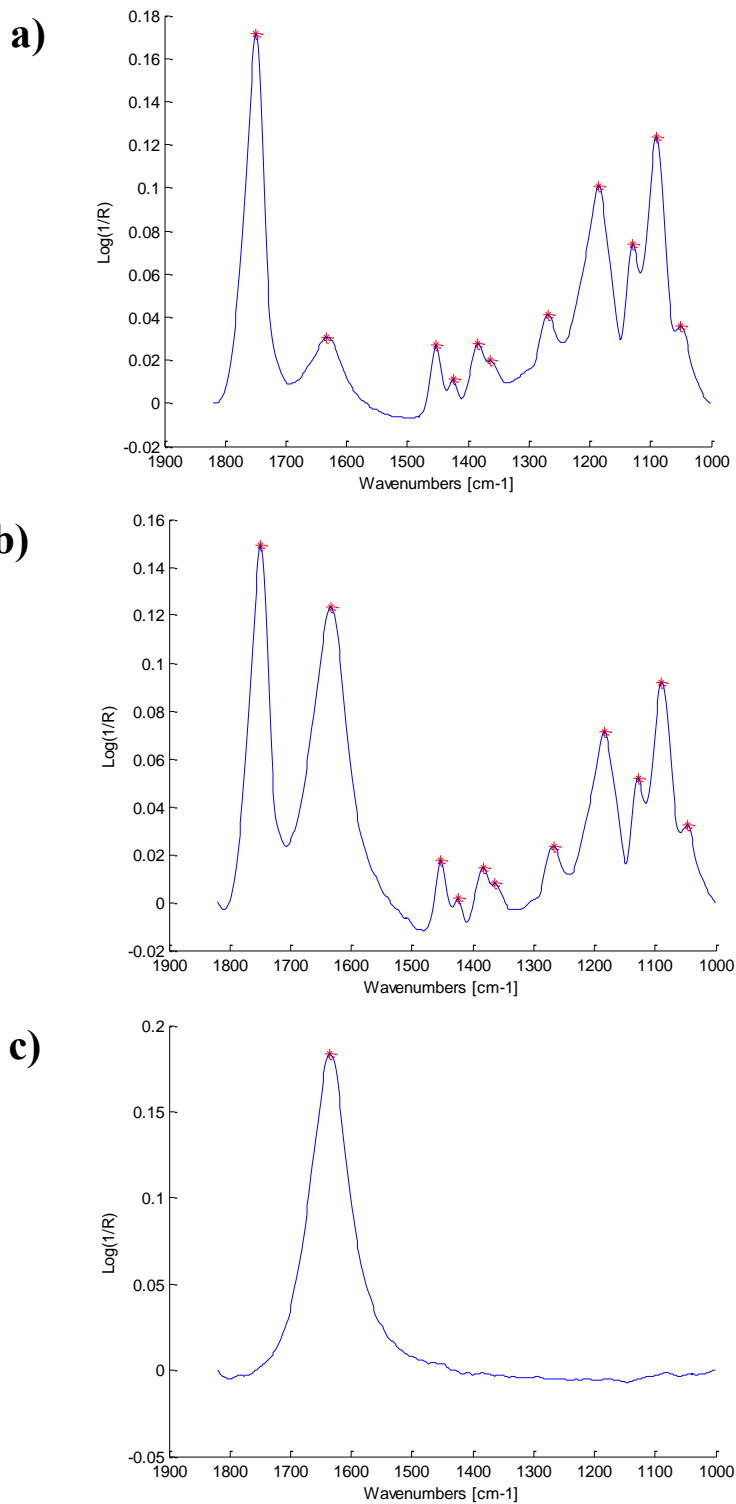
Figure 3.4 Spectra extracted from the grey line shown on the '0m wet' image in Figure 3.2(c). Red stars indicate detected peaks using the same X and 'delta' values, (a) typical polymer rich region, (b) typical interface spectrum and (c) typical water only spectrum.

2. When all peaks from each of the 18 selected pixels were correctly identified, 'Delta' was deemed to be optimised and fixed. This parameter was then applied to all 4096 pixels to detect all peaks in the image. Once the number of peaks at each pixel had been detected and stored (with their $k0$, $I(k0)$, Δ values), then upper and lower limits were defined for the rest of the parameters required for the fitting process namely M (the Pearson parameter) which defines the proportion of Gaussian, Lorentzian character for each peak and υ, which is the asymmetry parameter. The mean value of the upper and lower limits of these parameters were used as starting points at each pixel during the optimisation process.

3. The peak fits for the spectra in each pixel were optimised by using a gradient search algorithm ("trust-region", an improved version of Levenberg-Marquardt algorithm which provides a numerical solution to the problem of minimizing a nonlinear function, over a space of parameters of the function) defined in MATLAB library to perform a non-linear least squares fit to the measured data with $k0$, $I(k0)$, Δ, M and υ for each peak as free parameters to be varied until the sum of squares due to error is reached to its minimum or 500 iterations have been completed.

4. The fitting was started in the top right hand corner pixel of the image (pixel #64) and the optimised values for the matching detected peaks outlined in #1 were used as the starting point for the fit (described in #3). The second pixel fitted was pixel #1 i.e. the top left hand corner. If the number of peaks detected by the peak detection algorithm for the current pixel (pixel #1), matched the number of peaks used in the preceding fit, then the optimised preceding fit was used as the starting point for the fitting process. If there is a discrepancy in the number of peaks, then the optimised values for the matching detected peaks outlined in #1 was used as the starting point for the fit. This process was continued with the fitting order being pixel #64, pixel #1, pixel #63, pixel #2 etc. Once a row was completed then the pixels in the row below were fitted following the same protocol; working from the edge of the image to the centre, using the preceding image fit as the reference point.

5. Once the fitting for all 4096 pixels was complete, the peak centres, peak intensities and other parameters for each pixel were collated and the relevant

Pearson IV function with optimised parameters for water (peak centre close to ~1635 cm^{-1}) was removed from each pixel to be stored to represent the water spectrum for each pixel. The output for each pixel was therefore an equation containing up to 10 Pearson IV functions (Equation 2.9, Chapter 2), the sum of which represents the pure spectrum of PLGA at each pixel.

6. False colour images for the PLGA and water components were generated by plotting the total intensity for each equation (for PLGA containing up to 10 Pearson IV functions, for water 1 Pearson IV function, each function with their unique optimised constants ($k0$, $I(k0)$, Δ, M, and υ)) over 1820-1000 cm^{-1} range at each pixel.

7. The intensity of the fitted peaks with peak centres ($I(k0)$) at ~1456 and ~1424 cm^{-1}, were used to calculate k values for lactic acid and glycolic acid units respectively.

3.6 Results and Discussion

Figure 3.5 shows the result of analysis after pre-processing the same infrared images (dry and 0 m wet) of a single PLGA microparticle in four different ways; (i) using the peak height of a single peak in this case the ester carbonyl at ~1745 cm^{-1} (Figure 3.5a), (ii) plotting the distribution of a factor identified as deriving from PLGA in MCR-ALS (Figure 3.5b), (iii) by plotting the sum of 10 peaks fitted between 1800 and 1000 cm^{-1} which does not include the peak ~1635cm^{-1} assigned to the water bending mode resulting from a NLCF procedure (Figure 3.5c) and (iv) a linear fitting procedure using the Gaussian function (Equation 2.13, Chapter 2) (Figure 3.5d). Figure 3.5e shows the pre-processed raw spectra along each grey line in the images. Images were generated from measurements conducted on an as received scCO$_2$ processed PLGA microparticle and on the same PLGA microparticle, immediately after water had been brought into contact with it.

3.6.1 Spatial Resolution Comparison

In theory, the spatial resolution of a microscope is diffraction limited according to the Rayleigh criterion (Equation 2.10, Chapter 2) however in IR imaging systems employing a FPA detector, each detector unit is a not a point but 10 μm x 10 μm square and the wavelength of the incident light on each detector pixel is shorter than the detector size. Therefore in practice, the relation in Equation 2.10 is never observed directly. Furthermore, in the ATR experiment, the penetration depth (Equation 2.9, Chapter 2) can degrade the lateral resolution. Therefore for FPA imaging systems it has

been shown to be more appropriate to determine the spatial resolution based on real measurements [24,25,31,32].
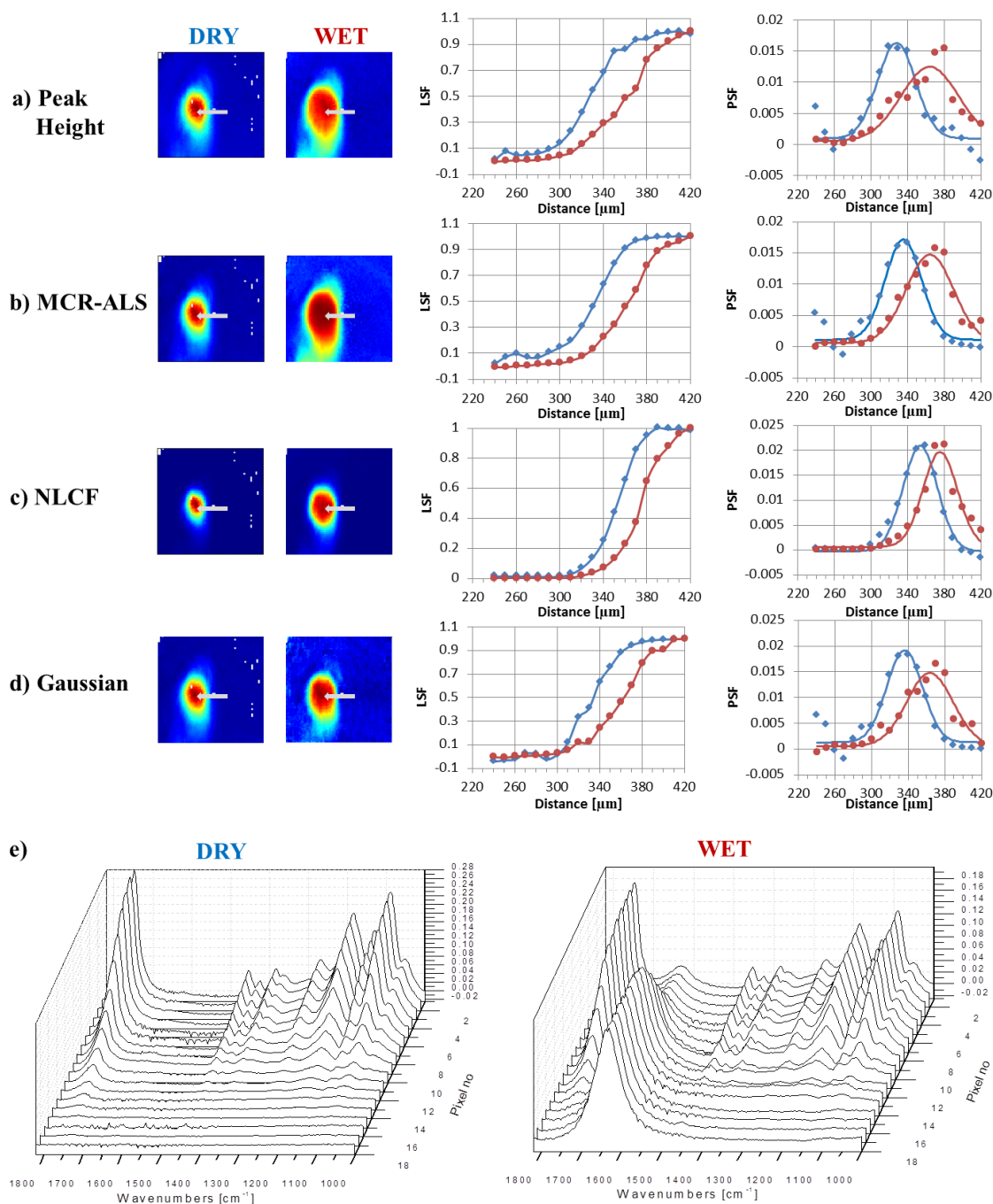
Figure 3.5 Data used to measure spatial resolution using the "step-edge" method for the dry PLGA particle (1ˢᵗ column of images and labelled 'DRY') and the same PLGA microparticle immediately after surrounding it with water as shown in Figure 3.2h (2ⁿᵈ column of images and labelled 'WET') for images processed using peak height (a) (PH), (b) MCR-ALS, (c) NLCF and (d) Gaussian. (e) The raw data along the grey arrow in each image from right to left with decreasing pixel number, respectively.

The practical method we have used is the 'step-edge' method which is based on the observation of a step change increase when the intensity of a selected wavelength is plotted along a chosen line parallel to one of the axes in the 2D image. This step shape represents the Line Spread Function (LSF) (Figure 3.5). The derivative of the LSF with respect to its variable (which is position or pixel number) is described as the Point Spread Function (PSF). The PSF is the response of the system to a point source and is generally considered to be an Airy function. The FWHM of the PSF gives the spatial resolution of the imaging system. Therefore, the FWHM of a Gaussian that is fitted to the PSF, as described by Offroy et al. [32] using an IR microscope calibration test sample the USAF (1951 1X 38257), has been used to define the spatial resolution in this thesis. Figure 3.5 shows the above mentioned steps being applied to images generated using peak heights, MCR-ALS, NLCF and linear Gaussian fits.

A study on the effect of sample geometry on spatial resolution of the same ATR-FTIR imaging system used in this study has been conducted by Everall *et al.* [24] for convex solid objects. In their work it was determined that this imaging system with a calculated NA of ~2 was underestimating the size of 20-140 μm objects and approximating solid spheres, of varying dimensions, to be the same size (~30-35 μm). The authors postulated that this was due to the shallow evanescent wave penetration (Equation 2.9, Chapter 2) and blurring caused by the finite spatial resolution. Our experiment however is different when compared to such a case, as the sample is a rather soft solid which, with a gentle anvil pressure, provides a flat central area that is quite large (~100 μm) and the convex shape only occurs at the edges. As the main purpose of this work is not to estimate the real size of the microparticle, but to compare the output of univariate, hard and soft multivariate tools, the aim was to see how the different data analysis approaches impact upon measured spatial resolution and the sharpness of the interfaces. The measured spatial resolution for each of the data analysis methods is summarised in Table 3.1.

Table 3.1 Summary of spatial resolution calculated using different image analysis approaches of the mid-IR image of a single PLGA microparticle under dry and wet conditions. All values are given in μm.

Method	Peak height	MCR-ALS	NLCF	Gaussian peak fitting
Dry	70.2±15.8	60.6±0.4	42.7±1.5	55.8±4.1
In water (0 m)	52.4±4.7	48.8±4.1	48.6±4	49.2±4.9

Table 3.1 shows that the NLCF approach improves the measured spatial resolution of a mid-IR image when there is a large discrepancy between the refractive index in adjoining pixels, i.e. an air/polymer interface. It was shown by Lasch and Naumann that the application of Fourier self-deconvolution to IR microspectroscopy images had led to an improvement in the spatial resolution by improving the spectral resolution at each pixel [31]. The NLCF approach used here is also acting in a spectral resolution enhancement manner and the ability, when used in a supervised manner, to discriminate between species in adjoining pixels more readily than the peak height, MCR-ALS and Gaussian peak fitting approaches that limits the blurring effects at interfaces. This is likely to be mainly due to the optimisation algorithm (trust region) falling into local minima as a result of a lack of change between consecutive iterations due to the limited number of parameters in the Gaussian fitting protocol not allowing an improvement in fit, due to variations in the symmetry of bands between pixels. In order to make the algorithm robust for not only this but different data sets and as we know that IR bands are asymmetric, the Pearson IV function was chosen to be used despite the delay in computation time. The merits of using this function compared to Gaussian and/or Lorentzian function(s) is also discussed in Chapter 2, Section 2.1.3.2.3.3 and in [22] and [33].

When the refractive index change at an interface is small, such as when a PLGA microparticle is surrounded by water, the blurring of the interface is reduced and the spatial resolution determined by this step-edge approach is comparable between the NLCF, peak height and MCR-ALS approaches.

3.6.2 Image Comparison

To explore the relative merits of a number of different analysis approaches (univariate peak height image plotting, soft and hard multivariate modelling), the interaction of a single PLGA75/25 microparticle with water as a function of time at 70 °C was studied. The experiment is setup in such a way that the interaction between the particle and water will only occur at the interfaces being monitored.

a) Pre-processed IR spectrum showing selected peak height positions
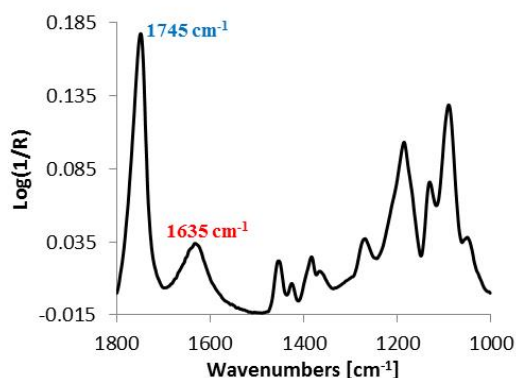
b) Peak height images
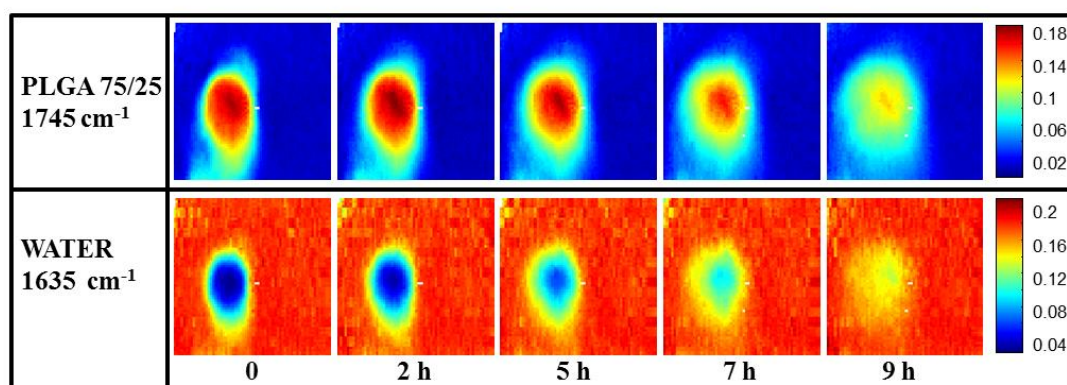
Figure 3.6 (a) ATR-FTIR spectrum of a pixel on the left hand side chosen from the core of the particle from the first image collected immediately after surrounding the PLGA particle with water and (b) a set of false colour images representing temporal peak height distribution of PLGA on the top and water at the bottom.

Figure 3.6 shows five false colour images obtained using the univariate peak height method and a spectrum taken from close to the 'dry' polymer/hydrated polymer interface in the t=0 image. From this spectrum one can see both of the bands used to determine the polymer distribution (the ester carbonyl at ~1745 cm^{-1}) and the water distribution (the OH bending mode ~1635 cm^{-1}). The two images at the extreme left show the distribution of polymer (top) and water (bottom), within the ATR field of view, immediately after the experiment was started. Even at this short time (data collection was ~5 minutes) there is evidence of an interface layer of hydrated PLGA around the particle, with an apparent concentration gradient from the particle centre outwards towards the aqueous media. As the contact time with water increases, a number of phenomena occur. Firstly the microparticle (defined by the red zone) initially appears to increase in size (2 h), which is indicative of swelling and the hydrated PLGA layer

(yellow) becomes thicker. Images collected at times exceeding 2 hours show the particle decreasing in size and the boundaries of the particle becoming less well defined. The complementary images pertaining to water concentration show an inverse relationship, as one would expect in a binary system. The changes to the interface layer as a function of time will be discussed later. It is clear however, that the overlap between the bands used to determine the distribution of the two components in this system must influence the sharpness of this image and increase the magnitude of the measured interface.

Figure 3.7 shows the equivalent false colour infrared images for the same data described in Figure 3.6 this time, obtained using a MCR-ALS approach. In Figure 3.7a the spectral features shown to the left hand side of the images are the 'pure component spectra' for PLGA and water generated using this soft modelling method and are often referred to as factors. As one can see that the image quality (SNR, spatial resolution) is better when using 2 factors than when using 3 or 4 factors and the same as using 5 factors as illustrated in Figure 3.7a, b, c and d, respectively. Therefore MCR-ALS software was ran for 2 factors and only these results were used in the following discussions.

MCR-ALS data (Figure 3.7a) is in general agreement with the findings from the peak height measurement approach shown in Figure 3.6. Closer inspection indicates that the interfaces in this set of images are blurred as were those observed in the univariate data set (Figure 3.6) and less sharp than those obtained using the hard modelling approach (Figure 3.8). But this data set does exhibit improved SNR compared to the univariate data (Figure 3.6). The blurring of the interfaces is the result of the 'pure component spectrum' representing PLGA still displaying a feature at ~1635 cm^{-1} associated with water and due to the fact that the MCR factor for PLGA has fixed peak centres and band widths meaning they approximate rather than exactly replicate the spectrum at each pixel. The improvement in the SNR is the result of the elimination of water vapour in the pure spectral factors combined with the fact that the signal comes from many more spectral data points compared to the peak height data.

It is important to note that MCR results might be improved by using different strategies that were not covered in this work and/or more soft constraints or hard constraints [34,35]. For example, as it will be discussed in Chapter 4, when the data were cropped down to 1820-1500 cm^{-1} zone which includes the PLGA carbonyl (~1745cm^{-1}) and water δOH (~1635 cm^{-1}) MCR results were improved.
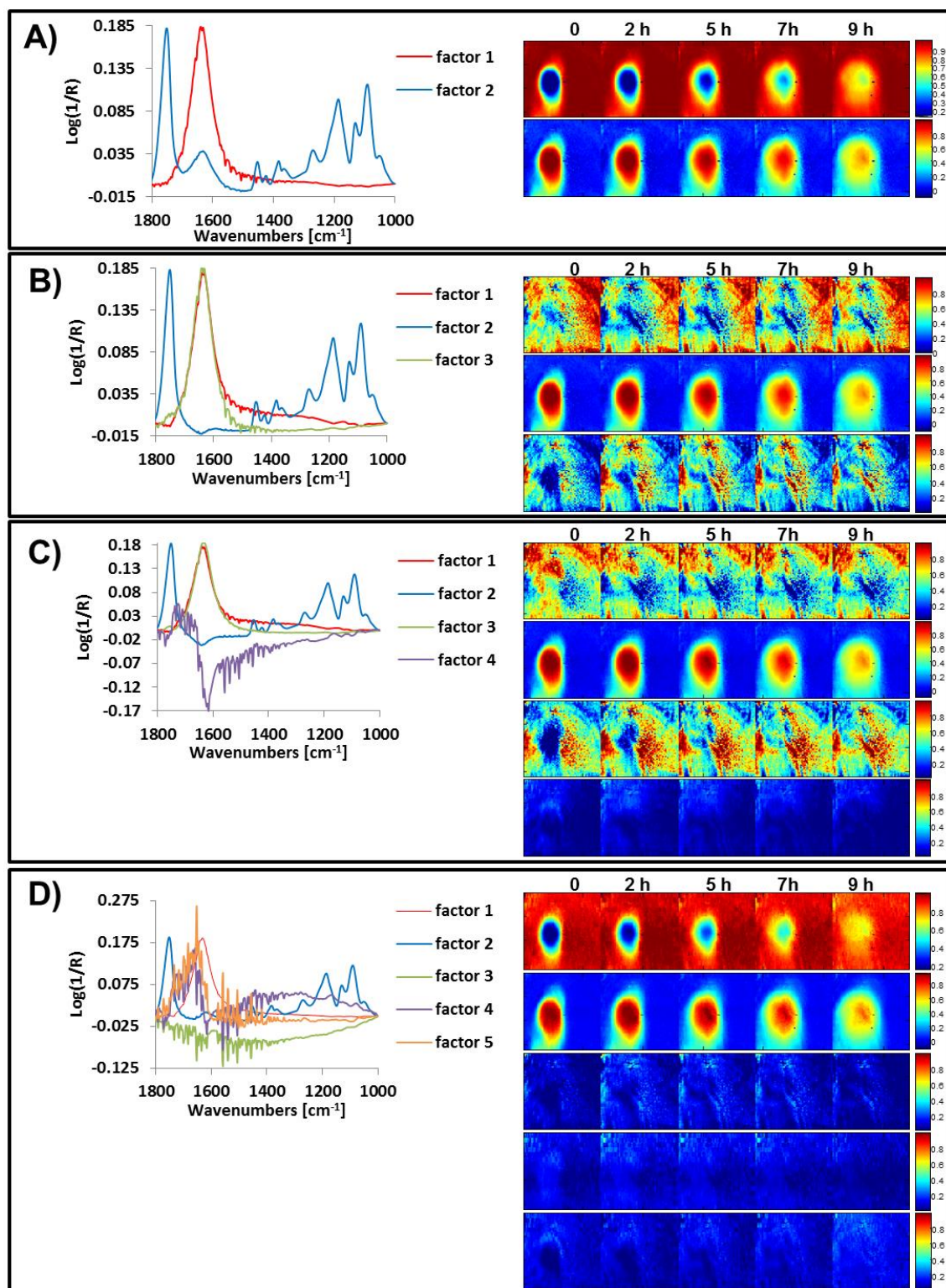
Figure 3.7 MCR-ALS output using MCRv1.6 software utilising (a) 2 factors, (b) 3 factors, (c) 4 factors and (d) 5 factors where calculated factor spectra are shown on the left and resulting images are shown on the right with increasing factor index from top to bottom respectively.

Another interesting, but rather lengthy, strategy that could have been considered was removing the solvent IR background contributions as developed and demonstrated by Kuligowski *et al.* [36] in liquid chromatography infrared detection. In their work the solvent background was estimated successfully and by two different methods; principal component analysis and simple-to-use interactive self-modeling analysis (SIMPLISMA) and after subtracting the estimated background contributions from their data sets, MCR-ALS provided improved SNR and resolved overlapping chromatographic peaks.

As the shape of the δ(OH) band was shown to change from pixel to pixel in FTIR imaging data, it was anticipated that using the simple subtraction of a pure water spectrum at each pixel would introduce spurious peaks due to imperfect subtraction and hinder the MCR analysis. Therefore, for the purposes of this study and to keep the MCR analysis as a soft modelling approach, it was decided to use no prior information of the pure components and utilise the whole fingerprint region of the IR spectra (1820-1000 cm^{-1}) for the MCR-ALS analysis.

Figure 3.8 shows 5 false colour images equivalent to those described in Figure 3.6 and Figure 3.7a. However, this time they were obtained using the nonlinear curve-fitting approach and are the result of the summation of the peaks, generated during the fitting process, that have been assigned to PLGA (upper row) and water (lower row). The data to the left of these images shows the 11 component peaks used to fit the spectrum, from the same pixel used to obtain the peak height and MCR-ALS data within the PLGA/water interface. The dotted line denotes the synthetic spectrum generated from the combination of the fitted peaks, which matches the real spectrum at that pixel. The upper set of images shows the distribution of PLGA determined using all of the fitted peaks except the peak with a maximum at 1635 cm^{-1} which is used to obtain the distribution of the water within the ATR field of view. These images are, in general, in agreement with the data shown in Figure 3.6 in that they indicate the formation of a hydrated region around a dry PLGA particle that increases in thickness over the first 2 hours and that this occurs concurrently with particle swelling. Closer inspection and comparison with the data in Figure 3.7a indicates that the interfaces and boundaries in this set of images are much sharper and the data exhibits less noise, i.e. there is less variation in colour intensity between equivalent pixels.

a) NCLF peaks and resulting spectrum
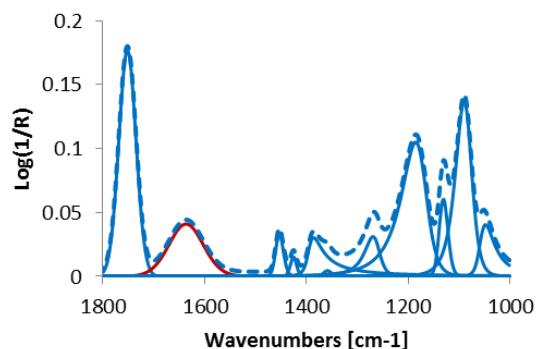
b) NLCF images
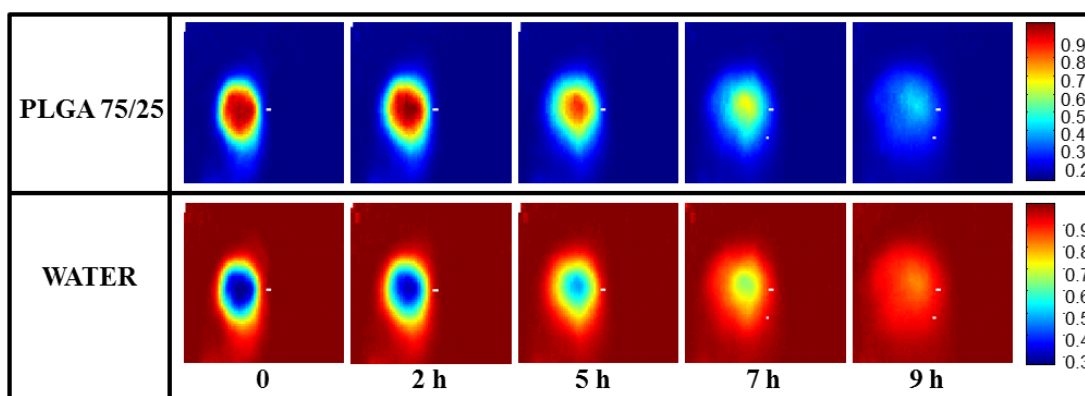
Figure 3.8 ATR-FTIR spectrum of a pixel chosen from the core of the particle from the 0 m wet image (a) and a set of false colour images representing temporal distribution of PLGA on the top and water at the bottom for NLCF method.

This (apparent) improvement in resolution and SNR in each image is achieved by the elimination of contributions from overlapping features at each pixel such as other chemical species, instrument noise and atmospheric water vapour. Another contributing factor to the broadening of the interfaces in the MCR-ALS images when compared with those generated using NLCF, is the fact that the NLCF peak centres are optimised for each peak within each pixel, whereas the MCR-ALS images used a fixed factor, with fixed peak centres and band widths. It is likely that during ALS optimisation, then a linear combination of the water and PLGA factors may give a better mathematical fit in some of the interface pixels resulting in a less well defined image, whereas the NLCF approach is better able to discriminate between water and PLGA. This does come at a considerable time and convenience penalty. The images shown in Figure 3.6 and Figure 3.7 can be obtained in seconds and minutes, respectively, whilst the data shown in Figure 3.8 takes approximately 5 hours to generate using a PC with an Intel® Core[TM] i7-2620M CPU @ 2.7 GHz and 8 Gb of RAM. In many applications this approach may

not be feasible due to a number of considerations such as time, CPU availability and, more importantly, spectral data which is too challenging to fit due to a lack of knowledge of the species within that system. Fortunately, an understanding of the components within this system, i.e. water and PLGA provides confidence in the peak assignments. The MCR-ALS approach facilitates the collection of false colour images in a few minutes and thus offers an attractive/acceptable compromise between the slow but accurate hard modelling methodology and the rapid univariate approaches.

3.6.3   Interface Analysis

The generation of false colour images using the peak height approach which is the most practical and therefore common way, from the mid-infrared imaging dataset highlighted here (Figure 3.6), facilitates the rapid assimilation of trends in physical processes such as particle swelling, particle shrinkage, hydration layer formation etc. but cannot readily be used to obtain quantitative information about such processes. This can be problematic when a particle is not uniform in shape and often the dimensions are estimated by assuming a particular geometry (circle, square etc.) that may not be appropriate. To compare the quality of the output generated using the NLCF approach with standard image generation strategies (peak heights and MCR-ALS) it is appropriate to compare the findings along the centre line across the particle as a function of time.

When water is introduced into this system, there exist domains where only water is measured, others where polymer is the dominant signal and others where a clear mixture of water and polymer are observed; a hydrated zone. Determining the exact point where each domain ends and another domain begins is somewhat arbitrary, but some form of definition is necessary if one is to quantitatively compare data extracted from images generated using different approaches. Therefore to facilitate comparison between data analysis approaches two parameters that can readily be extracted from each polymer response profile; namely the full width at half maximum height (A) and the region of the right hand side of the profile where the polymer intensity is <90% of its maximum value and >10% of its minimum value (B) have been defined. Figure 3.9 shows a typical polymer response profile and the parameters A and B derived from that profile using the NLCF approach.
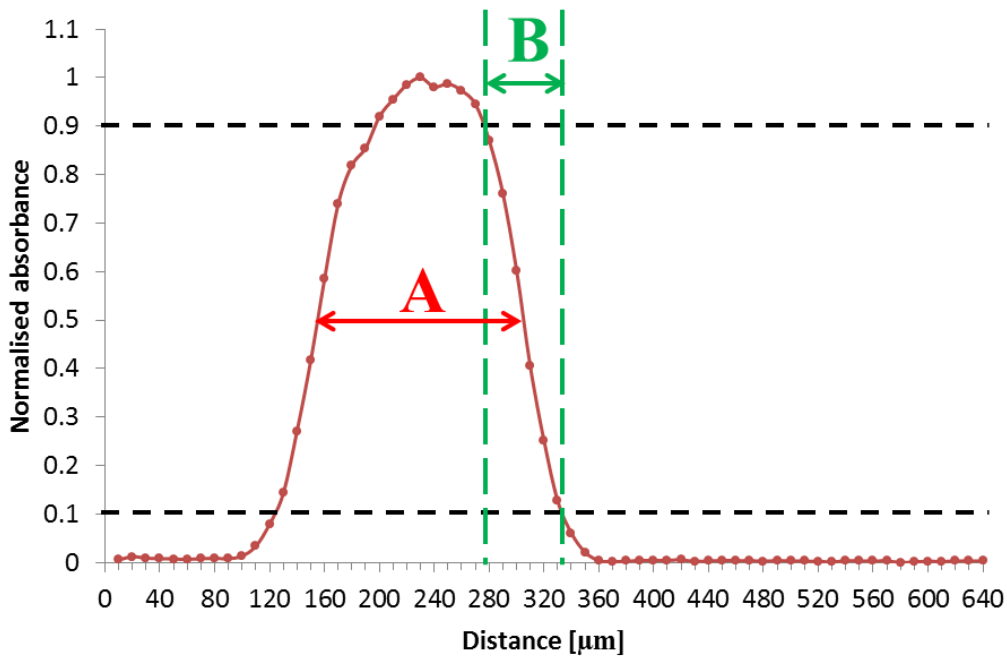
Figure 3.9 A PLGA line profile for NLCF processed t=0 m image showing the derivation of the parameters (A) full width at half maximum height of the normalised PLGA signal and (B) the dimension of the right hand side interface.

Figure 3.10a and b show peak height values extracted from across the centre line (from left to right) of the pre-processed and peak height generated water and PLGA images shown in Figure 3.6. Figure 3.10a shows the evolution of the intensity of the water peak at each pixel across the image as a function of time and Figure 3.10b shows the associated normalised plot of the PLGA from which full width at half height, parameter 'A' , can be observed. The evolution of the dimension of the right handside water polymer interface, parameter 'B', and FWHM, parameter 'A', are plotted in Figure 3.10c and d, respectively.

From Figure 3.10a it is possible to observe that the overall water concentration across the particle increases as a function of time as one might reasonably expect; rising from an intensity ~15% of its maximum value at the local minimum at t=0 h to a value of ~75% of its maximum value at the local minimum at t=9 h. The profile at t=0, which is ~5 minutes after the particle has been subjected to water, indicates that the initial ingress of water into the particle is rapid, most likely due to the porous nature of the scCO$_2$ processed starting material. The shape of the profile initially appears to be fairly uniform and becomes less so as time progresses which may reflect the irregular shape of

the particles. It is likely that initial compression onto the ATR crystal may make the analysed surface uniform (the ATR experiment collects data from the first 2-10 µm in direct contact with the crystal) but as the particle hydrates, swells and hydrolyses, the signal obtained via the ATR crystal will depend on the volume of the particle directly above the evanescent field and how it swells and or moves, potentially resulting in a loss of uniformity. It is also important to note that one can observe the decrease in SNR overtime by following smoothness of the peaks in Figure 3.10a because as time progresses each line profile fluctuates more than previous one.
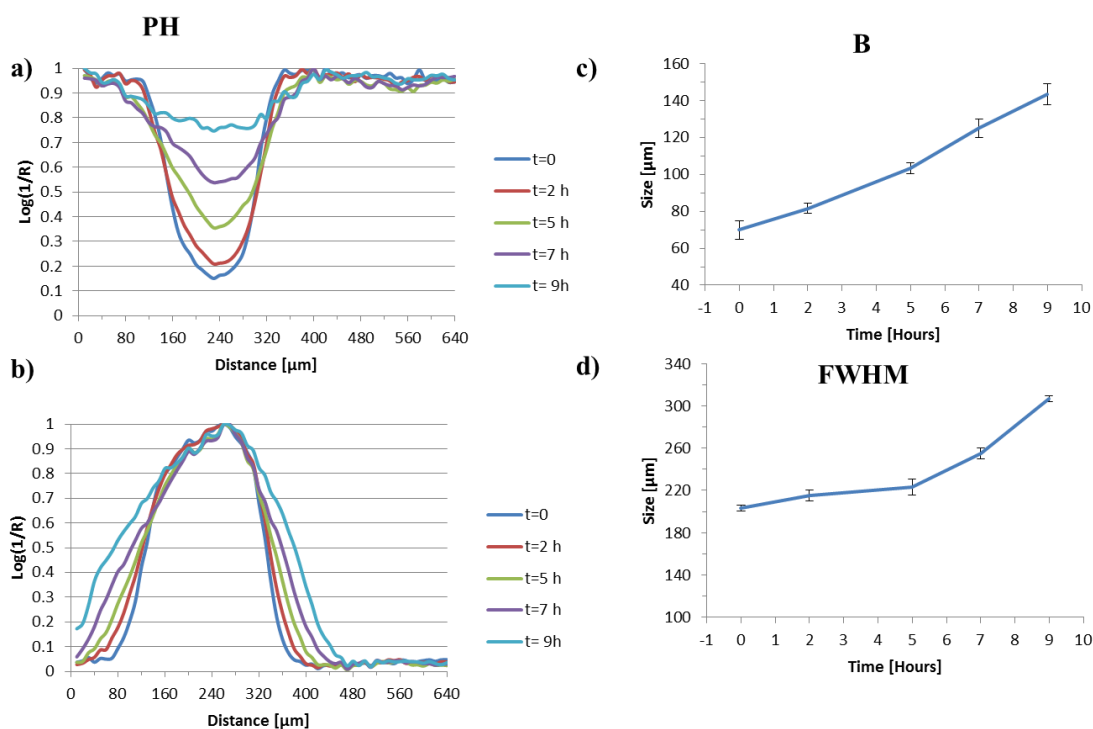
Figure 3.10 (a) The normalised change in the intensity of the water peak at each pixel across the image as a function of time, (b) the normalised plot of intensity of the polymer particle, (c) the evolution of parameter 'A' as a function of time and (d) the evolution of the parameter 'B' as a function of time for the peak height derived images.

Figure 3.10b shows the complementary data to that in Figure 3.10a relating to the intensity of the polymer particle extracted from across the centre line of the peak height generated images. As the particle swells, the concentration of polymer measured within any given pixel will decrease and the concentration of water within that same pixel will increase. Therefore the intensity of the polymer peak (which should be the inverse of the water peak in this binary system) would provide an indication of the degree of

swelling in the z-direction. Instead, here the change in width of the normalised intensity of the peak height of polymer peak as a function of time is used to provide an indication of the degree of swelling in the y-direction. This data is normalised as it facilitates the observation of the change in full width at half height maximum (FWHHM) better than the equivalent data with the non-normalised y values, which decrease over time. For the peak height derived images one can clearly see the width of this peak increasing as a function of time and this is plotted in Figure 3.10c.

As described above, a hydrated zone 'B' has been defined where both the water intensity and the polymer band intensity are below a certain threshold (10% of the maximum value). Figure 3.10c shows the plot of the B zone for the peak height derived images as a function of time. The size of this zone increases quite dramatically over the course of this experiment, with dimensions around 70 μm at t=0 and expanding to 140 μm at t=9 h. This increase in thickness of the outer hydration layer is an interesting finding and in broad agreement with confocal fluorescence images generated by Bajwa *et al.* [37] of hydrating HPMC tablets. In the HPMC system an outer hydration layer of ~100 μm increasing to 200 μm was measured over the course of a 'wetting' experiment. Clearly the timescales are different between the two systems due to the inherently different hydrophilicities, but nonetheless this adds credence to the nature of these measurements and the definition of B.

Figure 3.11a-d show data comparable to that presented in Figure 3.10, this time derived from the MCR-ALS generated images shown in Figure 3.7a. Figure 3.11a and Figure 3.11b show the evolution of the water intensity and the normalised plot of the polymer factor intensity respectively. The shape and the intensities of the profiles in these figures are similar to those derived from the peak height measurements, but there was less noise in the MCR derived data (most evident in comparison to Figure 3.10a) particularly at longer time points, where the band intensities of the polymer peaks are quite low. This improvement of SNR occurs because the peak height data is derived from a single point and the MCR-ALS data is derived from a large number of data points. There is perhaps some evidence of the polymer band intensity profile being less sharp at longer time points and at its maximum, which could be related to the contribution of water within the extracted pure factor associated with the polymer (MCR Factor 2 in Figure 3.7a) and will also be a function of the fixed lineshape of factor with its associated peak maxima and minima which will not be able to exactly match the spectrum at each pixel.
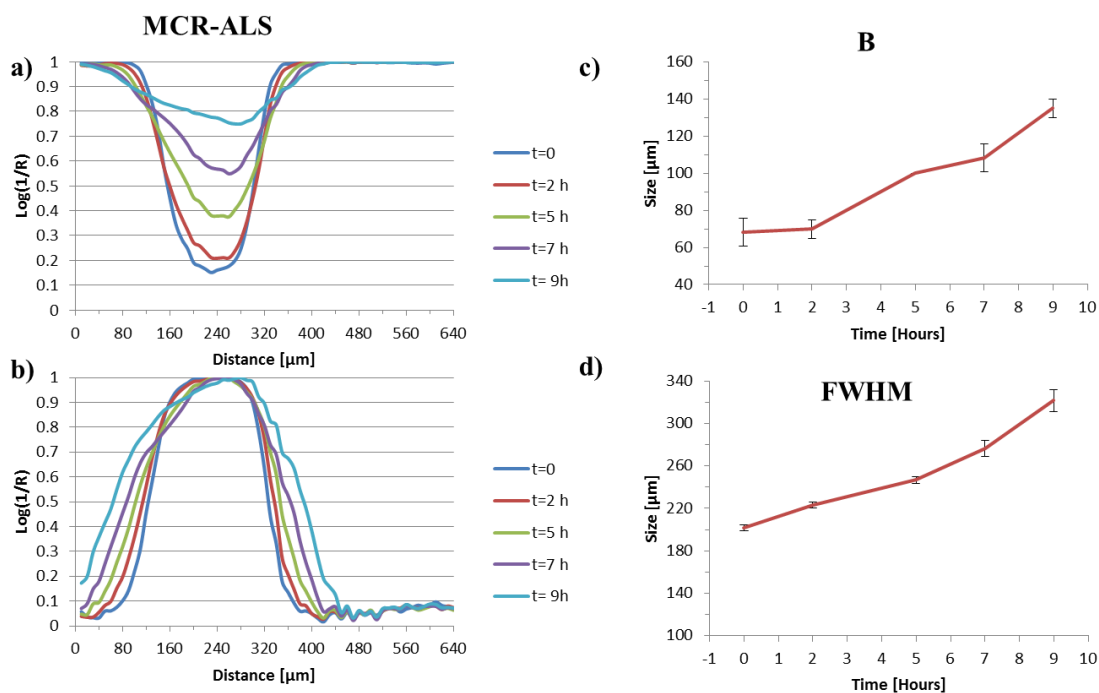
Figure 3.11 (a) The normalised intensity of the water peak at each pixel across the image as a function of time, (b) the normalised plot of intensity of the polymer particle, (c) the evolution of parameter 'A' as a function of time and (d) the evolution of the parameter 'B' as a function of time for the MCR-ALS derived images.

Both the B values (Figure 3.11c) and the full width at half maximum height values (Figure 3.11d) as a function of time are very similar to those shown in Figure 3.10c and Figure 3.10d. This indicates that there is perhaps no significant improvement in the quality of output obtained for this system when performing an MCR-ALS analysis on the data when compared to the more rapid peak height approach. Of course the MCR-ALS method can be used without any prior knowledge of the system; therefore there is no need to identify a peak specific to each component within it, which could be advantageous in some instances.

Figure 3.12a-d show data comparable to that shown in Figure 3.10 and Figure 3.11, this time derived from the NLCF generated images (Figure 3.8). Figure 3.12a shows the intensity of the curve fitted water band as a function of time. Both the intensities and width of these profiles are somewhat different to those observed in those derived from the peak height (Figure 3.10a) and MCR-ALS (Figure 3.11a). Firstly the intensities are generally higher than those observed for the data derived using the other two approaches, this is more pronounced at short times, with the values at t=0 being

approximately 30% of their final intensity (c.f. 15% for both peak heights and MCR-ALS).
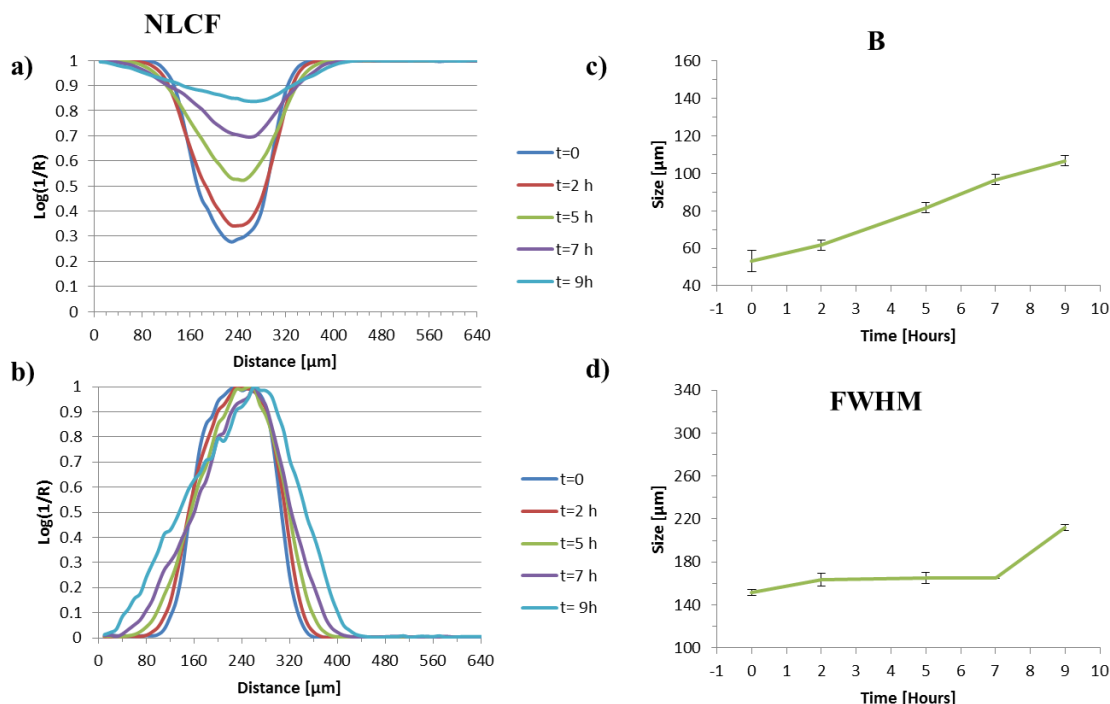
Figure 3.12 (a) The increase in the intensity of the water peak at each pixel across the image as a function of time, (b) the normalised plot of intensity of the polymer particle, (c) the evolution of parameter 'A' as a function of time and (d) the evolution of the parameter 'B' as a function of time for the NLCF derived images.

Some explanation was found in the consideration of the factors/bands used to generate the initial images from which these line profiles were generated. In the case of the peak height data, it is clear that the vector normalisation and baseline correction has enhanced SNR of the images (Figure 3.2), but it is entirely feasible that this will exert some influence on the intensity values generated for each spectrum within a given pixel.

In the case of the MCR-ALS the extracted pure factor for the polymer contains a contribution from water (Figure 3.7a) and therefore when the scores at each pixel for the pure water factor are calculated then they will be underestimated. As the NLCF approach is able to generate both a pure water signal and a pure polymer signal free from interference, it is anticipated that the intensities presented in these profiles will be more likely to match the true concentration profile.

Figure 3.12b is also somewhat different to the analogous peak height and MCR-ALS data; in that it is narrower and different in shape. Once more it is the convolution of the

water and polymer bands in both the peak height and MCR-ALS spectra that contributes to the broadening of this profile, relative to the NLCF data.

Figure 3.12c shows the increase in the B zone dimension as a function of time. The values plotted here are lower than those obtained via both the peak height and MCR-ALS approaches and the error determined at each time point is somewhat lower than the corresponding values for the other two methods. This is a clear indication of the ability of the NLCF procedures to eliminate noise from the processed images. Figure 3.12d shows the FWHM of the normalised polymer band profile generated from the NLCF images (Figure 3.8) and this also shows a reduction in width in comparison with the analogous data generated using the other two methods. The reduction in size of the B zone and the FWHM in comparison with the data generated using peak heights and MCR-ALS is a reflection of the ability of the NLCF method to discriminate between the water and polymer contributions at each pixel, reducing the blurring effect of convoluted spectra.

3.6.4   Degradation Rate Calculation

PLGA microparticles are widely used as sustained delivery vehicles, where the rate of hydrolysis will control the release rate in both diffusion and erosion scenarios (Figure 1.1, Chapter 1). Parameters that govern the hydrolytic degradation of PLGA include molecular weight, structure and morphology and PLGA degradation dynamics. FTIR spectroscopy has routinely been used to follow hydrolysis kinetics, but this is the first time that such measurements have been undertaken on single microparticles in this manner. Two infrared bands have been observed at ~1452 cm^{-1} and ~1424 cm^{-1} that correspond to the antisymmetric bending of CH_3 from the lactic acid units and the symmetric bending of CH_2 from the glycolic acid units of the PLGA polymer. The relative intensities of these two bands can be used to estimate the relative quantity of glycolic and lactic acid units present in the polymer and has been used to determine the rate of hydrolysis of the two co-polymer segments within the same experiment. Work by Vey *et al.* [8] has shown that the lactic acid units hydrolyse ~1.3 times slower than the glycolic acid units. Unlike large-sized (a few mm) PLA/GA polymer devices, microspheres less than 300 μm in diameter have been shown to undergo homogeneous degradation with the rate of degradation of the core being equivalent to that at the surface [38,39]. Therefore rate constants from different regions within a microparticle would be expected to give the same calculated rate.
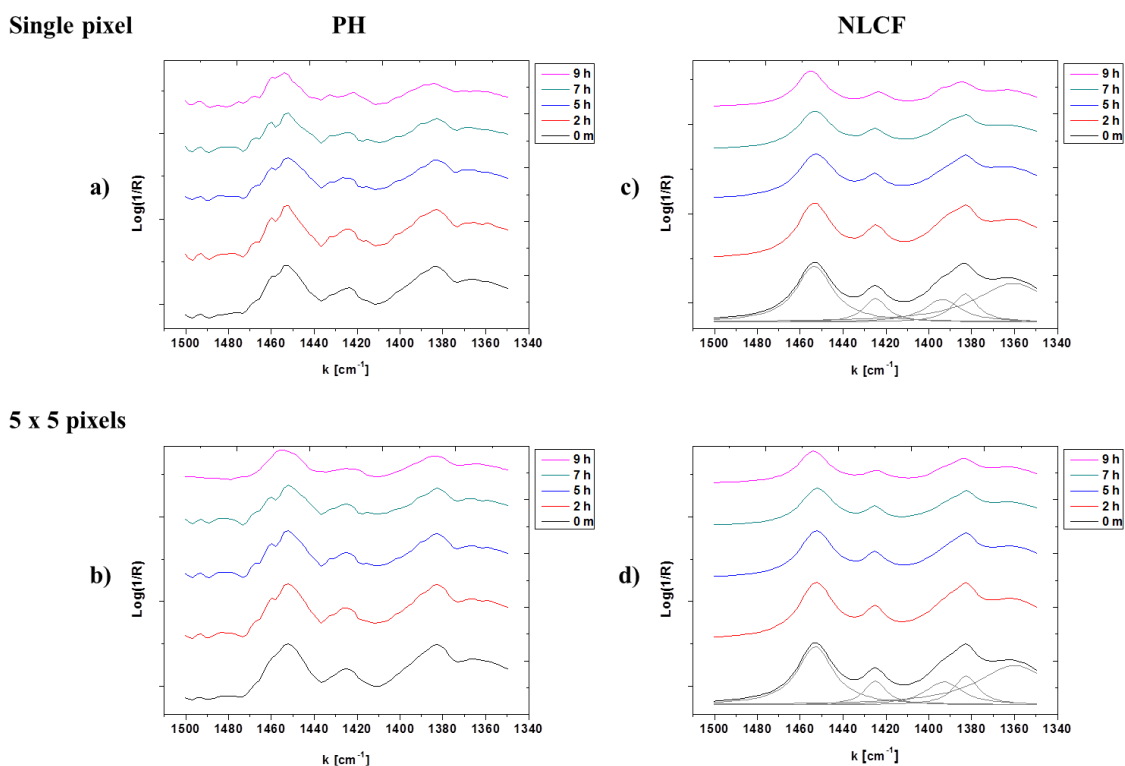
Figure 3.13 Typical single pixel and averaged (over 5x5 pixels) spectra of pre-treated raw ((a) and (b)) and non-linear curve fitted ((c) and (d)) data. Spectra from bottom to top were obtained at t=0, t=2h, t=5h, t=7h and t=9h, respectively.

Figure 3.13 shows typical single pixel spectra (Figure 3.13a), spectra resulting from the binning of 5x5 pixels (Figure 3.13b), the resultant peak fits from a single pixel (Figure 3.13c)) and the result of peak fits from the binning of 5x5 pixels (Figure 3.13d) which have been used to calculate the rate constants. It is important to note that 5x5 pixel regions are within the microparticle and 5 pixels apart from each other and the single pixels are chosen from the centre of these 5x5 regions of interest, therefore standard deviation between the triplicates of regions and pixels are not influenced by any neighbourhood effects.

To compare the relative merit of each of the data analysis approaches used in this study, the hydrolysis rates for both the glycolic and lactic blocks independently within the same experiment have been calculated. MCR-ALS was unable to provide pure component spectra for both the lactic and glycolic segments of PLGA, probably due to the nature of the iterative extraction process. MCR-ALS relies on variance within spectral data sets to extract pure component factors and as the ratio between the glycolic and lactic units during hydrolysis is constant throughout the experiment (i.e. the data is

co-linear) the algorithm does not detect any variance. Consequently a single 'PLGA' pure component is generated.

Hard constraints such as pure spectra and/or different compositions of pure PLGA spectra were not used as initial estimates of the MCR-ALS factors in the image set. Each of these would have been valid approaches however were beyond the scope of this work which was to compare soft and hard modelling approaches without prior knowledge of component spectra.

Hydrolysis rate constants for the lactic units (k_L) and the glycolic units (k_G) were calculated using both the peak height data and the NLCF data from the logarithmic plot of peak intensity versus degradation time (Figure 3.14) using the band ~1452 cm^{-1} for the lactic units and that at ~1424 cm^{-1} for the glycolic units, using the spectra shown in Figure 3.13. First order kinetics as defined in Equation 3.4 and Equation 3.5 were assumed;

$$\ln(I) = -k_L t + n \qquad \textbf{Equation 3.4}$$

for the lactic unit and,

$$\ln(I) = -k_G t + n \qquad \textbf{Equation 3.5}$$

for the glycolic unit.

Rate constants were calculated by selecting the spectrum (or extracted factor) at 3 random pixels within each image. For comparison, the same positions were used for each of the peak height and NLCF image analysis approaches and the mean of the three values are shown in Table 3.2.

Table 3.2 List of degradation rate constants of the glycolic and lactic units in day^{-1} calculated for triplicates of averaged 5x5 pixels and single pixel spectra using peak height values and curve fitted area values over the course of the 9 h hydrolysis experiment. Errors quoted are the standard deviation of 3 measurements taken from 3 different regions of the same particle.

	5x5 pixels		Single pixel	
Method	k_L	k_G	k_L	k_G
Peak Height	1.13±0.2	1.41±0.35	0.9±0.53	1.53±0.98
NLCF	1.47±0.1	2.06±0.13	1.29±0.21	1.67±0.34

Figure 3.14 First order kinetic plots used to determine the hydrolysis rates for (a) peak height data using single pixels, (b) peak height data using binned 5x5 areas, (c) MCR-ALS data from single pixels, (d) MCRALS data using binned 5x5 areas, (e) NLCF data using single pixels and (f) NLCF data using binned 5x5 areas.

Rate constants were also determined by binning the spectra/factor score from 3 areas of 5x5 pixels from random regions within each image. Once more the same regions were used for each of the peak height, MCR-ALS and NLCF image analysis approaches and the calculated rate data (where possible) are shown in Table 3.2 and are the result of the mean of three values.

The same hydrolysis experiment was also repeated for 2 other scCO$_2$ processed PLGA 75/25 microparticles in order to evaluate the reproducibility and accuracy of the degradation rate calculation using images obtained from such experiment. Figure 3.15a and b show the peak height images of the PLGA particles and water distribution for selected time points. It can be seen that it takes longer for the microparticle in Figure 3.15a to degrade completely (~12 h) whilst the other 2 relatively smaller microparticles

in Figure 3.15b degrade in a somewhat similar time frame (~9 h) to the previously discussed microparticle (Figure 3.6b).
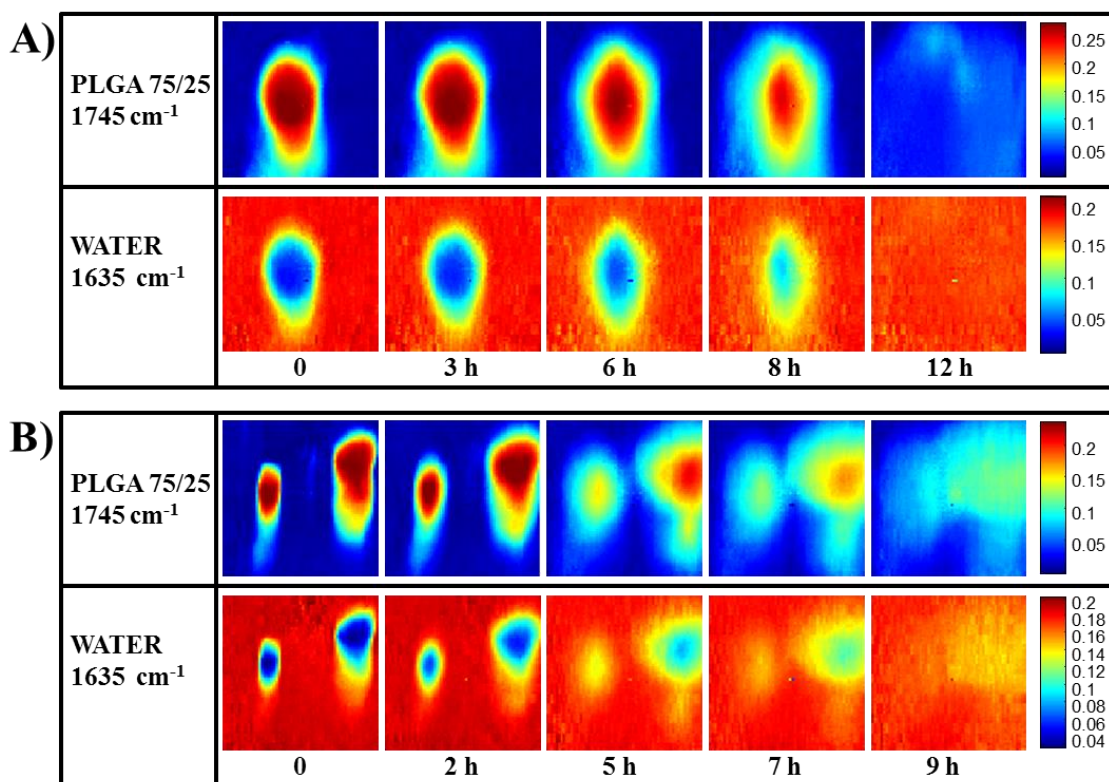
Figure 3.15 A set of false colour images representing temporal peak height distribution of two PLGA 75/25 microparticle(s) on the top and water at the bottom, in both (a) and (b), respectively.

However as one would expect the degradation rate of the particles is very close to eachother as listed in Table 3.3. These experiments shown in Figure 3.15 and the calculated degradation rates listed in Table 3.3 have shown that such hydrolysis experiment was reproducible and confidence was established in the accuracy of the degradation rate calculation.

Tracy *et al.* [40] studied the degradation of poly(lactide-co-glycolide) microspheres *in vivo* and *in vitro* and determined degradation rate constants by measuring the polymer molecular weight as a function of time by gel-permeation chromatography. They found that the *in vivo* degradation rate was higher than *in vitro* degradation one. Their calculations of *in vivo* rate constant by GPC analysis for ester capped and uncapped (-COOH) PLGA50/50 microspheres were 0.033 ± 0.006 day^{-1} and 0.13 ± 0.05 day^{-1} respectively.

Table 3.3 List of degradation rate constants of the glycolic and lactic units in day^{-1} calculated for six of averaged 5x5 pixels and single pixel spectra using peak height values of glycolic and lactic units over the course of the 2 hydrolysis experiments shown in Figure 3-15. Errors quoted are the standard deviation of 6 measurements each taken from a different region of the same particle in each image set.

	5x5 pixels		Single pixel	
Experiment	k_L	k_G	k_L	k_G
Figure 3.15a	1.09±0.2	1.31±0.31	0.96±0.44	1.43±0.73
Figure 3.15b	1.21±0.18	1.48±0.33	1.02±0.31	1.48±0.44

Considering that the PLGA microparticle studied here was scCO$_2$ processed therefore very porous, and a calibration (i.e. %GA or %LA versus IR absorbance) was not considered as in [8], due to having one polymer composition, the k values calculated are in reasonable agreement with each other and with the values determined by Tracy *et al.* [40] and, as one might anticipate, the error obtained when calculating rate constants by binning a number of spectra is somewhat lower than that obtained from a single pixel. The errors are larger for the peak height derived calculations than those from the NLCF measurements. It is also clear that the ratio of the rate constants calculated for the lactic and glycolic groups is also comparable with that determined by Vey *et al.* [8]; the ratio of rate constants were determined to be 1.2 (peak height binned pixels), 1.7 (peak height single pixels), 1.4 (NLCF binned pixels) and 1.3 (NLCF single pixels). Interestingly the error determined for the k calculations for the MCR-ALS processed images seemed to be independent of the number of pixels used to determine them. It is unclear if this finding is real or an anomaly of the pixels chosen to make the measurements.

3.7 Conclusions

The real-time hydrolytic degradation of a scCO$_2$ processed PLGA microparticle has been demonstrated using ATR-FTIR imaging for the first time. After pre-processing, the SNR was sufficient to monitor the swelling, shrinking and degradation of the microparticles using the rapid peak height measurement. However quantitative information such as hydrated layer size, FWHM of the particle was calculated with smaller errors when multivariate analyses were employed. Both multivariate approaches considered, hard (NLCF) and soft (MCR-ALS) improved the spatial resolution of the images compared to peak height measurements.

The supervised NLCF approach has been shown to have several advantages over traditional peak height measurements and a commonly applied multivariate tool; MCR-ALS. Firstly the application of NLCF routines to such data has been shown to enhance the spatial resolution within a sample with (a) overlapping spectral signals and (b) containing interfaces with large discrepancies in the refractive index (i.e. air/polymer). Secondly it has been shown to improve SNR and sharpen features such as interfaces in the processed images, due to its ability to discriminate between different species in a mixture, this is particularly pronounced when one compares this approach to standard peak height measurements. Thirdly unlike MCR-ALS the approach is not influenced by colinearity, therefore supervised NLCF can be used to extract chemical information from species changing at the same ratio during a kinetic process such as hydrolysis. Finally the high SNR at each pixel readily facilitates the calculation of rate constants from a single pixel with a low error when compared to traditional peak height approaches. All these advantages come at a significant time penalty; the NLCF algorithm described takes ~5 hours to extract information from a single mid-IR image containing 4096 spectra, this compares to ~2 seconds for peak height analysis and ~1 minute for MCR-ALS on the same image using the same PC.

With the help of fast developing computing hardware power, the supervised NLCF method developed in this project can be a useful IR imaging analysis tool providing high resolution images and quantitative analysis for many more cases particularly where hard modelling is the only option such as deconvoluting protein spectra when searching for changes in secondary structure. Also, as shown for calculating the degradation rate, the precision of pixel data may be useful to compensate the time penalty of the NLCF analysis when monitoring kinetic processes, as it can be applied to a limited number of pixels from a series of images to obtain rates. And as for the wet images MCR-ALS provides a spatial resolution that is close to that of NLCF, MCR-ALS processed images could be used for the qualitative image comparisons instead of NLCF. This aspect of a combining multivariate analysis, i.e. the use of both MCR-ALS and NLCF analyses to determine quantitative information from large image sets for different batches of a number of samples, is further discussed in the following chapter.

3.8 References

[1] E.N. Lewis, P.J. Treado, R.C. Reeder, G.M. Story, A.E. Dowrey, C. Marcott, I.W. Levin, Fourier Transform Spectroscopic Imaging Using an Infrared Focal-Plane Array Detector, Anal. Chem. 67 (1995) 3377-3381.

[2] P. R. Griffiths, J. A. de Haseth, Fourier Transform Infrared Spectrometry, 2nd ed., John Wiley & Sons Inc., Hoboken, New Jersey, 2007.

[3] R. Bhargava, Infrared Spectroscopic Imaging: The Next Generation, Appl. Spectrosc. 66 (2012) 1091-1120.

[4] S.G. Kazarian, K.L.A. Chan, Micro- and Macro-Attenuated Total Reflection Fourier Transform Infrared Spectroscopic Imaging, Applied Spectroscopy. 64 (2010) 135A-152A.

[5] S.G. Kazarian, K.L.A. Chan, Chemical Photography• of Drug Release, Macromolecules. 36 (2003) 9866-9872.

[6] F. M. Mirabella, Attenuated Total Reflection Spectroscopy, in: F. M. Mirabella (Ed.), Modern Techniques in Applied Molecular Spectroscopy, 1st ed., John Wiley & Sons, New York, 1998, pp. 160-178.

[7] S. Hajatdoost, C. Sammon, J. Yarwood, FTIR–ATR studies of diffusion and perturbation of water in polyelectrolyte thin films. Part 4. Diffusion, perturbation and swelling processes for ionic solutions in SPEES/PES membranes, Polymer. 43 (2002) 1821-1827.

[8] E. Vey, C. Rodger, J. Booth, M. Claybourn, A.F. Miller, A. Saiani, Degradation kinetics of poly(lactic-co-glycolic) acid block copolymer cast films in phosphate buffer solution as revealed by infrared and Raman spectroscopies, Polym. Degrad. Stab. 96 (2011) 1882-1889.

[9] J. van der Weerd, K.L.A. Chan, S.G. Kazarian, An innovative design of compaction cell for in situ FT-IR imaging of tablet dissolution, Vibrational Spectroscopy. 35 (2004) 9-13.

[10] S. Huotari, T. Pylkkanen, R. Verbeni, G. Monaco, K. Hamalainen, Direct tomography with chemical-bond contrast, Nature Materials. 10 (2011) 489-93.

[11] G. Sciutto, P. Oliveri, S. Prati, M. Quaranta, S. Bersani, R. Mazzeo, An advanced multivariate approach for processing X-ray fluorescence spectral and hyperspectral data from non-invasive in situ analyses on painted surfaces, Anal. Chim. Acta. 752 (2012) 30-38.

[12] D. Zhang, P. Wang, M.N. Slipchenko, D. Ben-Amotz, A.M. Weiner, J.X. Cheng, Quantitative Vibrational Imaging by Hyperspectral Stimulated Raman Scattering Microscopy and Multivariate Curve Resolution Analysis, Anal. Chem. 85 (2013) 98-106.

[13] P. Williams, P. Geladi, T. Britz, M. Manley, Near-infrared (NIR) hyperspectral imaging and multivariate image analysis to study growth characteristics and differences between species and strains of members of the genus Fusarium, Analytical and Bioanalytical Chemistry. 404 (2012) 1759-1769.

[14] J.M. Amigo, Practical issues of hyperspectral imaging analysis of solid dosage forms, Analytical and Bioanalytical Chemistry. 398 (2010) 93-109.

[15] R. Bhargava, S. Wang, J.L. Koenig, Processing FT-IR Imaging Data for Morphology Visualization, Appl. Spectrosc. 54 (2000) 1690-1706.

[16] C. Gendrin, Y. Roggo, C. Collet, Pharmaceutical applications of vibrational chemical imaging and chemometrics: A review, J. Pharm. Biomed. Anal. 48 (2008) 533-553.

[17] P. Bassett, Drug Delivery Systems: Trends, Technologies and Market Opportunuties, 2nd ed., Drug & Market Development, Southborough, MA, USA, 1999.

[18] S.G. Kazarian, K.L.A. Chan, Applications of ATR-FTIR spectroscopic imaging to biomedical samples, Biochimica et Biophysica Acta (BBA) - Biomembranes. 1758 (2006) 858-867.

[19] J. Jaumot, R. Gargallo, A. de Juan, R. Tauler, A graphical user-friendly interface for MCR-ALS: a new tool for multivariate curve resolution in MATLAB, Chemometrics Intellig. Lab. Syst. 76 (2005) 101-110.

[20] J. J. Andrew and T. M. Hancewicz, Rapid analysis of Raman image data using two-way multivariate curve resolution, Applied Spectroscopy. 52 (1998) 797-807.

[21] V.A. Solé, E. Papillon, M. Cotte, P. Walter, J. Susini, A multiplatform code for the analysis of energy-dispersive X-ray fluorescence spectra, Spectrochimica Acta Part B: Atomic Spectroscopy. 62 (2007) 63-68.

[22] L. Chen, M. Garland, Computationally Efficient Curve-Fitting Procedure for Large Two-Dimensional Experimental Infrared Spectroscopic Arrays Using the Pearson VII Model, Appl. Spectrosc. 57 (2003) 331-337.

[23] W. Xu, K. Chen, D. Liang, W. Chew, Hierarchical band-target entropy minimization curve resolution and Pearson VII curve-fitting analysis of cellular protein infrared imaging spectra, Anal. Biochem. 387 (2009) 42-53.

[24] N.J. Everall, I.M. Priestnall, F. Clarke, L. Jayes, G. Poulter, D. Coombs, M.W. George, Preliminary Investigations into Macroscopic Attenuated Total Reflection-Fourier Transform Infrared Imaging of Intact Spherical Domains: Spatial Resolution and Image Distortion, Appl. Spectrosc. 63 (2009) 313-320.

[25] K.L.A. Chan, S.G. Kazarian, New Opportunities in Micro- and Macro-Attenuated Total Reflection Infrared Spectroscopic Imaging: Spatial Resolution and Sampling Versatility, Appl. Spectrosc. 57 (2003) 381-389.

[26] A. de Juan, M. Maeder, T. Hancewicz, L. Duponchel, R. Tauler, Chemometric Tools for Image Analysis, in: R. Salzer, H.W. Siesler (Eds.), Infrared and Raman Spectroscopic Imaging, Wiley-VCH Verlag GmbH & Co., Berlin, 2009, pp. 65-109.

[27] W. H. Lawton, E. A. Sylvestri, Technometrics. 13 (1971) 617-633.

[28] J. Wang, P.K. Hopke, T.M. Hancewicz, S.L. Zhang, Application of modified alternating least squares regression to spectroscopic image analysis, Anal. Chim. Acta. 476 (2003) 93-109.

[29] H. Eskandari, S.E. Salcudean, R. Rohling, Tissue strain imaging using a wavelet transform-based peak search algorithm, Ultrasonics, Ferroelectrics and Frequency Control, IEEE Transactions on. 54 (2007) 1118-1130.

[30] A. Savitzky, M.J.E. Golay, Smoothing and Differentiation of Data by Simplified Least Squares Procedures, Anal. Chem. 36 (1964) 1627-1639.

[31] P. Lasch, D. Naumann, Spatial resolution in infrared microspectroscopic imaging of tissues, Biochimica et Biophysica Acta (BBA) - Biomembranes. 1758 (2006) 814-829.

[32] M. Offroy, Y. Roggo, P. Milanfar, L. Duponchel, Infrared chemical imaging: Spatial resolution evaluation and super-resolution concept, Anal. Chim. Acta. 674 (2010) 220-226.

[33] A.G. Michette and S.J. Pfauntsch, J. Phys. D: Appl. Phys. 33 (2000) 1186-1190.

[34] S. Piqueras, L. Duponchel, R. Tauler, A. de Juan, Resolution and segmentation of hyperspectral biomedical images by Multivariate Curve Resolution-Alternating Least Squares, Anal. Chim. Acta. 705 (2011) 182-192.

[35] S. Piqueras, J. Burger, R. Tauler, A. de Juan, Relevant aspects of quantification and sample heterogeneity in hyperspectral image resolution, Chemometrics Intellig. Lab. Syst. 117 (2012) 169-182.

[36] J. Kuligowski, G. Quintas, R. Tauler, B. Lendl, B. de la Guardia, Background Correction and Multivariate Curve Resolution of Online Liquid Chromatography with Infrared Spectrometric Detection, Anal. Chem. 83 (2011) 4855-4862.

[37] G.S. Bajwa, K. Hoebler, C. Sammon, P. Timmins, C.D. Melia, Microstructural imaging of early gel layer formation in HPMC matrices, J. Pharm. Sci. 95 (2006) 2145-2157.

[38] M. Vert, S. M. Li, H. Garreau, Attempts to map the structure and degradation characteristics of aliphatic polyesters derived from lactic and glycolic acids, J. Biomater. Sci. Polymer Edn. 6 (1994) 639-649.

[39] G. Spenlehauer, M. Vert, J.P. Benoit, A. Boddaert, In vitro and In vivo degradation of poly(D,L lactide/glycolide) type microspheres made by solvent evaporation method, Biomaterials. 10 (1989) 557-563.

[40] M.A. Tracy, K.L. Ward, L. Firouzabadian, Y. Wang, N. Dong, R. Qian, Y. Zhang, Factors affecting the degradation rate of poly(lactide-co-glycolide) microspheres in vivo and in vitro, Biomaterials. 20 (1999) 1057-1062.

4 Investigation of Factors Influencing the Hydrolytic Degradation of Single PLGA Microparticles

4.1 Introduction

As described in Chapter 1, PLGA is a random copolymer of Poly(glycolic acid) (PGA), poly(lactic acid) (PLA), and is a U.S. Food and Drug Administration (FDA) approved, biodegradable [1,2] synthetic polyester that is physically strong and highly processable [3]. PLGA has suitable properties for biomedical applications as a scaffold [4,5] and in controlled release drug delivery systems [6-8]. As outlined in Section 1.2 of Chapter 1, PLGA has been comprehensively studied as carrier matrix for macromolecules such as proteins and peptides which are considered promising for the treatment of a range of conditions such as cancer, human growth deficiency, and multiple sclerosis [9,10].

Understanding polymer degradation is pre-requisite for modifying the performance of any biodegradable polymeric drug delivery system. PLGA degrades via chain scissions of ester bond linkages in the polymer backbone by hydrolytic attack of water molecules. Lactic acid and glycolic acid, are the end products of degradation and after hydrolysis they are metabolised or ejected by the body [11,12]. The degradation and drug release rate mainly dependent on the carrier matrix, PLGA. The ratio of glycolic acid used to control the hydrophilicity of the matrix, particle size and morphology, temperature, and to a lesser extent molecular weight are the critical parameters in the rate of hydrolysis.

Factors affecting the hydrolytic degradation of PLGA devices that were in the form of microspheres [13,14], porous scaffolds [15], dense films [16,17] and cylinders [18] have been widely studied, but not using FTIR imaging which provides visual evidence of the morphological changes and chemistry during hydrolysis.

The hydrolytic degradation of devices based on lactic and glycolic acid polymers with different sizes (a few mm to µm) have been comprehensively investigated *in vivo* and *in vitro* by Vert *et al.* and a heterogeneous degradation mechanism in mm-sized devices was reported; characterized by a rate of degradation in the core which is greater than that at the surface of the device [19,20]. Interestingly Alexis *et al.* reported a homogeneous mode of degradation, with uniform rates of degradation throughout 40x25 mm^2 PLGA films. Furthermore a recent report, by Vey *et al.* who studied mm size PLA/GA polymer discs by FTIR and Raman spectroscopies [21], was supporting the heteregenous mode degradation in such devices.

Although the general assumption is that macroscopic PLGA devices degrade heterogeneously, unlike mm size devices, microspheres less than 300 microns in diameter have shown a homogeneous degradation with the rate of degradation of the core being equivalent to that at the surface [20,22]. Morphological assessment of microspheres from *in vivo* studies was shown to support the picture of homogeneous hydrolytic degradation of microspheres of PLGA copolymers [23]. Therefore biodegradation of the PLGA microparticle studied here was expected to occur through a homogeneous hydrolytic chain cleavage mechanism where the rates of polymer degradation are similar for both the surface and the bulk of the microparticles.

Pharmaceuticals often have to be sterilised before use and, γ-irradiation is a well-established method for sterilising polymeric microparticle drug delivery systems [24]. Because each polymer may respond differently to ionizing radiation, it was found essential to determine any effects that this process may have on the drug carrier, PLGA which makes up almost 90 wt% of the formulation studied in this thesis. Therefore this chapter outlines a study to determine the maximum dose that can be administered to sterilize PLGA 50/50, the drug carrier matrix, and the effect of such sterilisation method on the physiochemical evolution of the polymer during hydrolysis.

Using the experimental procedure and relevant image analysis methods developed in chapter 3, the real-time hydrolysis of un-processed and gamma irradiated PLGA50/50 polymer at 70 ºC and scCO$_2$ processed PLGA copolymer microparticles with L/G molar compositions of 100/0, 75/25 and 50/50 were studied at 50 ºC and 70 ºC. The effect of scCO$_2$ process, gamma irradiation, monomer ratio and temperature on the hydrolysis of PLGA microparticles was investigated to facilitate a better understanding of the physiochemical factors affecting the hydrolysis rate and the morphological changes of the PLGA polymers by which the drug release behaviour is governed.

4.2 Experimental

4.2.1 Materials

PLGA RG502H (50/50 lactide/glycolide, I.V. 0.16-0.24, Bohringer-Ingleheim), PLGA RG752H (75/25 lactide/glycolide, I.V. 0.16-0.24, Bohringer-Ingleheim) PLA R202H (100/0 lactide/glycolide, I.V. 0.16-0.24, Bohringer-Ingleheim), pharmaceutical grade CO_2 (BOC Special Gasses) were used as received. Lactic acid (DL-Lactic acid, W261114, Sigma-Aldrich Company Ltd.) was dried at 70 ºC for 1 day before use. Water used in the experiments was purified using a ELGA Purelab option-R water distiller (Up to 15 MΩ-cm, Type II water) and degassed using a Fisherbrand FB11004 ultrasonic bath at the relevant temperature (50 °C or 70 °C) using 100% ultrasound power for 15 minutes.

4.2.2 CriticalMix^{TM} Processing of PLGAs

Each batch of formulation used in this study was prepared at CPL following the general procedure as described in Chapter 3, Section 3.2.2.

4.2.3 γ-Irradiation

Un-processed PLGA50/50 polymer was γ-irradiated at 25 and 100 kGy total dose in air by Synergy Health PLC (Swindon, UK) as described in Chapter 2, Section 2.7.

4.2.4 Scanning Electron Microscopy

To investigate the morphology of the PLGA microparticles, SEM analyses were performed as described in Section 2.3 in Chapter 2.

4.2.5 Molecular Weight Determination

The molecular weight (M_w) and molecular number (M_n) of the un-processed PLGA 50/50, PLGA 75/25, PLA and un-processed but gamma-irradiated PLGA 50/50 were determined by Gel Permeation Chromatography (GPC) using a PL-120 (Polymer Labs) with a differential refractive detector, as described in Chapter 2, Section 2.9.1.2.

4.2.6 DSC

Glass transition temperature (T_g) of the un-irradiated and un-processed PLGA 50/50, PLGA 75/25, PLA and un-processed but gamma irradiated PLGA50/50 was measured as described in Section 2.8, Chapter 2.

4.2.7 Macro ATR-FTIR imaging of reactions with the Golden Gate^{TM} Sampling Accessory

Each hydrolysis experiment was setup and data was collected under the conditions described in Chapter 3, Section 3.2.4 at 50 °C or 70 °C as indicated.

4.3 Data Processing

The raw images were cropped between 1820 and 1000 cm^{-1} which provided a number of characteristic bands associated with PLGA and also included the water $\delta(OH)$ peak $\sim$1635 cm^{-1} and pre-processed as described in Chapter 3, Section 3.3. Water and PLGA images were then generated using MCRv1.6 as described in Chapter 3, Section 3.5.1. The data used to generate line profiles to investigate polymer-water interfaces and to calculate the degradation rate constants were NLCF processed as described in Chapter 3, Section 3.5.2. Since the error obtained when calculating rate constants by binning a number of spectra (5x5 pixels) was found to be lower than that obtained from a single pixel, as discussed in Section 3.6.4 in Chapter 3, three regions of interest were selected from each experiment, for each sample and binned spectra of these regions were used to calculate rate constants.

4.4 Results and Discussion

4.4.1 The Effect of scCO$_2$ Process on Morphology and Hydrolytic Degradation of PLGA Microparticles

As detailed in Chapter 1, it is a well-known finding that scCO$_2$ processed polymer microparticles possess a porous morphology mainly because the escaping CO$_2$ form bubbles that push against the solidifying polymer [25-27]. The only difficulty of this process may be that the escaping CO$_2$ must be controlled well in order to avoid macroporosity. However for the CriticalMix^{TM} process, the porosity and particle size were shown to be controllable parameters as by changing the temperature or pressure of the scCO$_2$ in the mixing vessel, the viscosity of the liquefied mixture was shown to be changing significantly, allowing to further control of particle size and morphology [25]. And porosity is a key advantage in producing micron sized drug delivery devices because it enhances the diffusion based release of the drug molecules as a result of increased surface area.

The effect of scCO$_2$ process on the microparticle morphology was investigated using SEM which is a well-established imaging modality used in the microscopic characterisation of particles and other polymer surfaces [28]. Figure 4.1a shows SEM

images, obtained under same conditions from the particles that were coated at the same time under same conditions, of two un-processed PLGA 50/50 polymers and two SEM images of the CriticalMix™ processed of the same polymer microparticles are shown in Figure 4.1b. As one can immediately observe, in Figure 4.1b the particles have a lot of pores that are about a few μm and in comparison the un-processed microparticles in Figure 4.1a are rather flake shaped with very rough surface topography that appears to look like a very fine mesh, that would certainly allow less solvent ingress (or water in the case considered here) when exposed to it. Considering these SEM results it can verified that the $scCO_2$ process does create porosity, however no macroporosity could be observed which indicates the success of the CriticalMix™ process.
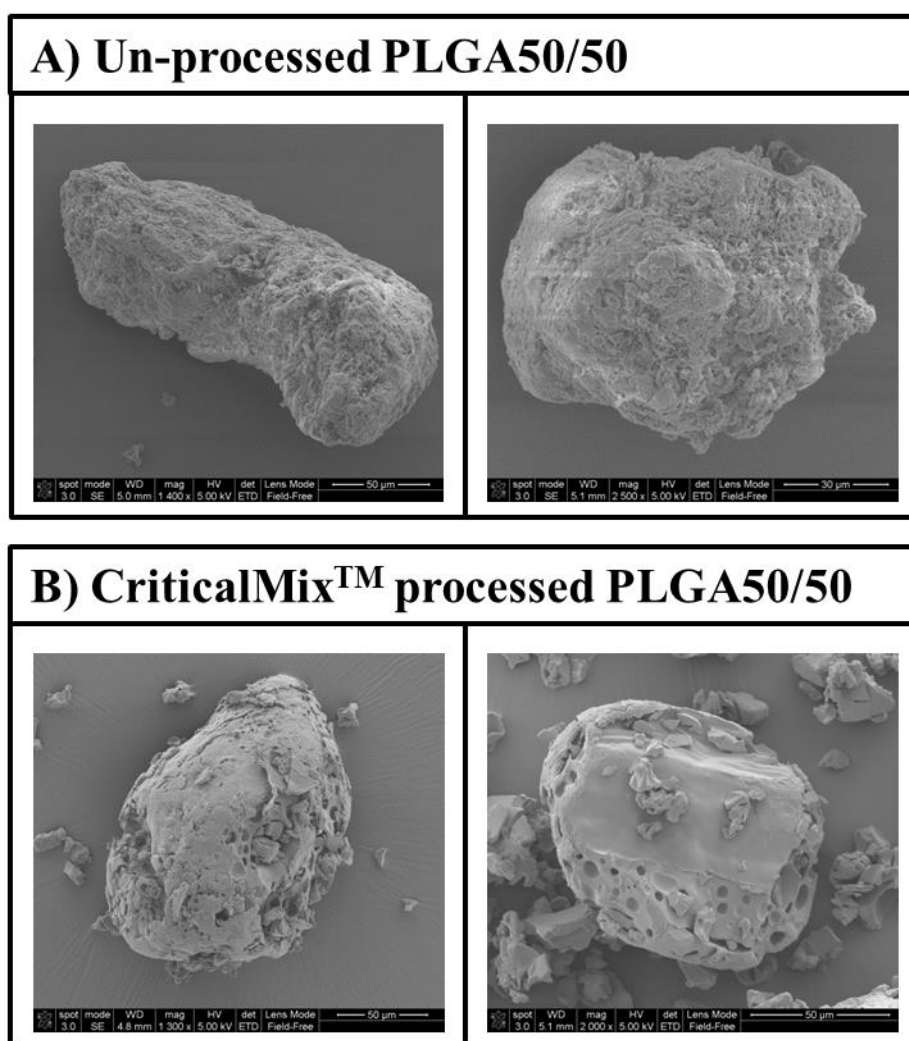
Figure 4.1 A set of SEM images of 2 particles in each row showing un-processed (a) and CriticalMix™ processed (b) PLGA 50/50 microparticles.

In order to facilitate an insight to the effect of scCO2 process (which resulted in a porous structure) on hydrolytic degradation behaviour of the PLGA 50/50 polymer,

FTIR imaging in ATR mode was studied as demonstrated in Chapter 3. The real-time hydrolytic degradation of two PLGA 50/50 microparticles; un-processed and CriticalMix^{TM} processed, were placed on to the ATR crystal and their interaction with water was monitored at 70 °C.

Figure 4.2a and b show the temporal distribution of MCR-ALS scores obtained for PLGA 50/50 at the top and water at the bottom, for an un-processed and a CriticalMix^{TM} processed microparticle, respectively. The 0 m images in both Figure 4.2a and b were collected over a period of ~ 5 m immediately after the water was added into the system. Even within this short collection time, as one could observe there is evidence of an interface layer of hydrated PLGA surrounding both the processed and un-processed particle, with an apparent concentration gradient from the particle centre outwards towards the water rich zone. It is evident that water ingresses immediately into the whole field of view, possibly between the particle and ATR crystal regardless of porosity. However although the water concentration is quite low (but not zero) in the 0 m images of both particles as indicated by the blue colour in the centre (or core), at the following time points, it can be observed that there is much more water with in the centre of the processed microparticle (turning from light blue to green as time proceeds) in comparison to the un-processed particle (a dark blue area that is decreasing size as time proceeds). And in the PLGA images that anticorrelate with the water images in both Figure 4.2a and b show a decrease in the size of the core region (red zone) in the 0 m images with increasing time points. However when one compares the last 3 PLGA images of un-processed and processed microparticles, it can be seen that after ~6 h the core of the processed particle almost completely disappears turning to yellow and light blue in 6.5 h and 8 h images respectively whereas a red zone at the centre of the un-processed microparticle still exists even after 9 h of water contact.

As discussed in Chapter 3, when water was introduced into the system, there were domains where only water is measured, others where polymer is the dominant signal and others where a clear mixture of water and polymer were observed; a hydrated zone. Therefore to facilitate better comparison between different microparticle systems, two parameters that were shown to be readily extracted from each polymer response profile in Chapter 3; namely the full width at half maximum height (A) and the region of the right hand side of the profile where the polymer intensity is <90% of its maximum value and >10% of its minimum value (B) (Figure 3.9 in Chapter 3).
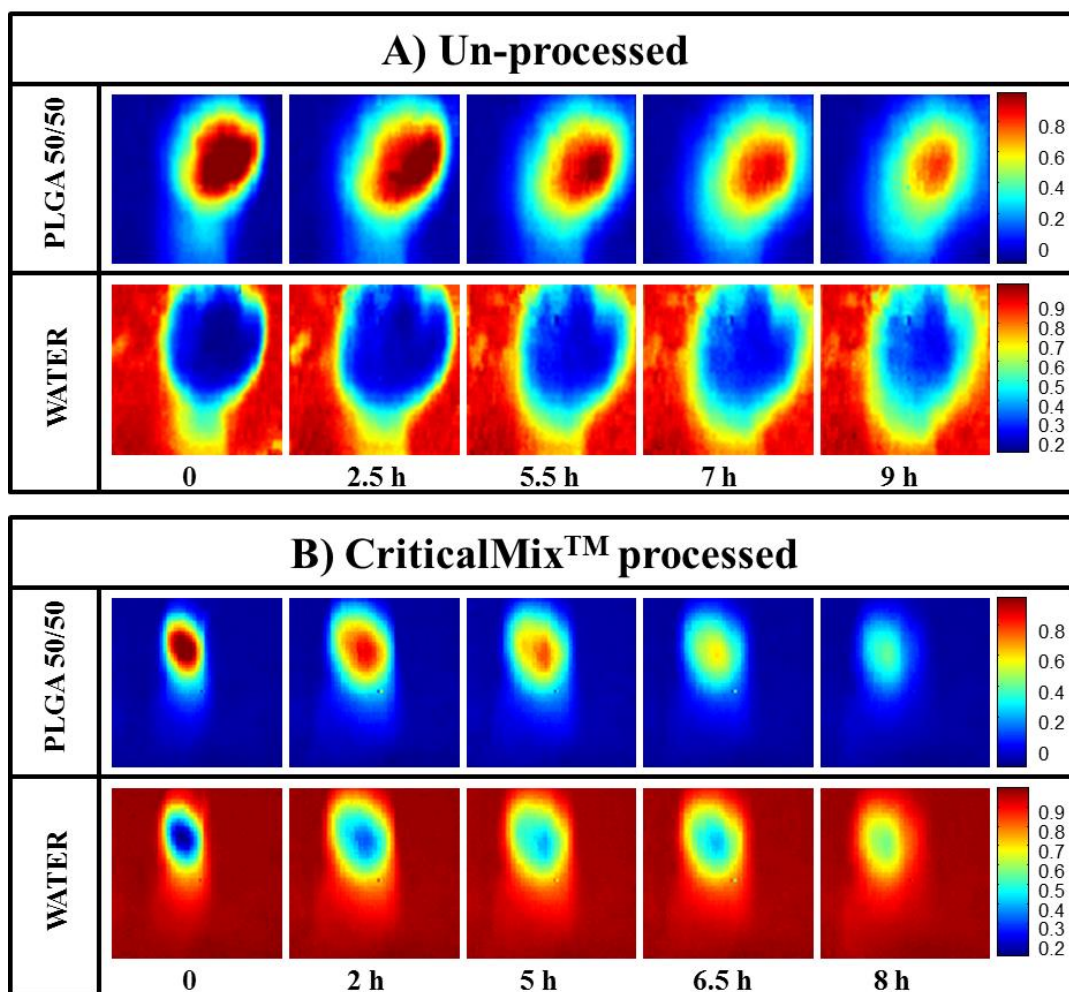
Figure 4.2 False colour IR images representing temporal distribution of un-processed PLGA50/50 on the top and water at the bottom (a) and analogous images of the same but scCO2 processed microparticle.

These parameters were both determined for the microparticles studied here. The parameters B and FWHM were generated using the NLCF algorithm for 3 consecutive parallel lines along the core of the microparticles as it provided slightly better spatial resolution in comparison to MCR-ALS images, and although this enhancement was not found necessary for generating the full image sets, due to the time penalty, NLCF processing of 3 lines of 64 pixels was deemed to be affordable.
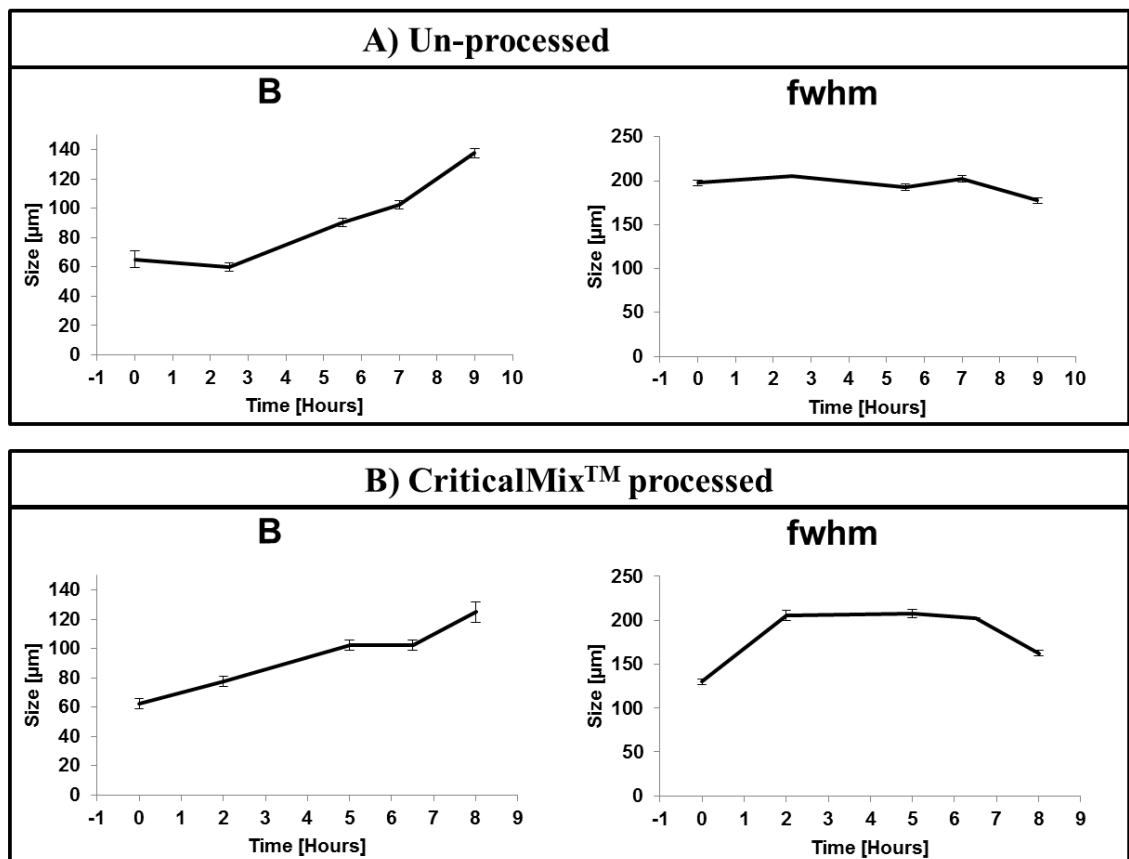
Figure 4.3 The evolution of the parameter 'B', as a function of time on the left and the evolution of parameter 'A', FWHM, as a function of time on the right hand side for the un-processed (a) and CriticalMix^{TM} processed (b) PLGA 50/50.

Figure 4.3a shows the evolution of the right hand side hydrated zone (B) and FWHM of the unprocessed microparticle. Although an increase in the hydrated zone is observed over time, the FWHM of the particle appeared to be quite steady; not showing much swelling or decrease in size, indicating very little amount of water ingress in to this zone as discussed previously. Figure 4.3b shows the analogous plots of B and FWHM this time for the CriticalMix^{TM} processed microparticle. The change of the size of the right hand side hydrated layer or B seems to be very similar to that of the un-processed particle in Figure 4.3a. This could indicate that the magnitude of the hydrated zone was independent on porosity however it should also be noted that this argument is only valid within a regime with a spatial resolution of ~43 µm and if there was any difference less than this it would be difficult to probe or compare. The FWHM of the processed microparticle is quite different to that of the unprocessed microparticle in that after an initial swelling it decreases to a much greater extent in comparison. This was thought to be an indication of more water accessing to the core through the pores, causing faster

degradation and hence the greater decrease in its FWHM compared to that of un-processed microparticle.

As demonstrated in Chapter 3, using the relative intensities of two infrared bands at ~1452 cm^{-1} and ~1424 cm^{-1} that correspond to the antisymmetric bending of CH_3 from the lactic acid units and the symmetric bending of CH_2 from the glycolic acid units of the PLGA polymer that were deconvoluted by NLCF method, the relative quantity of glycolic and lactic acid units present in the polymer was shown to be used to determine the rate of hydrolysis of the two co-polymer segments within the same experiment. Using the same procedure for 3 5x5 binned pixels of selected regions within the temporal image sets the degradation rate constants were calculated for both processed and un-processed PLGA 50/50. Calculated rate constants for lactic and glycolic units for the 2 polymers at 70 °C are listed in Table 4.1. Un-processed PLGA 50/50 was found to degrade slower than processed, which is expected as processed samples are more porous. This result was in agreement with those obtained by Odelius *et al.* [15] who studied hydrolytic degradation of polylactide (PLA) scaffolds with porosities above 90% and different pore size ranges. They showed that both porosity and pore size was regulating the degradation rate of porous PLA scaffolds and that the degradation rate of the porous structures was decreasing with decreasing pore size.

Table 4.1 List of calculated degradation rates in day^{-1} for glycolic and lactic units and their ratios for unprocessed and processed PLGA50/50.

PLGA 50/50	kL	kG	kG/kL
Un-processed	0.98±0.12	1.26±0.14	1.28
CriticalMix^{TM} Processed	1.71±0.21	2.27±0.24	1.32

Also for both microparticles, glycolic units were found to degrade ~1.3 times faster than lactic units. It was interesting that although polymer morphology was shown to have an impact on degradation rate and swelling behaviour as discussed previously, the lactic and glycolic units were found to degrade at an almost constant rate with respect to each other which was independent of the morphology. This agrees with the findings reported by Vey *et al.* that glycolic units were found to degrade ~1.3 times faster than the lactic units in a range of PLGA films [16] in phosphate buffer solution. Therefore it was anticipated that although the degradation rate of the glycolic and lactic units and the

hydration and swelling behaviour was dependent on size and morphology of the PLGA device, the ratio between degradation rates of the glycolic and lactic units was not.

4.4.2 The effect of Composition and Temperature on Hydrolytic Degradation Kinetics of scCO$_2$ processed PLGA

In Chapter 3 and in the previous section of this chapter, FTIR imaging in macro ATR mode coupled with multivariate analysis was demonstrated to be a robust toolbox facilitating an understanding of both morphological and physiochemical changes within PLGA microparticles.

It has been frequently reported that copolymer ratio (i.e. LA:GA) is the main factor that governs the hydrolytic degradation of PLGA [11,13,14,16,20]. In order to understand the tuning criteria of the degradation of scCO$_2$ processed PLGA microparticles, 3 compositions of CriticalMix^{TM} processed PLGA (Table 4.2) were studied at 70°C and also at 50 °C which also allows one to obtain information regarding the effect of temperature on PLGA hydrolysis.

Table 4.2 List of PLGA samples studied where *L/G* is the copolymer lactic/glycolic units molar ratio, M$_n$ is the number average molecular weight, M$_w$ is the weight average molecular weight, PDI is the polydispersity (M$_w$/ M$_n$) and T$_g$ is the glass transition temperature.

PLGA	L/G	M$_n$ (g/mol)	M$_w$ (g/mol)	PDI	T$_g$ (°C)
RG502H	50/50	1927	9560	4.9610844	45.7
RG752H	75/25	3063	8722	2.8475446	47
RG202H	100/0	5758	12170	2.1135848	51

Figure 4.4a b and c show five false colour MCR-ALS images of the scCO$_2$ processed PLGA 100/0 (or PLA), PLGA 75/25 and PLGA 50/50 microparticles, respectively undergoing hydrolysis at 70 °C. The polymer distribution is given at the top and the water distribution is given at the bottom, at different time points for each composition of PLGA. Comparing the polymer distribution images for each composition at 70 °C in a, b and c, it can be seen that the polymer core (indicated by a dark red colour) decreases in all three PLGA image sets, however this decrease can be seen to occur at a greater extent as the LA:GA ratio decreases, in other words although PLA is exhibiting an ongoing swelling behaviour with a slightly decreasing polymer core zone (red) even at

24 h time point, PLGA 75/25 and PLGA 50/50 have almost completely hydrolysed within ~5 h, with almost no core area (red) remaining. Instead one can observe a very hydrated polymer rich region (yellow) clearly at 9 h in PLGA 75/25 and even earlier in PLGA 50/50 at 6.5 h. Water images that anticorrelate with the PLGA 100/0 images in Figure 4.4a, show a noticeable difference in comparison to that of PLGA 75/25 and PLGA 50/50 in that, although there still is a decreased blue zone after 24 h compared to earlier time points in the water images of PLA, the colour of these zones in water images of PLGA 75/25 and PLGA 50/50 are more light-blue or green colour at 7 h onwards for PLGA 75/25 and for the PLGA 50/50 even earlier, at 5 h onwards. Visually indicating the rate of hydrolysis decreasing proportional to the increasing LA/GA ratio of PLGA.

As described previously, changes of this so called 'core' or less hydrated zone can be monitored quantitatively by calculating the FWHM of the microparticle. Figure 4.5a, b and c show the FWHM and the hydrated layer size at 70 °C as a function of degradation time for PLA, PLGA 75/25 and PLGA 50/50, respectively. In Figure 4.5a after an initial swelling, FWHM of the PLA microparticle can be seen to be almost constant, as one would expect at an early stage of hydrolytic degradation. Both FWHMs of the PLGA 75/25 and PLGA 50/50 microparticles in Figure 4.5b and c respectively indicate an initial swelling which is slightly more apparent for PLGA 50/50. After ~7 h the FWHM of the PLGA 50/50 decreases (Figure 4.5c) whereas the FWHM of the PLGA 75/25 increases (Figure 4.5b). This may well be the result of the different in the images showing different degradation stages; in Figure 4.4b PLGA 75/25 can be seen to almost disappear at 9 h whilst in comparison, in Figure 4.4c, PLGA 50/50 still has a core that is decreasing in size. Comparing the water distribution images of PLGA 75/25 (Figure 4.4b) and PLGA 50/50 (Figure 4.4c) it can be predicted that there is more water in the core of PLGA 75/25 microparticle than that of PLGA 50/50 microparticle. An explanation to this might be possible to find by examining the morphology of the microparticles. Figure 4.6a, b and c show two SEM images of PLGA 50/50, PLGA 75/25 and PLA microparticles respectively. Although the morphology of the PLGA 50/50, PLGA 75/25 and PLA look broadly similar, it can be seen that the pore size of the PLGA 75/25 particles in Figure 4.6b are somewhat greater than those of PLGA 50/50 microparticles shown in Figure 4.6a. Therefore it could be anticipated that water
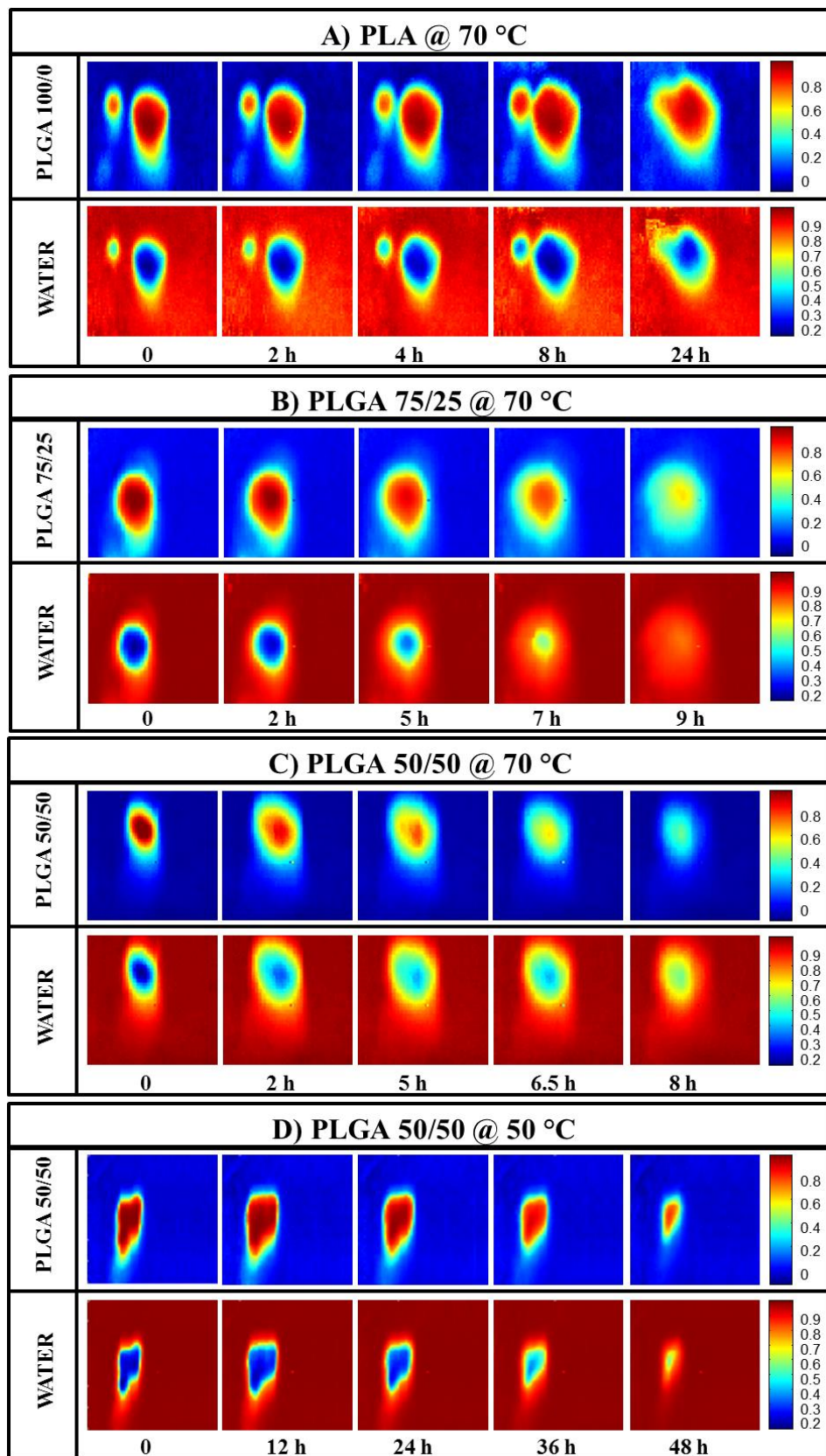
Figure 4.4 False colour MCR-ALS processed images representing temporal distribution of PLGA at the top and water at the bottom for scCO2 processed PLA at 70 °C (a), PLGA 75/25 at 70 °C (b), PLGA 50/50 at 70 °C (c) and PLGA 50/50 at 50 °C (d).

would diffuse into the PLGA 75/25 microparticle at a greater extent than it would into the PLGA 50/50 microparticle due to having narrower pathways.

An interface layer of hydrated PLGA around the particle starting from the 0 m PLGA images in Figure 4.4a b and c can be seen quite clearly for all three microparticles. However as one can notice, although the thickness of this hydrated layer (light blue to yellow) is roughly similar size to the first two images of the polymers in comparison to each other, in the last three images the hydrated layer of PLGA 75/25 and PLGA 50/50 are wider than those of the PLA. This observation was also quantified by plotting the parameter B that represented the hydrated layer size as explained earlier. Comparing the hydrated layer size of PLA over time in Figure 4.5a to that of PLGA 75/25 in Figure 4.5b and PLGA 50/50 in Figure 4.5c, it can be seen that although hydrated layer of PLGA 75/25 and PLGA 50/50 increases from ~60 to ~100 μm within 5 h, the hydrated layer size of PLA only increases from ~50 to ~60 μm. This was thought to be a result of different hydrolysis rates being observed within the images. It could be expected that even at 24 h PLA is still at an early stage of hydrolysis, still showing early stage swelling and a consistent core size or FWHM (Figure 4.5a).

Figure 4.4d shows images that are analogous to Figure 4.4c, of a scCO$_2$ processed PLGA 50/50 microparticle undergoing hydrolysis but this time at 50 °C and at different time points. An immediate difference that can be observed between the PLGA 50/50 images at 50 °C and 70 °C is that the size of the hydrated layer is much less at 50 °C than at 70 °C. This observation is more evident in the hydrated layer size plot in Figure 4.5d as it is ~20 μm in the first 24 h showing a very slight increase, perhaps than 5 μm. Even after 48 h, the hydrated layer size is only ~50 μm at 50 °C where as that of the microparticle at 70 °C increases from 60 μm to 120 μm within 8 h. An initial increase of swelling can also be observed for the PLGA 50/50 microparticle at 50 °C in the FWHM plot in Figure 4.5d, which is similar to that exhibited at 70 °C (Figure 4.5c) but on a shorter time scale. A similar relation between the two temperatures (50 °C and 70 °C) for the other compositions of PLGA (images not shown), PLGA 75/25 and PLA, was also observed.
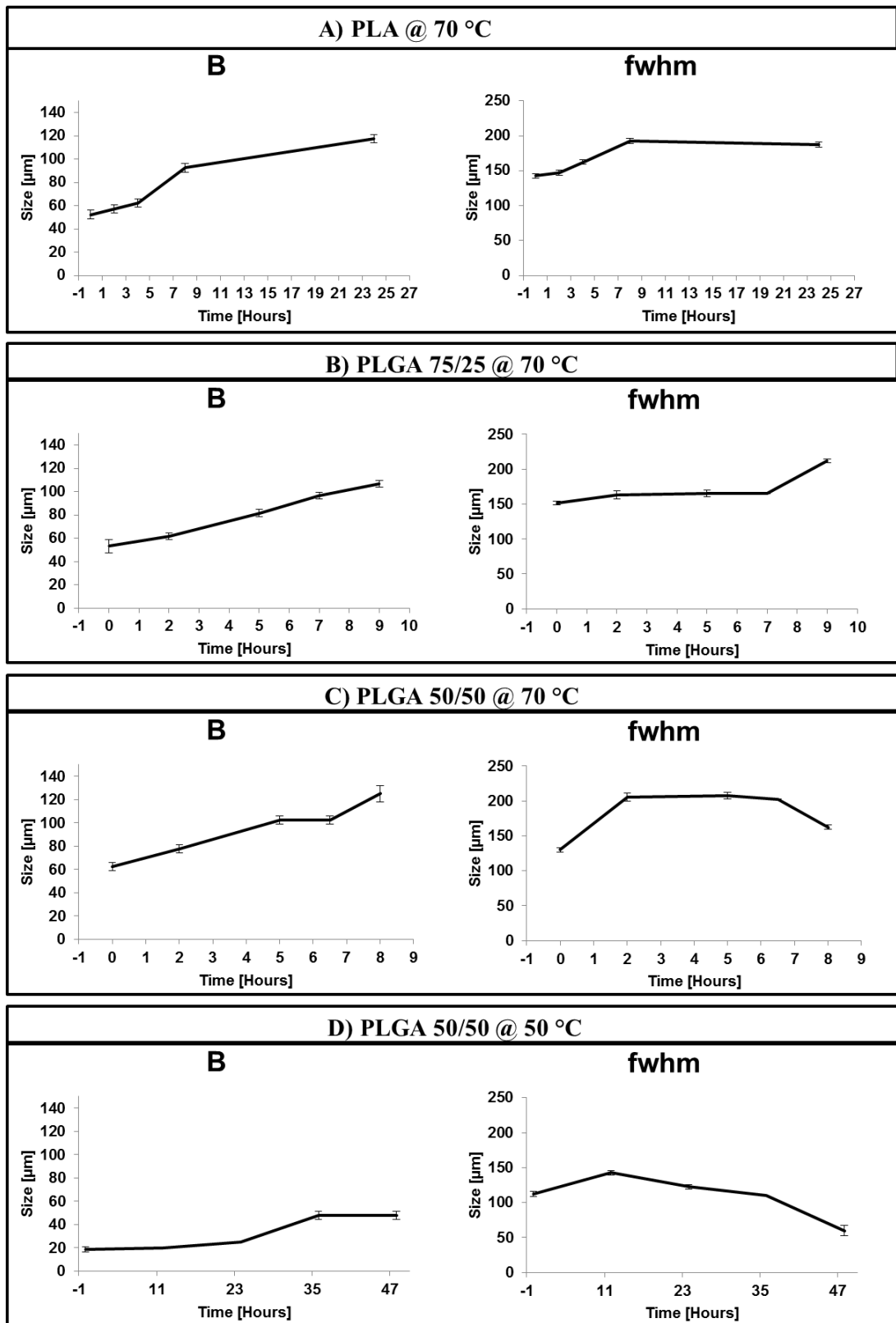
Figure 4.5 The evolution of the hydrated zone, 'B', as a function of time on the left and the evolution of parameter 'A', FWHM, as a function of time on the right hand side for the scCO2 processed PLA at 70 °C (a), PLGA 75/25 at 70 °C (b), PLGA 50/50 at 70 °C (c) and PLGA 50/50 at 50 °C (d).
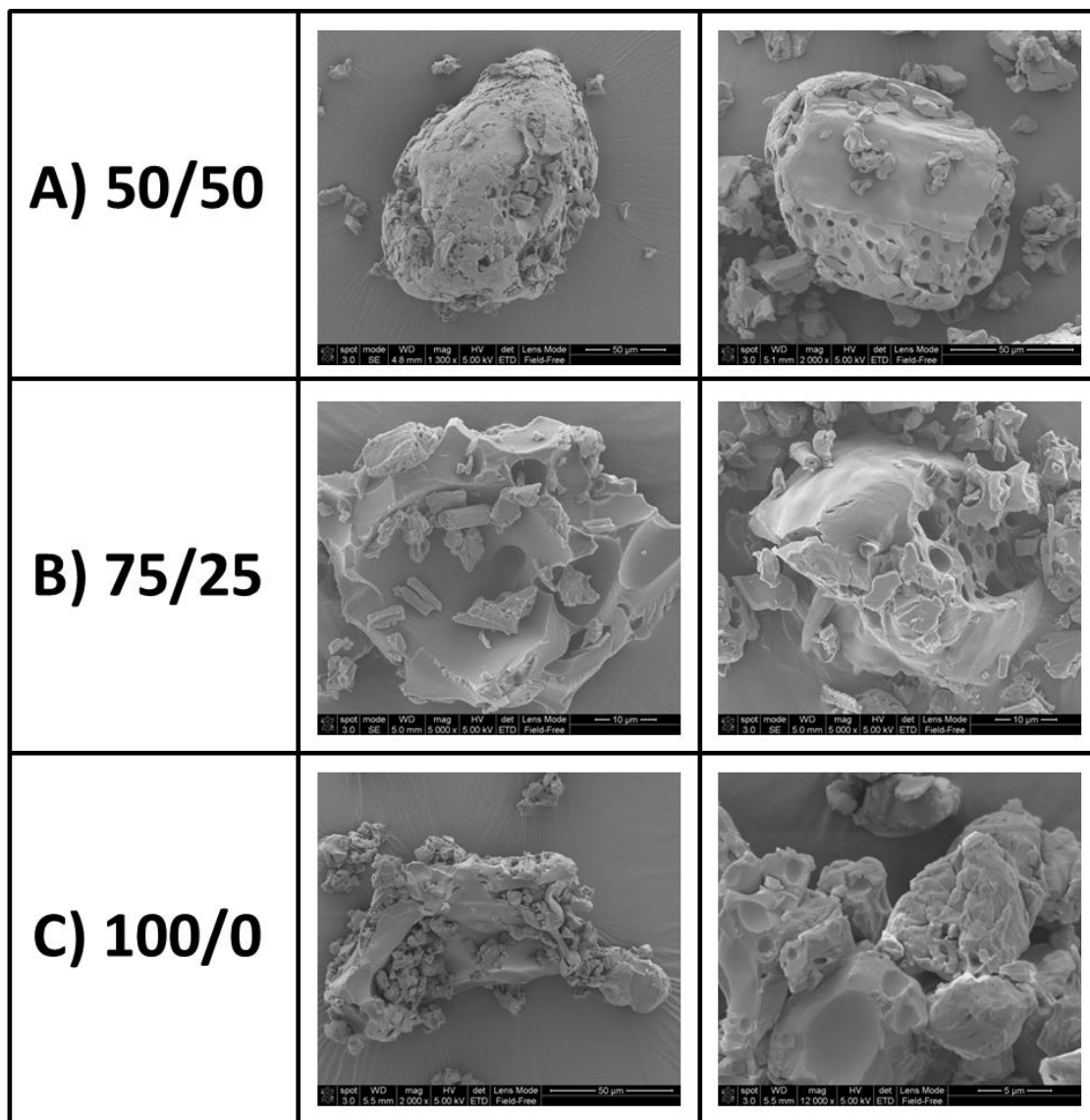
Figure 4.6 SEM images of two CriticalMix^TM processed PLGA 50/50 (a), PLGA 75/25 (b) and PLA microparticles in each row.

As demonstrated in Chapter 3 and earlier in this Chapter, the hydrolysis rates of both lactic acid and glycolic acid units of the PLGA 50/50 and PLGA 75/25 and the hydrolysis rate of PLA at both 50 °C and 70 °C was calculated and listed in Table 4.3.

It could be observed in Table 4.3 immediately that the glycolic acid units were once more shown to have hydrolysed ~1.3 times faster than lactic acid units, regardless of the temperature, morphology, scCO$_2$ process or composition. It is well established that increasing the glycolic acid content of PLGA polymers results in a higher hydrolysis rate, mainly because the higher hydrophilicity of glycolic repeat units results in a greater degree of water uptake during hydrolysis [14,16,20]. All 3 PLGA compositions showed

a higher degradation rate for both lactic and glycolic (not for PLA) units at 70 °C than that of at 50 °C and this finding was found to be in agreement with those of Agrawal *et al.* [18] who studied the elevated temperature degradation of PLGA 50/50 using GPC.

Table 4.3 List of degradation rate constants of the glycolic and lactic units in day^{-1} calculated for different compositions of scCO$_2$ processed PLGAs at 50 °C and 70 °C and unprocessed PLGA 50/50 at 70 °C.

	50 °C			70 °C		
LA/GA	kL	kG	kG/kL	kL	kG	kG/kL
100/0	0.19±0.03			0.39±0.02		
75/25	0.57±0.08	0.76±0.14	1.33	1.47±0.1	2.06±0.13	1.4
50/50	0.74±0.11	1.05±0.1	1.41	1.71±0.21	2.27±0.24	1.32
50/50 un-processed				0.98±0.12	1.26±0.14	1.28

Calculation of degradation rates of different compositions of PLGA microspheres and mm sized discs were conducted by Tracy *et al.* [48] and Vey *et al.* [16,21], respectively. The PLGA microparticles studied here were scCO$_2$ processed resulting in a very porous structure therefore the rates obtained were higher than those of Tracy *et al.* and Vey *et al.* as expected.
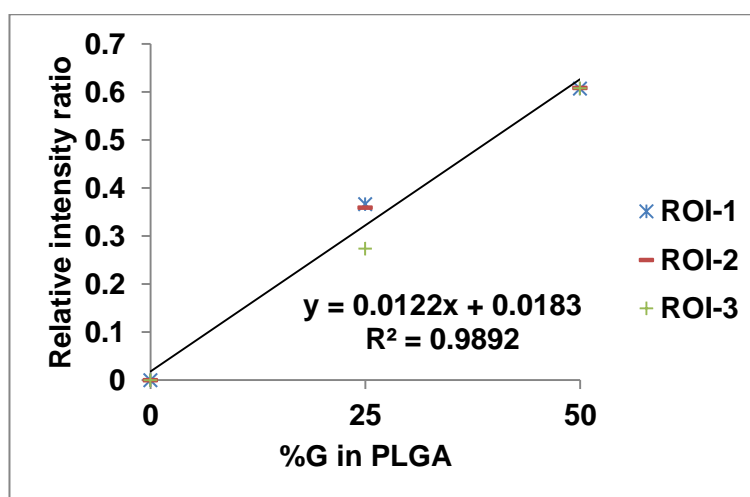
Figure 4.7 Calibration curve showing the relative intensity ratio vs. %G in PLGA microparticles.

Although Vey *et al.* studied a different form of PLGAs (i.e. mm sized discs) using IR and Raman spectroscopies their data analysis approach on IR spectroscopic data was similar to the one developed here, in that they also fitted the IR bands, but to a Voigt

function, and monitored the lactic and glycolic units by using fitted peak intensities at 1452 cm^{-1} and 1422 cm^{-1}, respectively.

However although such analysis was found adequate in obtaining degradation rates from binned pixels in this work, they have generated a calibration curve using this data (plot of $I_{G/L}=I_G/(I_L+I_G)$ (where I_G and I_L are the fitted band intensities of glycolic and lactic units, respectively) vs. %G (molar percentage of glycolic units)) for the dry PLGA samples with known compositions and used it to evaluate the composition of the copolymers during degradation. However also within their calculation they have measured and used the weight of the remaining PLGA at each time point of degradation to calculate the relative mass of glycolic units and lactic units remaining. A similar calibration plot (Figure 4.7) was also generated here using the data obtained from 3 averaged 5x5 pixel zones from each of the 3 compositions of dry PLGA images. The parameters of the calibration curve were found to be very similar to those of Vey *et al.* as given in Table 4.4 however their experiment facilitated the determination of the mass of the remaining polymer at each time point whereas the experiment conducted here did not. Furthermore their data revealed a two stage process for degradation and their study was conducted at 37 °C in phosphate buffer solution and under these conditions their experiments lasted up to 40 days. Therefore one can easily anticipate that the observation of higher rates of degradation and a single stage process degradation may observed when compared to those of Vey *et al.*, firstly because temperatures studied here were above the T_g (in the presence of water, which is a known plasticiser) and secondly the samples studied here were porous microparticles rather than mm sized discs as in their study. Nevertheless, the calculated ratios between the rate constants of glycolic and lactic units was ~1.3 and this finding was in agreement with those of Vey *et al.* and k values calculated are in reasonable agreement with each other and with the values determined by Tracy *et al.* [14] and Vey *et al.* [16].

Table 4.4 Values of the slope, *a*, and the intercept, *b*, for the different calibration curves where R^2 is the correlation coefficient.

Parameters measured	$I_{G/L}$	$I_{G/L}$ Vey *et al.* [16]
a	0.012±0.002	0.0109±0.0005
b	0.018±0.009	0.031±0.002
R^2	0.989	0.996

4.4.3 Visual Evidence of Lactic acid Diffusion from a Degrading PLA Microparticle

The degradation of PLGA involves chain scissions of ester bond linkages in the polymer backbone by hydrolytic attack of water molecules. Lactic acid and glycolic acid, which are biocompatible and rapidly cleared from the body via the renal system, are the end products of degradation [29]. PLGA degradation may result in a build-up of acidic by-products since it is made up of acidic monomers. And when labile drugs such as proteins and peptides are entrapped with in PLGA, this acidic environment may have an adverse effect on protein stability. Therefore one of the hydrolysis experiments, hydrolysis of the PLA microparticle at 70 °C (Figure 4.4a, images after 24 h were not shown to facilitate comparison with the rest of the PLGA image sets), was studied until there was no polymer left with in the field of view.

Figure 4.8a shows 2 12 h peak height images, one at 1755 cm^{-1} on the left, where PLA carbonyl absorbs intensely and one at 1741 cm^{-1} wavenumbers on the right where lactic acid absorbs intensely as can be seen in the IR spectrum of lactic acid in Figure 4.8c. At the chosen pixels indicated by the arrow in each image, there appear to be two distinct spectra shown beneath the images; PLA and water. Figure 4.8b shows the analogous results to that of Figure 4.8a, but this time at 88 h. The peak height image at 1755 cm^{-1} at 88 h, compared to that of at 12 h, show that almost the entire core zone of the PLA microparticle was degraded. The peak height image at 1741 cm^{-1} at 88 h, compared to that of at 12 h shows a carbonyl peak at 1741 cm^{-1} in the indicated pixel, at which there appears to be only water at 12h. The distribution of this peak at 1741 cm^{-1} shown in the right hand side image at 88h Figure 4.8b shows the distribution of the end product of the PLA degradation i.e. lactic acid.

PLGA 50/50 (25 kDa) microspheres prepared by a double-emulsion technique were studied by Fu *et al.* [30] using confocal fluorescence microscopy by probing pH-sensitive fluorescent dyes that were entrapped within the microspheres. Their study showed the formation of a very acidic environment within the particles with the minimum pH as low as 1.5. Their images showed a pH gradient, with the most acidic environment at the centre of the spheres and higher pH near the edges. However, as discussed in Section 1.5 in Chapter 1, the preparation method has a major effect on the morphology, structure and chemistry of the polymeric microparticles resulting in different degradation characteristics. For example, Ding *et al.* [31] also studied several
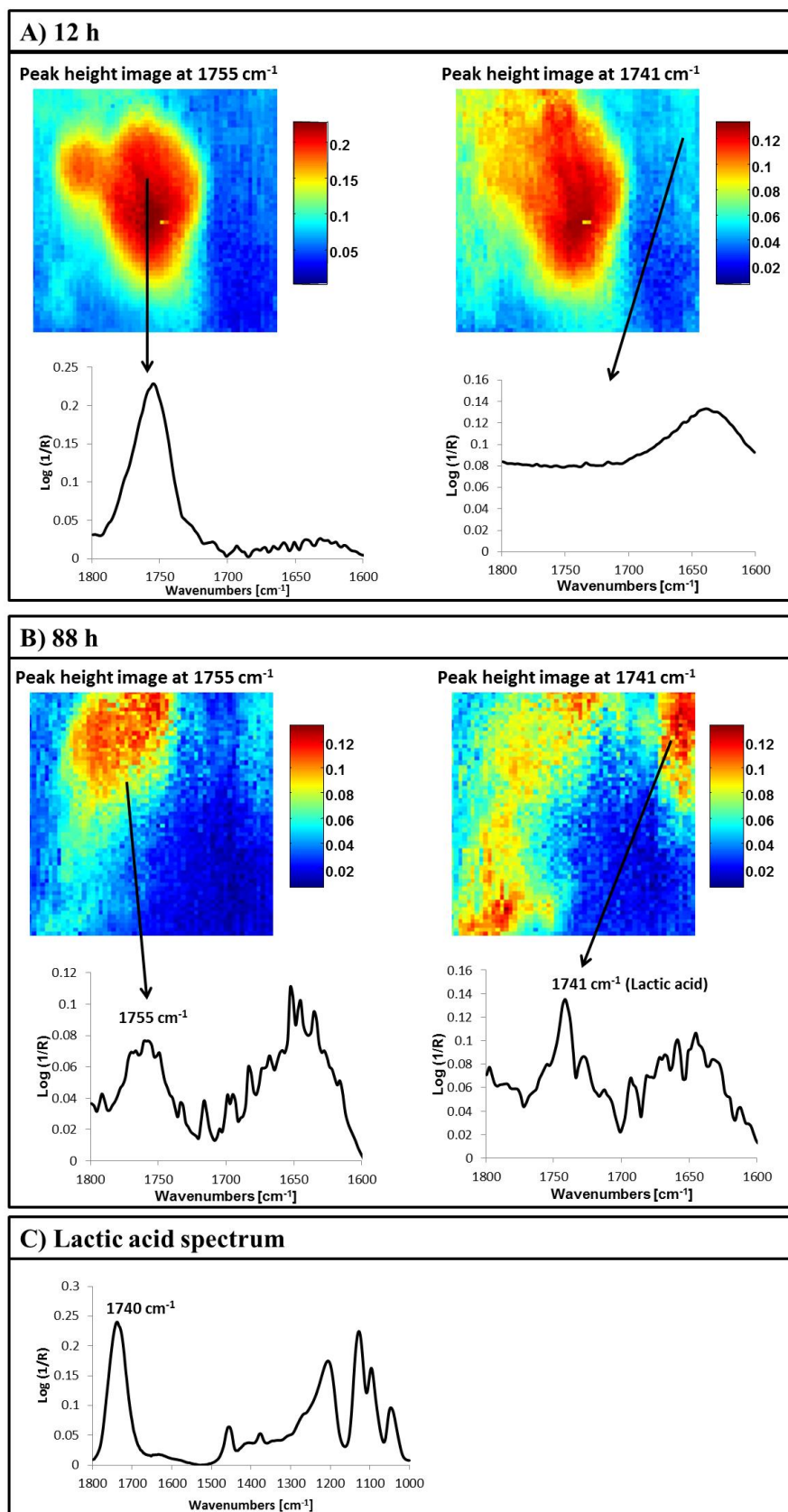
Figure 4.8 False colour peak height images of scCO2 processed PLA microparticle undergoing hydrolysis at 70 °C at 1755 cm^{-1} on the left and 1741 cm^{-1} on the right at (a) 12 h and (b) 88 h where pixel spectrum indicated by the arrow is given at the bottom of each of the images. (c) FTIR spectrum of lactic acid.

PLGA microspheres, prepared by oil-in-oil emulsion and double emulsion methods and labelled with fluorescent dyes, using confocal laser scanning microscopy. Their work indicated that microspheres prepared by the oil-in-oil emulsion method were less acidic than those prepared by double emulsion. The distribution of lactic acid in Figure 4.8b can be seen to somewhat surround the distribution of PLA microparticle, if one overlays the two images generated from bands at 1755 cm^{-1} and 1741 cm^{-1}, the implication is that that the lactic acid monomers has diffused out into water, since there is much less lactic acid with in the core of the PLA microparticle. This is an interesting finding; firstly because this was the first image showing lactic acid distribution within a degrading PLA microparticle in its natural environment (i.e. without modifying the sample using any chemical dyes) and secondly the lactic acid molecules were diffused out of the particle during hydrolysis which would certainly provide a better environment for any labile drug molecule entrapped therein.

4.4.4 The Effect of γ-Irradiation on Hydrolytic Degradation of PLGA 50/50

Biodegradable polymeric pharmaceuticals often have to be sterilised before use and, γ-irradiation is a well-established and most suitable method for sterilising polymeric microparticle drug delivery systems [24]. Because each polymer may respond differently to ionizing radiation, it was found essential to determine any effects that this process may have on the drug carrier, PLGA, which makes up 90 wt% of the formulation studied in this thesis as discussed in Chapter 5. Therefore the effect of a range of irradiation dose on PLGA 50/50 was investigated by performing a series of *in situ* hydrolysis studies at 70 °C using ATR-FTIR imaging and the multivariate analysis tools demonstrated in Chapter 3.

Figure 4.9a, b and c show the temporal false colour MCR-ALS images of un-processed and un-irradiated, 25 kGy γ-irradiated and 100 kGy γ-irradiated PLGA 50/50 at the top and the corresponding water images at the bottom, respectively.

Although the un-irradiated and 25 kGy irradiated PLGA 50/50 images in Figure 4.9a and b look similar in the first 2 images, a faster decrease in the polymer core zone (red) and a larger hydrated layer (from light blue and yellow) can be observed in the 25 kGy irradiated PLGA 50/50 images after 5 h, in comparison to that of un-irradiated PLGA 50/50, indicating a slightly faster degradation. And these differences were seen to be more pronounced in the 100 kGy irradiated PLGA 50/50 images in Figure 4.9c, when

compared to that of un-irradiated and 25 kGy irradiated PLGA 50/50, as the polymer core (in red) in 0 m image was seen to disappear immediately after 2 h indicating, in comparison, a greater degree of polymer hydration.
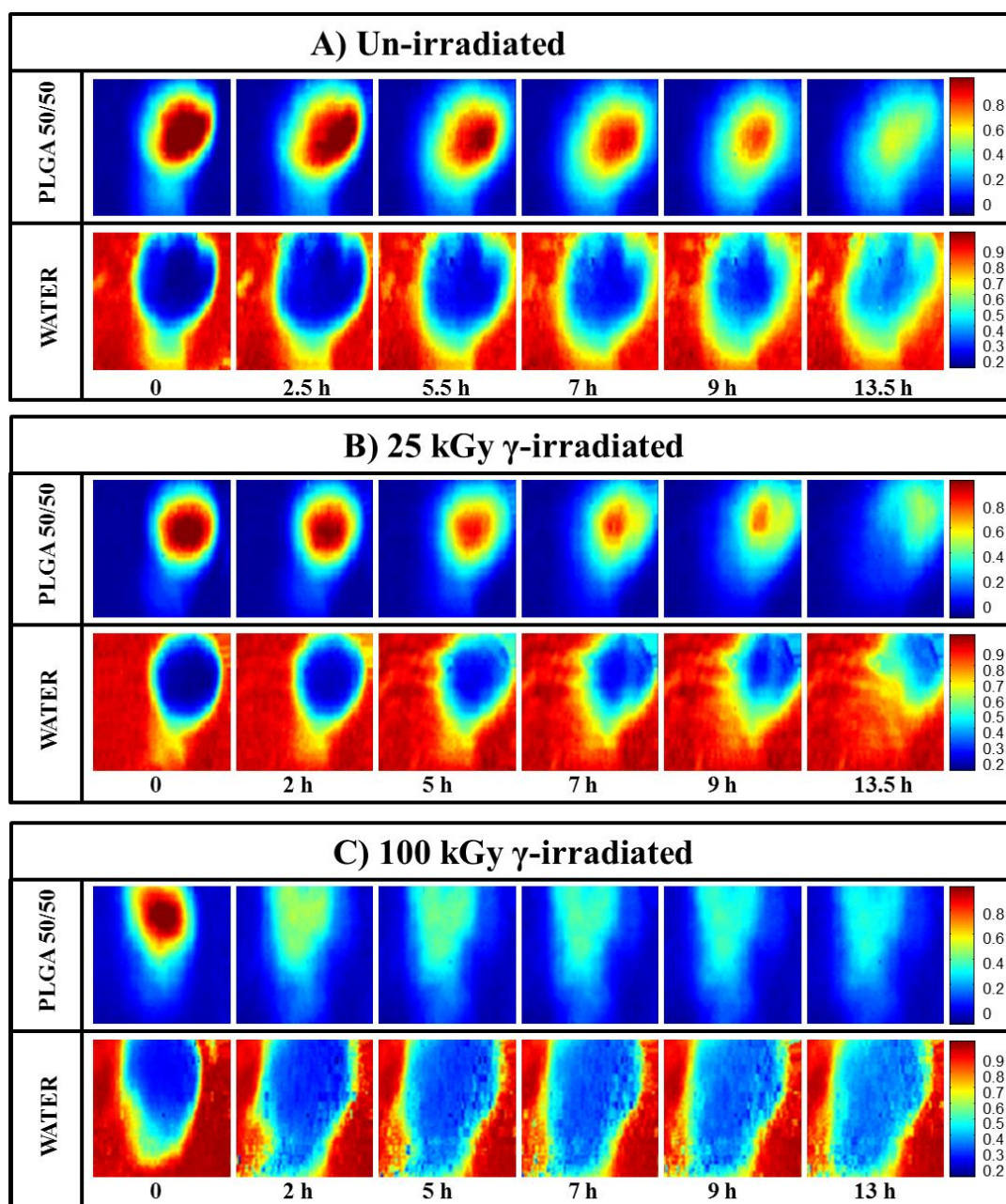
Figure 4.9 A set of false colour IR images representing temporal distribution of PLGA50/50 at 70 °C on the top and water at the bottom for samples that were subject to (a) 0, (b) 25 kGy and (c) 100 kGy γ-irradiation respectively.

The temporal water distribution images beneath each polymer image in each data set in Figure 4.9a, b and c complement this finding, in that although the water distribution within the un-irradiated and 25 kGy irradiated microparticles is very low (dark blue) at the first 2 hours and increasing gradually (light blue), in the 100 kGy irradiated

microparticle, after the first time point, there appears to be no clearly defined core zone where the water intensity would expected be low (dark blue), merely a very large light blue area that becomes lighter in colour indicating higher water content in comparison to that of un-irradiated and 25 kGy irradiated, as time proceeds.

As discussed previously, the microparticle morphology plays a major role in hydrolytic degradation of PLGA polymers. SEM analysis of the un-processed and un-irradiated PLGA 50/50, 25 kGy γ-irradiated PLGA 50/50 and 100 kGy γ-irradiated PLGA 50/50 was conducted in order to provide an insight into the effect of gamma irradiation on the microparticle morphology. In order to facilitate an unbiased discussion between SEM images, all of the microparticles were coated at the same time and imaged under the same conditions.

Figure 4.10a, b and c show the SEM images of un-irradiated, 25 kGy irradiated and 100 kGy irradiated PLGA 50/50 microparticles. The un-irradiated particle has a rough, non-uniform morphology and, in comparison, the 25 kGy irradiated particle appears to have a smoother surface. The 100 kGy particle looks quite different to un-irradiated and 25 kGy irradiated microparticles, mainly in that it is structured than both at a large scale, but interestingly there also appears to be some evidence of lumpyness.
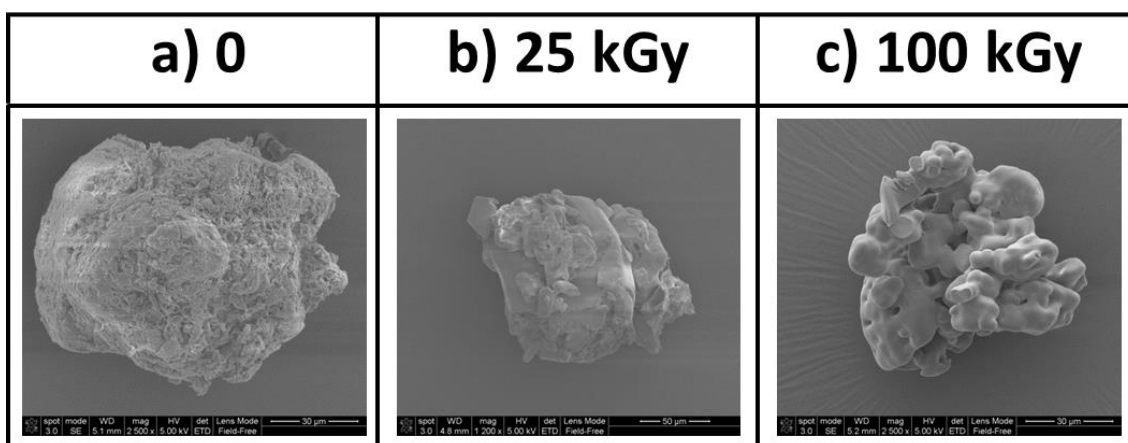
Figure 4.10 A set of SEM images un-processed PLGA 50/50 microparticles that are (a) un-irradiated, (b) 25 kGy γ-irradiated and (c) 100 kGy γ-irradiated.

Applying the NLCF procedure to 5x5 pixels binned regions in reach image set shown in Figure 4.9, hydrolysis rates of both lactic acid and glycolic acid units of the un-irradiated, 25 kGy irradiated and 100 kGy irradiated PLGA 50/50 at 70 °C were calculated. Table 4.5 shows the list of degradation rates. Gamma irradiation was seen to degrade the PLGA 50/50 to such an extent that both glycolic and lactic units had an

increased hydrolytic degradation rate as a function of applied gamma dose. And interestingly, once again the ratio between the degradation rate of glycolic and lactic units was ~1.3, indicating that the relationship between the degradation rates of the two components was independent of gamma dose.

Table 4.5 List of degradation rate constants of the glycolic and lactic units in day^{-1} calculated for un-processed PLGA 50/50s at 70 °C that were subject to 0, 25 and 100 kGy γ-irradiation.

Gamma Dose [kGy]	kL	kG	kG/kL
0	0.98±0.12	1.26±0.14	1.28
25	1.38±0.13	1.76±0.21	1.27
100	1.89±0.28	2.34±0.24	1.23

It is well known that when subjected to irradiation, polymers can show a decrease in their molecular weight due to chain scission [32,33]. GPC and DSC are often used to investigate such processes since they facilitate monitoring molecular weight and thermal properties of polymers as discussed in Chapter 2.

Figure 4.11a shows the irradiation dependent change in M_w and PDI of PLGA 50/50 and Figure 4.11b shows the change in % M_w with respect to its un-irradiated state to
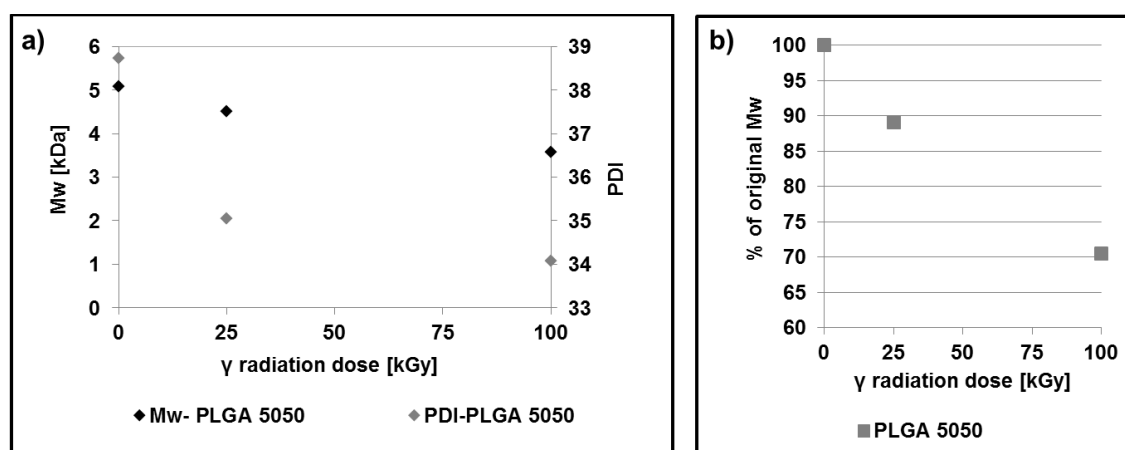
Figure 4.11 GPC results for non-irradiated and irradiated PLGA 50/50 showing the changes in M_w and PDI in (a) and % change in polymer's M_w with respect to its un-irradiated state, to facilitate better comparison in (b).

facilitate a better comparison. With increasing gamma exposure, a decrease in M_w and PDI of the PLGA 50/50 was observed with increased applied gamma dose indicating the domination of a chain scission mechanism occurring within PLGA 50/50 upon

irradiation. Figure 4.11a also shows that PDI of PLGA 50/50 decreases proportional to applied gamma dose indicating a decrease in chain lengths of PLGA 50/50 due to gamma induced chain cleavage.

DSC analyses were conducted on the irradiated and un-irradiated PLGA 50/50 in order to monitor the effect of gamma irradiation on the polymer's thermal properties. Figure 4.12 shows the DSC thermograms of the un-irradiated (a), 25 kGy γ-irradiated (b) and 100 kGy γ-irradiated (c) PLGA50/50. It can be observed in all three of the thermograms that PLGA 50/50 exhibits a glass transition temperature (T_g). The T_gs that were read from the thermograms are listed in Table 4.6. Table 4.6 shows that the T_g of PLGA 50/50 decreases as a function of applied gamma dose. This finding also supported the observation that PLGA 50/50 was degrading via a chain scission mechanism due to gamma irradiation.

Table 4.6 List of glass transition temperatures of un-irradiated and γ-irradiated PLGA50/50.

T_g (°C)	T_g (°C) after 25 kGy γ exposure	T_g (°C) after 100 kGy γ exposure
45.7	43.4	41.9

These findings using IR imaging, SEM, GPC and DSC were found to be in agreement with those of Nughoro *et al.* [33] who investigated γ radiation-induced degradation of PLA by using GPC and DSC. In their work PLA glass transition temperature (T_g), melting temperature(Tm) and number-average molecular weight (M_n) was shown to be decreasing with increasing irradiation dose up to 200 kGy, indicating a predominant degradation by random chain-scission. They also indicated that decrease in M_n, T_m and T_g of the PLA in air was faster than in vacuum because of oxidative chain-scission. Loo *et al.* [32] studied e-beam irradiation induced degradation of PLGA films using GPC, DSC and FTIR spectroscopy and also reported a linear relationship between the decrease in molecular weight with respect to radiation dose. In their work, monitoring the reduction in the average molecular weight, T_c, T_g and T_m, it was indicated that the dominant effect of e-beam irradiation on PLGA polymer films was chain scission.
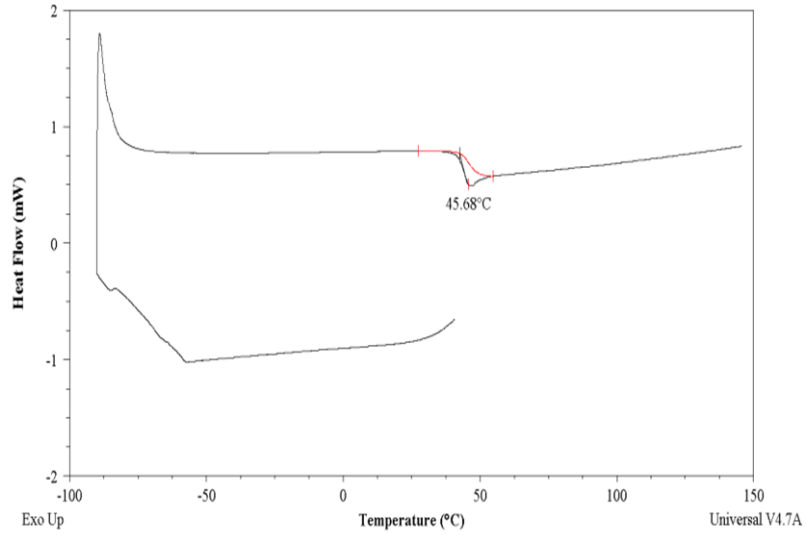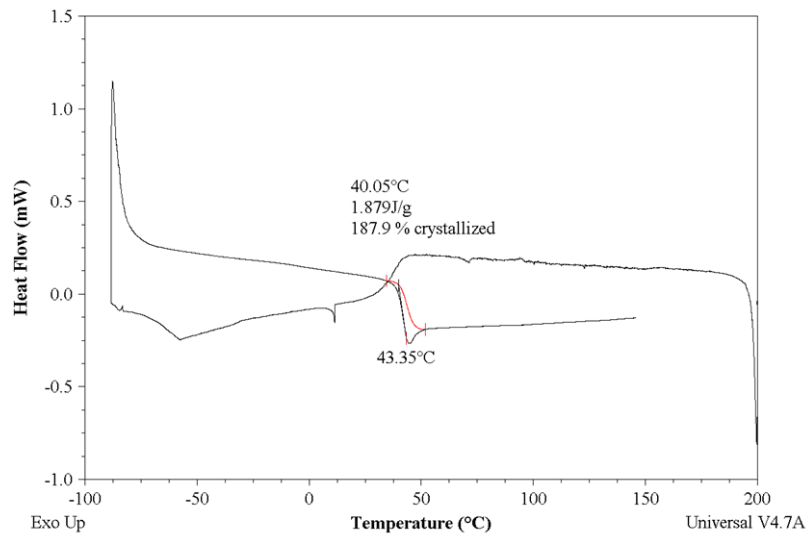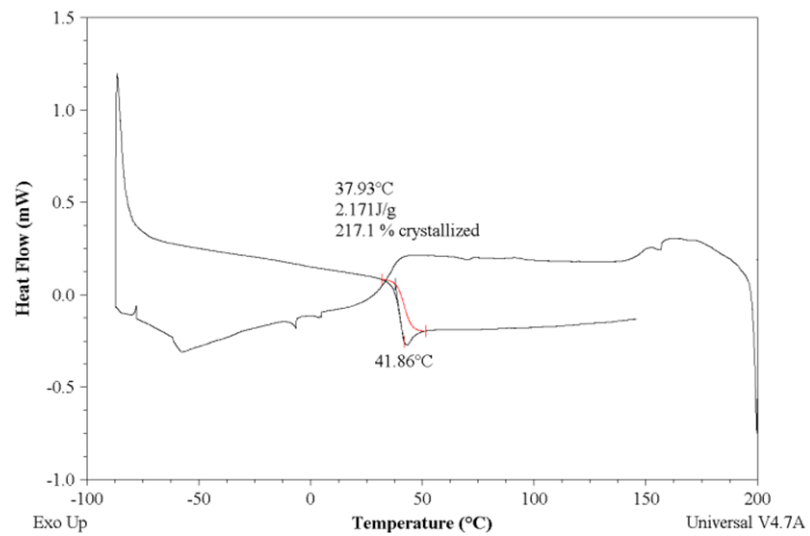
Figure 4.12 DSC thermograms of un-irradiated (a), 25 kGy irradiated (b) and 100 kGy irradiated (c) PLGA 50/50.

4.5   Summary of the Findings

- SEM images revealed that $scCO_2$ processing increased the porosity of the microparticles.

- IR imaging data indicated that un-processed the PLGA 50/50 microparticle was degrading slower than the $scCO_2$ processed PLGA 50/50 microparticle which was found to be mainly as a result of increased porosity occurring as a result of $scCO_2$ processing.

- IR imaging data of PLGA copolymer microparticles with L/G molar compositions of 100/0, 75/25 and 50/50 that were studied at 50 ℃ and 70 ℃ indicated an increase in degradation rates of all PLGA compositions with increasing temperature.

- Degradation rate was also found to decrease with increasing lactic unit/glycolic unit ratio of the copolymers. The degradation rate of PLGA 75/25 was found to be lower than that of PLGA 50/50 at both temperatures (50 ℃ and 70 ℃) but not to a great extent and this was found to be a result of morphological differences between processed PLGA 50/50 and PLGA 75/25 in that $scCO_2$ processed PLGA 50/50 was more porous than $scCO_2$ processed PLGA 75/25.

- The infrared images of a hydrolysing $scCO_2$ processed PLGA 50/50 microparticle exhibited a small hydrated layer ~20 μm in the first 24 h showing a very slight increase that is less than 5 μm from its dry state. And even after 48 h the hydrated layer size was found to be only ~50 μm at 50 °C where as that of the microparticle at 70 °C increased from 60 μm to 120 μm within 8 h.

- Visual evidence of lactic acid formation was probed around the degrading PLA microparticle using IR imaging for the first time.

- SEM images of irradiated and un-irradiated PLGA 50/50 microparticles showed a decrease in surface roughness proportional to applied gamma dose. 100 kGy irradiated particle was found to somewhat melted in to aggregated very smooth pieces. This finding was implicated as the reason for the higher water content in the temporal IR images of the 100 kGy irradiated microparticle, when compared to that of the temporal IR images of the un-irradiated and 25 kGy irradiated microparticles.

- Real-time IR imaging data revealed that PLGA 50/50 was degrading faster when subject gamma irradiation. An increase in degradation rate as a function of applied gamma dose was observed.

- GPC analyses of un-irradiated and irradiated PLGA 50/50 indicated a noticeable decrease in M_w of PLGA 50/50 as a function of γ exposure, indicating a chain scission mechanism of gamma induced degradation.

- DSC analyses of un-irradiated and irradiated PLGA 50/50 supported the finding from GPC data showing a decrease in T_g of PLGA50/50 as a function of applied γ dose.

4.6   Conclusions

ATR-FTIR imaging and multivariate analysis developed in this thesis has been shown to be a successful method to monitor the degradation of PLGA microparticles *in situ*, providing quantitative information including hydrated layer size surrounding the particles, FWHM of the particles and perhaps more importantly the degradation rate. The degradation rates of glycolic and lactic units in a group of PLGAs were differentiated and quantified successfully.

Using SEM, $scCO_2$ processing was seen to create a high number of pores within PLGA microparticles. From the real-time ATR-FTIR imaging hydrolysis study of un-processed and processed microparticles, the findings from the SEM images gave a credible explanation for the higher degradation rate that was observed in the processed microparticles when compared to the un-processed ones.

Degradation rate constants for lactic and glycolic units were shown to decrease with increasing initial lactic content of the copolymer, suggesting that the ability of a water molecule to diffuse in the sample has a high impact on the degradation kinetics of the copolymers within the microparticles. A noticeable decrease in hydrated layer size was observed for the $scCO_2$ processed PLGA 50/50 microparticle at 50 °C compared to that of at 70 °C. In addition an increase in temperature resulted in an increase in degradation rates of all PLGAs with different compositions (50/50, 75/25, 100/0). SEM images also indicated that $scCO_2$ processed PLGA 50/50 was more porous than $scCO_2$ processed PLGA 75/25 and this resulted in degradation rate of PLGA 75/25 being less than, but close to that of PLGA 50/50.

The distribution of lactic acid was probed during hydrolysis of single PLA microparticle. The lactic acid molecules were seen to surround the PLA microparticle in the aqueous media, indicating that the lactic acid monomers diffused out into water as there was much less lactic acid with in the core of the PLA microparticle. This was the first image

showing lactic acid distribution within a degrading PLA microparticle in its natural environment (i.e. without modifying the sample using any chemical dyes).

The effect of gamma irradiation on the hydrolytic degradation behaviour of PLGA 50/50 polymer microparticles was also investigated. SEM images indicated an increase in lumpyness as a function of increased applied gamma dose. The 100 kGy irradiated PLGA 50/50 microparticle looked much less rough compared to un-irradiated and 25 kGy irradiated PLGA 50/50 microparticles. A noticeable increase in water uptake was observed in 100 kGy irradiated PLGA 50/50 microparticle compared to the others and this was thought to be a result of the severe change in morphology of the 100 kGy irradiated microparticle. IR imaging data revealed that the degradation rate was increasing as a function of increasing the applied gamma dose. GPC analysis showed a decrease in molecular weight of the PLGA 50/50 samples with increased gamma irradiation, indicating a chain scission degradation mechanism and DSC analysis was complementing these finding as it exhibited a decrease in the T_g of PLGA 50/50 as a function of applied gamma dose. These findings were in agreement with those of Nughoro *et al.* [33] Loo *et al.* [32].

4.7 References

[1] U. Edlund, A.C. Albertsson, Degradable Aliphatic Polyesters, advances in polymer science. 157 (2002) 67-112.

[2] D. Lemoine, C. Francois, F. Kedzierewicz, V. Preat, M. Hoffman, P. Maincent, Stability study of nanoparticles of poly(ε-caprolactone), poly(d,l-lactide) and poly(d,l-lactide-co-glycolide), Biomaterials. 17 (1996) 2191-2197.

[3] C. Wischke, S.P. Schwendeman, Principles of encapsulating hydrophobic drugs in PLA/PLGA microparticles, Int. J. Pharm. 364 (2008) 298-327.

[4] E. Gang, C. Ki, J. Kim, J. Lee, B. Cha, K. Lee, Y. Park, Highly porous three-dimensional poly(lactide-co-glycolide) (PLGA) microfibrous scaffold prepared by electrospinning method: A comparison study with other PLGA type scaffolds on its biological evaluation, Fibers and Polymers. 13 (2012) 685-691.

[5] H. Tai, M.L. Mather, D. Howard, W. Wang, L.J. White, J.A. Crowe, S.P. Morgan, A. Chandra, D.J. Williams, S.M. Howdle, K.M. Shakesheff, Control of pore size and structure of tissue engineering scaffolds produced by supercritical fluid processeing, European Cells and Materials. 14 (2007) 64-77.

[6] D. Blanco, M.J. Alonso, Protein encapsulation and release from poly(lactide-co-glycolide) microspheres: effect of the protein and polymer properties and of the co-encapsulation of surfactants, European Journal of Pharmaceutics and Biopharmaceutics. 45 (1998) 285-294.

[7] W. B. Liechty , D. R.Kryscio, B. V. Slaughter, N. A. Peppas, Polymers for drug delivery systems, Annual Review of Chemical and Biomolecular Engineering. 1 (2010) 149-173.

[8] C.E. Upton, C.A. Kelly, K.M. Shakesheff, S.M. Howdle, One dose or two? The use of polymers in drug delivery, Polym. Int. 56 (2007) 1457-1460.

[9] R.A. Jain, The manufacturing techniques of various drug loaded biodegradable poly(lactide-co-glycolide) (PLGA) devices, Biomaterials. 21 (2000) 2475-2490.

[10] F. Jordan, A. Naylor, C.A. Kelly, S.M. Howdle, A. Lewis, L. Illum, Sustained release hGH microsphere formulation produced by a novel supercritical fluid technology: In vivo studies, J. Controlled Release. 141 (2010) 153-160.

[11] M.L. Houchin, E.M. Topp, Chemical degradation of peptides and proteins in PLGA: A review of reactions and mechanisms, Journal of pharmaceutical sciences. 97 (2008) 2395-2404.

[12] R.A. Kenley, M.O. Lee, T.R. Mahoney, L.M. Sanders, Poly(lactide-co-glycolide) decomposition kinetics in vivo and in vitro, Macromolecules. 20 (1987) 2398-2403.

[13] T.G. Park, Degradation of poly(lactic-co-glycolic acid) microspheres: effect of copolymer composition, Biomaterials. 16 (1995) 1123-1130.

[14] M.A. Tracy, K.L. Ward, L. Firouzabadian, Y. Wang, N. Dong, R. Qian, Y. Zhang, Factors affecting the degradation rate of poly(lactide-co-glycolide) microspheres in vivo and in vitro, Biomaterials. 20 (1999) 1057-1062.

[15] K. Odelius, A. Hoglund, S. Kumar, M. Hakkarainen, A.K. Ghosh, N. Bhatnagar, A.C. Albertsson, Porosity and Pore Size Regulate the Degradation Product Profile of Polylactide, Biomacromolecules. 12 (2011) 1250-1258.

[16] E. Vey, C. Rodger, J. Booth, M. Claybourn, A.F. Miller, A. Saiani, Degradation kinetics of poly(lactic-co-glycolic) acid block copolymer cast films in phosphate buffer solution as revealed by infrared and Raman spectroscopies, Polym. Degrad. Stab. 96 (2011) 1882-1889.

[17] F. Alexis, S. Venkatraman, S.K. Rath, L.H. Gan, Some insight into hydrolytic scission mechanisms in bioerodible polyesters, Journal of Applied Polymer Science. 102 (2006) 3111-3117.

[18] C.M. Agrawal, D. Huang, J.P. Schmitz, and K.A. Athanasiou, Elevated Temperature Degradation of a 50:50 Copolymer of PLA-PGA, Tissue Engineering. 3 (1997) 345-352.

[19] M. Vert, J. Mauduit, S. Li, Biodegradation of PLA/GA polymers: increasing complexity, Biomaterials. 15 (1994) 1209-1213.

[20] M. Vert, S.M. Li, H. Garreau, Attempts to map the structure and degradation characteristics of aliphatic polyesters derived from lactic and glycolic acids, J Biomater Sci Polym Ed. 6 (1994) 639-649.

[21] E. Vey, C. Roger, L. Meehan, J. Booth, M. Claybourn, A.F. Miller, A. Saiani, Degradation mechanism of poly(lactic-co-glycolic) acid block copolymer cast films in phosphate buffer solution, Polym. Degrad. Stab. 93 (2008) 1869-1876.

[22] G. Spenlehauer, M. Vert, J.P. Benoit, A. Boddaert, In vitro and In vivo degradation of poly(D,L lactide/glycolide) type microspheres made by solvent evaporation method, Biomaterials. 10 (1989) 557-563.

[23] B.S. Zolnik, D.J. Burgess, Effect of acidic pH on PLGA microsphere degradation and release, Journal of Controlled Release. 122 (2007) 338-344.

[24] M.B. Sintzel, A. Merkli, C. Tabatabay, R. Gurny, Influence of Irradiation Sterilization on Polymers Used as Drug Carriers—A Review, Drug Dev. Ind. Pharm. 23 (1997) 857-878.

[25] J. Hao, M.J. Whitaker, B. Wong, G. Serhatkulu, K.M. Shakesheff, S.M. Howdle, Plasticization and Spraying of Poly (DL-lactic acid) Using Supercritical Carbon Dioxide: Control of Particle Size, Journal of pharmaceutical sciences. 93 (2004) 1083-1090.

[26] J. Hao, M.J. Whitaker, G. Serhatkulu, K.M. Shakesheff, S.M. Howdle, Supercritical fluid assisted melting of poly(ethylene glycol): a new solvent-free route to microparticles, J. Mater. Chem. 15 (2005) 1148-1153.

[27] M.J. Whitaker, J. Hao, O.R. Davies, G. Serhatkulu, S. Stolnik-Trenkic, S.M. Howdle, K.M. Shakesheff, The production of protein-loaded microparticles by supercritical fluid enhanced mixing and spraying, J. Controlled Release. 101 (2005) 85-92.

[28] V. Klang, C. Valenta, N.B. Matsko, Electron microscopy of pharmaceutical systems, Micron. 44 (2013) 45-74.

[29] S.S. Davis, L. Illum, S. Stolnik, Polymers in drug delivery, Current Opinion in Colloid & Interface Science. 1 (1996) 660-666.

[30] K. Fu, D. Pack, A. Klibanov, R. Langer, Visual Evidence of Acidic Environment Within Degrading Poly(lactic-co-glycolic acid) (PLGA) Microspheres, Pharm. Res. 17 (2000) 100-106.

[31] A.G. Ding, S.P. Schwendeman, Acidic Microclimate pH Distribution in PLGA Microspheres Monitored by Confocal Laser Scanning Microscopy, Pharm. Res. 25 (2008) 2041-2052.

[32] J.S.C. Loo, C.P. Ooi, F.Y.C. Boey, Degradation of poly(lactide-co-glycolide) (PLGA) and poly(l-lactide) (PLLA) by electron beam radiation, Biomaterials. 26 (2005) 1359-1367.

[33] P. Nugroho, H. Mitomo, F. Yoshii, T. Kume, Degradation of poly(l-lactic acid) by γ-irradiation, Polym. Degrad. Stab. 72 (2001) 337-343.

5 Investigation of Physiochemical Factors Affecting the Protein Release from γ-Irradiated PLGA Microparticles

5.1 Introduction

Pharmaceutically relevant microparticles for parenteral use must be well characterized in terms of their size range, morphology and function. Chemical characterisation of sustained release microparticles is critically important, not only because it aids achieving success in producing the designed drug, demonstrating desired properties but also because, as in case of any side effects that may elevate after injection, it would be very difficult to rectify them due to the long lasting (up to several weeks) efficacy of the drug. It is widely understood that the chemistry and morphology of microparticles have a degree of interdependence as the morphology of microspheres can vary depending on their chemical state after preparation. This therefore can strongly affect drug release behaviour from microspheres [1-3].

Real time hydrolytic degradation of a PLGA microparticle using ATR-FTIR imaging and analysis was investigated in Chapter 3 and the factors affecting the degradation of the PLGA polymers that were used to encapsulate protein based APIs in this project were studied in Chapter 4. In this Chapter, the real time release of a protein, human growth hormone (hGH), from a more complex formulation including both PLGA and PLA polymers and a GRAS (generally recognised as safe) excipient (Poloxamer 407) is investigated in light of the information obtained from the PLGA microparticles in previous chapters.

Novel sustained release formulations of hGH prepared by supercritical fluid processing of PLGA/PLA (the CriticalMix™ process, Section 1.5.3.4.1, Chapter 1) were produced in the form of microparticles for subcutaneous injection by the collaborating company (Critical Pharmaceuticals Ltd.) [4]. Here, a formulation that has been evaluated *in vivo* in rats and monkeys, showing up to two weeks more of efficacious hGH release compared to a daily injection of soluble hGH, is investigated to study the real time release using ATR-FTIR imaging for the first time.

Often, pharmaceuticals have to be sterilised before use and for polymeric microparticle drug delivery systems, γ-irradiation is a well-established method to achieve this [3,5]. Prior to sterilization of pharmaceutical products using γ-irradiation, it is essential to determine any effects that this process may have on the materials, as each polymer

responds differently to ionizing radiation. Therefore the maximum dose that can be administered to sterilize the product must to be validated. This study will evaluate the effect of γ-irradiation on the physical and chemical structure of the microparticles and attempt to draw links between chemical and morphological changes and the *in vivo* release of the entrapped hGH from single microparticles for the first time.

As demonstrated in Chapter 3 and Chapter 4, Fourier transform infrared (FTIR) spectroscopic imaging has become a popular spectroscopic imaging approach, particularly for pharmaceutical research, as it allows not only monitoring the physical and chemical changes of individual components over time, but also gives quantitative information such as polymer matrix degradation rate and drug release rate from the same experiment [6-9].

FTIR spectroscopy has been used for studying the interactions of carbohydrates with dried proteins [10], assessing the integrity of the hGH encapsulated in PLGA by spray-freeze-drying and water-in-oil-in-water double emulsion methods [11] and assessing the effect of excipients in Lysozyme and BSA loaded microspheres prepared by a double-emulsion technique [12]. Lysozyme distribution in microtomed PLGA microspheres prepared by a w-o-w solvent evaporation method has been studied by FTIR imaging in transmission mode and the second derivative protein amide I band images shown a homogenous distribution of protein [13]. The use of real time FTIR imaging for characterisation of a drug delivery system [7], dissolution of tablets [14,15] and morphological evaluation of different components, redistribution and/or release of species at polymer/solvent interfaces and the occurrence of new species during chemical reactions under the conditions of interest [6,8,16,17] have been demonstrated. However the release of active pharmaceutical ingredients (APIs) from single polymeric microparticles and monitoring the redistribution of API 'inside' a microparticle has not previously been studied by ATR-FTIR imaging.

The following aspects of vibrational spectroscopy applied to microparticle characterisation were investigated;

    (i)   Investigating the spatial distribution of protein within the microparticle in order to validate the formulation model.

    (ii)   Monitoring the release of proteins from biodegradable microparticles *in situ.*

    (iii)   The assessment of the effect of γ- irradiation on the stability of PLGA microparticles and on the release of the protein from the microparticles.

In order to facilitate a better understanding of the FTIR imaging results coupled with SEM analyses, the formulation and/or its components were further investigated using a combination of conventional bulk (i.e. multiple microparticles) methods including; differential scanning calorimetry (DSC) to understand thermal properties of irradiated and un-irradiated pure polymers, gel permeation chromatography (GPC) to monitor effect of irradiation on the molecular weight of the polymers, UV-Vis spectrophotometry to monitor; (i) *in vitro* API release from the microparticles using dissolution apparatus, (ii) *in vitro* dissolution of irradiated and unirradiated, spray dried hGH (sdhGH) particles, in an aqueous buffer solution and size exclusion chromatography (SEC) to determine protein aggregation and stability.

5.2 Experimental

The GPC, DSC, HPLC-SEC and UV-Vis dissolution experiments were conducted at CPL using standard protocols.

The samples were prepared by CPL using standard protocols.

5.2.1 Materials

PLGA RG502H (50:50 lactide:glycolide, Bohringer-Ingleheim) with an inherent viscosity of 0.16–0.24 dl/g, PLA R202H (100:0 lactide:glycolide, Bohringer-Ingleheim) with an inherent viscosity of 0.16–0.24 dl/g, pharmaceutical grade CO_2 (BOC Special Gasses) were used as received. hGH was kindly donated by Bioker (Sardinia, Italy) and Poloxamer 407 (Lutrol® F127) was purchased from BASF (Ludwigshafen, Germany). D_2O (613398-10G, min. 99.996 atom) and bee's wax (243248-100G) were purchased from Sigma-Aldrich Company Limited. UK. Technovit 7100 embedding resin kit was purchased from Kulzer & Co, Germany. HEPES, Tween 20, NaOH (1M), DCM and HPLC grade acetone were obtained from Fisher and used as received.

5.2.2 Spray Drying of hGH

In order to obtain a suitable particles size of the protein for encapsulation, the hGH was spray dried by dissolving 8 g hGH and 2 g trehalose in 500 ml of 5 mM phosphate buffer. 2.5 ml of Tween-20 (20 %w/v) was then added to this solution. A further 500ml of 5mM phosphate buffer was taken and 200µl of 3.2M $ZnCl_2$ added to it. The two solutions were combined and spray dried using a Buchi B-290 spray dryer. The system was equilibrated at an inlet temperature of 85 ºC, using an aspirator setting of 100 %, an atomisation pressure of 6.5 bar and water feed rate of 2.0 ml/min, until the outlet temperature stabilised. The typical outlet temperature obtained was 53-55ºC.

The sample was then dried under the same conditions and followed through with 10 ml water. The sdhGH was recovered from the collection jar/cyclone.

5.2.3   Preparation of Microparticles Using scCO$_2$ Processing

As detailed in Section 1.5.3.4 of Chapter 1, the method of PGSS (Particles from Gas Saturated Solutions) uses the ability of scCO$_2$ to depress the glass transition and melting temperature of biodegradable polymers at ambient temperatures and moderate pressures. scCO$_2$ acts effectively as a molecular lubricant, thus liquefying polymers at temperatures significantly lower than those typically needed. The near ambient temperatures together with the absence of any aqueous or organic solvents makes the PGSS method particularly suited to the processing of thermally or solvent labile proteins and peptides, with the advantage that they can be encapsulated with 100% efficiency with no protein degradation or loss of activity.

A formulation of hGH loaded PLGA/PLA microparticles was prepared using the CriticalMix™ process, as described in Section 1.5.3.4.1 in Chapter 1 and in [4], by adding 2 g of pre-weighed combination of spray dried hGH (10 wt% of the formulation), PLGA and PLA in 90:10 ratio respectively (81 wt% of the formulation) and GRAS excipient, Poloxamer 407 (9 wt% of the formulation), to the PGSS apparatus. A blank formulation (i.e. without the protein) was also produced using the CriticalMix™ process under the same conditions to be used for DSC studies.

5.2.4   Sieving of Microparticles

In order to facilitate consistency in the characterisation methods the hGH encapsulated formulation was sieved using a 100 µm sieve as described in Section 2.5, Chapter 2.

5.2.5   Sample Preperation for Micro-ATR-FTIR Imaging

hGH loaded PLGA/PLA microparticles were embedded in a hydroxyethyl methacrylate based resin (Technovit 7100) as described by van de Weert *et al.* [13] and sliced to 4 µm thickness using a Reichert-Jung Ultracut E ambient ultramicrotome with a glass knife.

5.2.6   γ-Irradiation

ScCO$_2$ produced microparticle formulations and the polymers used in them were γ-irradiated at 25 and 100 kGy total dose in air by Synergy Health PLC (Swindon, UK) as described in Chapter 2, Section 2.7.

5.2.7 ATR-FTIR Spectroscopy

ATR-FTIR spectra were collected on a Thermo Nicolet Nexus instrument as single beam spectra by co-adding 128 scans at a spectral resolution of 4 cm^{-1} and ratioed against the single beam spectrum of the blank ATR crystal at room temperature.

5.2.8 Transmission FTIR Imaging

Transmission FTIR images were collected as described in Section 2.1.3 in Chapter 2.Images were collected with a 4 cm^{-1} spectral resolution in the mid-infrared range (3800 to 950 cm^{-1}) co-adding 128 scans for both background (2 mm thick CaF$_2$ slide in air) and samples.

5.2.9 Micro-ATR-FTIR Imaging

Micro-ATR-FTIR images were collected as described in Section 2.1.3 in Chapter 2. Images were collected with a 4 cm^{-1} spectral resolution in the mid-infrared range (3800 to 950 cm^{-1}) co-adding 64 scans for both background (Ge crystal in air) and samples.

5.2.10 Macro-ATR-FTIR Imaging of Drug Release from Individual Microparticles

Mid-infrared (3800 to 950 cm^{-1}) spectroscopic imaging data in Macro-ATR mode were acquired as described in Section 3.2.3 in Chapter 3, at 37 °C with 128 co-added scans at an 8 cm^{-1} spectral resolution, and processed by ratioing against a background of the blank ATR crystal with 256 co-added scans also collected at 37 °C.

A single microparticle was placed on to the centre of the square surface of the ATR crystal with the aid of a 40x binocular microscope. A uniform contact between the particle and the crystal with minimal deformation was obtained applying sufficient pressure to the auto-level sapphire anvil [18]. Minimal deformation was ensured such that the same particle could be picked up using the same needle without leaving any residue on the ATR crystal. After collecting a 'dry' image at 37 °C, ~2 ml of D$_2$O that had been pre-heated to 37 °C was injected into the cell in such a way that access to the particle was limited to the sides only as shown in Figure 5.1. The experiment cell was then sealed with bee's wax that is a natural air sealant, to avoid any exchange between D$_2$O and atmosphere.
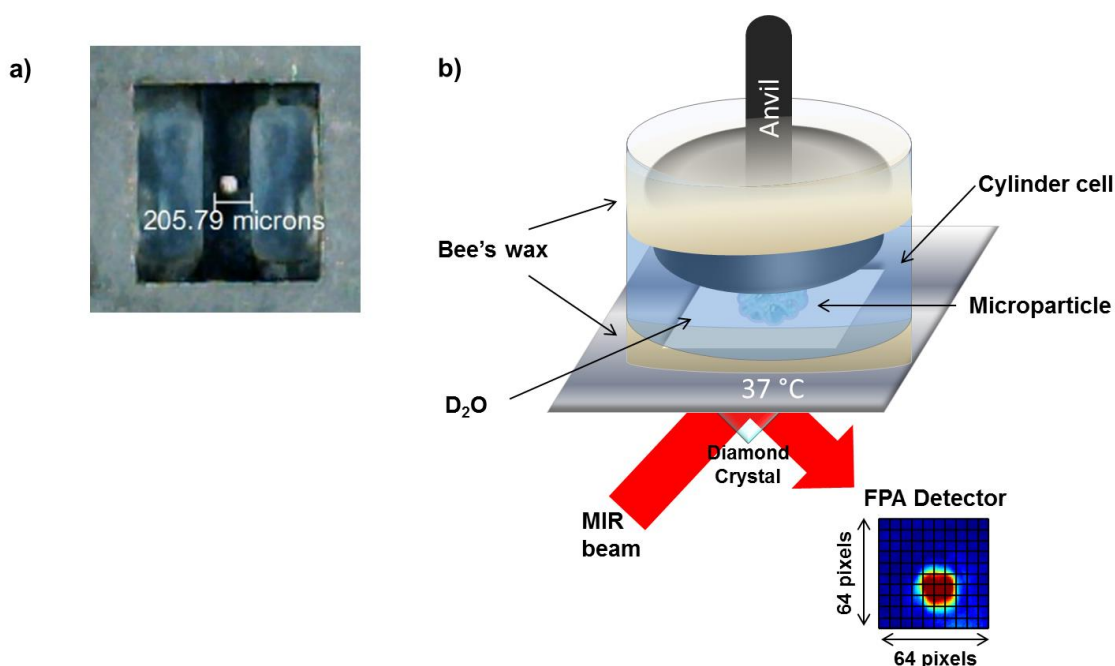
Figure 5.1(a) White light image of a microparticle placed on the ATR crystal prior to star of the experiment. (b) Schematic of the dissolution experiment; the anvil applies sufficient pressure to ensure good contact between the particle and the ATR crystal, whilst making sure D$_2$O can only access the particles from the sides and the experiment cell is isolated from atmosphere using bee's wax.

5.2.11 FTIR Imaging Data Processing

Hyperspectral image cubes were processed using Malvern Instruments' ISys 5.0 chemical imaging software. Raw processed image files were cropped between 1820 and 1000 cm^{-1}, a region which contains a number of characteristic bands associated with PLGA/PLA polymers, protein amide I band ~1650 cm^{-1} and the δ(OD) band of D$_2$O at ~1207 cm^{-1}.

A Savitzky-Golay second derivative with a polynomial order of 3 and filter length of 29 was applied to cropped imaging data in order to eliminate baseline drift. Second derivative images were then vector normalised in order to remove systematic discrepancies such as variations in detector sensitivity or sample contact and therefore to minimise intensity (Log(1/R)) variance.

5.2.12 Scanning Electron Microscopy

To investigate the morphology of the microparticles SEM analyses were performed as decribed in Section 2.3 in Chapter 2.

5.2.13 UV-Vis Spectrophotometry of Pure hGH

UV-Vis transmission spectra for the irradiated and non-irradiated pure hGH particles were acquired between 190 nm and 1100 nm at 5 nm spectral resolution (with 12.5 ms dwell time at each wavelength step) at 22 °C using a Carry60 UV-Vis spectrophotometer (Agilent, USA) using D_2O as a blank.

5.2.14 In vitro Drug Release

The amount of hGH released in to HEPES solution at 37 °C at each time point was obtained using UV-Vis dissolution testing at 280 nm, as described in Section 2.4 in Chapter 2.

5.2.15 DSC

Melting temperature (T_m) and glass transition temperature (T_g) of the non-irradiated and irradiated polymers and the polymer blend without the hGH were measured as described in 2.8, Chapter 2.

5.2.16 Evaluation of hGH Stability and Integrity

In order to detect the formation of any hGH aggregates following irradiation, irradiated and non-irradiated hGH were analysed using HPLC-SEC as described in Section 2.9.1.1 in Chapter 2.

5.2.17 Molecular Weight Determination

The molecular weight (M_w) and molecular number (M_n) of the irradiated and non-irradiated polymer samples were determined by Gel Permeation Chromatography (GPC) using a PL-120 (Polymer Labs) with a differential refractive detector, as described in Chapter 2, Section 2.9.1.2.

5.3   Results and Discussion

5.3.1   Determination of The Spatial Distribution of Encapsulated hGH within The Microparticles

As discussed in Section 1.2 in Chapter 1, the key requirement for a sustained release drug formulation; to follow a diffusion and/or erosion based release route from the biopolymer carrier matrix. This could only be achieved by obtaining a homogenous distribution of the drug within the matrix.

The CriticalMix^{TM} process is thought to produce a homogenous distribution of drug throughout the porous microparticles as depicted in the illustration in Figure 5.2a. As demonstrated by van de Weert *et al.* [13] using transmission mode FTIR imaging, protein based API can be readily mapped in PLGA microparticles.

Following a similar sample preparation methodology explained thoroughly in [13] and in Section 2.6 in Chapter 2, a group of hGH encapsulated PLGA/PLA microparticles within an embedding medium highlighted by the red box in Figure 5.2b and Figure 5.2d. were microtomed to 4 μm sections.

The distribution of polymer and API within these microparticles was determined using mid-IR imaging in micro–ATR mode utilising a Ge ATR crystal which provided a spatial resolution of ~4 μm within ~64x64 μm field of view and in transmission mode by floating the sample on a 2mm thick IR transparent (CaF$_2$) slide which provided a spatial resolution of ~13 μm within ~350x350 μm field of view.

Table 5.1 shows the list of important peaks included in fingerprint region of the ATR-FTIR spectra obtained from pure samples. From this table, it can be seen that the most intense Poloxamer 407 peaks overlap with PLGA/PLA peaks however very strong peaks are readily available in distinct wavenumbers for the rest of the samples. As discussed later in the macro-ATR image section, the δ(OD) of D$_2$O also becomes distinct when a second derivative is applied, therefore D$_2$O was used instead of H$_2$O to perform the imaging experiments in order to circumvent the difficulty of having to deconvolute the water δ(OH) peak ~1635 cm^{-1} that would overlap with the protein Amide I ν(C=O) peak ~1658 cm^{-1}.

Figure 5.2a illustrates a typical, CriticalMix^{TM} processed microparticle where yellow strings represent mixed polymers and blue dots represent the homogenously distributed protein particles. Figure 5.2b and d show the white light image of microparticles from the same formulation batch, embedded in resin and microtomed to 4 μm thickness. Figure 5.2c shows the false colour Micro-ATR image of the red boxed area indicated in Figure 5.2b, that represent the integrated peak height distribution of the resin at 1727 cm^{-1}, PLGA/PLA at 1755 cm^{-1} and hGH at 1650 cm^{-1} from left to right respectively. Figure 5.2e shows false colour transmission IR second derivative peak height images from the area shown with the red box in the white light image in Figure 5.2d, showing

Table 5.1 Infrared assignments for PLGA 50/50, PLA, Poloxamer 407, resin, D_2O and hGH within the finger print region (1820-1000 cm^{-1} wavenumbers); as antisymmetric, s symetric, δ bending, ρ rocking, ν stretching, τ twisting, ω wagging, all given in cm^{-1}.

PLGA	PLA	hGH	Poloxamer 407	Resin	D_2O	Assignment
1745	1745			1727		ν(C=O)
		1658				Amide I, ν(C=O)
				1635		δ(OH)
		1540				Amide II, δ(NH)
1452	1450	1450	1466	1484		δ_{as}(CH$_3$)
1422				1450		δ(CH)
1394		1394		1395		ω(CH)
1381	1379		1374			δ_s(CH$_3$)
1360	1362	1304	1359, 1341	1323		δ(CH)
1270	1266		1280, 1241	1274, 1249		τ(CH$_2$)
		1245				ν_{as}(PO)
					1207	δ(OD)
1167	1184	1146	1144, 1100	1154		ν_{as}(COC)
1131	1127					ρ_{as}(CH$_3$)
		1104				ν_s(PO)
1086	1084	1077		1074		ν_s(COC)
1048	1045	1049	1059	1020		ν(C-CH$_3$)
		990				ν_s(PO)
957	957	942	962	948		ρ(CH$_3$)

resin (1722 cm^{-1}), PLGA/PLA (1758 cm^{-1}) and hGH (1650 cm^{-1}) from left to right respectively.
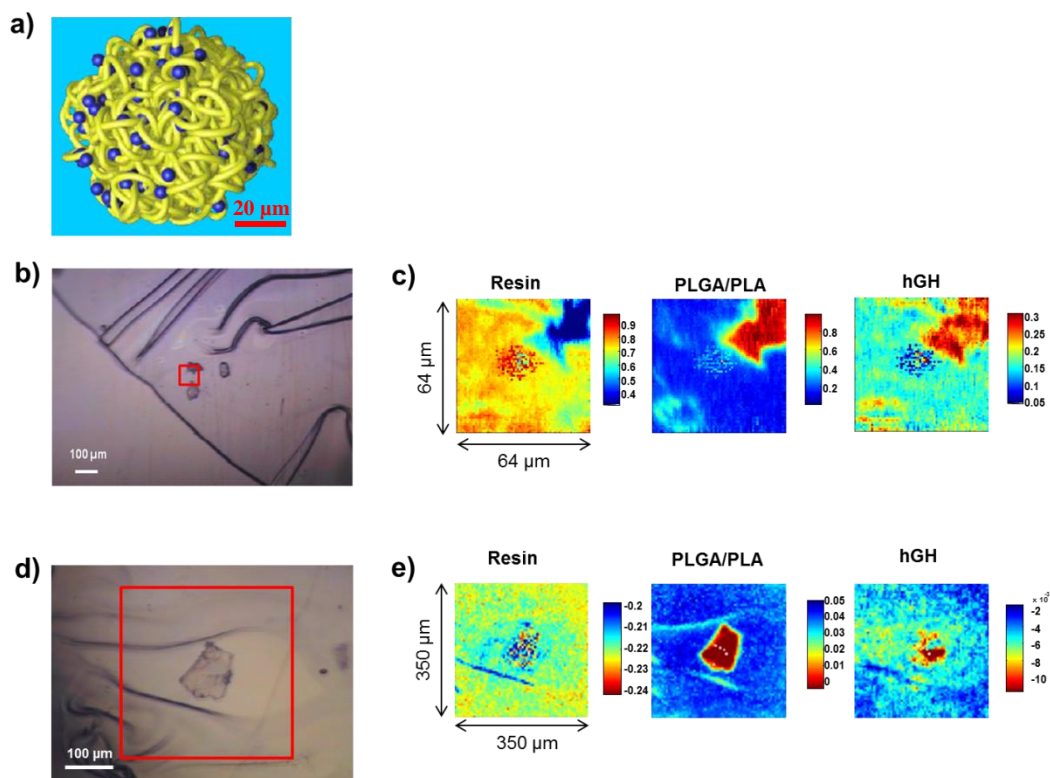
Figure 5.2 (a) An illustration of a typical, CriticalMix^{TM} processed microparticle. (b) White light image of 3 microparticles embedded in resin and microtomed to 4 µm thickness. (c) False colour Micro ATR (Ge) peak area images from the area shown with the red box in the white light image. (d) White light image of another microparticle from the same formulation batch, embedded in resin and microtomed to 4 µm thickness. (e) Transmission IR second derivative peak height images from the area shown with the red box in the white light image in (d).

The distribution of PLGA/PLA and hGH, middle and right hand side images in Figure 5.2c and Figure 5.2e respectively, clearly show a good correlation between the high intensity (red) regions of PLGA/PLA and hGH. This is in contrast to the resin distribution, which shows an anti-correlation with both components. This strong evidence of the homogenous distribution of hGH protein with in the PLGA/PLA microparticle layers, not only demonstrates the success in producing an ideal controlled release drug formulation from which the API would be released by diffusion through the pores and/or degradation of the biopolymer matrix, but also, considering the crucial aim in characterising such micro devices; *in situ* imaging of the samples in their natural state (i.e. without any sample preparation), brings the key advantage that this system

136

can be monitored using ATR-FTIR. Because as explained in Section 2.1.2.2.1 in Chapter 2, due to the shallow penetration depth of the evanescent field (~10 µm) ATR only probes the near-surface of a sample. This is favourable if one needs to study the evolution of a sample in aqueous media, as the strong absorption of water can be minimised due to the limited effective sampling volume, and having a sample that is physiochemically consistent at both the surface and in the bulk, ATR-FTIR imaging can be used to monitor the real time release of API from such a microparticle.

5.3.2 Visualisation of Protein Release from a Single Microparticle

The use of ATR-FTIR imaging in macro mode to investigate the morphological and chemical evolution of a protein loaded polymeric microparticle in real time was studied.

A microparticle from the formulation was taken and its interaction with water was monitored as a function of time at 37 °C. The experiment was setup in such a way that the interaction between the particle and water would only occur at the interfaces that we are monitoring, effectively creating a 2D experiment (Figure 5.1).

Figure 5.3 shows six false colour images obtained by plotting the intensity distribution of the PLGA/PLA ester carbonyl (1755 cm^{-1}), protein (hGH) Amide I (1650 cm^{-1}) and D$_2$O δ(OD) (1207 cm^{-1}).
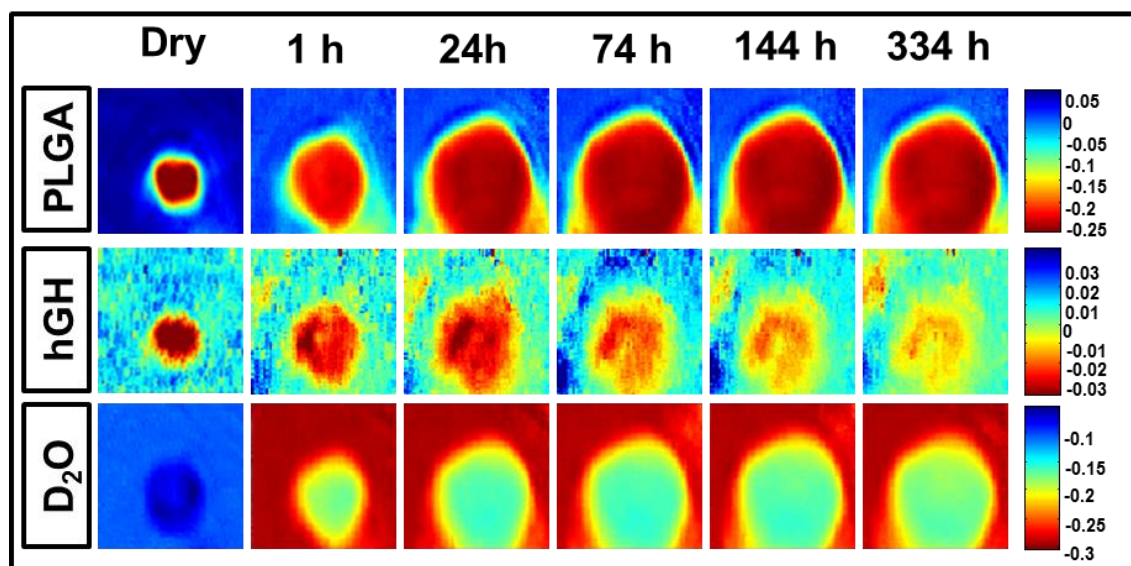
Figure 5.3 False colour ATR-FTIR images of a microparticles showing second derivative peak height distribution of PLGA at 1755 cm^{-1}, hGH at 1650 cm^{-1} and D$_2$O at 1207 cm^{-1} as a function of time.

The first column of images show the distribution of polymer, hGH and D_2O, respectively, before the dissolution experiment was started and are therefore labelled 'dry'. From these 'dry' images a homogenous distribution of hGH within the polymer matrix can be observed once again, complementing the micro-ATR and transmission images of the sliced samples shown in Figure 5.2c and Figure 5.2e, respectively. Therefore the gaining confidence that the surface (up to ~10 μm) that was being probed with IR light in this macro–ATR experiment was representative of the internal structure of the microparticle, as expected from the CriticalMix[TM] manufacture of drug loaded microparticles [4,19].

The first row of images shown in Figure 5.3 shows the change in the distribution of the PLGA/PLA component of the microparticle. To a first approximation this set of images can be used to monitor the dimensional changes of the microparticle during the dissolution experiment. In the PLGA/PLA image collected after 1 h, there is evidence of an interface layer of hydrated PLGA/PLA around the particle even at this short time, with a decreasing D_2O concentration from the aqueous dissolution medium towards the particle centre and some evidence of particle swelling. Within 24 h the PLGA/PLA microparticle (red) appears to have swollen further, becoming larger, whilst still being surrounded by a hydrated PLGA/PLA layer (yellow), and over time the size of the particle stays almost the same in terms of visual representation. The bottom row of Figure 5.3 shows the complementary image data set of D_2O distribution as a function of time. These images show a strong anti-correlation with the PLGA/PLA image dataset and verify the significant amount of swelling in this system, as one might expect, due to the inclusion of the excipient Poloxamer 407 at 9 wt% in the formulation, making the microparticles more hydrophilic [20,21]. It is worth noting that after ~1 h, D_2O is present, albeit at a low level, everywhere within the particle, almost certainly due to a combination of the particle hydrophilicity and its porosity. Over the duration of this experiment (334 h, ~14 days) there was not any major evidence of 'shrinking' of the PLGA/PLA particle, implying this observation would require a much longer sampling period, perhaps several months at 37 °C. This not only shows the well-documented suitability of PLGA and PLA to act as biodegradable drug carriers, providing sustained release for several weeks to months, but also suggests that protein release from this system is dominated by diffusion rather than erosion, during the first 2 weeks, which may be expected due to the system being porous. The hGH distribution images (middle row, Figure 5.3a), were generated by plotting the Amide I peak height at ~1650 cm^{-1},

and show a change in the distribution at short times (<24 h) as the polymers are initially swollen and this is followed by a gradual decrease of overall hGH intensity distribution as a function of time. As one could observe, the dimensions of the hGH rich region are somewhat smaller than their polymer and D_2O counterparts. One explanation for this is that the hGH is being lost into the D_2O media (~2 ml within the experiment cell) at the D_2O particle interface.

5.3.3 Effect of Gamma Irradiation on Redistribution and Release of hGH from Single Microparticles

To investigate the effect of γ-irradiation on protein loaded PLGA/PLA microparticles, the interaction of 2 single microparticles, that had been subjected to γ-irradiation at doses of 25 and 100 kGy, with water were monitored as a function of time under the same conditions as for the non-irradiated microparticle discussed in Section 5.3.2.
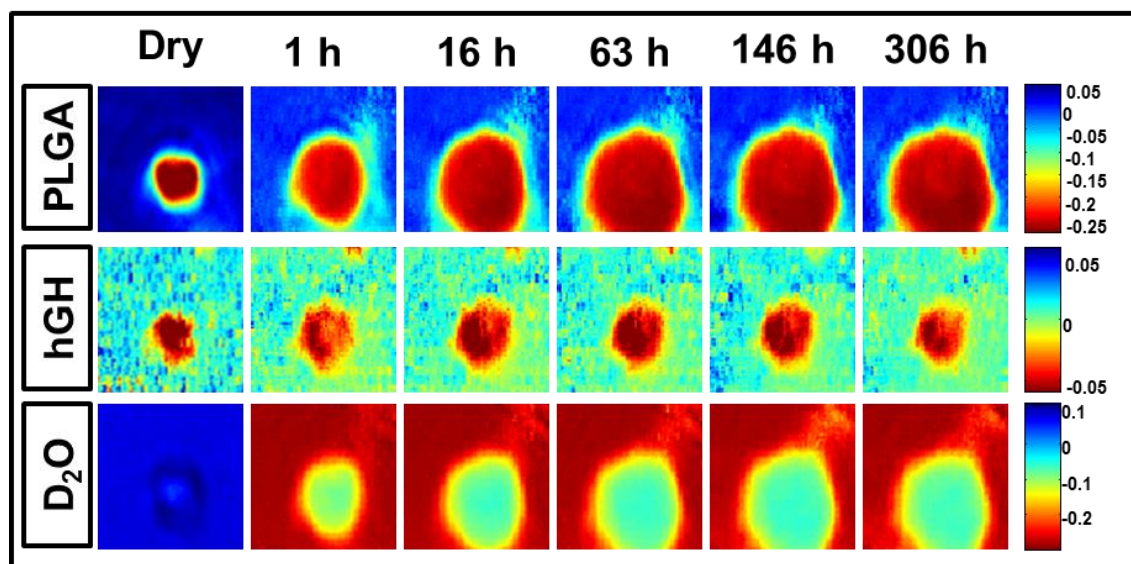
Figure 5.4 False colour ATR-FTIR images of a 25 kGy γ-irradiated microparticle showing second derivative peak height distribution of PLGA at 1755 cm⁻¹, hGH at 1650 cm⁻¹ and D₂O at 1207 cm⁻¹ as a function of time.

Figure 5.4 shows the equivalent false colour infrared images for the data described in Figure 5.3, obtained from a hGH loaded PLGA/PLA microparticle that has been subjected to 25 kGy γ-irradiation. The PLGA/PLA and D_2O distribution maps are quite similar to those shown in Figure 5.3, and the hGH distribution images are once more much smaller than both the polymer and D_2O images. Any change to the colour intensity of the hGH rich region as a function of time after 24 h is more difficult to ascertain by visual inspection.

139
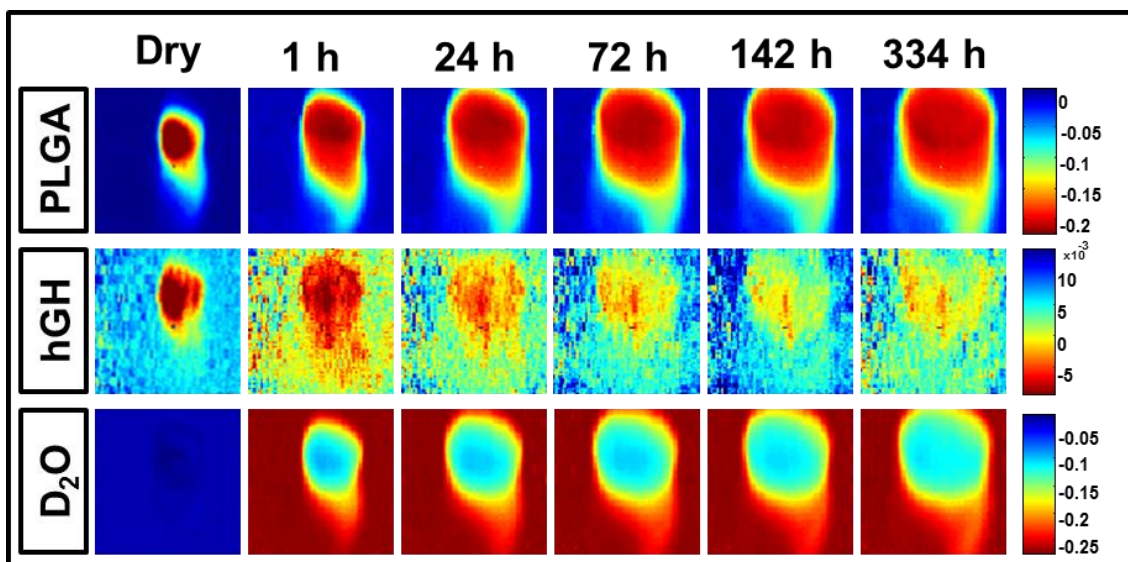
Figure 5.5 False colour ATR-FTIR images of a 100 kGy γ-irradiated microparticle showing second derivative peak height distribution of PLGA at 1755 cm^{-1}, hGH at 1650 cm^{-1} and D$_2$O at 1207 cm^{-1} as a function of time.

Figure 5.5 shows analogous image data sets for a hGH loaded PLGA/PLA microparticle that has been subjected to 100 kGy γ-irradiation, and although at first glance the polymer and D$_2$O distribution images look similar to those depicted in Figure 5.3 and Figure 5.4, a remarkably rapid release of hGH around the microparticle can be seen in the 1 h image and to a lesser extent, in 24 h image, this may be due to the hGH being dissolved in the surrounding media during the ensuing 23 h. The subsequent time resolved hGH distribution maps contain fewer red pixels (i.e. high intensity regions) within the hGH images compared to the earlier time points, therefore it can be assumed that the most of hGH has been released during this initial hydration process; the so called burst release effect. Subsequent time resolved images show a slow reduction in intensity of the hGH distribution maps. Upon closer inspection of the D$_2$O distribution maps, one could observe a higher concentration of D$_2$O (as denoted by the blue/green colour) within the body of the microparticle from 1 h when compared to both the un-irradiated and 25 kGy γ-irradiated hGH loaded microparticles.

5.3.4   SEM of hGH Loaded Formulations

It is clear that both geometry and morphology could have a strong influence on the release characteristics of a hGH loaded polymer microparticle, with porosity in particular likely to determine the rate of hydrolytic degradation and therefore drug release from such systems [22].

SEM was used to explore the morphology of the non-irradiated and irradiated microparticles. SEM is a tool that is readily applied to the microscopic characterisation of particles and other polymer surfaces [23].

Figure 5.6 shows the SEM images of (a) non-irradiated, (b) 25 kGy γ-irradiated and (c) 100 kGy γ-irradiated microparticles. In order to facilitate an unbiased discussion between SEM images of the microparticles shown in Figure 5.6, all of the microparticles were coated under same conditions at the same time.

The low magnification images in Figure 5.6-Column i. shows aggregation of microparticles occurring proportional to applied gamma dose. In Figure 5.6-Column ii. there are clear differences in morphology between the different microparticles, the γ-irradiated particles have a smooth surface and appear to be non-porous (more apparent in zoomed images in Figure 5.6-Column iii.) but with significant amounts of irregular particles, possibly hGH, attached to the surface. However the non-irradiated particle has a rough, non-uniform and porous morphology with inherently higher surface area than the γ-irradiated microparticles. Figure 5.6-Column iv. shows cross-sections of the microparticles that were flash frozen in liquid N_2 and cracked-opened before electron microscopy was conducted. An interesting finding that can be easily seen in Figure 5.6-column iv is that although the inner structure of non-irradiated microparticles are porous similar to their surface structure, gamma radiation seems to have penetrated through them decreasing porosity throughout the particles, again proportional to applied γ dose.
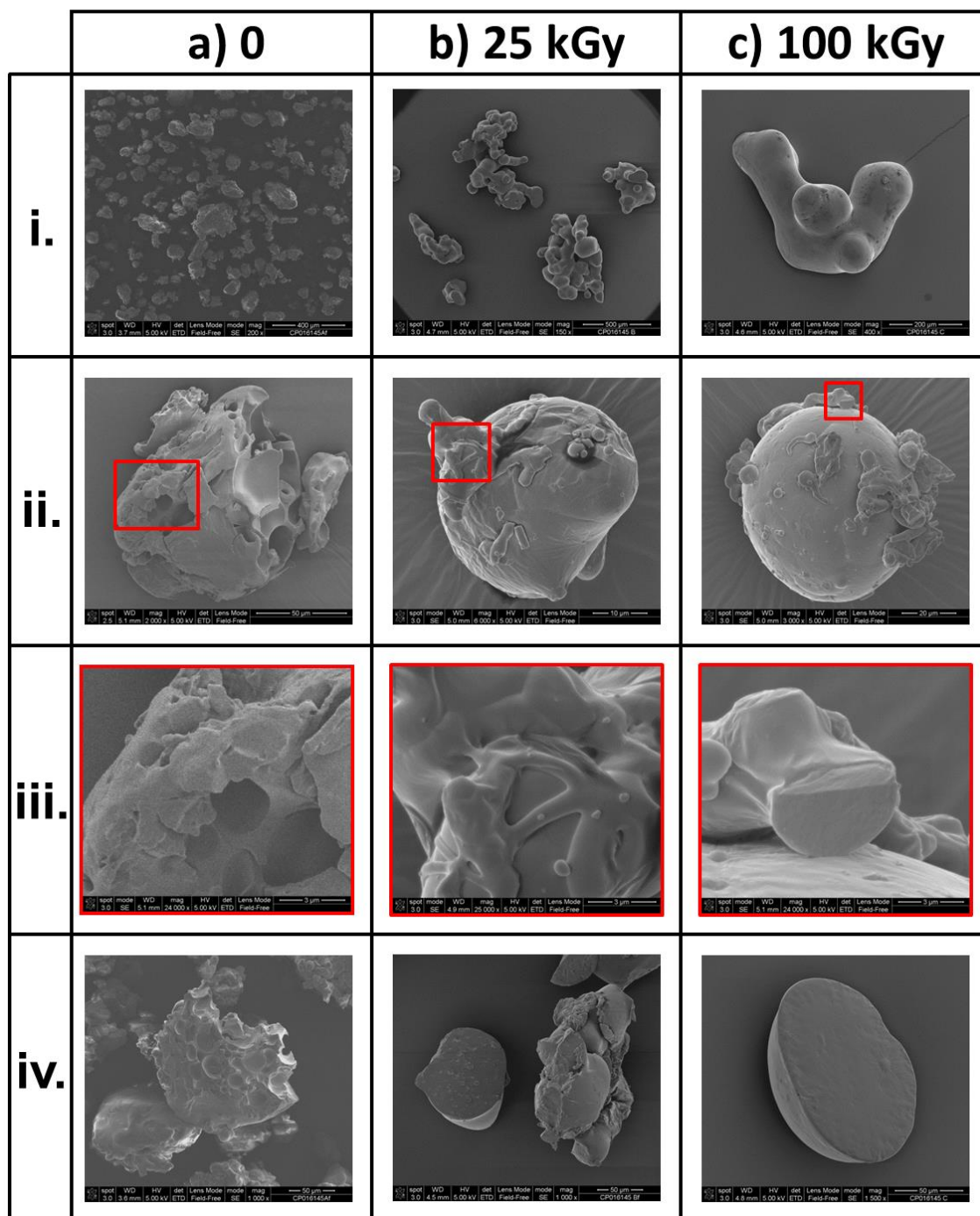
Figure 5.6 SEM images showing typical (a) non-irradiated, (b) 25 kGy and (c) 100 kGy γ-irradiated microparticles. In each row a low magnification image (i.), a single microparticle image (ii.), the zoomed area (iii.) indicated with the red box drawn in (ii.), and images of crack-opened microparticles showing inner structure (iv.), from left to right respectively.

5.3.5 Determination and Comparison of Dissolution Profiles Obtained from FTIR Images

The use of FTIR imaging data to monitor drug release has been validated previously using an experimental setup that combined a UV detector to monitor the release of API from a tablet subjected to water flow during macro ATR-FTIR imaging and compared this to conventional dissolution test data of the same sample type [24]. Release profiles obtained from the two methods were shown to be very similar. By conducting measurements *in situ* using FTIR imaging, chemical changes could be followed by monitoring specific IR bands of components in a fixed area in a temporal image set and the relative amount of that species being released during a dissolution process could be quantified.
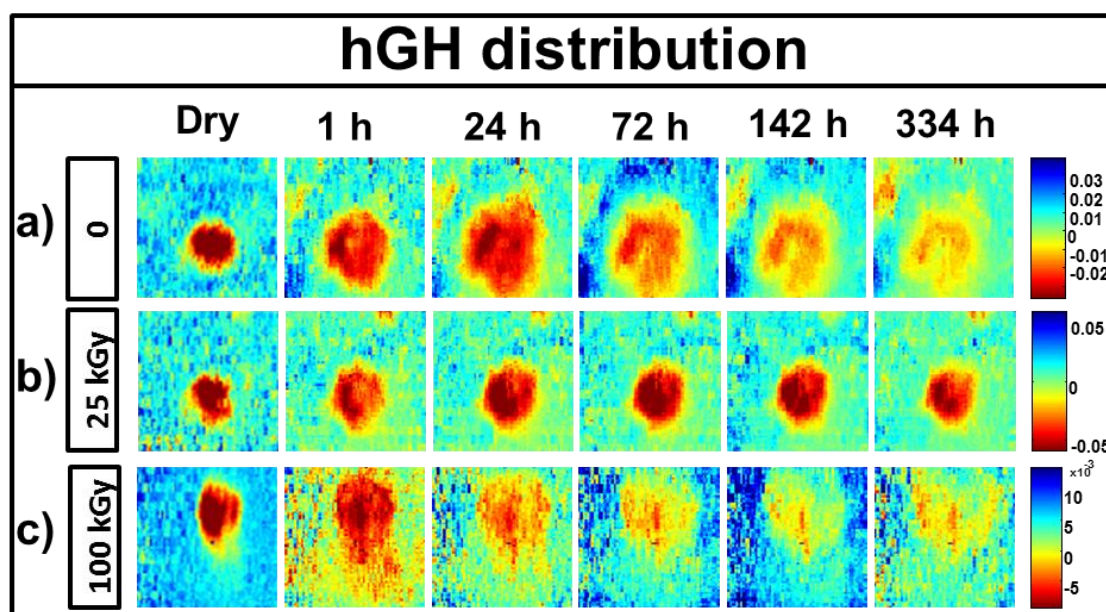
Figure 5.7 False colour ATR-FTIR images of (a) non-irradiated, (b) 25 kGy γ-irradiated and (c) 100 kGy γ -irradiated microparticles showing second derivative peak height distribution of hGH at 1650 cm^{-1} as a function of time.

In each set of temporal images in Figure 5.7; non-irradiated, 25 kGy irradiated and 100 kGy irradiated, 3 square regions (50x50 μm) of interest (ROI) from hGH rich zones within the microparticles were chosen by visually assessing the 1 h images in each data set. By calculating the decrease in area under the amide-I peak at ~1650 cm^{-1} in the binned, normalised temporal spectra from the ROIs, a release profile can be generated by assuming the decrease in hGH signal at time = t (compared to hGH signal at time=0) is proportional to hGH released at that time point was obtained. Using this approach it
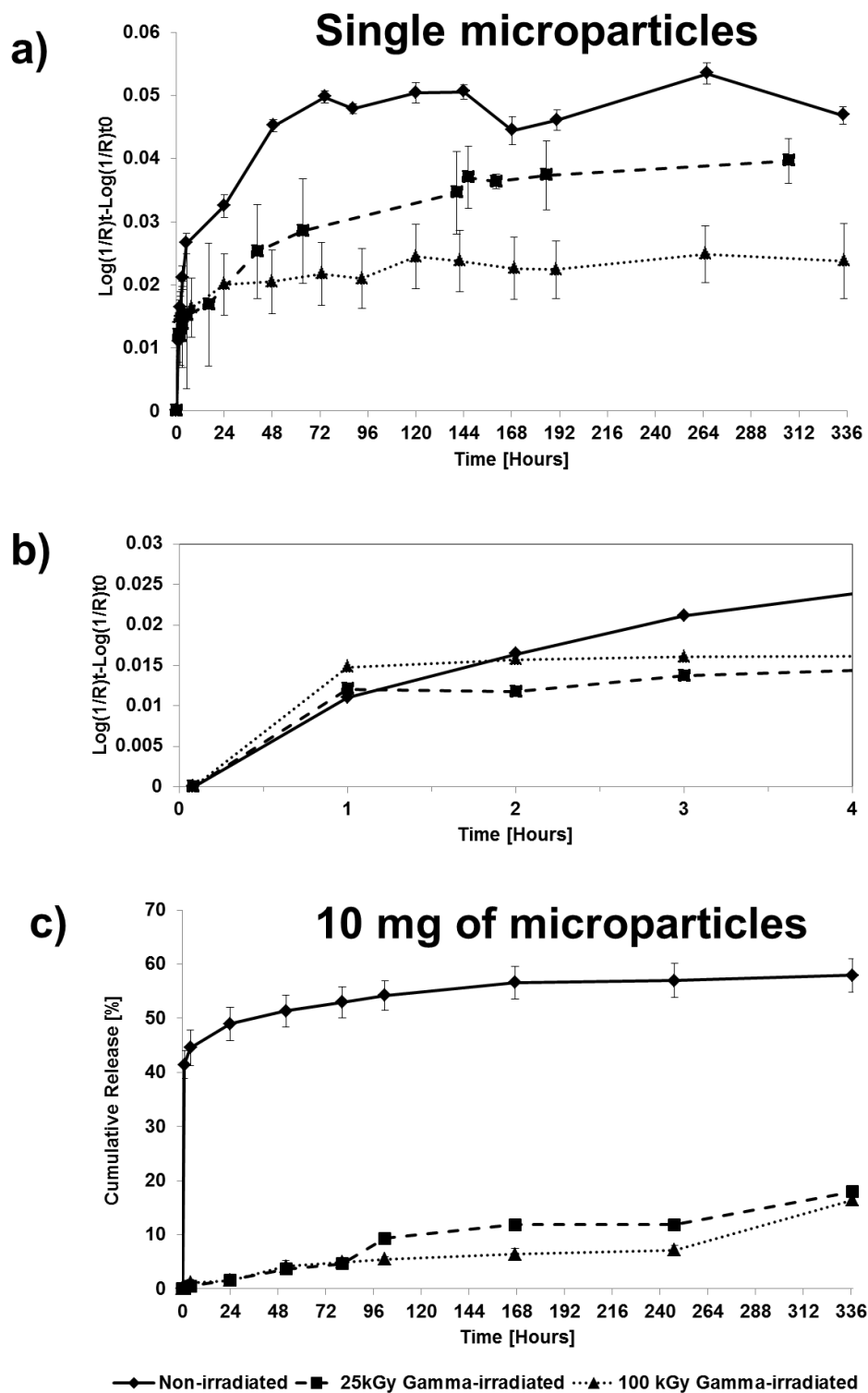
Figure 5.8 (a)Release profiles obtained from 5x5 pixels regions of images of non-irradiated and γ-irradiated microparticles undergoing dissolution.(b) The first 4 h data shown in (a) (to provide clarity error bars are removed). (c) UV-Vis dissolution data of 10 mg of the non-irradiated and γ-irradiated formulation batches.

was feasible to generate a dissolution plot that was analogous to a release profile from a standard USP I UV-dissolution experiment.

Figure 5.8a shows the 3 release profiles obtained from temporal hGH image sets of 0, 25 kGy and 100 kGy γ-irradiated hGH loaded single microparticles shown in Figure 5.7a, b and c respectively, including additional time points for images not shown. Data points in Figure 5.8a are generated from the average of overall intensity from the 3 binned and normalised ROIs and error bars indicate the standard deviation. It is evident that in Figure 5.8a for all three release profiles there are two distinct regions; firstly a rapidly increasing initial period followed by a second phase that almost represents a first order line profile with a slope close to zero.

In Figure 5.8b, this initial period in Figure 5.8a up to 4 h, is plotted once again for better visualisation for evaluation of the burst release phenomenon. The release profile from the non-irradiated hGH loaded microparticle is showing an initial burst within the first few hours followed by a slower rate release for the duration of the experiment reaching a plateau sometime after ~72 h whereas for 25 kGy irradiated particle this plateau arguably occurs after around 144 h which indicates a delay in reaching a consistent release period in comparison to non-irradiated particle.

The hGH release profile from the hGH loaded PLGA/PLA microparticle which has undergone 100 kGy irradiation, once again, shows a markedly high initial burst release particularly within the first 2 hours (Figure 5.8b) which was also evident in Figure 5.7c in the 1h image compared to the rest of the images in that row, indicating an immediate and high release of hGH that is too fast to be polymer degradation or diffusion controlled. γ- irradiation causing this kind of an increased burst effect was also reported by Carrascosa *et al*. [25] who investigated the morphology of recombinant human insulin-like growth factor-I (rhIGF-I) loaded PLGA microspheres by SEM, and determined API release mechanisms using UV-dissolution and differential scanning calorimetry (DSC). It is also evident from the SEM images that the 100 kGy irradiated hGH loaded microparticle has a smooth surface at a smaller scale and appears to have a lumpy morphology (Figure 5.6c) compared to the very porous non-irradiated particle (Figure 5.6a), therefore the initial burst from 100 kGy γ-irradiated particle is likely to be occurring due to surface bound hGH, that is made available from the surface of the microparticle during the γ-irradiation process. Unlike both the un-irradiated and the 25 kGy γ-irradiated sample, following its burst release, the 100 kGy γ-irradiated

formulation shows little measurable release after 48 h. For the non-irradiated and 25 kGy γ-irradiated microparticles it takes up to 3 days for this to be the case. It is also worth remarking that the total amount of hGH that is being released after the initial burst appears to be much less than is observed in the other microparticles.

The release from the 25 kGy γ-irradiated formulation shows similarities to both the non-irradiated and 100 kGy γ-irradiated microparticles; its initial burst profile is similar to 100 kGy γ-irradiated formulation, indicating high protein availability at its surface, but it takes longer to reach a plateau similarly to that observed in the non-irradiated microparticle and the total amount of protein released appears to be in between that of non-irradiated and 100 kGy γ-irradiated sample, indicating an intermediate level of protein release due to degradation of the polymers at longer times. Considering that the morphology of the 25 kGy γ-irradiated microparticles (Figure 5.6b) are very similar to typical 100 kGy γ-irradiated particles; non-porous and smooth, a lower amount of release at longer times when compared to non-irradiated particles could be expected. This is a finding which is in agreement with that of Dorati *et al.* [2] who studied effect of γ-irradiation on PLGA microparticles containing ovalbumin using a combination of NMR, SEM and EPR.

Figure 5.8c shows the UV-Vis dissolution data that was obtained from 10 mg of the irradiated and un-irradiated batches from which the single microparticles of which the hGH distribution are shown in Figure 5.7, were taken. This bulk release data (Figure 5.8c) is very similar to release data obtained from single microparticles (Figure 5.8a). And, particularly if one compares release profiles of un-irradiated microparticle(s) in Figure 5.8a and Figure 5.8c, it can be seen that both data are suggesting a rapid initial release based on diffusional escape through the pores existing in the microparticles, followed by a slower sustained release based on degradation of the polymers, indicating a high encapsulation efficiency (~100% [4]).

Figure 5.8a and c also indicate that the total hGH release from the irradiated formulations is lower overall and particularly after reaching the plateau levels compared to the non-irradiated microparticle. This may be due to changes in the particle morphology, changes in the chemistry of the microparticle or some combination of the two.

Although, as discussed previously, Figure 5.8a and c show similar findings, there are also differences, mainly in that the release profile of 25 kGy irradiated single

microparticle in Figure 5.8a lies between that of the 0 and 100 kGy irradiated single microparticles whereas it is almost same as the 100 kGy irradiated batch in the UV-Vis release plot (Figure 5.8c). Moreover, the high burst release from the 100 kGy irradiated single microparticle (Figure 5.7c and the dotted profile in Figure 5.8a) is not evident in bulk release data of the batch from which this microparticle was taken (dotted profile in Figure 5.8c).

In order to investigate these two main differences between the micro and macro scale release data of irradiated samples; (i) higher amount of protein release from the 25 kGy microparticle and (ii) very high initial burst release from the 100 kGy irradiated microparticle in release data obtained from IR images in comparison to that of UV-Vis dissolution data, a solubility test of irradiated and non-irradiated pure hGH samples was conducted. It should be noted that microscopic release medium was D_2O and the macroscopic release medium was HEPES, which is more similar to H_2O than it is to D_2O resulting in the possibility that formulation might slightly be more soluble in HEPES that in is D_2O [26].
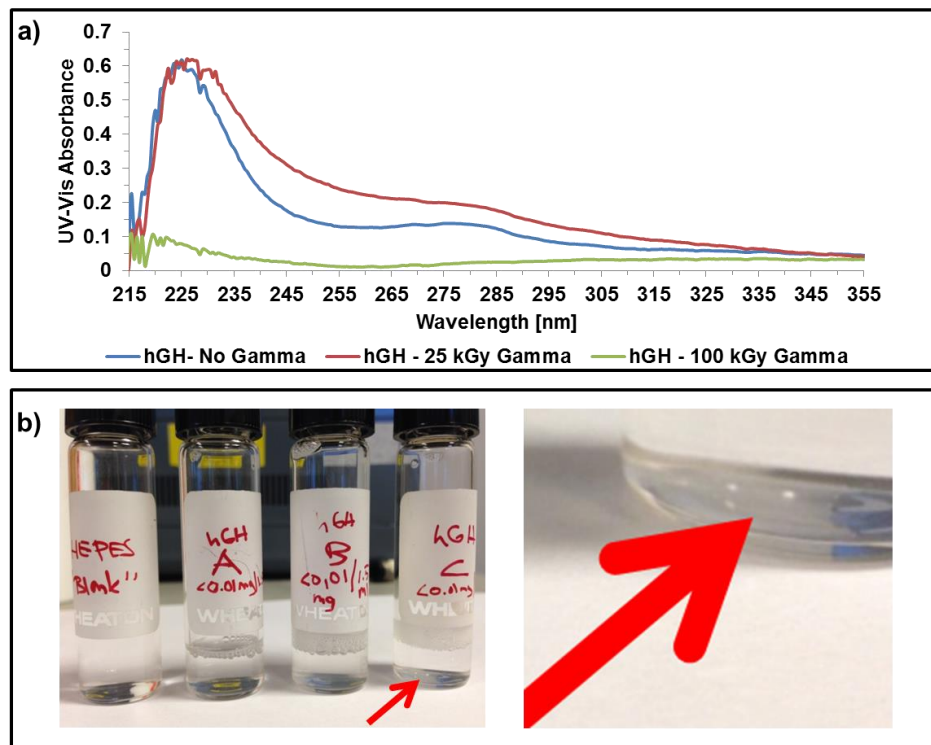
Figure 5.9 (a) Pictures of the bottles; blank (1.5 ml hepes solution only) and in which was <0.01 mg (Pure hGH)/1.5 ml hepes (b)UV-Vis spectra of non-irradiated and γ-irradiated pure hGH samples.

To determine the effect of gamma irradiation on the solubility of hGH, ~0.01 mg of protein was placed into ~1.5ml of HEPES solution at room temperature (~22 °C), stirred manually for a minute and the UV-Vis absorbance spectrum was collected, importantly, with the beam passing through the upper portion of the cuvette. Figure 5.9a shows the UV-Vis absorbance spectra (between 215-355nm) of the un-irradiated (blue), 25 kGy irradiated (red) and 100 kGy irradiated (green) hGH/HEPES samples. It should be noted that although a wide spectroscopic range was scanned (from 190 nm to 1200 nm) no absorbance was observed in any of the three hGH samples other than in the region shown in Figure 5.9a. For the non-irradiated and for 25 kGy irradiated hGH solutions, two peaks, one at ~220 nm and one at ~280 nm can easily be seen, whereas there were no absorbance peaks for the 100 kGy irradiated sample. One possible explanation for the differences between these three profiles is that there is aggregation occurring between hGH particles at the higher gamma dose, resulting in a decrease in the solubility of the protein. This is confirmed by observation of the presence of particulate matter in the bottom of the 100 kGy sample vessel. This is shown in Figure 5.9(b) and indicated by the red arrow. This simple and qualitative dissolution test was found to be rather informative in that it clearly indicates protein aggregation at higher gamma doses, a finding which could explain the observed release being proportional to the applied gamma dose as indicated in the bulk (UV-Vis) and microscale (*in situ* FTIR) release profiles.

Larger (aggregated) protein particles formed within the formulation would explain their retarded release into the solvent in proportion to the applied gamma dose. An explanation for the increase in the amount of hGH being released for the 25 kGy microparticle in the *in vivo* release profile in Figure 5.8a in comparison to UV-Vis release profile in Figure 5.8c, could be that the ATR measurement determines the quantity of material in the evanescent field, which may be somewhat different to the concentration of the material in solution. Therefore material released from the particle, but not necessarily solubilised, could be readily observed via the ATR measurement but not so via the UV-Vis release experiment. This is supported by the SEM images shown in Figure 5.6b (i), and in the SEM images in Figure 5.6b (iii and iv) and in Figure 5.6c (iii and iv) for 25 kGy and 100 kGy irradiated microparticles. In these figures, gamma irradiation appears to have induced protein migration towards the surface of the particles. And as it was mentioned previously, this would also support the findings for the 100 kGy irradiated particle release studies, where its burst release is due to surface

attached protein particles that are released rapidly in comparison to 0 and 25 kGy irradiated particles.

It is clear that both FTIR (Figure 5.11b) and UV-Vis (Figure 5.9a) spectroscopies detect all sizes of proteins, as a result of absorbances included under the Amide-I IR peak and as a result of absorbances included under the UV-Vis peaks at 220 nm and 280 nm respectively, therefore do not facilitate the discrimination of the release data based on protein size. These findings indicate protein aggregation being the cause of retardation of release from these microparticles. Therefore in the next section this is explored further.

5.3.6   The Nature of Released Species

Protein aggregation; the formation of higher molecular weight complex species such as dimers and trimers, upon heating, wetting or light exposure is a well-known phenomenon [27,28] and as discussed in Section 2.9 in Chapter 2, size exclusion chromatography is a well-established method of separating mixtures based on their size and obtaining their molecular-weight distributions. Therefore size exlusion chromatography (SEC) was used to investigate if the gamma irradiated hGH samples exhibited any differences in their size distribution.

Figure 5.10a shows the output of the SEC analysis of as received hGH that has undergone no further treatment. The output is a simple, symmetrical peak with a centre ~14.5 minutes and this can be ascribed to the hGH monomer. Figure 5.10b shows the analogous output taken from a hGH sample that has been subjected to 25 kGy gamma irradiation and the output is quite different. The peak at ~14.5 minutes is still present but there is evidence of an additional component with a peak centre ~12.9 min, that is likely to be due to dimerisation of the hGH as a direct result of gamma irradiation. Figure 5.10c shows the analogous data for a hGH sample that has been subjected to 100 kGy of gamma irradiation and here the output is very different. There are a group of complex peaks with centres at 9.6, 12.9 and 14.5 minutes and this is likely to be the result of dimer and trimer formation as a direct result of gamma irradiation.
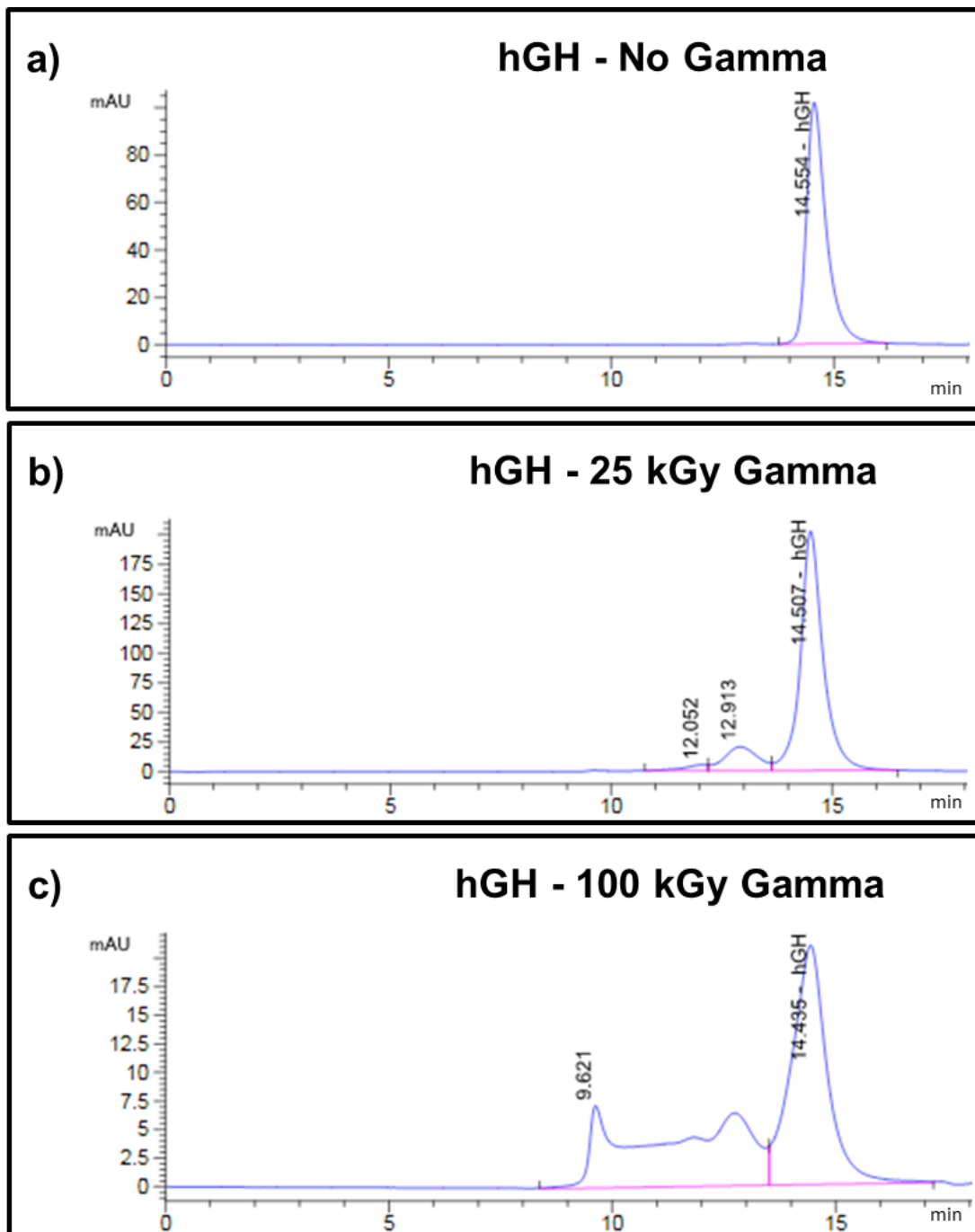
Figure 5.10 SEC analysis (at 214 nm) of non-irradiated and γ-irradiated pure hGH samples to detect formation of aggregates.

These findings not only support the supposition that protein aggregation is proportional to the applied gamma dose, but also facilitate a further step in the understanding of the comparison of UV-Vis and FTIR release profiles. Because it can be clearly seen in Figure 5.10 that the hGH monomers are present in all three hGH samples; 0, 25 and 100 kGy irradiated, however with decreasing amounts proportional to applied gamma dose. Therefore it can be anticipated that UV-Vis dissolution data of the non-irradiated formulation (Figure 5.8c (continuous line)) is only representative of hGH monomer, as

this is the only soluble species present, and also is the only species detected by SEC (Figure 5.10a.). However the bulk release profiles of the irradiated formulations in Figure 5.8c (25 kGy (dashed line) and 100 kGy (dotted line)) are representative of decreasing amount of monomers proportional to the applied gamma dose and probably dimers and trimers to a much lesser extent as a result of their high molecular size hindering their diffusion. The intense decrease in microparticle porosity and aggregation as shown in Figure 5.6b and c was also thought to have an effect on protein release, hindering the diffusion of protein molecules from irradiated formulations.

5.3.7 Effect of γ-irradiation on the Chemistry of PLGA, PLA and Poloxamer 407

Single point ATR-FTIR spectroscopy, collecting the average IR signal from a sample facilitates very high signal to noise ratio (SNR) in each spectrum when compared to imaging with an FPA IR detector, hence may provide much more detailed vibrational information that may not be readily obtained from data collected using FPA detectors in imaging mode. In order to assess the effect of γ-irradiation on the chemistry of the microparticles and therefore infer their influence on hGH release, ATR-FTIR measurements on bulk samples (both γ-irradiated and un-irradiated) were also conducted.

Figure 5.11 shows the fingerprint region (1820-1000 cm^{-1}) of ATR-FTIR spectra of the non-irradiated, 25 kGy γ-irradiated and 100 kGy γ-irradiated hGH loaded microparticles and pure components of the formulation. No noticeable change in the infrared spectra was observed as a result of being subjected to γ-irradiation on the hGH loaded microparticles, the PLGA, PLA or hGH components. (Figure 5.11a-d).

However, close inspection of the data collected from the Poloxamer 407 samples showed the appearance of a carbonyl band with increasing intensity proportional to the applied γ dose, indicating γ-irradiation induced degradation. As mentioned in Section 1.3.1.3 of Chapter 1, poloxamers are excipients that are used in drug carriers, such as PLGA micro or nano particle formulations, to enhance the release of drugs by acting as a plasticiser [20,21]. For example Yan *et al.* [20] reported that up to 20% increase in the amount of docetaxel released from PLGA microparticles is observed when compared to the same formulation without Poloxamer 188. Therefore the degradation of Poloxamer 407 is likely to have an impact on the release rate of the hGH loaded samples.
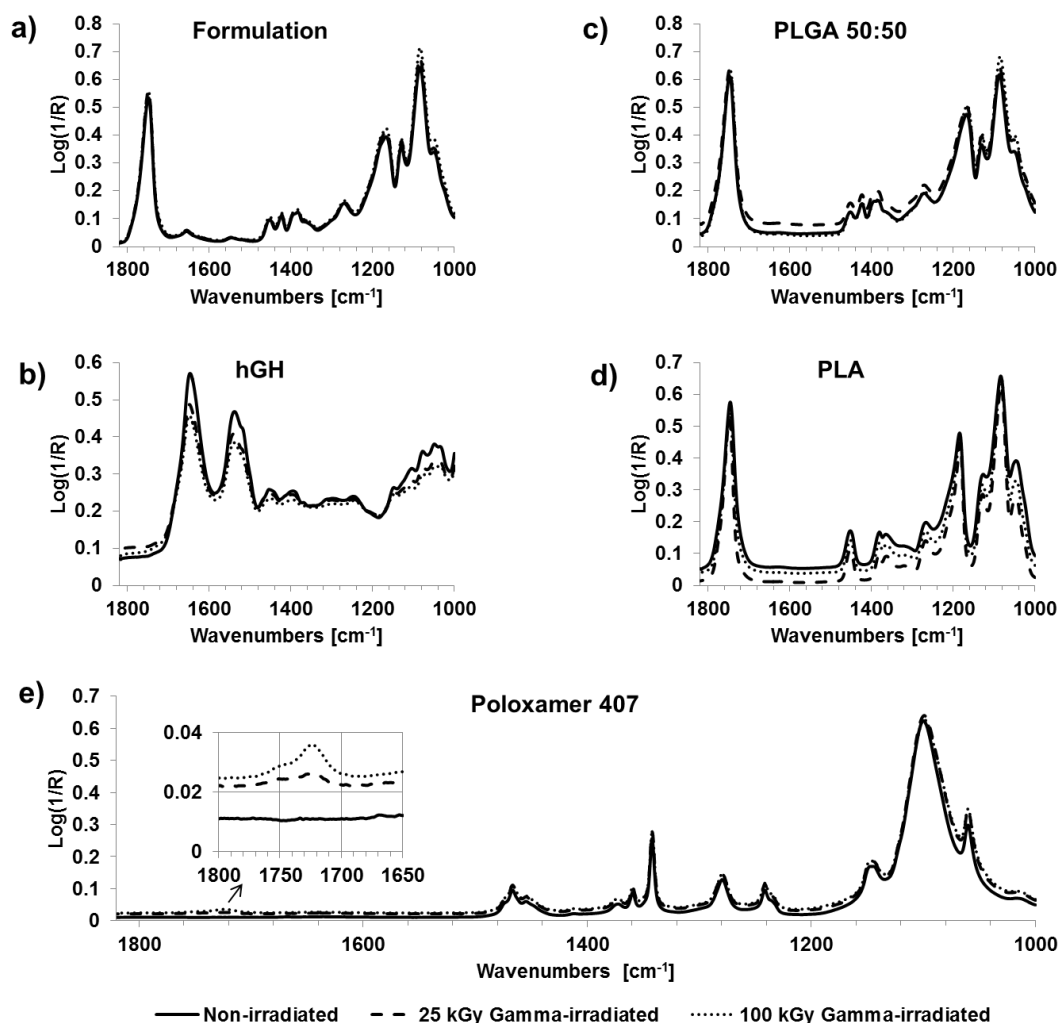
Figure 5.11 ATR-FTIR spectra of non-irradiated and γ-irradiated; formulation (a), hGH (b), PLGA50/50 (c), PLA (d) and Poloxamer 407 (e) showing the carbonyl peak occurring with increasing intensity proportional to applied gamma dose zoomed in the inset graph.

It is well known that when subjected to irradiation, polymers may undergo chain scission resulting in a decrease in their molecular weight or cross-linking. As demonstrated in the previous chapter for PLGA50/50 polymer, GPC is often used to investigate such processes, therefore we have further investigated the effect of γ-irradiation on the molecular weight of the PLA and Poloxamer 407.

The discrimination between the chain scission and the crosslinking mechanisms occurring in polymers as an effect of applied irradiation dose can be investigated numerically [1,29,30] by calculating chain scission yield G(s) and cross linking yield G(x) of polymers. A G(s)/G(x) ratio >4 has been assumed to illustrate the dominance of chain scission over crosslinking reactions in irradiated polymer samples at various doses.

Because of the limited number of irradiation data points (25 kGy and 100 kGy only) in this dataset such a calculation was not conducted, however Figure 5.12b shows the change in % M_w with respect to its original (un-irradiated) state to facilitate a better comparison in between the polymers, indicating a decrease in M_w of all three polymers and this too is a clear indication of the domination of a chain scission reaction for all 3 polymers upon irradiation. Although the M_w decrease rate (i.e. slope of a linear fit to 3 data points in the plots for each sample) for PLGA50/50 and PLA seems to be quite close in Figure 5.9b, it can be seen that the decrease in M_w of Poloxamer 407 occurs at a higher rate in comparison to PLGA50/50 and PLA. These results are in agreement of those reported by Dorati *et al*. [1] who have shown that for PEG based polymers at higher γ-irradiation doses, chain scission was the predominant process leading to a greater number of oxygenated species and shorter PEG chain lengths.
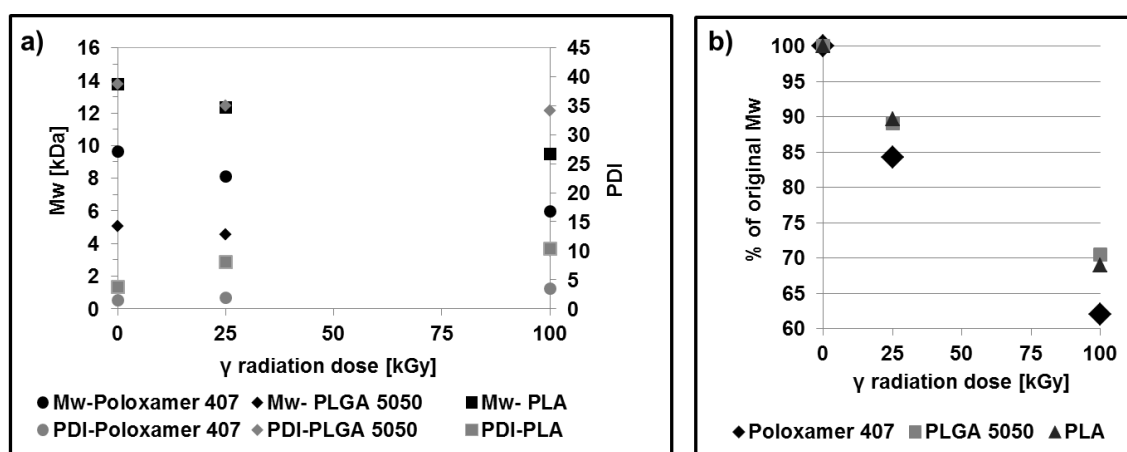
Figure 5.12 GPC results for non-irradiated and irradiated polymer samples showing the changes in M_w and PDI in (a) and % change in polymers' M_w with respect to their non-irradiated state, to facilitate better comparison in (b).

Thermal behaviour changes of the polymers were also investigated using differential scanning calorimetry (DSC) to follow the irradiation dependent polymer degradation.

Poloxamer 407

a) Un-irradiated
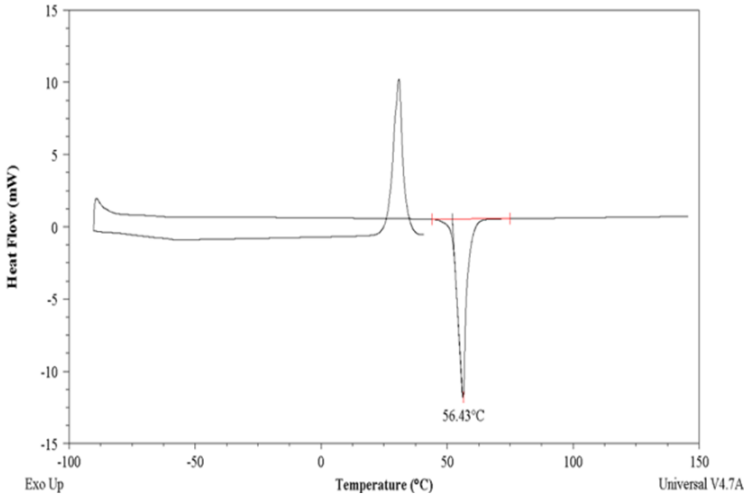
b) 25 kGy γ-irradiated

c) 100 kGy γ-irradiated

Figure 5.13 DSC thermograms for for un-irradiated (a), 25 kGy irradiated (b) and 100 kGy irradiated (c) Poloxamer 407.

PLGA50/50

a) Un-irradiated
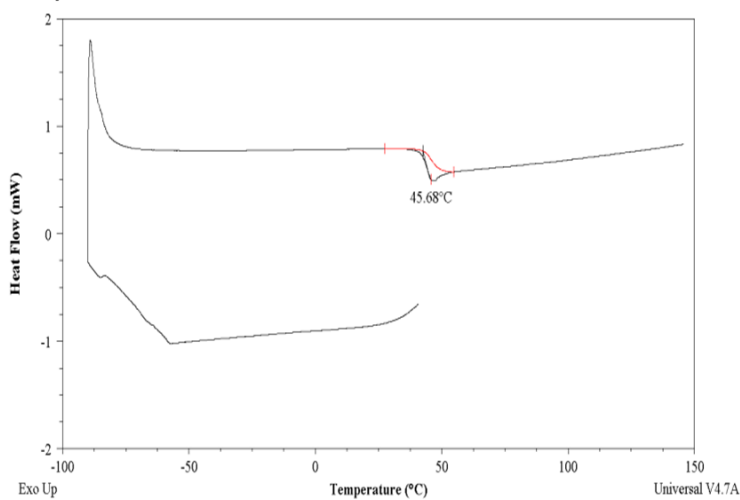
b) 25 kGy γ-irradiated

c) 100 kGy γ-irradiated

Figure 5.14 DSC thermograms for for un-irradiated (a), 25 kGy irradiated (b) and 100 kGy irradiated (c) PLGA 50/50.

155
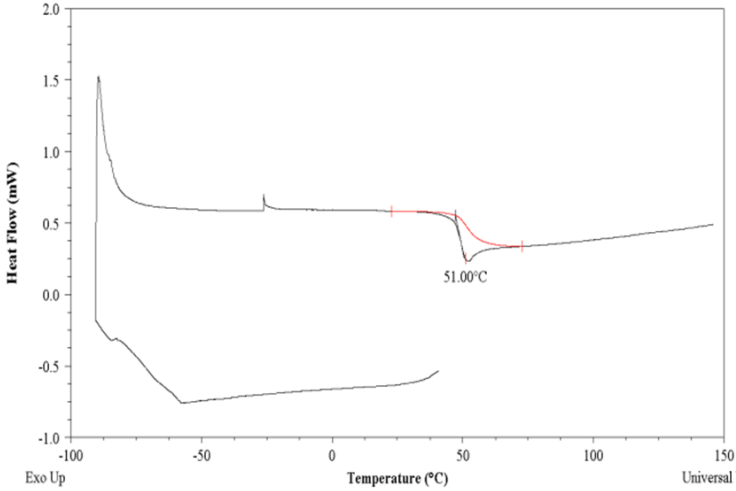
Figure 5.15 DSC thermograms for for un-irradiated (a), 25 kGy irradiated (b) and 100 kGy irradiated (c) PLA.

Formulation without hGH

a) Un-irradiated
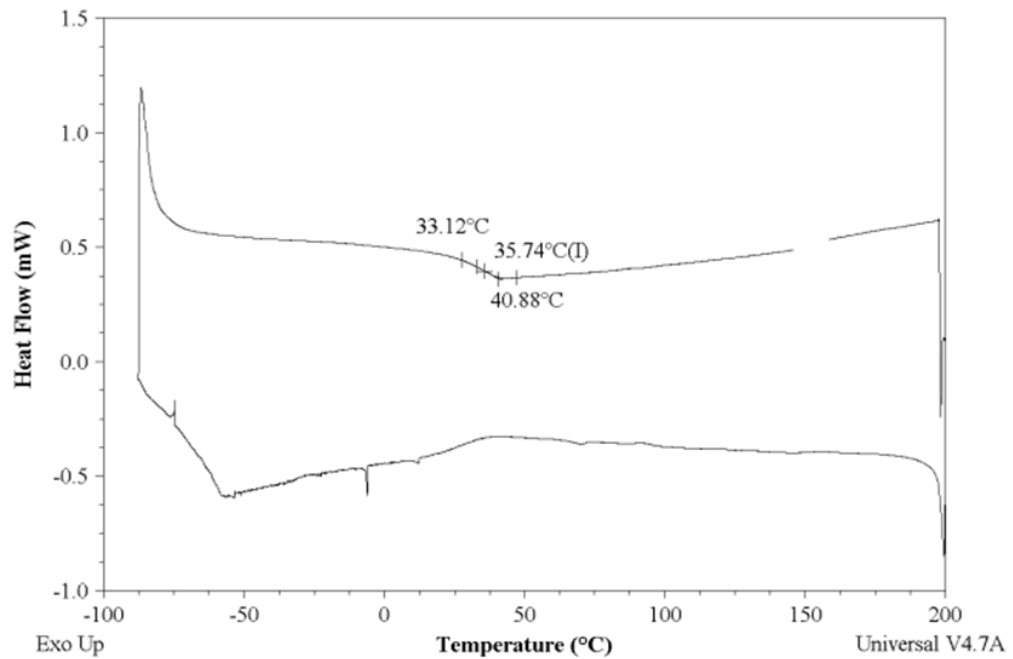
b) 25kGy and 100 kGy γ-irradiated
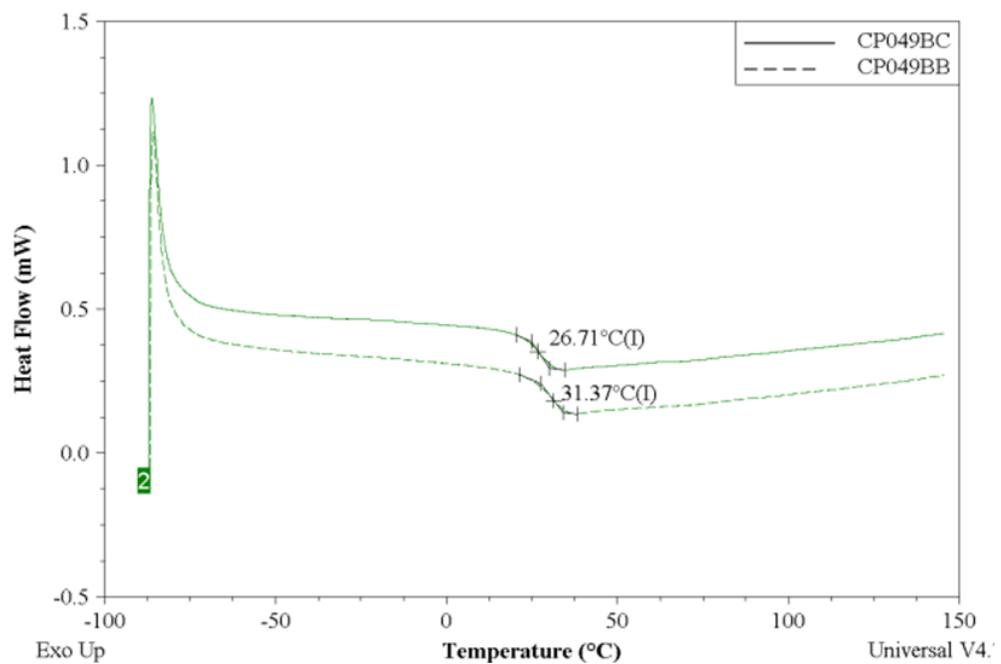
Figure 5.16 DSC thermograms for (a) non-irradiated, (b) 25 kGy irradiated (dashed line) and 100 kGy irradiated (straight line) formulation (10 wt% Poloxamer407 + 81 wt% PLGA50/50 + 9 wt% PLA) that does not contain hGH.

DSC analyses were conducted on the irradiated and un-irradiated polymers of the formulation in order to obtain more detail of the effect of irradiation process on the thermal properties of the polymers. Since we were interested in the effect of γ-irradiation on protein release from the formulation, the same formulation but without the hGH (10 wt% Poloxamer 407, 81 wt% PLGA50/50 and 9 wt% PLA) was also prepared under same processing conditions by CPL in order to investigate overall thermal properties of the polymer mixture.

Figure 5.13, Figure 5.14, Figure 5.15 and Figure 5.16 show the DSC thermograms of the irradiated and un-irradiated PLGA50/50, PLA, Poloxamer 407 and the CriticalMix^{TM} processed polymer mix without hGH respectively. The observable transitions from these figures are listed in Table 5.2a and Table 5.2b.

Table 5.2. List of glass transition temperatures of un-irradiated and γ-irradiated PLGA50/50, PLA and the formulation without hGH in (a) and list of melting temperatures of un-irradiated and γ-irradiated Poloxamer 407.

(A)	T_g (°C)	T_g (°C) after 25 kGy γ exposure	T_g (°C) after 100 kGy γ exposure
PLGA 50/50	45.7	43.4	41.9
PLA	51	50.5	48.7
Formulation without hGH	35	31	26

(B)	T_m (°C)	T_m (°C) after 25 kGy γ exposure	T_m (°C) after 100 kGy γ exposure
Poloxamer 407	30	27.9	23.8

The results listed in Table 5.2a are showing a decrease in T_g of PLGA, PLA and the polymer mix without hGH proportional to the applied gamma dose. Although PLGA and PLA polymers did not exhibit a melting temperature within the temperature range scanned as they are amorphous and they have high melting points (>200 °C), Poloxamer 407 data showed a crystallisation peak ~25 °C and a melt peak ~30 °C which is decreasing proportional to the applied gamma dose as indicated in Table 5.2b. These findings are in agreement with GPC results, indicating degradation based on a chain scission mechanism in all three polymers.

The DSC thermogram of the un-irradiated formulation Figure 5.16a has indicated a T_g of 35 °C and the DSC thermograms of the 25 kGy irradiated (dashed line) and the 100 kGy irradiated (solid line) formulations in Figure 5.16b has indicated T_gs of 31 °C and 26 °C, respectively as also listed in Table 5.2a. From this decrease in T_g of the polymer mixture, as one would expect as the formulation is dominated by PLGA/PLA, it is clear that the formulation itself is also degrading via a chain scission mechanism in the same way as the individual polymers.

Increasing the number of oxygenated species in a microparticle is likely to have a significant impact on the dynamics of hydration due to an increase in the hydrophilicity and the strength and nature of interactions occurring between the species contained within that microparticle. In this instance, the increase in the number of oxygenated species appears to have significantly increased the rate of hydration, leading to a faster and more pronounced initial burst release of hGH. The increase in the number of oxygenated species within the microparticle may also influence the strength of interactions between the polymeric species and the encapsulated hGH, leading to a retardation of the sustained release rate after the initial burst. These findings were in agreement with those of Dorati *et al*. [2] who ascribed a retardation in the release rate of OVA from γ-irradiated PLGA-PEG microspheres, when compared to their un-irradiated counterparts, to be due to a combination of changes in the morphology of the microparticles and an increase in the magnitude of the interaction between the polymer matrix and the protein. Although the system was not identical to that studied by Dorati and co-workers [2], Poloxamer 407 is a tri-block copolymer of PEG-PPG-PEG, therefore it could be anticipated that the effect of γ-irradiation on these hGH loaded microparticles would be quite similar.

5.3.8   Summary of the Findings

- Using transmission and micro ATR FTIR imaging, hGH was shown to be distributed homogenously at the surface and within the bulk of the un-irradiated, processed microparticles.
- *In situ* release profiles of the un-irradiated formulation, obtained from ATR-FTIR imaging data, have been shown to be similar to the bulk release profiles obtained by UV-Vis dissolution experiments.
- SEM images of the microparticles indicated a decrease in surface roughness, a decrease in porosity and the occurrence of aggregated surface bound

proportional to applied gamma dose. SEM images indicated that very small particles were also seen to be attached to the surface of the particles at higher irradiation doses.

- A high initial burst release from the 100 kGy irradiated microparticle was visually observed by ATR-FTIR imaging and such data was not available from bulk UV-Vis dissolution experiment. In the ATR imaging data, 25 kGy microparticle had exhibited a release profile that is between those obtained for 0 and 100 kGy irradiated microparticles however from UV-Vis dissolution data the bulk release was shown to be similar to the 100 kGy formulation.

- SEC analyses indicated protein aggregation resulting in the occurrence of dimers and trimers along with a decreasing amount of monomers proportional to the applied gamma dose.

- UV-Vis spectrophotometry of irradiated and un-irradiated hGH showed that almost no hGH was dissolved into HEPES solution when irradiated at 100 kGy dose, indicating the occurrence of large protein aggregates.

- ATR-FTIR spectroscopy showed no evidence for a change in the formulation, hGH, PLGA50/50 or PLA, but indicated degradation via the occurrence of a carbonyl band in the spectrum of Poloxamer 407 as a function of applied gamma dose.

- GPC analyses indicated a noticeable decrease in M_w of all polymers as a function of γ exposure, indicating a chain scission mechanism of gamma induced degradation.

- DSC analyses supported the finding of GPC, showing a decrease in T_g of formulation mix without protein, PLGA50/50 and PLA. Poloxamer 407 exhibited a T_m that was again decreasing proportional to γ exposure.

5.4 Conclusions

ATR-FTIR has been shown to be a successful method to monitor, *in situ*, the release of hGH from PLGA/PLA microparticles, providing important information about the mechanism of release. Utilising the chemical selectivity of the infrared methodology, hGH release profiles, analogous to those obtained using standard dissolution apparatus have been obtained for micropartcicles subjected to a range of γ-irradiation doses. The release mechanism of hGH from these microparticles has been elucidated with the release kinetics changing as a result of modifications to the microparticle morphology and chemistry during γ-irradiation. SEM analysis of the microparticles indicated that γ-

160

irradiation made them less porous, reduced the surface area and forced some material, most likely hGH to the surface of the individual microparticles. And this was thought to be the main reason for observing a high initial burst release of hGH in the 100 kGy microparticle, that was not observed by bulk dissolution measurements using UV-Vis detection. However in the IR images, the overall amount of hGH at the surface of this particle was lower than that of un-irradiated and 25 kGy irradiated microparticles, and this indicated the formation of aggregates resulting in a decrease in the overall hGH monomer concentration in the microparticle.

Another interesting finding from the IR imaging data was that the release profile of the 25 kGy irradiated microparticle was in between that of un-irradiated and 100 kGy irradiated microparticles, unlike its bulk release profile which was very similar to that of the 100 kGy irradiated batch. This was thought to be as a result of hGH aggregation and a decrease in porosity occurring as a function of applied gamma dose which was clearly indicated in the SEM images. Because the bulk microparticles were seen to be somewhat aggregated and IR imaging was applied to selected individual microparticles (i.e. not clusters), the diffusional release of hGH in the bulk measurement was hindered by high aggregation and decreased porosity. Aggregation was not occurring only between microparticles but also between hGH molecules as SEC analyses showed formation of dimers and trimers within the irradiated microparticles along with monomers. Monomers were the only hGH species observed in the un-irradiated microparticles.

GPC analyses showed a decrease in M_w of all of the polymers past gamma irradiation indicating a chain scission mechanism occurring proportional to the applied gamma dose. This gamma induced decrease in M_w was in agreement with the findings of Loo *et al.* [30] who quantitated the decrease in M_w of PLGA and PLLA films occurring proportional to applied e-beam irradiation and those of Dorati *et al.* [1] who studied gamma induced degradation of PEGd,lPLA and PEG-PLGA multiblock copolymers. The percentage of M_w reduction was more prominent for Poloxamer 407 than that of PLGA and PLA polymers. The gamma induced degradation of Poloxamer 407 was also probed by ATR-FTIR spectroscopy, although no spectroscopic change was observed for the other polymers in this system. This indicated that γ-irradiation was leading to chain scission in the Poloxamer 407 excipient, increasing the number of oxygenated species within the microparticle and influencing the strength of interactions between the entrapped hGH and the polymeric matrix. DSC analyses showed a decrease in T_g of

PLGA50/50 and PLA as well as the polymer mixture that did not contain hGH and a decrease in melting temperature of Poloxamer 407. This also indicated a gamma induced degradation of the polymers based on chain scission mechanism.

These findings were found to be in good agreement with work conducted by Dorati *et al*. [2] and Carrascosa *et al*. [25] on PLGA based microparticles containing different protein based APIs.

.

5.5   References

[1] R. Dorati, C. Colonna, M. Serra, I. Genta, T. Modena, F. Pavanetto, P. Perugini, B. Conti, gamma-irradiation of PEGd,lPLA and PEG-PLGA multiblock copolymers: I. Effect of irradiation doses, Aaps Pharmscitech. 9 (2008) 718-725.

[2] R. Dorati, I. Genta, L. Montanari, F. Cilurzo, A. Buttafava, A. Faucitano, B. Conti, The effect of gamma-irradiation on PLGA/PEG microspheres containing ovalbumin, J. Controlled Release. 107 (2005) 78-90.

[3] C. Martínez-Sancho, R. Herrero-Vanrell, S. Negro, Study of gamma-irradiation effects on aciclovir poly(d,l-lactic-co-glycolic) acid microspheres for intravitreal administration, J. Controlled Release. 99 (2004) 41-52.

[4] F. Jordan, A. Naylor, C.A. Kelly, S.M. Howdle, A. Lewis, L. Illum, Sustained release hGH microsphere formulation produced by a novel supercritical fluid technology: In vivo studies, J. Controlled Release. 141 (2010) 153-160.

[5] M.B. Sintzel, A. Merkli, C. Tabatabay, R. Gurny, Influence of Irradiation Sterilization on Polymers Used as Drug Carriers—A Review, Drug Dev. Ind. Pharm. 23 (1997) 857-878.

[6] J. van der Weerd, K.L.A. Chan, S.G. Kazarian, An innovative design of compaction cell for in situ FT-IR imaging of tablet dissolution, Vibrational Spectroscopy. 35 (2004) 9-13.

[7] C.A. Coutts-Lendon, N.A. Wright, E.V. Mieso, J.L. Koenig, The use of FT-IR imaging as an analytical tool for the characterization of drug delivery systems, J. Controlled Release. 93 (2003) 223-248.

[8] S. Sasic, Y. Ozaki, Raman, Infrared, and Near-Infrared Chemical Imaging, John Wiley & Sons, Inc., Hoboken, New Jersey, 2010.

[9] T. Ribar, J.L. Koenig, R. Bhargava, FTIR Imaging of Polymer Dissolution. 2. Solvent/Nonsolvent Mixtures, Macromolecules. 34 (2001) 8340-8346.

[10] J.F. Carpenter, J.H. Crowe, An infrared spectroscopic study of the interactions of carbohydrates with dried proteins, Biochemistry. 28 (1989) 3916-3922.

[11] T.H. Yang, A. Dong, J. Meyer, O.L. Johnson, J.L. Cleland, J.F. Carpenter, Use of infrared spectroscopy to assess secondary structure of human growth hormone within biodegradable microspheres, J. Pharm. Sci. 88 (1999) 161-165.

[12] K. Fu, K. Griebenow, L. Hsieh, A.M. Klibanov, R. Langera, FTIR characterization of the secondary structure of proteins encapsulated within PLGA microspheres, Journal of Controlled Release. 58 (1999) 357-366.

[13] M. van de Weert, R. van 't Hof, J. van der Weerd, R.M.A. Heeren, G. Posthuma, W.E. Hennink, D.J.A. Crommelin, Lysozyme distribution and conformation in a biodegradable polymer matrix as determined by FTIR techniques, J. Controlled Release. 68 (2000) 31-40.

[14] S.G. Kazarian, K.W.T. Kong, M. Bajomo, J. Van Der Weerd, K.L.A. Chan, Spectroscopic Imaging Applied to Drug Release, Food Bioprod. Process. 83 (2005) 127-135.

[15] P.S. Wray, G.S. Clarke, S.G. Kazarian, Dissolution of tablet-in-tablet formulations studied with ATR-FTIR spectroscopic imaging, European Journal of Pharmaceutical Sciences. 48 (2013) 748-757.

[16] R. Salzer, H.W. Siesler, Infrared and Raman Spectroscopic Imaging, Wiley-VCH, US, 2009.

[17] S.G. Kazarian, K.L.A. Chan, Micro- and Macro-Attenuated Total Reflection Fourier Transform Infrared Spectroscopic Imaging, Appl. Spectrosc. 64 (2010) 135A-152A.

[18] G. Thomson and G. Poulter, US Patent US20060261274 A1 (2006).

[19] M.J. Whitaker, J. Hao, O.R. Davies, G. Serhatkulu, S. Stolnik-Trenkic, S.M. Howdle, K.M. Shakesheff, The production of protein-loaded microparticles by supercritical fluid enhanced mixing and spraying, J. Controlled Release. 101 (2005) 85-92.

[20] F. Yan, C. Zhang, Y. Zheng, L. Mei, L. Tang, C. Song, H. Sun, L. Huang, The effect of poloxamer 188 on nanoparticle morphology, size, cancer cell uptake, and

cytotoxicity, Nanomedicine: Nanotechnology, Biology and Medicine. 6 (2010) 170-178.

[21] G. Dumortier, J. L.Grossiord, F. Agnely, J. C. Chaumeil, A Review of Poloxamer 407 Pharmaceutical and Pharmacological Characteristics, Pharmaceutical Research. 23 (2006) 2709-2728.

[22] H.K. Kim, T.G. Park, Comparative study on sustained release of human growth hormone from semi-crystalline poly(l-lactic acid) and amorphous poly(d,l-lactic-co-glycolic acid) microspheres: morphological effect on protein release, J. Controlled Release. 98 (2004) 115-125.

[23] V. Klang, C. Valenta, N.B. Matsko, Electron microscopy of pharmaceutical systems, Micron. 44 (2013) 45-74.

[24] J. van der Weerd, S.G. Kazarian, Combined approach of FTIR imaging and conventional dissolution tests applied to drug release, J. Controlled Release. 98 (2004) 295-305.

[25] C. Carrascosa, L. Espejo, S. Torrado, J.J. Torrado, Effect of Gamma-Sterilization Process on PLGA Microspheres Loaded with Insulin-Like Growth Factor - I (IGF-I), Journal of Biomaterials Applications. 18 (2003) 95-108.

[26] K.A. Connors, Chemical Kinetics : The Study of Reaction Rates in Solution, 1st ed., Wiley-VCH, New York, 1990.

[27] M.S. Salnikova, C.R. Middaugh, J.H. Rytting, Stability of lyophilized human growth hormone, Int. J. Pharm. 358 (2008) 108-113.

[28] M.J. Pikal, K.M. Dellerman, M.L. Roy, R.M. Riggin, The effects of formulation variables on the stability of freeze-dried human growth hormone, Pharmaceutical Research. 8 (1991) 427-436.

[29] R.L. Cleek, K.C. Ting, S. G. Eskin, A.G. Mikos, Microparticles of poly(dl-lactic-co-glycolic acid)/poly(ethylene glycol) blends for controlled drug delivery, J. Controlled Release. 48 (1997) 259-268.

[30] J.S.C. Loo, C.P. Ooi, F.Y.C. Boey, Degradation of poly(lactide-co-glycolide) (PLGA) and poly(l-lactide) (PLLA) by electron beam radiation, Biomaterials. 26 (2005) 1359-1367.

6 Overall Conclusions and Further Work

6.1 Introduction

This chapter outlines the research described in this thesis and provides an outlook on possible future work.

The aims of this thesis were to (i) develop robust and reproducible protocols to better characterise the morphological and physicochemical evolution of biopolymeric microparticles *in situ* during hydrolytic degradation, (ii) monitor protein release from such microparticle systems and (iii) determine the factors influencing release rate during dissolution. To achieve this, the following strategies were implemented;

(i)   The application of vibrational spectroscopic imaging to understand the dynamics of microparticle degradation and drug release from polymeric microparticles.

(ii)   Development and optimisation of multivariate image analysis tools for analysing the acquired mid-infrared spectroscopic images.

(iii)   The use of scanning electron microscopy and conventional bulk characterisation methods to verify and better understand findings acquired using mid-IR imaging such as morphology, polymer degradation and protein redistribution and release.

6.2 Overall Conclusions

This thesis has demonstrated that mid-IR imaging and analysis can be effectively used to study polymeric drug delivery systems that are in the form of microparticles. Valuable information such as polymer degradation and drug release was studied in real-time on a single microparticle without any chemical labels or dyes, but by utilising the chemical sensitivity and spatial selectivity of ATR imaging and analysis.

The application of real-time ATR-FTIR imaging to obtain visual evidence of hydrolysis of a single microparticle was demonstrated for the first time. A novel, partially supervised peak detecting non-linear curve fitting (NLCF) algorithm was developed to identify and fit peaks to the infrared spectrum obtained from each pixel within the acquired temporal images. The output from the NLCF was compared directly and numerically with the traditional peak height (PH) data analysis approach and multivariate curve resolution alternating least squares (MCR-ALS) analysis for the same images. Quantitative information such as hydrated layer size, FWHM of the

particle was shown to be calculated with smaller errors when multivariate analyses were employed. Both multivariate approaches considered, hard (NLCF) and soft (MCR-ALS), improved the spatial resolution of the images compared to peak height measurements. The MCR-ALS method was influenced by colinearity, therefore degradation rates could not be calculated from MCR-ALS data. However, the spatial resolution of the wet images were close to those determined from NLCF processed ones and therefore considering the time penalty of the NLCF procedure, a combination of MCR-ALS and NLCF analysis was considered to be applied for larger data sets.

Using the protocol developed in Chapter 3, the effect of $scCO_2$ process, γ-irradiation (a common sterilisation method), monomer ratio and temperature on the hydrolysis of a family of PLGA microparticles was investigated to facilitate a better understanding of the physiochemical factors effecting the hydrolysis rate and changes in morphology of the PLGA polymers by which drug release behaviour is governed. A noticeable decrease in hydrated layer size was observed for the $scCO_2$ processed PLGA 50/50 microparticles at 50 °C compared to those of at 70 °C. The degradation rate constants for glycolic and lactic units of PLGAs were shown to stay at a constant ratio (~1.3) regardless of composition, temperature or γ exposure. Degradation rate was seen to increase with increasing initial glycolic content of the copolymer or with increasing temperature or with increasing γ exposure. GPC and DSC analysis showed a decrease in molecular weight of PLGA 50/50 indicating a chain scission mechanism proportional to applied γ dose. SEM images indicated a decrease in surface roughness and particle aggregation proportional to the applied γ dose. There was some evidence of lactic acid monomers diffusing out into water during the hydrolysis of PLA microparticles.

The real-time release of hGH from a group of PLGA/PLA microparticles that included Poloxamer 407 excipient during a set of dissolution experiments at 37 °C in D_2O were studied by ATR-FTIR imaging. It was found difficult to deconvolute all of the components in this complex system using multivariate analysis tools previously investigated due to high overlapping and low loadings of the components within the finger print region however second derivative peak height analysis was found to provide sufficient contrast in PLGA/PLA and hGH images and facilitated obtaining hGH release profiles, analogous to those obtained using standard dissolution apparatus.

Using ATR-FTIR imaging, increasing the γ dose was shown to have a profound influence on the nature of the release mechanism, with higher γ doses leading to a

dramatic increase in the initial burst release followed by retardation in the sustained release and a lower total level of hGH release over the dissolution experiment.

SEM analysis of the microparticles indicated that γ-irradiation made them less porous, and lumpy. SEC analyses showed formation of hGH dimers and trimers within the irradiated microparticles along with hGH monomers. hGH monomers were the only species observed in un-irradiated microparticles. SEM images also indicated that microparticles tend to aggregate upon irradiation. This information is important because bulk measurements would be effected by this due to reduction in the surface area of the microparticles as they aggregate, and this has once more indicated the importance of microscopic information that could be obtained from single microparticles.

GPC and DSC analyses showed a decrease in M_w of all of the polymers post γ irradiation, indicating a chain scission mechanism occurring as a function of the applied γ dose. The percentage of M_w reduction was more prominent for Poloxamer 407 than that of PLGA and PLA polymers. The γ induced degradation of Poloxamer 407 was also probed by ATR-FTIR spectroscopy, although no change was observed in the spectra of the other polymers in this system. This indicated that γ-irradiation was leading to chain scission in the Poloxamer 407 excipient, increasing the number of oxygenated species within the microparticle and influencing the strength of interactions between the entrapped hGH and the polymeric matrix. These findings suggested that;

(i) Gamma sterilisation doses >25 kGy should be avoided due to shown adverse effects and the required dose should be optimised to ensure that morphological and chemical changes are kept minimum post γ-irradiation.

(ii) Although gamma irradiation is the most common sterilisation method for such biopolymer based microparticle systems, other methods, such as e-beam irradiation which may create less adverse effects on the morphology and stability of the formulations, could be considered.

(iii) The excipient, Poloxamer 407, was shown to degrade remarkably even after 25 kGy γ-irradiation. Inorder to overcome the stability issues addressed for the studied formulation, other excipients which may show greater resistance to γ-irradiation compared to Poloxamer 407 could be studied.

6.3 Further Work

6.3.1 FTIR Imaging of Microparticles

Since most pharmaceuticals are in the form of microparticles and information such as drug loading per microparticle is very important in characterisation, the possibility of studying a single microparticle during a kinetic process such as degradation for a PLGA microparticle as demonstrated here, providing wealth of chemical and morphological information could be taken further by investigating many other microparticulate systems. Transflection or transmission IR imaging of microtomed sections, as well as micro-ATR imaging of flash frozen and cracked opened sections coupled with relevant multivariate analysis tools could certainly provide key information between different formulations even at dry stage in comparison.

6.3.2 Multivariate Analysis of FTIR Images for Studying Kinetic Processes in Microparticle Systems

Spectroscopic deconvolution is an interesting area of analytical microscopy and spectroscopy, bringing several disciplines together including mathematics, statistics and chemistry. In this thesis, components of a microparticle system that has been undergoing hydrolysis have been shown to successfully deconvoluted or separated within the temporal image sets.

Since the NLCF procedure developed in this thesis uses a peak shape function that can simulate a peak shape that is between a straight line and a needle, it should certainly be further applied to other systems, particularly to systems that cannot be deconvoluted by soft modelling tools. And for systems such as PLGA/PLA formulation that included a low loading of hGH and Poloxamer 407, the use of genetic algorithms should be considered to better optimise fitted parameters. This would require more processing time however parallel computing could be used to decrease the NLCF processing time down to a few minutes.

Another strategy to deconvolute this formulation or any other difficult formulation could be applying the same experimental procedure on components, i.e. acquiring real time images of hGH, Poloxamer etc. on its own, and using these component spectra at each time point of the images of the formulation. A linear regression using fitted component spectra to the formulation spectra at each time point may then provide deconvoluted images with a true contrast. However this would require more experiment time (i.e. number of components x time required per micro-dissolution experiment)

which was therefore not feasible to do during this work but such idea may be feasible for studying relatively faster processes.

6.3.3   Real-time Monitoring of Polymer Degradation Using FTIR Imaging

Physiochemical evolution of a family of PLGAs were characterised in terms of their degradation rates and size during hydrolysis. Although lactic acid was probed after ~48 h of for a PLA microparticle, this was not possible to do for other formulations studied. This was thought to be due to the rather large size of the ATR dissolution cell (an 18 mm high, 20 mm wide cylinder) used and the large volume of water (~2 ml).

A much smaller cell (2 mm x 2 mm x 1 mm) that only covers the ATR crystal could be designed for such experiments, which would certainly increase the chances of having reduced circulation thereby increasing the possibility of keeping mobile molecules within the field of view.

The decrease in M_w of PLGA upon γ irradiation was demonstrated. Therefore implementing a flow cell on to the ATR accessory with very low flow speed could also be used in line with gel permeation chromatography facilitating probing different degradation products that would provide information on effect of processes such as irradiation etc.

6.3.4   Real-time Monitoring of Drug Release Using FTIR Imaging

HPLC-SEC analysis indicated protein aggregation and formation of hGH dimers and trimers post γ- irradiation. Due to the time constraints detailed image analyses were not conducted on deconvoluting protein secondary structure and second derivative spectra did not facilitate discrimination between hGH monomers, dimers and trimers which were all detected by IR.

Although it was possible to conclude that aggregated protein molecules were not being released but monomers were, it is still an unknown whether at any stage during the real-time 'micro' dissolution experiment, if dimers and/or trimers were actually being released too. Therefore a flow cell fitted on to the ATR accessory and the use of very low flow velocity could also be used in line with a HPLC-SEC system in order to answer this question.

Due to the time constraints, the effect of storage conditions (i.e. relative humidity, temperature) was not studied during this work. Further research could be conducted on the formulation studied here and certainly with formulations including different

amounts and/or types of excipients because Poloxamer 407 was shown to degrade at a great extent compared to other components of the formulation. The effect of excipients on real-time *in situ* protein release could be conducted using the ATR-FTIR imaging methodology developed in this thesis.

SEM was shown to provide valuable information on the morphology of the microparticles at 20 nm spatial resolution that was not possible even by micro ATR imaging (~5 μm). However considering the sample preparation procedure, i.e. coating with gold, and the effect of e-beam radiation on the samples, although minimal, atomic force microscopy (AFM) could also be used to characterise the morphology. Particularly, the postulated protein redistribution towards the sample surface, induced by gamma irradiation, could be better characterised by AFM.

Further work could also include investigating the distribution and nature of the microparticles and the protein(s) within the microparticles with in tissue after injection. Tissue sections could easily be imaged non-distructively by FTIR imaging in transmission or transflection modes which could be used to probe the microparticles within tissue and release and redistribution of proteins therein.
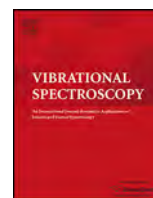
Word Count

The word count of this thesis is 43,258.

Appendix

PAPER I

Studying the release of hGH from gamma-irradiated PLGA microparticles using ATR-FTIR imaging ☆

Hakan Keles [a], Andrew Naylor [b], Francis Clegg [a], Chris Sammon [a],*

[a] Sheffield Hallam University, Materials and Engineering Research Institute, Sheffield S1 1WB, United Kingdom
[b] Critical Pharmaceuticals Limited, BioCity, Pennyfoot Street, Nottingham NG1 1GF, United Kingdom

ABSTRACT

Attenuated total reflection-Fourier transform infrared (ATR-FTIR) imaging has been applied for the first time to monitor the redistribution and release of hGH from a range of PLGA/PLA microparticles during a set of dissolution experiments at 37 °C in D_2O. The effect of gamma-irradiation, a common sterilisation method, on hGH release kinetics from such systems has been demonstrated. Increasing the gamma dose was shown to have a profound influence on the nature of the release mechanism, with higher gamma doses leading to a dramatic increase in the initial burst release followed by a retardation in the sustained release and a lower total level of hGH release over the dissolution experiment. These changes were shown to be the result of a combination of factors; firstly, *via* scanning electron microscopy (SEM), gamma-irradiation was shown to strongly influence the morphology of the PLGA/PLA microparticles; reducing their overall porosity and reducing the available surface area, whilst forcing some of the entrapped hGH to the microparticle surface. Secondly, from FTIR measurements, gamma-irradiation was shown to increase the number of oxygenated components in the Poloxamer 407 excipient, by a process of chain scission, thereby increasing the strength of interaction between the microparticle and the entrapped hGH.

© 2014 Published by Elsevier B.V.

1. Introduction

Peptides and proteins cannot readily be delivered by traditional routes such as by oral, nasal or pulmonary delivery due to their high molecular weight, hydrophilicity and labile nature. Consequently such drugs are normally administered by injection to therapeutically tackle a number of conditions. To treat growth hormone (hGH, a 22 kDa protein) deficiency in children with hypopituitary disorders and in adults, this normally results in the need for daily injections for a period of several years which is particularly challenging for children. Encapsulation of drugs such as proteins in biodegradable polymer matrices, such as PLGA for sustained release, offers a solution to the problem of delivery of drugs effectively to the patient with minimal inconvenience and also controlling drug's release into the body over time, thereby removing the necessity for frequent administration and improving patient compliance and treatment efficacy.

A sustained release formulation of hGH can be achieved by its encapsulation into injectable microparticles of biodegradable and biocompatible polymers such as PLGA or PLA. After injection the encapsulated microparticle slowly releases the hGH *via* a degradation mechanisms of the polymer to lactic or glycolic acid which are rapidly cleared from the body *via* the renal system.

To date solvent-based methods such as emulsification have been most often used to manufacture PLGA based microparticle drug delivery systems. However, the use of solvents can lower the biological activity of any encapsulated protein or peptide through degradation at phase boundaries [1]. One route to overcome these difficulties is to use supercritical carbon dioxide ($scCO_2$) that removes the need for solvents during processing, such as in the PGSS (particles from gas saturated solutions) method for the production of sustained release systems including polymer matrix microparticles [2]. Novel sustained release formulations of hGH prepared by supercritical fluid processing of PLGA/PLA (the CriticalMix™ process) were produced in the form of microparticles for subcutaneous injection [3]. We have taken a formulation that has been evaluated *in vivo* in rats and monkeys, showing up to two weeks more of efficacious hGH release compared to a daily injection of soluble hGH, and investigated its real time release using ATR-FTIR imaging for the first time. This study also evaluates the effect of γ-irradiation on the physical and chemical structure of the

microparticles and attempts to draw links between chemical and morphological changes and the *in vivo* release of the entrapped hGH from single microparticles.

Pharmaceutically relevant microparticles for parenteral use must be well characterised in terms of their size range, morphology and function. It is widely understood that the chemistry and morphology of microparticles have a degree of interdependence as the morphology of microspheres can vary depending on their chemical state after preparation. This therefore can strongly affect drug release behaviour from microspheres [4–6].

Often, pharmaceuticals have to be sterilised before use and for polymeric microparticle drug delivery systems, γ-irradiation is a well-established method to achieve this [6,7]. Prior to sterilisation of pharmaceutical products using γ-irradiation, it is essential to determine any effects that this process may have on the materials, as each polymer reacts differently to ionising radiation. Therefore the maximum dose that can be administered to sterilise the product must to be validated.

Fourier transform infrared (FTIR) spectroscopic imaging facilitates spatiotemporal images of individual components of multicomponent systems under dynamic conditions such as dissolution [8]. It has become a popular spectroscopic imaging approach, particularly for pharmaceutical research, as it allows not only monitoring the physical and chemical changes of individual components over time, but also gives quantitative information such as drug release rate and polymer matrix degradation rate from the same experiment [8–10].

Collecting thousands of IR spectra simultaneously using a 2D focal plane array detector in which each pixel acts as an individual detector, a stack of 2D images at a range of mid-IR energies can be generated within a few minutes.

The application of the attenuated total reflectance (ATR) sampling technique in FTIR imaging has been increasingly reported particularly in pharmaceutical research [11,12] as it is advantageous compared to transmission and transflection FTIR mainly in that the shallow (2–10 μm) depth of penetration (*i.e.* the depth at which the electric field amplitude is attenuated to e^{-1} of its initial value at the sample surface) of IR light in to the sample facilitates the visualisation of formulations within aqueous media (as the water bands cannot suppress the signal from the sample as a result of this shallow penetration depth) and species can be probed in their natural state as no sample preparation is necessary [13].

Micro-ATR-FTIR imaging with a Ge internal reflection element (IRE) provides higher spatial resolution when compared to transmission and transflection measurements but with a much smaller field of view [14]. Consequently, ATR-FTIR imaging in macro mode in which the infrared beam from the spectrometer is passed through the IRE and collected at the FPA without the use of a microscope is more convenient compared to micro-ATR as it provides a larger field of view and readily facilitates the use of a temperature controlled environment for studying dynamic systems [15].

FTIR spectroscopy has been used for studying the interactions of carbohydrates with dried proteins [16], assessing the integrity of the hGH encapsulated in PLGA by spray-freeze-drying and water-in-oil-in-water double emulsion methods [17] and assessing the effect of excipients in lysozyme and BSA loaded microspheres prepared by a double-emulsion technique [18]. The lysozyme distribution in microtomed PLGA microspheres prepared by a w-o-w solvent evaporation method has been studied by FTIR imaging in transmission mode and the second derivative protein amide I band images shown a homogenous distribution of protein [19]. The use of real time FTIR imaging for characterisation of a drug delivery system [9] and dissolution of tablets [20,21] has been demonstrated. Although distinct sample-solvent interfaces along one axis of the field of view were monitored and release and redistribution of various active pharmaceutical ingredients (APIs) were

investigated in these FTIR imaging studies, there is no literature regarding demonstration of the application of real time FTIR imaging to (i) study the release of proteins or peptides from biodegradable microparticles *in situ* and (ii) the assessment of the effect of γ-irradiation on stability of PLGA microparticles and on the release of the protein from the microparticles, therefore our study aims to address these aspects of vibrational spectroscopy applied to pharmaceutical research. Generally, kinetic processes such as release (including the burst release phenomenon, which is critically important for assessing sustained release from drug delivery devices) and matrix degradation in protein based API loaded biopolymer microparticles are monitored by a combination of various conventional methods including; differential scanning calorimetry (DSC), gel permeation chromatography (GPC), x-ray diffraction and infrared (IR) absorption spectroscopies [6], nuclear magnetic resonance (NMR) and electron paramagnetic resonance (EPR) spectroscopies [5] and UV–vis spectrophotometry [3] on bulk samples (*i.e.* multiple microparticles). This paper demonstrates the possibility of obtaining such important quantitative chemical information by using FTIR spectroscopic imaging alone on a single microparticle which allows the morphological visualisation of the kinetic processes involved, which is not available by bulk methods.
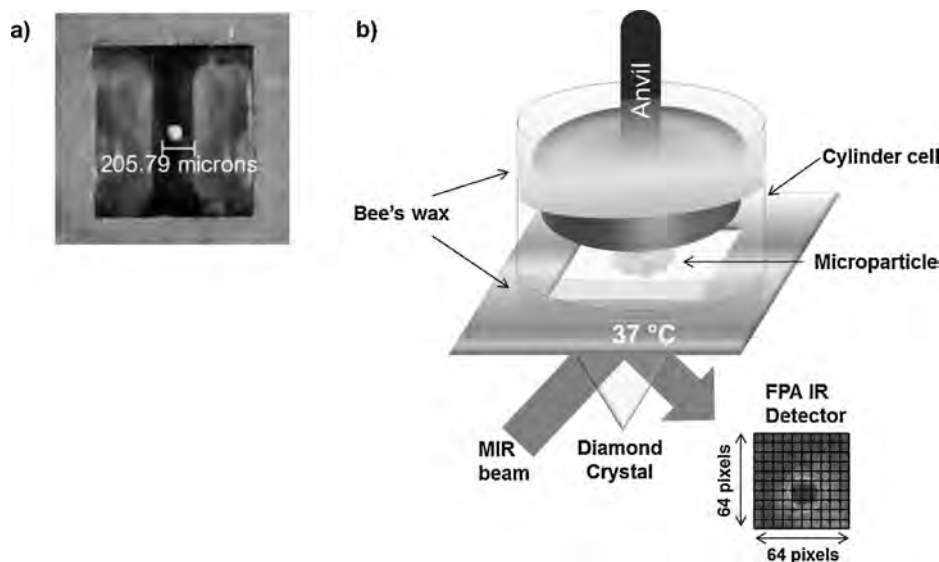
2. Experimental

2.1. Materials

PLGA RG502H (50:50 lactide:glycolide, I.V. 0.16–0.24, Bohringer-Ingleheim) with an inherent viscosity of 0.16–0.24 dl/g, PLA R202H (100:0 lactide:glycolide, I.V. 0.16–0.24, Bohringer-Ingleheim), with an inherent viscosity of 0.16–0.24 dl/g, pharmaceutical grade CO_2 (BOC Special Gasses) were used as received. hGH was kindly donated by Bioker (Sardinia, Italy) and Poloxamer 407 (Lutrol® F127) was obtained from BASF (Ludwigshafen, Germany). D_2O (613398-10G, min. 99.996 atom) and bee's wax (243248-100G) were purchased from Sigma–Aldrich Company Limited, UK. Technovit 7100 embedding resin kit was purchased from Kulzer & Co., Germany.

2.2. Preparation of microparticles using scCO₂ processing

The method of PGSS (particles from gas saturated solutions) uses the ability of scCO₂ to depress the glass transition and melting temperature of biodegradable polymers at ambient temperatures and moderate pressures. scCO₂ acts effectively as a molecular lubricant, thus liquefying polymers at temperatures significantly lower than those typically needed. The near ambient temperatures together with the absence of any aqueous or organic solvents makes the PGSS method particularly suited to the processing of thermally or solvent labile proteins and peptides, with the advantage that they can be encapsulated with 100% efficiency with no protein degradation or loss of activity.

A formulation of hGH loaded PLGA/PLA microparticles were prepared using a CriticalMix™ process by adding 2 g of pre-weighed combination of spray dried hGH (10%, w/w of the formulation), PLGA and PLA in 90:10 ratio respectively (81%, w/w of the formulation) and GRAS excipient, Poloxamer407 (9%, w/w of the formulation), to the PGSS apparatus which was sealed and pressurised with CO₂ to 700 psi (48 bar) and once heated to above 32 °C the pressure was increased to 2030 psi (140 bar). The scCO₂ was dissolved into the liquefied mixture which was then stirred at 150 rpm for 1 h, after which time stirring was stopped and the homogenous mixture was depressurised through a nozzle generating free flowing microparticles into a collection chamber [3].

Fig. 1. (a) White light image of a microparticle placed on the ATR crystal prior to starting the experiment. (b) Schematic of the dissolution experiment; the anvil applies sufficient pressure to ensure good contact between the particle and the ATR crystal, whilst making sure D_2O can only access the particles from the sides.

2.3. Sample preparation for micro-ATR-FTIR imaging

hGH loaded PLGA/PLA microparticles were embedded in a hydroxyethyl methacrylate based resin (Technovit 7100) as described by van de Weert et al. [19] and sliced to 4 μm thickness using a Reichert-Jung Ultracut E ambient ultramicrotome with a glass knife.

2.4. Scanning electron microscopy

To obtain topographic contrast of the microspheres before and after irradiation, scanning electron microscopy (SEM) was performed using a FEI NOVA 200 NanoSEM. Images were formed using the secondary electron signal with a spatial resolution of ~2 nm. The sample was sprinkled onto an adhesive carbon tab on an aluminium stub and sputter coated with gold (~20 nm) in an Argon atmosphere.

2.5. γ-Irradiation

Raw polymers and scSO$_2$ produced microparticle formulations were irradiated by using ^{60}Co as irradiation source (Synergy Health PLC, Swindon, UK) at a few kGy/h dose rates ensuring a targeted total dose in accordance with the ISO 11137 standard. The sample temperature was kept at near room temperature during irradiation using thermometric controls. 30 mg of the polymer samples were sealed in a glass container and irradiated at 25 and 100 kGy total dose in air.

2.6. ATR-FTIR spectroscopy

ATR-FTIR spectra were collected on a Thermo Nicolet Nexus instrument as single beam spectra by co-adding 128 scans at a spectral resolution of 4 cm^{-1} and ratioed against the single beam spectrum of the blank ATR crystal at room temperature.

2.7. Micro-ATR-FTIR imaging

Micro-ATR-FTIR images were collected with the setup that consists of an Agilent 680-IR FT-IR spectrometer operating in rapid scan mode attached to an Agilent 620-IR microscope with a Ge ATR crystal fitted on to a 15× Cassegrain objective and a liquid nitrogen cooled mercury cadmium telluride focal plane array detector MCT-FPA (64 × 64 pixels).

Images were collected with a 4 cm^{-1} spectral resolution in the mid-infrared range (3800–950 cm^{-1}) co-adding 64 scans for both background (Ge crystal in air) and samples. The high refractive index (4) of the germanium crystal allowed a spatial resolution of ~4 μm within the ~64 μm × 64 μm field of view for this setup.

2.8. Macro-ATR-FTIR imaging of drug release from individual microparticles

Mid-infrared (3800–950 cm^{-1}) spectroscopic imaging data in Macro-ATR mode were acquired using an Agilent 680-IR FT-IR spectrometer attached to a large sample (LS) external compartment holding a Golden Gate^{TM} Imaging Single Reflection ATR Accessory (Specac Ltd.) which has a Diamond internal reflection element with corrective optics that adjusts the plane of best focus to sit on the crystal surface minimising any distortion. The infrared beam from the spectrometer was projected directly on to a liquid nitrogen cooled MCT-FPA (64 × 64 pixels, 10 μm × 10 μm pixel size) after passing through the ATR sampling accessory. This ATR-FTIR imaging setup was capable of simultaneously collecting 4096 spectra from an image area of 640 μm × 640 μm with an angle of incidence of the infrared beam of 45° and numerical aperture (NA) of 0.32.

A single microparticle was placed on to the centre of the square surface of the ATR crystal with the aid of a 40× binocular microscope. A uniform contact between the particle and the crystal with minimal deformation was obtained applying sufficient pressure to the auto-level sapphire anvil [22]. Minimal deformation was ensured, such that the same particle could be picked up using the same needle without leaving any residue on the ATR crystal. After collecting a 'dry' image at 37 °C, ~2 ml of D_2O that had been pre-heated to 37 °C was injected into the cell in such a way that access to the particle was limited to the sides only as shown in Fig. 1. The raw images were collected in rapid scan mode taking ~5 min using the Agilent Technologies' ResolutionsPro FTIR Spectroscopy software version 5.2.0(CD846) with 128 co-added scans at an 8 cm^{-1} spectral resolution, and processed by ratioing against a background of the blank ATR crystal with 256 co-added scans also collected at 37 °C.
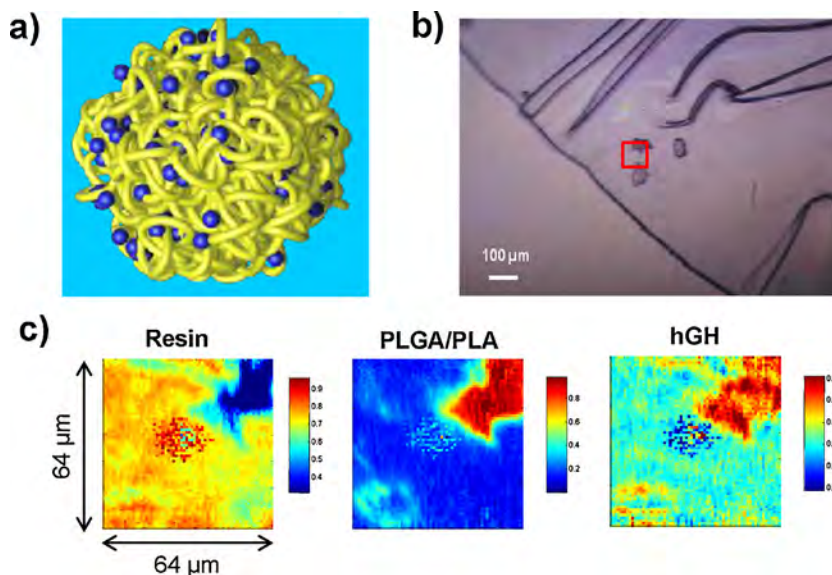
Fig. 2. (a) An illustration of a typical, CriticalMix™ processed microparticle where strands represent mixed polymers and dots represent the homogenously distributed hGH particles. (b) White light image of 3 microparticles embedded in resin and microtomed to 4 μm thickness (c) Micro ATR (Ge) peak height images from the area shown with the box in the white light image, showing resin (1724 cm^{-1}), PLGA/PLA (1755 cm^{-1}) and hGH (1650 cm^{-1}) from left to right respectively.

2.9. Data processing

Hyperspectral image cubes were processed using Malvern Instruments' ISys 5.0 chemical imaging software. Raw processed image files were cropped between 1820 and 1000 cm^{-1}, a region which contains a number of characteristic bands associated with PLGA/PLA polymers, protein amide I band ∼1650 cm^{-1} and the δ(OD) band of D$_2$O at ∼1207 cm^{-1}.

A Savitzky–Golay second derivative with a polynomial order of 3 and filter length of 29 was applied to cropped imaging data in order to eliminate baseline drift. Second derivative images were then vector normalised in order to remove systematic discrepancies such as variations in detector sensitivity or sample contact and therefore to minimise intensity (Log(1/R)) variance.

3. Results and discussion

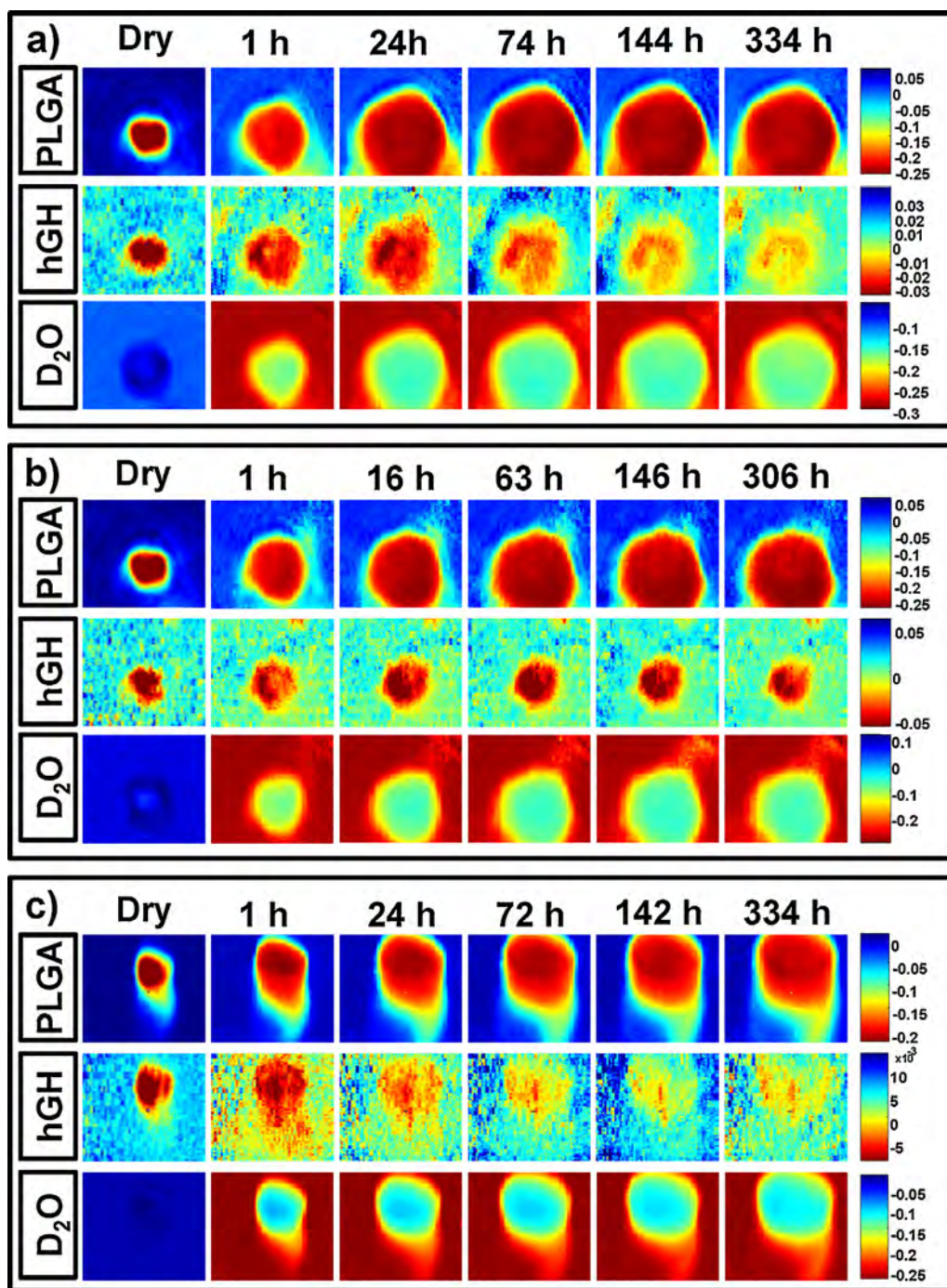ATR-FTIR spectroscopy facilitates the generation of chemical fingerprints of individual species and permits the monitoring of reaction and/or release kinetics due to the fact that unique molecular vibrations within a mixture can be assigned to different components within that mixture. As the evanescent wave effectively limits sample thickness, strongly absorbing molecules such as water can be observed facilely and this opens up the opportunity to observe systems where a sample is placed in contact with an aqueous medium. FTIR imaging permits the collection of temporal images of such multicomponent systems in aqueous media in which changes in the chemistry of such species can be spatially resolved in real time. In pharmaceutical research, this hyperspectral imaging approach using non-destructive IR light, particularly in ATR mode requiring no sample preparation or the use of dyes or chemical labels, is a unique toolbox for formulation design allowing characterisation of static samples, with as high as ∼4 μm spatial resolution in micro mode, whilst facilitating the monitoring of dynamic physical and chemical changes occurring within formulations [10].

The CriticalMix process is thought to produce an homogenous distribution of API throughout the porous microparticles as

Table 1
Vibrational assignments for PLGA 50/50, PLA, Poloxamer 407, resin, D$_2$O and hGH within the finger print region (1820–1000 cm^{-1}); as antisymmetric, s symetric, δ bending, ρ rocking, ν stretching, τ twisting, ω wagging, all given in cm^{-1}.

PLGA	PLA	hGH	Poloxamer 407	Resin	D$_2$O	Assignment
1745	1745			1727		ν(C=O)
		1658				Amide I, ν(C=O)
				1635		δ(OH)
		1540				Amide II, δ(NH)
1452	1450	1450	1466	1484		δ_{as}(CH$_3$)
1422				1450		δ(CH)
1394		1394		1395		ω(CH)
1381	1379		1374			δ_s(CH$_3$)
1360	1362	1304	1359, 1341	1323		δ(CH)
1270	1266		1280, 1241	1274, 1249		τ(CH$_2$)
		1245				ν_{as}(PO)
					1207	δ(OD)
1167	1184	1146	1144, 1100	1154		ν_{as}(COC)
1131	1127					ρ_{as}(CH$_3$)
		1104				ν_s(PO)
1086	1084	1077		1074		ν_s(COC)
1048	1045	1049	1059	1020		ν(C—CH$_3$)
		990				ν_s(PO)
957	957	942	962	948		ρ (CH$_3$)

Fig. 3. False colour ATR-FTIR images of (a) non-irradiated, (b) 25 kGy γ-irradiated and (c) 100 kGy γ-irradiated microparticles showing second derivative peak height distribution of PLGA at 1755 cm^{-1}, hGH at 1650 cm^{-1} and D$_2$O at 1207 cm^{-1} as a function of time.

depicted in the illustration in Fig. 2(a). This was evaluated by microtoming a 4 μm section of a group of microparticles within an embedding medium highlighted by the red box in Fig. 2(b). Using mid-IR imaging in micro-ATR mode utilising a Ge ATR crystal which provided a spatial resolution of ~4 μm within ~64 μm × 64 μm field of view, the distribution of polymer and API within these particles was determined.

Table 1 shows the list of important peaks included in finger-print region of the ATR-FTIR spectra obtained from pure samples. From this table, it can be seen that the most intense poloxamer 407 peaks overlap with PLGA/PLA peaks however very strong peaks are readily available at discrete wavenumbers for the rest of the

samples. Also it will be discussed later on in the macro-ATR images, the δ(OD) of D$_2$O also becomes distinct when a second derivative is applied.

Fig. 2(c) shows the integrated peak height distribution of the resin at 1727 cm^{-1}, PLGA/PLA at 1755 cm^{-1} and hGH at 1650 cm^{-1} from left to right respectively. The distribution of PLGA/PLA and hGH, middle and right hand side images in Fig. 2(c) respectively, clearly show a good correlation between the high intensity (red) regions of PLGA/PLA and hGH. This is in contrast to the resin distribution, which shows an anti-correlation to both components. This is strong evidence of the homogenous distribution of hGH protein with in the PLGA/PLA microparticle layer.
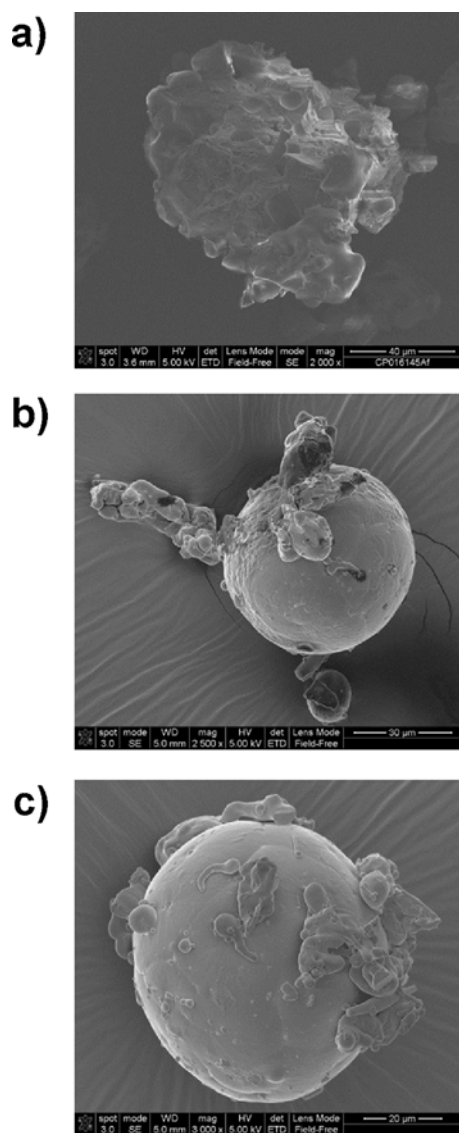
Fig. 4. SEM images showing typical (a) non-irradiated, (b) 25 kGy and (c) 100 kGy γ-irradiated microparticles.

FTIR imaging in macro-ATR mode has been demonstrated to facilitate imaging a variety of temporal information such as the morphological evaluation of different components, redistribution and/or release of species at polymer/solvent interfaces and the occurrence of new species during chemical reactions under the conditions of interest [10,12,15,23]. However release of active pharmaceutical ingredients (APIs) form single polymeric microparticles and monitoring the redistribution of API 'inside' a microparticle has not previously been studied by ATR-FTIR imaging.

To investigate the morphological and chemical evolution of a protein loaded polymeric microparticle in real time using ATR-FTIR imaging in macro mode and to explore the effect of γ-irradiation on such protein loaded PLGA/PLA microparticles, we have taken 3 single microparticles that had been subjected to γ-irradiation at doses of 25 and 100 kGy, as well as a control sample (same formulation without γ-irradiation) and monitored their interaction with water as a function of time at 37 °C. The experiment is setup in such a way that the interaction between the particle and water will only occur at the interfaces that we are monitoring, effectively creating a 2D experiment.

Fig. 3(a) shows six false colour images obtained by plotting the intensity distribution of the PLGA/PLA ester carbonyl (1755 cm^{-1}), protein (hGH) Amide I (1650 cm^{-1}) and D$_2$O δ(OD) (1207 cm^{-1}). The first column of images show the distribution of polymer, hGH and D$_2$O, respectively, before the dissolution experiment was started and are therefore labelled 'dry'. From these 'dry' images a homogenous distribution of hGH within the polymer matrix can be observed once again, complementing the micro-ATR image of the sliced sample shown in Fig. 2(c). Therefore we have confidence that the surface (up to ~10 μm) we are probing with IR light in this experiment is representative of internal structure of the microparticle, as expected from the CriticalMix^{TM} manufacture of drug loaded microparticles [2,3].

The first row of images shown in Fig. 3(a) shows the change in the distribution of the PLGA/PLA component of the control, *i.e.* un-irradiated, hGH loaded PLGA/PLA microparticle. To a first approximation this set of images can be used to monitor the dimensional changes of the microparticle during the dissolution experiment. In the PLGA/PLA image collected after 1 h, image set there is evidence of an interface layer of hydrated PLGA/PLA around the particle even at this short time, with a decreasing D$_2$O concentration from the aqueous dissolution medium towards the particle centre and some evidence of particle swelling. Within 24 h the PLGA/PLA microparticle (red) appears to have swollen further, becoming larger, whilst still being surrounded by a hydrated PLGA/PLA layer (yellow), and over time the size of the particle stays almost the same in terms of visual representation. The bottom row of Fig. 3(a), shows the complementary image data set of D$_2$O distribution as a function of time. These images show a strong anti-correlation with the PLGA/PLA image dataset and verify the significant amount of swelling in this system, as one might expect, due to the inclusion of the excipient Poloxamer 407 at 9% (w/w) in the formulation, making the microparticles more hydrophilic [24,25]. It is worth noting that after ~1 h, D$_2$O is present, albeit at a low level, everywhere within the particle, almost certainly due to a combination of the particle hydrophilicity and its porosity. Over the duration of this experiment (334 h, ~14 days) we cannot observe any major evidence of 'shrinking' of the PLGA/PLA particle, implying this observation would require a much longer sampling period, perhaps several months at 37 °C. This not only shows the well-documented suitability of PLGA and PLA to act as biodegradable drug carriers, providing sustained release for several weeks to months, but also suggests that protein release from this system is dominated by diffusion rather than erosion, during the first 2 weeks, which may be expected due to the system being porous. The hGH distribution images (middle row, Fig. 3(a)), were generated by plotting the Amide I peak height at ~1650 cm^{-1}, show a change in the distribution at short times (<24 h) as the polymers are initially swollen and this is followed by a gradual decrease of overall hGH intensity distribution as a function of time. It is worth noting that the dimensions of the hGH rich region are somewhat smaller than their polymer and D$_2$O counterparts. One explanation for this is that the hGH is being lost into the D$_2$O media at the interfaces.

Fig. 3(b) shows the equivalent false colour infrared images for the data described in Fig. 3(a), obtained from a hGH loaded PLGA/PLA microparticle that has been subjected to 25 kGy γ-irradiation. The PLGA/PLA and D$_2$O distribution maps are quite similar to those shown in Fig. 3(a), and the hGH distribution images are once more much smaller than both the polymer and D$_2$O images. Any change to the colour intensity of the hGH rich region as a function of time after 24 h is more difficult to ascertain by visual inspection.

Fig. 3(c) shows analogous image data sets for a hGH loaded PLGA/PLA microparticle that has been subjected to 100 kGy γ-irradiation, and although at first glance the polymer and D$_2$O
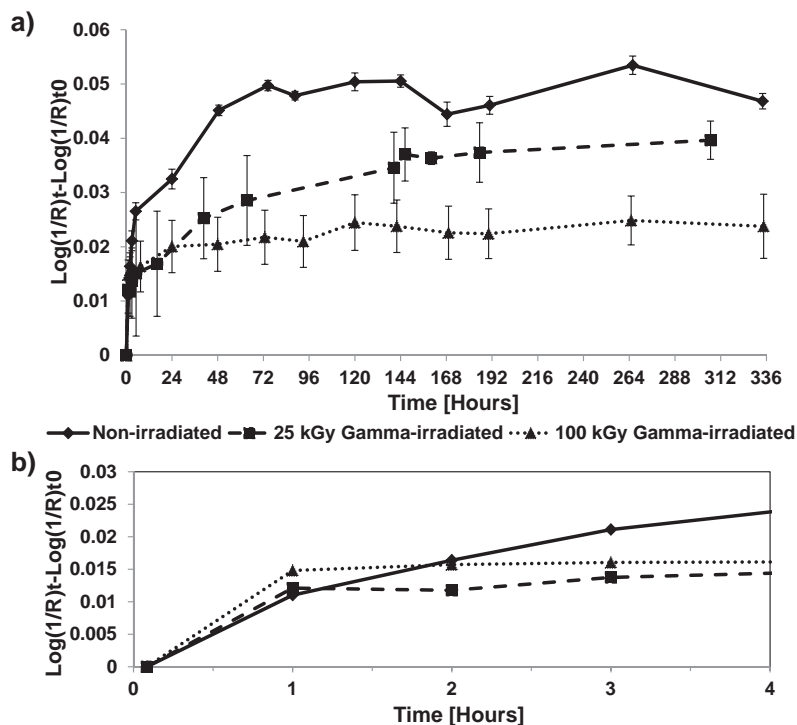
Fig. 5. (a)Release profiles obtained from 5 × 5 pixels regions of images of non-irradiated and γ-irradiated microparticles undergoing dissolution. Error bars indicate standard deviation between 3 ROIs used to obtain each data point.(b) The first 4 h data shown in (a), to provide clarity error bars are removed.

distribution images look similar to those depicted in Fig. 3(a) and (b), a remarkable rapid release of hGH around the microparticle can be seen in the 1 h image and to a lesser extent, in 24 h image, this may be due to the hGH being dissolved in the surrounding media during the ensuing 23 h. The subsequent time resolved hGH distribution maps contain fewer red pixels (*i.e.* high intensity regions) within the hGH images compared to the earlier time points, therefore it can be assumed that the most of hGH has been released during this initial hydration process; the so called burst release effect. Subsequent time resolved images show a slow reduction in intensity of the hGH distribution maps. Closer inspection of the D_2O distribution maps, show a higher concentration of D_2O (as denoted by the blue/green colour) within the body of the microparticle from 1 h when compared to both the un-irradiated and 25 kGy γ-irradiated hGH loaded microparticles.

It is clear that both geometry and morphology could have a strong influence on the release characteristics of a hGH loaded polymer microparticle, with porosity in particular likely to determine the rate of hydrolytic degradation and therefore drug release from such systems [26]. SEM was used to explore the morphology of the non-irradiated and irradiated microparticles. SEM is a tool that is readily applied to the microscopic characterisation of particles and other polymer surfaces [27].

Fig. 4 shows the SEM images of (a) non-irradiated, (b) 25 kGy γ-irradiated and (c) 100 kGy γ-irradiated microparticles. There are clear differences in morphology between the different microparticles, the γ-irradiated particles have a smooth surface and appear to be non-porous but with significant amounts of irregular particles, possibly hGH, attached to the surface. However the non-irradiated particle has a rough, non-uniform and porous morphology with inherently higher surface area than the γ-irradiated microparticles.

The use of FTIR imaging data to monitor drug release has been validated previously using an experimental setup that combined a UV detector to monitor the release of API from a tablet subjected to water flow during macro ATR-FTIR imaging and compared this

to conventional dissolution test data of the same sample type [28]. Release profiles obtained from the two methods were shown to be very similar. By conducting measurements *in situ* using FTIR imaging, we can follow chemical changes by monitoring specific IR bands of components in a fixed area in a temporal image set and quantify the relative amount of that species released during a dissolution process. In each set of temporal images; non-irradiated, 25 kGy irradiated and 100 kGy irradiated, we have chosen 3 square regions (50 μm × 50 μm) of interest (ROI) from hGH rich zones within the microparticles by visually assessing the 1 h images in each data set. By calculating the decrease in area under amide-I peak at ~1650 cm^{-1} in the binned, normalised temporal spectra from the ROIs we can generate a release profile by assuming the decrease in hGH signal at time = t (compared to hGH signal at time = 0) is proportional to hGH released at that time point. Using this approach it is feasible to generate a dissolution plot that is analogous to a release profile from a standard USP I UV-dissolution experiment.

Fig. 5(a) shows the 3 release profiles obtained from temporal image sets of 0, 25 kGy and 100 kGy γ-irradiated hGH loaded microparticles shown in Fig. 3(a), (b) and (c), respectively, including additional time points for images not shown. Data points in Fig. 5(a) are generated from the average of overall intensity from the 3 binned and normalised ROIs and error bars indicate standard deviation. It is evident that in Fig. 5(a) for all three release profiles there are two distinct regions; firstly a rapidly increasing initial period followed by a second phase that almost represents a first order line profile with a slope close to zero.

In Fig. 5(b), this initial period in Fig. 5(a) up to 4 h, is plotted once again for better visualisation for evaluation of the burst release phenomenon. The release profile from the non-irradiated hGH loaded microparticle is showing an initial burst within the first few hours followed by a slower rate release for the duration of the experiment reaching a plateau sometime after ~72 h. This release profile, obtained from a single microparticle, is very similar to the release profile obtained by standard dissolution testing using UV detection [3] for the 10 mg of a similar formulation, both suggesting a
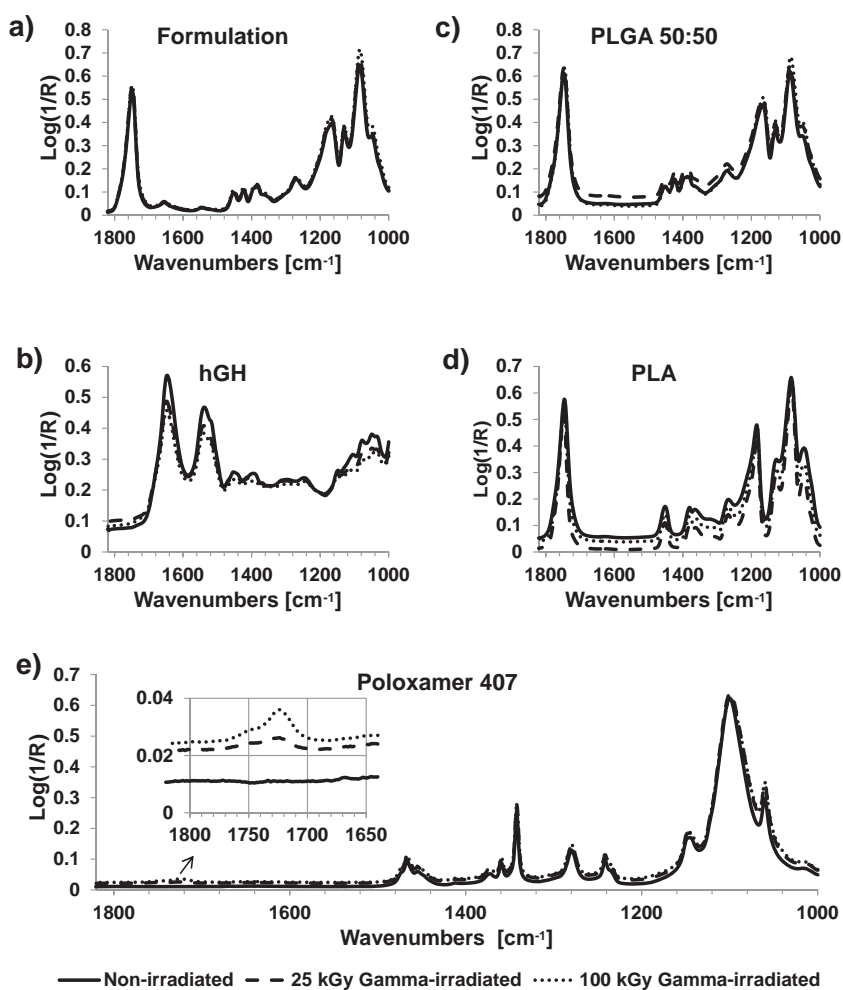
Fig. 6. ATR-FTIR spectra of non-irradiated and γ-irradiated; (a)formulation, (b)hGH, (c)PLGA50/50, (d)PLA and (e)Poloxamer 407.

rapid initial release based on diffusional escape through the pores existing in the microparticles, followed by a slower sustained release based on degradation of the polymers, indicating a high encapsulation efficiency (∼100% [3]).

Fig. 5(a) also indicates that the total hGH release from the irradiated formulations is lower overall and particularly after reaching the plateau levels compared to the non-irradiated microparticle. This may be due to changes in the particle morphology, changes in the chemistry of the microparticle or some combination of the two.

The hGH release profile from the hGH loaded PLGA/PLA microparticle which has undergone 100 kGy irradiation, once again, shows a markedly high initial burst release particularly within the first 2 h (Fig. 5(b)) which was also evident in Fig. 3(c) in the 1 h image compared to the rest of the images in that row, indicating an immediate and high release of hGH that is too fast to be a polymer degradation or diffusion controlled. γ-irradiation causing this kind of an increased burst effect was also reported by Carrascosa et al. [29] who investigated recombinant human insulin-like growth factor-I (rhIGF-I) release from PLGA microspheres by SEM, UV-dissolution and differential scanning calorimetry (DSC). It is also evident from the SEM images that the 100 kGy irradiated hGH loaded microparticle has a smooth surface and appears have a non-porous morphology (Fig. 4(c)) compared to the very porous non-irradiated particle (Fig. 4(a)), therefore the initial burst from 100 kGy γ-irradiated particle is likely to be occurring due to surface bound hGH, that is made available at the surface of the microparticle during the γ-irradiation process. Unlike both the un-irradiated

and the 25 kGy γ-irradiated sample, following its burst release, the 100 kGy γ-irradiated formulation shows zero measurable release after 48 h. For the non-irradiated and 25 kGy γ-irradiated microparticles it takes about up to 3 days for this to be the case. It is also worth remarking that the total amount of hGH that is being released after the initial burst appears to be much less than is observed in the other microparticles.

The release from the 25 kGy γ-irradiated formulation shows similarities to both the non-irradiated and the 100 kGy γ-irradiated microparticles; its initial burst profile is similar to the 100 kGy γ-irradiated formulation, indicating high protein availability at its surface, but it takes longer to reach a plateau similarly to that observed in the non-irradiated microparticle and the total amount of protein released appears to be in between that of non-irradiated and 100 kGy γ-irradiated samples, indicating an intermediate level of protein release due to degradation of the polymers at longer times. Considering the morphology of the 25 kGy γ-irradiated microparticles (Fig. 4(b)) being very similar to typical 100 kGy γ-irradiated particles; non-porous and smooth, a lower amount of release at longer times when compared to non-irradiated particles could be expected. This is a finding which is in agreement with that of Dorati et al. [5] who studied effect of γ-irradiation on PLGA microparticles containing ovalbumin using a combination of NMR, SEM and EPR.

Single point ATR-FTIR spectroscopy, collecting the average IR signal from a sample facilitates very high signal to noise ratio (S/N) in each spectrum when compared to imaging with an FPA

IR detector, hence may provide much more detailed vibrational information that may not be readily obtained from data collected using FPA detectors in imaging mode. Therefore in order to assess the effect of γ-irradiation on the chemistry of the microparticles and therefore infer their influence on hGH release, we also conducted ATR-FTIR measurements on bulk samples (both γ-irradiated and un-irradiated).

Fig. 6 shows the fingerprint region ($1820–1000\,cm^{-1}$) of ATR-FTIR spectra of the non-irradiated, 25 kGy γ-irradiated and 100 kGy γ-irradiated hGH loaded micropartcles and pure components of the formulation. No noticeable change in the infrared spectra was observed as a result of being subjected to γ-irradiation on the hGH loaded microparticles, the PLGA, PLA or hGH components. (Fig. 6 (a)–(d)).

However, close inspection of the data collected from the Poloxamer 407 samples showed the appearance of a carbonyl band with increasing intensity proportional to the applied γ dose, indicating γ-irradiation induced degradation. Poloxamers are excipients that are used in drug carriers, such as PLGA micro or nano particle formulations, to enhance the release of drugs [24,25]. Therefore the degradation of Poloxamer407 is likely to have an impact on the release rate of the hGH loaded samples. When subjected to γ-irradiation, polymers may undergo chain scission or cross-linking. Dorati et al. [4] have shown that for PEG based polymers at higher γ-irradiation doses, chain scission is the predominant process leading to a greater number of oxygenated species and shorter PEG chain lengths. Increasing the number of oxygenated species in a microparticle is likely to have a significant impact on the dynamics of hydration due to an increase in the hydrophilicity and the strength and nature of interactions occurring between the species contained within that microparticle. In this instance, the increase in the number of oxygenated species appears to have significantly increased the rate of hydration, leading to a faster and more pronounced initial burst release of hGH. The increase in the number of oxygenated species within the microparticle may also influence the strength of interactions between the polymeric species and the encapsulated hGH, leading to a retardation of the sustained release rate after the initial burst. These findings are in agreement with those of Dorati et al. [5] who ascribed a retardation in the release rate of OVA from γ-irradiated PLGA-PEG microspheres, when compared to their un-irradiated counterparts, to be due to a combination of changes in the morphology of the microparticles and an increase in the magnitude of the interaction between the polymer matrix and the protein. Although our system is not identical to that studied by Dorati and co-workers [5], Poloxamer 407 is a tri-block copolymer of PEG-PPG-PEG, therefore we can anticipate the effect of γ-irradiation on these hGH loaded microparticles to be quite similar.

4. Conclusions

ATR-FTIR has been shown to be a successful method to monitor, *in situ*, the release of hGH from PLGA/PLA microparticles, providing important information about the mechanism of release. Utilising the chemical selectivity of the infrared methodology, hGH release profiles, analogous to those obtained using standard dissolution apparatus have been obtained for microparticles subjected to a range of γ-irradiation doses. The release mechanism of hGH from

these microparticles has been elucidated with the release kinetics changing as a result of modifications to the microparticle morphology and chemistry during γ-irradiation. SEM analysis of the microparticles indicated that γ-irradiation made them less porous, reduced the surface area and forced some material, most likely hGH to the surface. FTIR-ATR analysis of the individual microparticle components, indicated that γ-irradiation was leading to chain scission in the Poloxamer 407 excipient, increasing the number of oxygenated species within the microparticle and influencing the strength of interactions between the entrapped hGH and the polymeric matrix. These findings are in good agreement with work conducted by Dorati et al. [5] and Carrascosa et al. [29] on PLGA based microparticles containing different protein based APIs.

References

[1] C. Wischke, S.P. Schwendeman, Int. J. Pharm. 364 (2008) 298–327.
[2] M.J. Whitaker, J. Hao, O.R. Davies, G. Serhatkulu, S. Stolnik-Trenkic, S.M. Howdle, K.M. Shakesheff, J. Control. Release 101 (2005) 85–92.
[3] F. Jordan, A. Naylor, C.A. Kelly, S.M. Howdle, A. Lewis, L. Illum, J. Control. Release 141 (2010) 153–160.
[4] R. Dorati, C. Colonna, M. Serra, I. Genta, T. Modena, F. Pavanetto, P. Perugini, B. Conti, AAPS PharmSciTech 9 (2008) 718–725.
[5] R. Dorati, I. Genta, L. Montanari, F. Cilurzo, A. Buttafava, A. Faucitano, B. Conti, J. Control. Release 107 (2005) 78–90.
[6] C. Martíínez-Sancho, R. Herrero-Vanrell, S. Negro, J. Control. Release 99 (2004) 41–52.
[7] M.B. Sintzel, A. Merkli, C. Tabatabay, R.t. Gurny, Drug Dev. Ind. Pharm. 23 (1997) 857–878.
[8] T. Ribar, J.L. Koenig, R. Bhargava, Macromolecules 34 (2001) 8340–8346.
[9] C.A. Coutts-Lendon, N.A. Wright, E.V. Mieso, J.L. Koenig, J. Control. Release 93 (2003) 223–248.
[10] S.G. Kazarian, K.L.A. Chan, Macromolecules 36 (2003) 9866–9872.
[11] K.L.A. Chan, S.G. Kazarian, Vib. Spectrosc. 35 (2004) 45–49.
[12] R. Salzer, H.W. Siesler, Infrared and Raman Spectroscopic Imaging, Wiley-VCH, US, 2009.
[13] N.J. Everall, I.M. Priestnall, F. Clarke, L. Jayes, G. Poulter, D. Coombs, M.W. George, Appl. Spectrosc. 63 (2009) 313–320.
[14] S.E. Glassford, L. Govada, N.E. Chayen, B. Byrne, S.G. Kazarian, Vib. Spectrosc. 63 (2012) 492–498.
[15] K.L.A. Chan, S.G. Kazarian, Appl. Spectrosc. 64 (2010) 135A–152A.
[16] J.F. Carpenter, J.H. Crowe, Biochemistry 28 (1989) 3916–3922.
[17] T. Yang, A. Dong, J. Meyer, O.L. Johnson, J.L. Cleland, J.F. Carpenter, J. Pharm. Sci. 88 (1999) 161–165.
[18] K. Fu, K. Griebenow, L. Hsieh, A.M. Klibanov, Robert Langera, J. Control. Release 58 (1999) 357–366.
[19] M. van de Weert, R. van't Hof, J. van der Weerd, R.M.A. Heeren, G. Posthuma, W.E. Hennink, D.J.A. Crommelin, J. Control. Release 68 (2000) 31–40.
[20] S.G. Kazarian, K.W.T. Kong, M. Bajomo, J. Van Der Weerd, K.L.A. Chan, Food Bioprod. Process. 83 (2005) 127–135.
[21] P.S. Wray, G.S. Clarke, S.G. Kazarian, Eur. J. Pharm. Sci. 48 (2013) 748–757.
[22] G. Thomson, G. Poulter, US Patent US20060261274 A1 (2006).
[23] J. van der Weerd, K.L.A. Chan, S.G. Kazarian, Vib. Spectrosc. 35 (2004) 9–13.
[24] F. Yan, C. Zhang, Y. Zheng, L. Mei, L. Tang, C. Song, H. Sun, L. Huang, Nanomed. Nanotechnol. Biol. Med. 6 (2010) 170–178.
[25] G. Dumortier, J.L. Grossiord, F. Agnely, J.C. Chaumeil, Pharm. Res. 23 (2006) 2709–2728.
[26] H.K. Kim, T.G. Park, J. Control. Release 98 (2004) 115–125.
[27] V. Klang, C. Valenta, N.B. Matsko, Micron 44 (2013) 45–74.
[28] J. van der Weerd, S.G. Kazarian, J. Control. Release 98 (2004) 295–305.
[29] C. Carrascosa, L. Espejo, S. Torrado, J.J. Torrado, J. Biomater. Appl. 18 (2003) 95–108.

PAPER II

The application of non-linear curve fitting routines to the analysis of mid-infrared images obtained from single polymeric microparticles†

Hakan Keles,[a] Andrew Naylor,[b] Francis Clegg[a] and Chris Sammon*[a]

For the first time, we report a series of time resolved images of a single PLGA microparticle undergoing hydrolysis at 70 °C that have been obtained using attenuated total reflectance-Fourier transform infrared spectroscopic (ATR-FTIR) imaging. A novel partially supervised non-linear curve fitting (NLCF) tool was developed to identify and fit peaks to the infrared spectrum obtained from each pixel within the 64×64 array. The output from the NLCF was evaluated by comparison with a traditional peak height (PH) data analysis approach and multivariate curve resolution alternating least squares (MCR-ALS) analysis for the same images, in order to understand the limitations and advantages of the NLCF methodology. The NLCF method was shown to facilitate consistent spatial resolution enhancement as defined using the step-edge approach on dry microparticle images when compared to images derived from both PH measurements and MCR-ALS. The NLCF method was shown to improve both the S/N and sharpness of images obtained during an evolving experiment, providing a better insight into the magnitude of hydration layers and particle dimension changes during hydrolysis. The NLCF approach facilitated the calculation of hydrolysis rate constants for both the glycolic (k_G) and lactic (k_L) acid segments of the PLGA copolymer. This represents a real advantage over MCR-ALS which could not distinguish between the two segments due to colinearity within the data. The NLCF approach made it possible to calculate the hydrolysis rate constants from a single pixel, unlike the peak height data analysis approach which suffered from poor S/N at each pixel. These findings show the potential value of applying NLCF to the study of real-time chemical processes at the micron scale, assisting in the understanding of the mechanisms of chemical processes that occur within microparticles and enhancing the value of the mid-IR ATR analysis.

Introduction

Multivariate analysis of hyperspectral imaging data is a rapidly developing research field and has received considerable attention over the last decade.[1] Hyperspectral images that provide spatial and spectral information at the same time in an array of pixels and an individual pixel, respectively, can be obtained by a number of techniques including, X-ray tomography,[2] X-ray fluorescence,[3] Raman microscopy,[4] and near infrared (NIR) imaging.[5]

Over the last two decades Fourier transform infrared (FTIR) spectroscopic imaging has become routine, facilitating chemical characterization of multicomponent systems under both

[a]Sheffield Hallam University, Materials and Engineering Research Institute, Sheffield, S1 1WB, UK. E-mail: C.Sammon@shu.ac.uk; Fax: +44 (0)114 225 3501; Tel: +44 (0) 114 225 3069

[b]Critical Pharmaceuticals Limited, BioCity, Pennyfoot Street, Nottingham, NG1 1GF, UK

† Electronic supplementary information (ESI) available. See DOI: 10.1039/c3an01879b

static and kinetic conditions.[6,7] Currently more than 80% of all pharmaceutical formulations are delivered in a powder format[8] and attenuated total reflectance (ATR) mode has proved advantageous, particularly for pharmaceutically relevant systems, because the sample can be in any phase, form or shape therefore no sample preparation is necessary.[9] Micro-ATR-FTIR imaging with a germanium objective provides a higher spatial resolution compared to transmission and transflection due to the effective magnification imparted by the high refractive index of the ATR crystal material. Conveniently, ATR-FTIR imaging in macro mode, i.e. without the use of a microscope, provides a temperature controlled environment for studying dynamic systems with a larger field of view.[10] In the macro ATR mode, kinetic processes can be probed with IR light such that each of the 2D array of pixels of the focal plane array detector acts as an individual detector, allowing the collection of thousands of IR spectra simultaneously. Consequently, a stack of 2D images at a range of IR wavelengths can be collected within a few minutes, proving good temporal resolution for relatively slow processes.[11]

The use of ATR sampling in infrared spectroscopy is based upon the fact that, although total internal reflection occurs at

the sample–crystal interface, radiation does in fact penetrate a short distance into the sample, this is known as the evanescent field. The distance that the evanescent field can travel within a sample in direct contact with the ATR crystal is defined as the depth of penetration (d_p). Harrick and duPre[12] defined d_p as the value at which the initial electric field strength (E_o) decays to a value of $E_o \exp^{-1}$ and can be given as;

$$d_p = \frac{\lambda}{2\pi n_1 \sqrt{\sin^2 \theta - (n_1/n_2)^2}} \tag{1}$$

where λ is the wavelength of light, θ is the angle of incidence, n_1 and n_2 are the refractive indices of the ATR crystal and the sample in contact with it, respectively.[13] For example, for the conditions of the experimental setup and sample used in this study; diamond crystal ($n_1 = 2.42$) in contact with PLGA ($n_2 = \sim1.45$), eqn (1) gives a calculated d_p of ~1 μm for $\lambda = 5.7$ μm (1745 cm^{-1} where the PLGA carbonyl band shows high absorption). In practice, the true depth of penetration is ~3 times more than the calculated d_p value.[13] Clearly, ATR imaging only probes the near-surface of a sample but this permits the study of samples in aqueous media ($n_2 = \sim1.33$) which can be very challenging using traditional approaches such as transmission. Eqn (1) also shows that a good optical contact between the sample and ATR crystal is critical for obtaining a uniform absorbance profile avoiding artefacts within the field of view. The Golden Gate™ Imaging Single Reflection Diamond ATR Accessory (Specac Ltd) has corrective optics that adjust the plane of best focus to be situated on the crystal surface thus minimising any anamorphism and an auto-levelling sapphire anvil that ensures a uniform contact between the crystal and sample.[14]

FTIR images, consisting of spectral and spatial information, must be analysed in detail to convert the data into chemically and physically significant information.[6] Several methods for spectral and spatiotemporal data modelling can be used independently or in combination, however, the choice of analysis approach(es) for a series of hyperspectral image sets is determined by the nature and quality of the spectra and the information that needs to be extracted.[15]

The main challenge in hyperspectral image analysis on time-resolved multicomponent data sets is the extraction of the important information from the large volume of data generated including overlapping spectral features and noise. For time resolved experiments that continue for longer than a few hours unavoidable contributions from variations of atmospheric water vapour during the experiment has a huge effect particularly when the spectral region of interest is between 1500–1700 cm^{-1}. This creates complications in the image analysis because the true peak centre, required for peak height measurements, may vary between pixels due to the superimposition of the rotational fine structure of atmospheric water onto the sample spectrum. Algorithms for subtracting atmospheric water vapour superimposed on the sample spectrum using a known water vapour spectrum can be employed for bulk ATR measurements collected using a single pixel detector. However, this does not always eliminate the problem in hyperspectral imaging,

because of spectral variations between pixels emerging from the inherent low signal to noise ratio (S/R) compared to single point IR measurements. Applying a derivative is a common approach which eliminates baseline effects in univariate analysis but the water vapour bands are magnified by derivatives to such a degree that spectral information from the sample may be difficult to observe. Therefore spectra need to be deconvoluted by using soft or hard multivariate methods so that bands from the sample can be elucidated from the interfering water vapour signal. The most commonly applied multivariate tools to extract information from hyperspectral images include principal components analysis (PCA) and multivariate curve resolution (MCR) and comparisons between their application have been discussed elsewhere.[1,16,17]

The aim of this paper is to evaluate the advantages and limitations of univariate, hard and soft multivariate approaches for the analysis of ATR-FTIR images, collected during a dynamic process in real time. We also investigate the suitability of each of these analysis approaches for extracting quantitative information regarding the changes in the hydration and chemistry of a single poly(lactic-*co*-glycolic) acid (PLGA) microparticle and calculate the reaction rate during hydrolytic degradation.

Experimental

Materials

PLGA RG752H (75 : 25 lactide : glycolide, I.V. 0.16–0.24, Bohringer-Ingleheim) pharmaceutical grade CO_2 (BOC Special Gasses) were used as received. Water used in the experiments was purified with the ELGA Purelab option-R water distillation apparatus (Up to 15 MΩ cm, Type II water) and degassed using a Fisherbrand FB11004 ultrasonic bath at ambient temperature and 100% ultrasound power for 15 minutes.

CriticalMix™ process

PLGA is a random copolymer of poly(glycolic acid) (PGA), poly(lactic acid) (PLA), and is a U.S. Food and Drug Administration (FDA) approved, biodegradable[18,19] synthetic polyester that is physically strong and highly processable.[20] PLGA has suitable properties for biomedical applications as a scaffold[21] and sustained release systems[22] and has been comprehensively studied as carrier matrix for macromolecules such as proteins and peptides which are considered promising for the treatment of a range of conditions such as cancer, human growth deficiency, and multiple sclerosis.[23] The manufacturing process used to produce the microparticles used in this study was a simple, one-step process which has been used recently to encapsulate protein based drugs with 100% encapsulation efficiency.[22,24] When PLGA is exposed to scCO$_2$ in a pressure vessel, the polymer is liquefied. If the liquid is depressurised through a nozzle, whereby the CO_2 returns to a gaseous state, the polymer solidifies resulting in the production of microparticles. Careful control of the nozzle dimensions and depressurisation rate determines the particle size. Batches used in this study were prepared by adding 2.1 g of pre-weighed polymer, to the Particles from Gas Saturated Solutions (PGSS) apparatus.

The apparatus was sealed, pressurised with CO_2 to 700 psi (48 bar) and heated to 40 °C. Once at temperature, the pressure was increased to 2030 psi (140 bar). The liquefied polymer was then stirred at 150 rpm for 1 hour, after which time stirring was stopped and the mixture was depressurised through a nozzle generating microparticles. These were collected in a cyclone and recovered as a free flowing white powder.

Real time ATR-FTIR imaging of reactions

Infrared images were collected using an Agilent 680-IR FT-IR spectrometer coupled with a liquid nitrogen cooled mercury cadmium telluride focal plane array detector MCT-FPA (64 × 64 pixels), capable of simultaneously collecting 4096 spectra from an image area of 640 μm × 640 μm using the Golden Gate™ Imaging Single Reflection ATR Accessory (Specac Ltd). This accessory has a diamond internal reflection element with corrective optics that adjusts the plane of best focus to sit on the crystal surface, eliminating any distortion, so that a symmetrical point spread function can be assumed. The angle of incidence of the infrared beam was 45° and the numerical aperture (NA) of the system was 0.32. Images were recorded in rapid scan mode and typical collection times were ∼5 minutes. The detector was mounted on a Large Sample (LS) external sample compartment and the infrared beam from the spectrometer was projected directly on to the FPA after passing through the ATR sampling accessory. The physical size of each FPA pixel is 40 μm × 40 μm and with 4× magnification, each pixel represents a 10 μm × 10 μm square in the image.

To set up the hydrolysis experiment, a single PLGA microparticle was placed in direct contact with the ATR crystal using a 40× microscope standing on top of the ATR accessory and sufficient pressure was applied using the sapphire anvil to ensure good contact between the particle and the crystal resulting in some deformation of the spherical particle. The images collected were not circular, most likely showing some evidence of anamorphism despite the use of corrective optics and this issue when using such collection optics has been observed previously by Everall et al.[25] and Chan et al.[26] Once a satisfactory 'dry' image was collected water was introduced into the chamber in such a way that access to the particle was limited to the sides only as depicted in Fig. 1. Images were collected using the Agilent Technologies' ResolutionsPro FTIR Spectroscopy software version 5.2.0(CD846) at pre-determined time intervals and the collection parameters used were 128 co-added scans at a 4 cm^{-1} spectral resolution, in the mid-infrared (MIR) range (3800 to 950 cm^{-1}). The raw processed images were obtained by ratioing against a background of the blank ATR crystal comprising of 256 co-added scans.

Data pre-processing

Raw processed image files were cropped between 1820 and 1000 cm^{-1} which provided a number of characteristic bands associated with PLGA and also included the water δ(OH) peak ∼1635 cm^{-1}. In order to remove systematic discrepancies such as variations in detector sensitivity or sample thickness, raw images were vector normalised to minimise absorbance
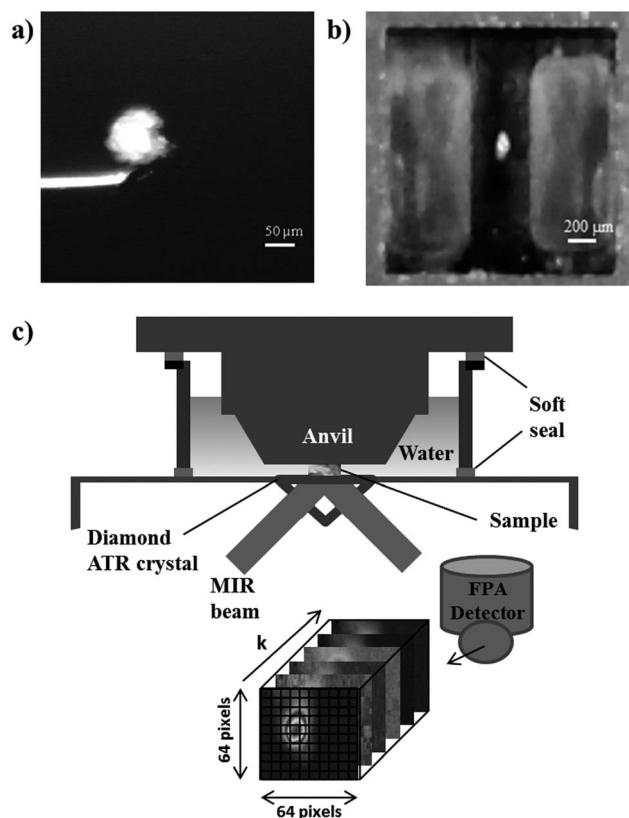

Fig. 1 (a) A microparticle on the Agar microtool straight needle T5340 to be placed on the ATR crystal. (b) A microparticle placed on the ATR crystal before the anvil was brought into contact with it. (c) Schematic of the experiment setup after the particle was placed, anvil was in contact and water was added.

variance. Vector normalisation works such that each spectrum is divided to the vector length which is square root of the sum of all absorbance values squared. Instrumental factors such as fluctuations caused by the changes in the IR source intensity or temperature or detector sensitivity and optical artefacts caused by mismatch of the refractive index of species being imaged are known to cause a slope in the baseline in FTIR spectroscopy. In order to eliminate this slope, a second derivative can be applied, however caution is advised if there are very weak infrared bands of interest as a second derivative will magnify the noise and some low intensity peaks may be lost in the noise. However a first order baseline correction between the two end points of the previously cropped spectral range was found useful for elimination of the baseline drift when collecting an image. The full data pre-processing procedure is described in the ESI section including Fig. S1.†

Univariate analysis. Univariate analysis, or functional group imaging, only considers the peak height of, or the integrated absorbance under, a peak of interest, therefore chemical information can be obtained based on the association of the peak position with certain functional groups. Although it is useful in providing a quick overview of the species in the raw image data, a peak height image usually convolutes the underlying chemical information from the overlapping peaks in

the intensity map. Integrating the absorbance for a particular peak over a spectral region of interest may provide a better distribution map by increasing the S/N. However, as in most cases, a complex heterogeneous mixture will not include an isolated band of interest therefore the integrated values will not represent the amounts present at different locations in the image with the required certainty. Another draw-back of functional group imaging is that a homogeneous object may be shown to be in a different location in the image when univariate images are created based on the integration of infrared bands observed in different parts of the spectrum. This occurs because the diffraction limited spatial resolution of the generated images strongly depend on the chosen part of the MIR spectral region.[27] These disadvantages can be overcome by using multivariate approaches, which allow all of the species to be searched in the same spectral range thus allowing a contribution from all the peaks of the same species (or factor). Another advantage of multivariate approaches is that the interferences such as water vapour can be detected as a factor, and may therefore be eliminated.

Multivariate curve resolution-alternating least squares. Multivariate curve resolution-alternating least squares (MCR-ALS) is a tool that facilitates the extraction of information from various spectroscopic and imaging techniques and is widely used in physical and biological sciences.[28] MCR methods are soft modelling tools that require no prior knowledge of the nature of the components in the mixtures to be deconvoluted[29] and can be grouped into, non-iterative and iterative approaches. Non-iterative MCR algorithms are unconstrained therefore may find unique profiles within the mixture being studied. However although these mathematically obtained unique profiles may be close to real chemical profiles that are to be resolved from the mixture data set, non-iterative methods often suffer from ambiguities that arise due to strong overlap between components of the species or low S/N of the data. On the other hand, with iterative MCR algorithms, soft concentration constraints such as non-negativity and unimodality or hard constraints such as the use of pure component profiles, which are compared with extracted profiles and modified accordingly, are implemented to minimise ambiguities.[30] By definition, MCR-ALS is a soft-modelling method that can extract component information from the raw measurement data alone, as long as this data contains some variance; spatially as one might anticipate in an image or as a function of time when monitoring a reaction. Detailed information about curve resolution techniques can be found elsewhere[31] however we would like to provide the necessary theory on the MCR-ALS software employed here (MCRv1.6) developed by Andrew and Hancewicz.[32]

The MCR-ALS algorithm used in this paper[32] has been developed for two-way data, therefore to use this approach, the 3D hyperspectral data cube must be unfolded into a two-dimensional matrix and refolded after analysis as shown in Fig. 2.

FTIR images have a bilinear structure and it is assumed that some form of a Beer–Lambert relationship exists between spectral intensity and concentration.[33] Therefore a bilinear model representing a spectroscopic image can be given as,

$$D_{uxv} = A_{uxz}B_{zxv} \qquad (2)$$

where $\mathbf{D}$ is the measured data matrix, $\mathbf{A}$ is the matrix of normalised spectra of pure chemical components and $\mathbf{B}$ is the related intensity matrix for each component.[34] The matrix size indices, u, v and z represent the number of spectroscopic resolution elements (wavenumbers), total number of spectra and number of resolvable components, respectively. Rearranging eqn (2) for the least squares estimation of $\mathbf{A}$ and $\mathbf{B}$ yields:

$$\mathbf{A} = (\mathbf{XB^T})(\mathbf{BB^T})^{-1} \qquad (3)$$

$$\mathbf{B} = (\mathbf{A^TA})^{-1}(\mathbf{A^TD}) \qquad (4)$$

To generate optimal matrices of $\mathbf{A}$ and $\mathbf{B}$, one first needs to estimate their initial values. In this paper, a non-linear iterative partial least squares (NIPALS) decomposition method has been applied, the merits of which when compared to using random numbers, eigenvalue decomposition, or dissimilarity criterion is discussed in detail elsewhere.[33] This is followed by the selection of the optimal number of factors to calculate and is achieved by considering the appropriateness of the initial estimate of the number of components. The final step, factor rotation, is a refining process where alternating least squares (ALS) is used to determine the optimal loadings and abstract factors matrices such that once recombined they most closely resemble the hyperspectral data matrix.

Although ALS is the most common method to decompose eqn (2) iteratively, a modified alternating least squares method (MALS) proposed by Wang *et al.*,[34] which has been shown to overcome unstable convergence properties giving a non-optimum least squares solution, has been used for decomposition for all the MCR images generated here. The MCR-ALSv1.6 software was run from its graphical user interface (GUI) that allowed the user to input the number of factors (or components) to be estimated, number of iterations (used 500), and an ALS non negativity constraint (in this instance we used MALS-2D). The rationale for the use of 2 factors is justified based on the fact that the image quality (S/N, resolution) is better when using 2 factors than when using 3 or 4 factors and the same as using 5 factors, see ESI, Fig. S2.† And it is important to note that MCR results might be improved by using different strategies that were not covered in this paper and/or more soft constraints or hard constraints.[35,36] For example, when the data were cropped down to the 1820–1500 cm^{-1} region which includes the PLGA carbonyl ($\sim$1745 cm^{-1}) and water δOH ($\sim$1635 cm^{-1}) MCR results were improved and although LA and GA peaks were not deconvoluted using MCR even when used cropped data between 1500 and 1300 cm^{-1}, they were deconvoluted when 2 other PLGA compositions (PLGA100/0 and PLGA50/50) were included in the data set.

Another interesting, but rather lengthy, strategy that could have been considered was removing the solvent IR background contributions as developed and demonstrated by Kuligowski *et al.*[37] in liquid chromatography infrared detection. They have estimated the solvent background successfully and by two different methods; principal component analysis and simple-to-
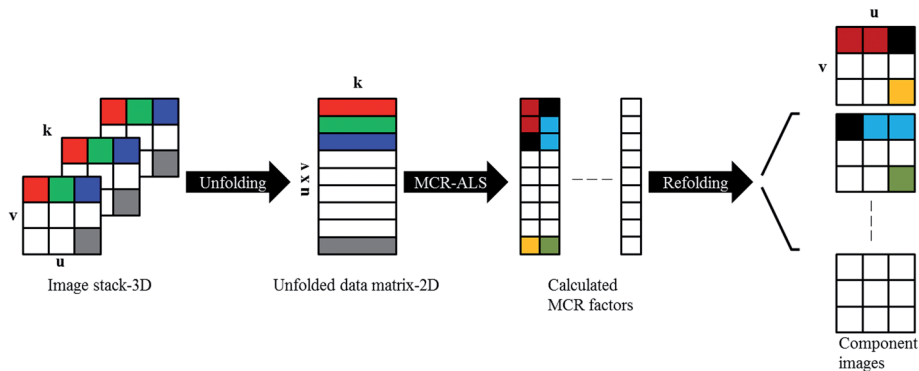
Fig. 2 Unfolding and re-folding spectroscopic imaging data to generate factor distribution images using MCR-ALS.

use interactive self-modeling analysis (SIMPLISMA) and after subtracting the estimated background contributions from their data sets, MCR-ALS provided improved S/N ratios and resolved overlapping chromatographic peaks. As the shape of the $\delta(OH)$ band has been shown to change from pixel to pixel in FTIR imaging data, we considered that using the simple subtraction of a pure water spectrum at each pixel would introduce spurious peaks due to imperfect subtraction and hinder the MCR analysis. Therefore, for the purposes of this study and to keep the MCR analysis as a soft modelling approach, we decided to use no prior information of the pure components and utilise the whole fingerprint region of the IR spectra (1820–1000 cm^{-1}) for the MCR analysis. We have not applied hard constraints such as pure spectra and/or different compositions of pure PLGA spectra as initial estimates of the MCR factors in the image set. Each of these would have been valid approaches but were beyond the scope of this work.

Nonlinear curve-fitting. The strategy behind curve fitting or hard modelling is to generate a model spectrum based on the sum of the component peaks that it contains. If the components within a spectrum and by extension an image are known, then an estimate of the relative amount of each component can be used as a starting point in the application of hard modelling. Here we have developed an efficient curve-fitting algorithm to optimise the parameters (lineshape, peak height, peak width) for infrared absorption bands and the percentage contribution of each fitted curve to the overall spectrum was used as the initial loading value.

In order to use curve-fitting procedures, analytical functions must be used which describe the lineshapes of the peaks. Typical lineshapes encountered in spectroscopic studies are the Gaussian

$$I(k) = I(k_0)\exp[-2.773(k - k_0)/\Delta^2] \quad (5)$$

and the Lorentzian

$$I(k) = I(k_0)/[1 + (2(k - k_0)/\Delta)^2] \quad (6)$$

where $I(k)$ is the intensity at wavenumber k, k_0 is the wavenumber at the peak centre and Δ is the full width at half maximum (FWHM).[38] The Lorentzian peak shape is often used to fit infrared absorption bands.[39] However in real infrared spectra, effects including hydrogen bonding, rotational fine

structure and, in FTIR-ATR, anomalous dispersion effects might affect the shape of the infrared band thus a true Lorentzian shape does not always occur. Due to the asymmetry and complexity of the bands within infrared spectra, these standard lineshapes should only be used with caution. In such situations a third lineshape function, the Voigt profile representing the convolution of a Gaussian and a Lorentzian, is often used.[39] However in practice, the use of the exact Voigt profile in curve fitting can be time consuming because it involves repeated convolutions. Each of the mentioned lineshapes are symmetric functions, but it is very important to note that unlike traditional IR spectra, IR imaging spectra are more susceptible to asymmetry even in transmission mode. It has often been assumed that recorded infrared imaging data are exactly like their traditional single point counterparts of bulk materials, and the spatial geometry of the sample was not thought to be an important factor in the processed IR image.[6] In transmission and reflection absorption measurements, it is recognized that there are differences in the data recorded from a bulk measurement and a microscopic measurement, caused by light focusing at the point of interaction with the sample when the microstructure of the sample is of the same length-scale as the wavelength of the interrogating radiation[40] and differences in the refractive indices of the rarer media at air/sample interface can result in artefacts in mid-IR images. In ATR-FTIR dispersion effects can lead to asymmetry in observed infrared bands, therefore in this paper we have considered the use of a family of peak curves called the Pearson profiles, specifically the Pearson IV profile which is asymmetric and is related to the Pearson VII,

$$I(k) = I(k_0)[1 + P^2]^{-M} \quad (7)$$

where $P = [2(k - k_0)\sqrt{2^{1/M} - 1}]/\Delta$ and M is known as the Pearson parameter. Eqn (7) reduces to the Lorentzian function when $M = 1$, approaches the Gaussian function when M becomes large and can approximate to the Voigt function for intermediate M.[38] Modifying eqn (7) with an exponential term provides the required asymmetry and for $M < 1$ the distribution has very broad wings. The Pearson IV function is given in terms of this by

$$I(k) = I(k_0)[1 + P^2]^{-M} \exp[-\nu \tan^{-1} P] \quad (8)$$

The exponential term has been shown to affect peak shapes when M is close to 1 (*i.e.* Lorentzian) more than it does for those where M is close to 10 (*i.e.* Gaussian).[38]

A routine in MATLAB Version 7.10 (R2010a), was developed to create fits for the each pixel within an IR imaging data set consisting of 4096 spectra individually. Peaks were detected using the algorithm described elsewhere[41] and height and width of the peaks in the raw spectra at detected positions were used as initial guesses for the iterative loop. Application of non-linear curve-fitting to large two-dimensional experimental infrared spectroscopic arrays[39] and a combination of non-linear curve-fitting and self-modelling curve resolution (SMCR)[42] have been demonstrated. Software packages such as PyMCA, which is a non-linear least-squares fitting application have previously been developed for X-ray imaging data.[43] However to the best of our knowledge, we are demonstrating a peak detecting non-linear optimisation algorithm applied to temporal ATR-FTIR imaging data for the first time.

The method by which we have approached this fitting procedure is described in detail in the ESI† and examples of the output from of the peak detection algorithm are given in Fig. S3.† To summarise our approach:

1. We select 18 spectra from the image based on their position; 6 from the water rich regions, 6 from the PLGA rich regions and 6 from the interface.

2. We iteratively and in a user supervised manner, adjust a peak detection threshold, such that all peaks in all 18 spectra are automatically detected by the peak detection algorithm. We fix the peak detection sensitivity parameter 'Delta'.

3. Using the fixed peak detection parameter we apply the peak detection algorithm to all 4096 spectra in an unsupervised manner.

4. We then fit peaks of all 4096 spectra based on the number of detected peaks and their positions using a gradient search algorithm which finds the best fit for the measured data optimising the variables; peak height, peak width, peak centre, Pearson parameter and asymmetry parameter for each peak.

5. We then use the intensity of the peak ~ 1635 cm^{-1} (selected in a supervised manner) to determine the distribution of water in the system and the sum of the intensity of all the peaks except the peak ~ 1635 cm^{-1} to determine the distribution of PLGA.

6. The intensity of the peaks ~ 1456 and ~ 1424 cm^{-1}, were used to calculate k values for lactic acid and glycolic acid units respectively.

Results and discussion

Fig. 3 shows the result of processing the same infrared image of a single PLGA microparticle in four different ways; using the peak height of a single peak in this case the ester carbonyl at ~ 1745 cm^{-1} (Fig. 3(a)), plotting the distribution of a factor identified as deriving from PLGA in MCR-ALS (Fig. 3(b)), by plotting the sum of 10 peaks fitted between 1800 and 1000 cm^{-1} which does not include the peak ~ 1635 cm^{-1} assigned to the water bending mode resulting from a NLCF procedure (Fig. 3(c)) and by plotting the sum of 10 peaks fitted between 1800 and

1000 cm^{-1} which does not include the peak ~ 1635 cm^{-1} resulting from a peak fitting procedure using solely Gaussian lineshapes procedure (Fig. 3(d)). Images were generated from measurements conducted on an as received PLGA microparticle and on the same PLGA microparticle, immediately after water had been brought into contact with it.

Spatial resolution comparison

The spatial resolution of a microscope is theoretically determined by the diffraction of radiation *i.e.* the Rayleigh criterion, which is defined in eqn (9) as

$$r = 0.61 \frac{\lambda}{\text{NA}} \tag{9}$$

where λ is the wavelength and NA is the numerical aperture. This implies that two objects are totally resolved if they are separated by $2r$.[44] Under these conditions, $2r$ is the definition of spatial resolution. However in an infrared imaging system, FPA detector pixels are not points and have a finite size that is greater than the wavelength of the IR light, therefore this relation is never observed. Furthermore, in the ATR experiment, the penetration depth (eqn (1)) can degrade the lateral resolution. Therefore for FPA imaging systems it has been shown to be more appropriate to determine the spatial resolution based on real measurements.[25,26,45] The practical method we have used is the 'step-edge' method[25] which is based on the observation of a step change increase when the intensity of a selected wavelength is plotted along a chosen line parallel to one of the axes in the 2D image. This step shape represents the Line Spread Function (LSF) (Fig. 3). The derivative of the LSF with respect to its variable (which is position or pixel number) is described as the Point Spread Function (PSF). The PSF is the response of the system to a point source and is generally considered to be an Airy function. The FWHM of the PSF gives the spatial resolution of the imaging system. Therefore, the FWHM of a Gaussian that is fitted to the PSF has been defined as the spatial resolution in this paper as described by Offroy *et al.*[44]

A study on the effect of sample geometry on spatial resolution of the same ATR-FTIR imaging system used in this study has been conducted by Everall *et al.*[25] for convex solid objects. They determined that this imaging system with a calculated NA of ~ 2 was underestimating the size of 20–140 μm objects and approximating solid spheres, of varying dimensions, to be the same size (~ 30 to 35 μm). The authors postulated that this was due to the shallow evanescent wave penetration (eqn (1)) and blurring caused by the finite spatial resolution. Our experiment however is different when compared to such a case, as the sample is a rather soft solid which, with a gentle anvil pressure, provides a flat central area that is quite large (~ 100 μm) and the convex shape only occurs at the edges. As the main purpose of this paper is not to estimate the real size of the microparticle, but to compare the output of univariate, hard and soft multivariate tools, we are more interested in seeing how the different data analysis approaches impact upon measured spatial resolution and the sharpness of the interfaces. The measured spatial resolution for each of the data analysis methods is
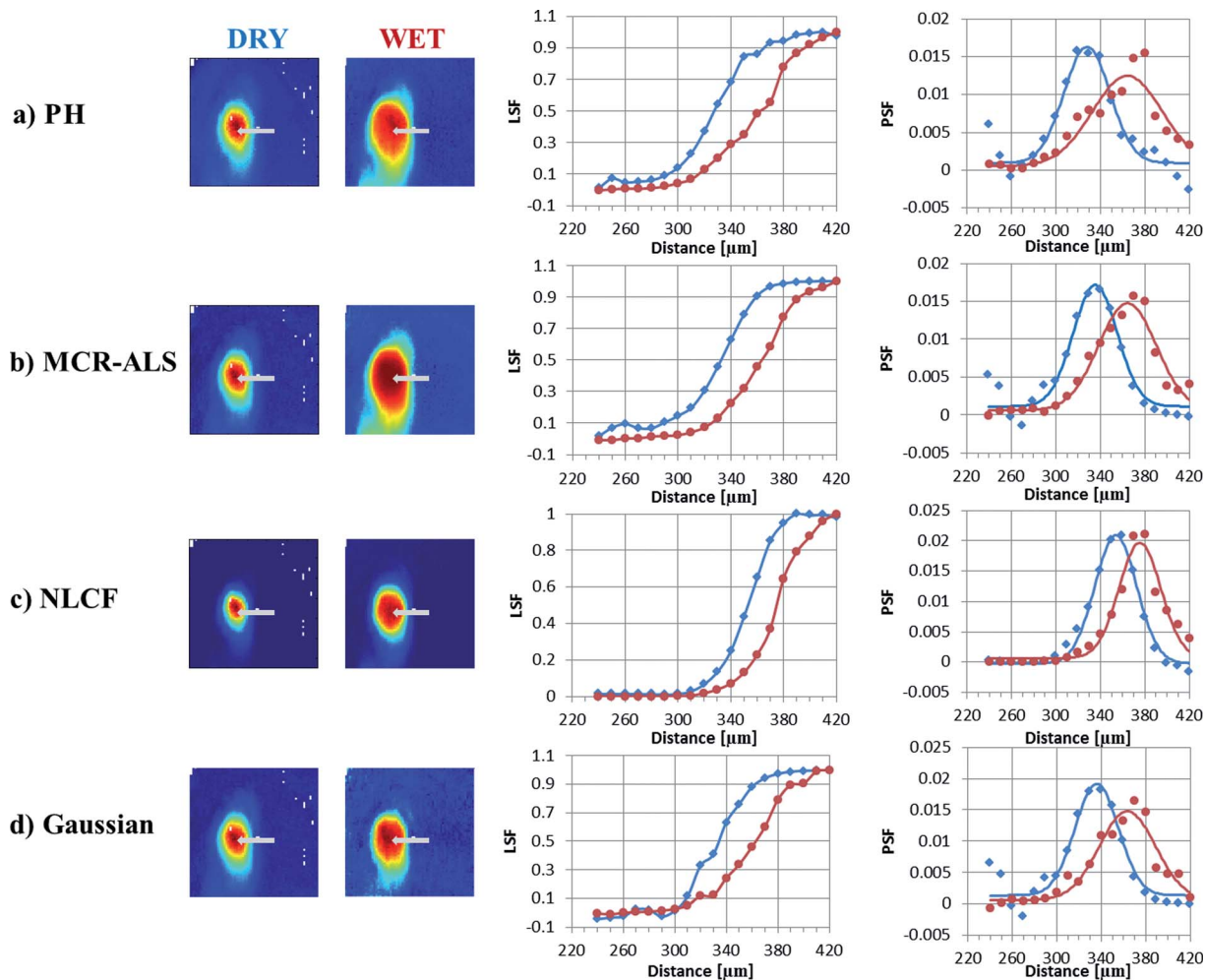
Fig. 3 Data used to measure spatial resolution using the "step-edge" method for the dry PLGA particle (1st column of images and labelled 'DRY') and the same PLGA microparticle immediately after surrounding it with water as shown in Fig. 1 (2nd column of images and labelled 'WET') for images processed using peak height (a) PH, (b) MCR-ALS, (c) NLCF and (d) Gaussian. The raw data along the grey arrow in each image is shown in Fig. S3.†

summarised in Table 1 and the spectra along the grey arrow on all spectra are shown in Fig. S4.†

Table 1 shows that the NLCF approach improves the measured spatial resolution of a mid-IR image when there is a large discrepancy between the refractive index in adjoining pixels, *i.e.* an air/polymer interface. Lasch and Naumann have shown the application of Fourier self-deconvolution to IR microspectroscopy images has led to an improvement in the spatial resolution by improving the spectral resolution at each pixel.[45] The NLCF approach we have used here, is also acting in

a spectral resolution enhancement manner and the ability, when used in a supervised manner, to discriminate between species in adjoining pixels more readily than the peak height, MCR-ALS and Gaussian peak fitting approaches that limits the blurring effects at interfaces.

The comparison between the images generated using NLCF and the images generated using traditional Gaussian fitting is an interesting one. The results are showing that NLCF facilitated an improvement in spatial resolution compared to a Gaussian fit. This is likely to be mainly due to the optimisation algorithm (trust region) falling into local minima as a result of a lack of change between consecutive iterations due to the limited number of parameters in the Gaussian fitting protocol not allowing an improvement in fit, due to variations in the symmetry of bands between pixels. In order to make the algorithm robust for not only this but different data sets and as we know that IR bands are asymmetric, we chose to use the Pearson IV function despite the delay in computation time. The merits of using this function compared to Gaussian and or Lorentzian functions is also discussed in the text and in ref. 38 and 39.

Table 1 Summary of spatial resolution calculated using different image analysis approaches of the mid-IR image of a single PLGA microparticle under dry and wet conditions. All values are given in μm

Method	Peak height	MCR-ALS	NLCF	Gaussian peak fitting
Dry	70.2 ± 15.8	60.6 ± 0.4	42.7 ± 1.5	55.8 ± 4.1
In water	52.4 ± 4.7	48.8 ± 4.1	48.6 ± 4	49.2 ± 4.9

When the refractive index change at an interface is small, such as when a PLGA microparticle is surrounded by water, the blurring of the interface is reduced and the spatial resolution determined by this step-edge approach is comparable between the each of the analysis approaches. It should be noted that for a sharp interface, such as the USAF (1951 1X 38257) target sample described in ref. 44, we have calculated the spatial resolution of the system to be ~18 μm using the step edge method.

Image comparison

As indicated previously FTIR imaging is a powerful tool that facilitates the collection of spatially resolved chemically relevant data from samples in real time. By conducting such measurements *in situ*, we can minimise the perturbations to the system and follow chemical changes from the same region of the same sample. One of the challenges presented is the efficient analysis of the huge data matrices that are generated during such experiments (4096 spectra at each time point). To explore the relative merits of a number of different analysis approaches (univariate peak height image plotting, soft and hard multivariate modelling), we have taken single PLGA75/25

microparticle and followed its interaction with water as a function of time at 70 °C. The experiment is setup in such a way that the interaction between the particle and water will only occur at the interfaces that we are monitoring.

Fig. 4(a) shows five false colour images obtained using the univariate peak height method and a spectrum taken from close to the 'dry' polymer/hydrated polymer interface in the $t = 0$ image. From this spectrum we are able to see both of the bands used to determine the polymer distribution (the ester carbonyl at ~1745 cm^{-1}) and the water distribution (the OH bending mode ~1635 cm^{-1}). The two images at the extreme left show the distribution of polymer (top) and water (bottom), within the ATR field of view, immediately after the experiment was started. Even at this short time (data collection was ~5 minutes) there is evidence of an interface layer of hydrated PLGA around the particle, with an apparent concentration gradient from the particle centre outwards towards the aqueous media. As the contact time with water increases, a number of phenomena occur. Firstly the microparticle (defined by the red zone) initially appears to increase in size (2 h), which is indicative of swelling and the hydrated PLGA layer (yellow) becomes thicker. Images collected at times exceeding 2 hours show the particle decreasing in size and the boundaries of the particle
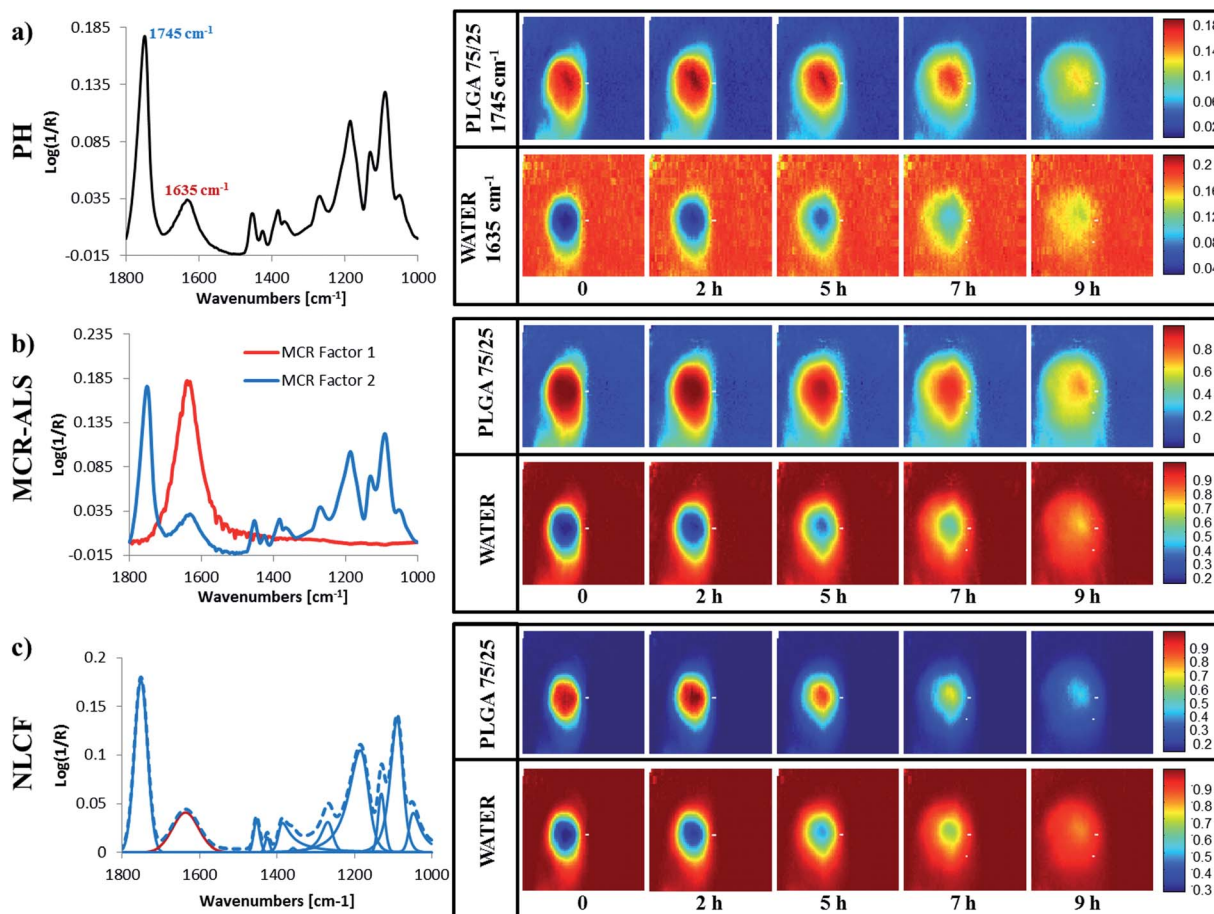

Fig. 4   ATR-FTIR spectrum of a pixel on the left hand side chosen from the core of the particle from the first image collected immediately after surrounding the PLGA particle with water and a set of false colour images representing temporal distribution of PLGA on the top and water at the bottom for (a) peak height (PH), (b) MCR-ALS and (c) NLCF methods respectively.

becoming less well defined. The complementary images pertaining to water concentration show an inverse relationship, as one would expect in a binary system. The changes to the interface layer as a function of time will be discussed later. It is clear however, that the overlap between the bands used to determine the distribution of the two components in this system must influence the sharpness of this image and increase the magnitude of the measured interface.

Fig. 4(b) shows the equivalent false colour infrared images for the same data described in Fig. 4(a), this time, obtained using a MCR-ALS approach and 2 factors. The spectral features shown to the left hand side of this figure are the 'pure component spectra' for PLGA and water generated using this soft modelling method and are often referred to as factors. This data is in general agreement with the findings from the peak height measurement approach shown in Fig. 4(a). Closer inspection indicates that the interfaces in this set of images are blurred as were those observed in the univariate data set (Fig. 4(a)) and less sharp than those obtained using the hard modelling approach (Fig. 4(c)). But this data set does exhibit improved S/N compared to the univariate data (Fig. 4(a)). The blurring of the interfaces is the result of the 'pure component spectrum' representing PLGA still displaying a feature at $\sim$1635 cm^{-1} associated with water and due to the fact that the MCR factor for PLGA has fixed peak centres and band widths meaning they approximate rather than exactly replicate the spectrum at each pixel. The improvement in the S/N is the result of the elimination of water vapour in the pure spectral factors combined with the fact that the signal comes from many more spectral data points compared to the peak height data.

Fig. 4(c) shows 5 false colour images equivalent to those described in Fig. 4(a) and (b). However, this time they were obtained using the nonlinear curve-fitting approach and are the result of the summation of the peaks, generated during the fitting process, that have been assigned to PLGA (upper row) and water (lower row). The data to the left of these images shows the 11 component peaks used to fit the spectrum, from the same pixel used to obtain the peak height and MCR-ALS data within the PLGA/water interface. The dotted line denotes the synthetic spectrum generated from the combination of the fitted peaks, which matches the real spectrum at that pixel. The upper set of images shows the distribution of PLGA determined using all of the fitted peaks except the peak with a maximum at 1635 cm^{-1} which is used to obtain the distribution of the water within the ATR field of view. These images are, in general, in agreement with the data shown in Fig. 4(a) in that they indicate the formation of a hydrated region around a dry PLGA particle that increases in thickness over the first 2 hours and that this occurs concurrently with particle swelling. Closer inspection and comparison with the data in Fig. 4(b) indicates that the interfaces and boundaries in this set of images are much sharper and the data exhibits less noise, *i.e.* there is less variation in colour intensity between equivalent pixels. This (apparent) improvement in resolution and S/N in each image is achieved by the elimination of contributions from overlapping features at each pixel such as other chemical species, instrument noise and atmospheric water vapour. Another

contributing factor to the broadening of the interfaces in the MCR-ALS images when compared with those generated using NLCF, is the fact that the NLCF peak centres are optimised for each peak within each pixel, whereas the MCR-ALS images used a fixed factor, with fixed peak centres and band widths. It is likely that during ALS optimisation, then a linear combination of the water and PLGA factors may give a better mathematical fit in some of the interface pixels resulting in a less well defined image, whereas the NLCF approach is better able to discriminate between water and PLGA. This does come at a considerable time and convenience penalty. The images shown in Fig. 4(a) can be obtained in seconds, whilst the data shown in Fig. 4(c) takes approximately 5 hours to generate using a PC with an Intel® Core™ i7-2620M CPU @ 2.7 GHz and 8 GB of RAM. In many applications this approach may not be feasible due to a number of considerations such as time, CPU availability and, more importantly, spectral data which is too challenging to fit due to a lack of knowledge of the species within that system Fortunately, the authors have amassed an understanding of the components within this system, *i.e.* water and PLGA thus generating confidence in the peak assignments. The MCR-ALS approach facilitates the collection of false colour images in a few minutes and thus offers an attractive/acceptable compromise between the slow but accurate hard modelling methodology and the rapid univariate approaches.

Interface analysis

The generation of false colour images, from the mid-infrared imaging dataset highlighted here, facilitates the rapid assimilation of trends in physical processes such as particle swelling, particle shrinkage, hydration layer formation *etc.* but cannot readily be used to obtain quantitative information about such processes. This can be problematic when a particle is not uniform in shape and often the dimensions are estimated by assuming a particular geometry (circle, square *etc.*) that may not be appropriate. To compare the quality of the output generated using the NLCF approach with standard image generation strategies (peak heights and MCR-ALS) we have compared the findings along the centre line across the particle as a function of time. To facilitate comparison between the data analysis types we have defined two parameters; the full width at half maximum height of the normalised particle profile (A) and the dimensions of the right hand side interface (B). Their derivation is shown in the ESI, Fig. S5.†

Fig. 5(a) and (b) show quantitative data extracted from across the centre line of the generated images shown in Fig. 4(a). Fig. 5(a) shows the evolution of the intensity of the water peak at each pixel across the image as a function of time and Fig. 5(b) shows the associated normalised plot of the full width at half height of the parameter 'A' for the images generated using peak heights.

From Fig. 5(a) it is possible to observe that the overall water concentration across the particle increases as a function of time as one might reasonably expect; rising from an intensity $\sim$15% of its maximum value at the local minimum at $t = 0$ h to a value of $\sim$75% of its maximum value at the local minimum at $t = 9$ h.
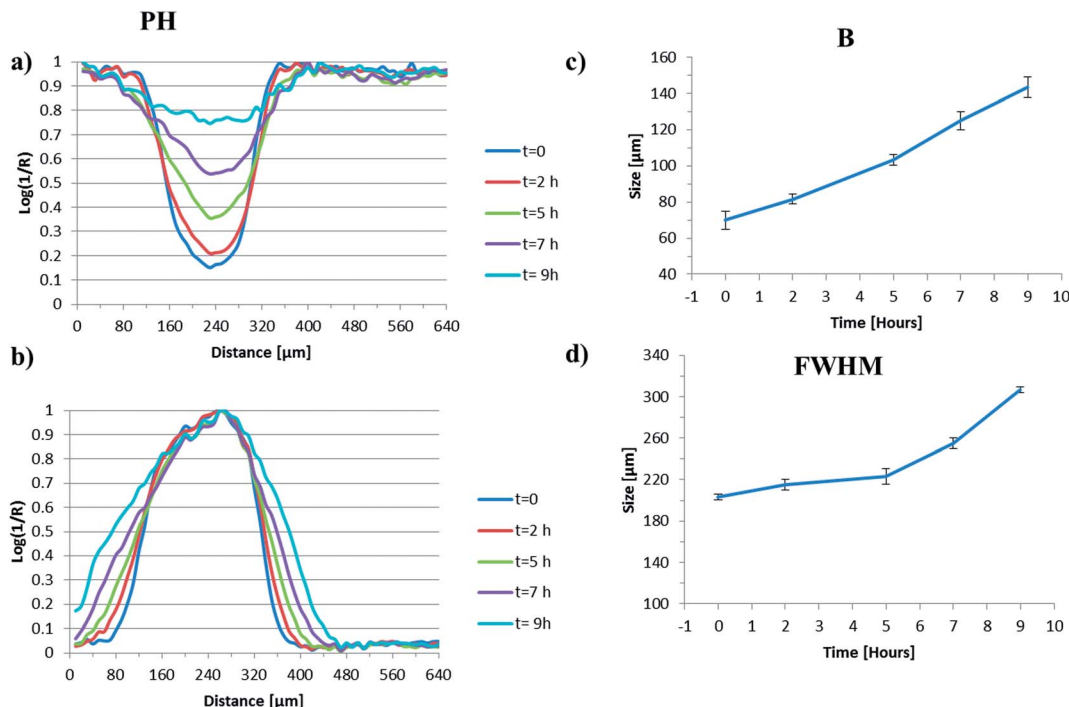
Fig. 5 (a) The normalised change in the intensity of the water peak at each pixel across the image as a function of time, (b) the normalised plot of intensity of the polymer particle, (c) the evolution of parameter 'A' as a function of time and (d) the evolution of the parameter 'B' as a function of time for the peak height derived images.

The profile at $t = 0$, which is ∼5 minutes after the particle has been subjected to water, indicates that the initial ingress of water into the particle is rapid, most likely due to the porous nature of the scCO$_2$ processed starting material. The shape of the profile initially appears to be fairly uniform and becomes less so as time progresses which may reflect the irregular shape of the particles. It is likely that initial compression onto the ATR crystal may make the analysed surface uniform (the ATR experiment collects data from the first 2–10 μm in direct contact with the crystal) but as the particle hydrates, swells and hydrolyses, the signal obtained *via* the ATR crystal will depend on the volume of the particle directly above the evanescent field and how it swells and or moves, potentially resulting in a loss of uniformity.

Fig. 5(b) shows the complementary data to that in Fig. 5(a) relating to the intensity of the polymer particle extracted from across the centre line of the peak height generated images. As the particle swells, the concentration of polymer measured within any given pixel will decrease and the concentration of water within that same pixel will increase. Therefore the intensity of the polymer peak (which should be the inverse of the water peak in this binary system) would provide an indication of the degree of swelling in the *z*-direction. Instead, we are using the change in width of the normalised intensity of the peak height of polymer peak, as a function of time, to provide an indication of the degree of swelling in the *y*-direction. We have chosen to normalise this data as it facilitates the observation of the change in full width at half height maximum (FWHHM) better than the equivalent data with the non-normalised *y*

values, which decrease over time. For the peak height derived images we clearly see the width of this peak increasing as a function of time and this is plotted in Fig. 5(c).

When water is introduced into our system, there exist domains where we only measure water, others where polymer is the dominant signal and others where we observe a clear mixture of water and polymer; a hydrated zone. Determining the exact point where each domain ends and another domain begins is somewhat arbitrary, but some form of definition is necessary if we are to quantitatively compare data extracted from images generated using different approaches. As described above we have defined a hydrated zone 'B' where both the water intensity and the polymer band intensity are below a certain threshold (10% of the maximum value). Fig. 5(d) shows the plot of the B zone for the peak height derived images as a function of time. The size of this zone increases quite dramatically over the course of this experiment, with dimensions around 70 μm at $t = 0$ and expanding to 140 μm at $t = 9$ h. This increase in thickness of the outer hydration layer is an interesting finding and in broad agreement with confocal fluorescence images generated by Bajwa *et al.*[46] of hydrating HPMC tablets. In the HPMC system an outer hydration layer of ∼100 μm increasing to 200 μm was measured over the course of a 'wetting' experiment. Clearly the timescales are different between the two systems due to the inherently different hydrophilicities, but nonetheless this adds credence to the nature of our measurements and our definition of B.

Fig. 6(a)–(d) show data comparable to that presented in Fig. 5, this time derived from the MCR-ALS generated images
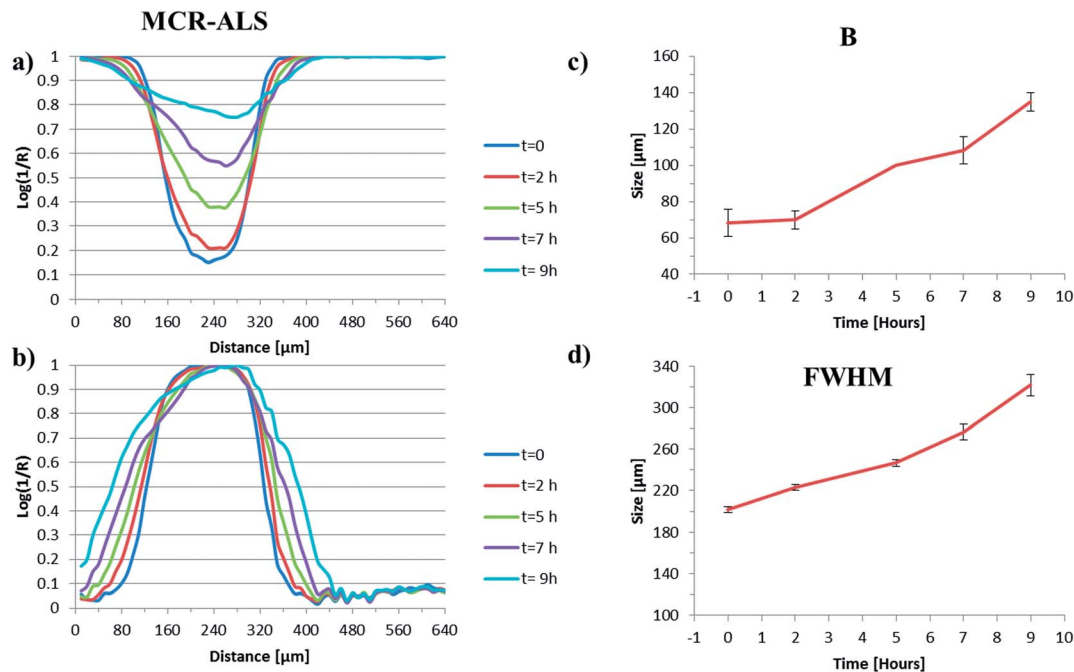
Fig. 6 (a) The normalised intensity of the water peak at each pixel across the image as a function of time, (b) the normalised plot of intensity of the polymer particle, (c) the evolution of parameter 'A' as a function of time and (d) the evolution of the parameter 'B' as a function of time for the MCR-ALS derived images.

shown in Fig. 4(b). Fig. 6(a) and (b) show the evolution of the water intensity and the normalised plot of the polymer factor intensity respectively. The shape and the intensities of the profiles in these figures are similar to those derived from the peak height measurements, but there was less noise in the MCR derived data (most evident in Fig. 6(a)), particularly at longer time points, where the band intensities of the polymer peaks are quite low. This improvement of S/N occurs because the peak height data is derived from a single point and the MCR-ALS data is derived from a large number of data points. There is perhaps some evidence of the polymer band intensity profile being less sharp at longer time points and at its maximum, which could be related to the contribution of water within the extracted pure factor associated with the polymer (MCR factor 2; Fig. 4(b)) and will also be a function of the fixed lineshape of factor with its associated peak maxima and minima which will not be able to exactly match the spectrum at each pixel.

Both the B values (Fig. 6(c)) and the full width at half maximum height values (Fig. 6(d)) as a function of time are very similar to those shown in Fig. 5(c) and (d). This indicates that there is perhaps no significant improvement in the quality of output obtained for this system when performing an MCR-ALS analysis on the data when compared to the more rapid peak height approach. Of course the MCR-ALS method can be used without any prior knowledge of the system; therefore there is no need to identify a peak specific to each component within it, which could be advantageous in some instances.

Fig. 7(a)–(d) show data comparable to that shown in Fig. 5 and 6, this time derived from the NLCF generated images (Fig. 4(c)). Fig. 7(a) shows the intensity of the curve fitted water band as a function of time. Both the intensities and width of

these profiles are somewhat different to those observed in those derived from the peak height (Fig. 5(a)) and MCR-ALS (Fig. 6(a)). Firstly the intensities are generally higher than those observed for the data derived using the other two approaches, this is more pronounced at short times, with the values at $t = 0$ being approximately 30% of their final intensity (cf. 15% for both peak heights and MCR-ALS). Some explanation is found in the consideration of the factors/bands used to generate the initial images from which these line profiles were generated. In the case of the peak height data, it is clear that the vector normalisation and baseline correction has enhanced S/N of the images (compare Fig. 4(a) with the data in ESI, Fig. S6†), but it is entirely feasible that this will exert some influence on the intensity values generated for each spectrum within a given pixel.

In the case of the MCR-ALS the extracted pure factor for the polymer contains a contribution from water (Fig. 4(b)) and therefore when the scores at each pixel for the pure water factor are calculated then they will be underestimated. As the NLCF approach is able to generate both a pure water signal and a pure polymer signal free from interference, we anticipate that the intensities presented in these profiles will be more likely to match the true concentration profile.

Fig. 7(b) is also somewhat different to the analogous peak height and MCR-ALS data; in that it is narrower and different in shape. Once more it is the convolution of the water and polymer bands in both the peak height and MCR-ALS spectra that contributes to the broadening of this profile, relative to the NLCF data.

Fig. 7(c) shows the increase in the B zone dimension as a function of time. The values plotted here are lower than those
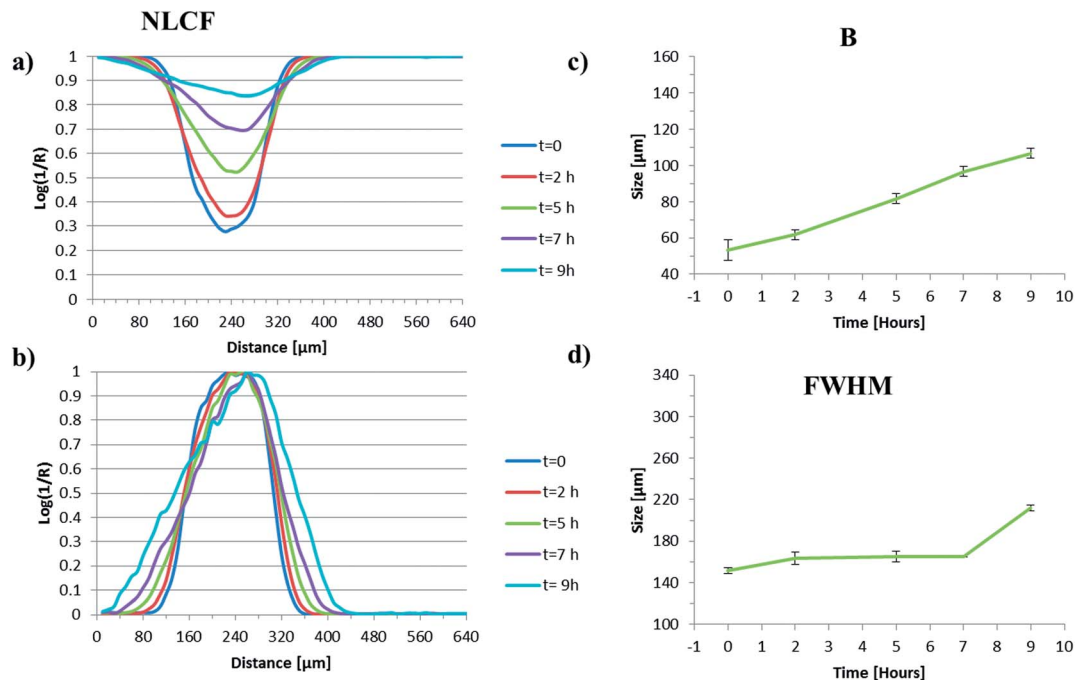
Fig. 7 (a) The increase in the intensity of the water peak at each pixel across the image as a function of time, (b) the normalised plot of intensity of the polymer particle, (c) the evolution of parameter 'A' as a function of time and (d) the evolution of the parameter 'B' as a function of time for the NLCF derived images.

obtained *via* both the peak height and MCR-ALS approaches and the error determined at each time point is somewhat lower than the corresponding values for the other two methods. This is a clear indication of the ability of the NLCF procedures to eliminate noise from the processed images. Fig. 7(d) shows the FWHM of the normalised polymer band profile generated from the NLCF images (Fig. 4(c)) and this also shows a reduction in width in comparison with the analogous data generated using the other two methods. The reduction in size of the *B* zone and the FWHM in comparison with the data generated using peak heights and MCR-ALS is a reflection of the ability of the NLCF method to discriminate between the water and polymer contributions at each pixel, reducing the blurring effect of convoluted spectra.

Degradation rate calculation

Coupling the chemical selectivity of infrared spectroscopy with the regional selectivity of an FPA detector facilitates remarkable insight into a wide range of processes. PLGA microparticles can be used as sustained delivery vehicles, where the rate of hydrolysis will control the release rate. Parameters that govern the hydrolytic degradation of PLGA include molecular weight, structure and morphology and PLGA degradation dynamics. FTIR spectroscopy has routinely been used to follow hydrolysis kinetics, but we believe this is the first time that measurements have been undertaken on single microparticles in this manner. Two infrared bands have been observed at $\sim$1452 cm^{-1} and $\sim$1424 cm^{-1} that correspond to the antisymmetric bending of CH_3 from the lactic acid units and the symmetric bending of CH_2 from the glycolic acid units of the PLGA polymer. The relative intensities of these two bands can be used to estimate

the relative quantity of glycolic and lactic acid units present in the polymer and has been used to determine the rate of hydrolysis of the two co-polymer segments within the same experiment. Work by Vey *et al.*[47] has shown that the lactic acid units hydrolyse $\sim$1.3 times slower than the glycolic acid units. Unlike large-sized (a few mm) PLA/GA polymer devices, microspheres less than 300 μm in diameter have been shown to undergo homogeneous degradation with the rate of degradation of the core being equivalent to that at the surface.[48,49] Therefore rate constants from different regions within a microparticle would be expected to give the same calculated rate.

Fig. 8 shows typical single pixel spectra (Fig. 8(a)), spectra resulting from the binning of 5 $\times$ 5 pixels (Fig. 8(b)), the resultant peak fits from a single pixel (Fig. 8(c)) and the result of peak fits from the binning of 5 $\times$ 5 pixels (Fig. 8(d)) which have been used to calculate the rate constants, shown in ESI, Fig. S6.† It should be noted that due to a deviation from a linear relationship between the ln(intensity) *versus* time plot, no *k* values for the MCR data could be determined.

To compare the relative merit of each of the data analysis approaches used in this study, we have calculated the hydrolysis rates for both the glycolic and lactic blocks independently within the same experiment. MCR-ALS was unable to provide pure component spectra for both the lactic and glycolic segments of PLGA, probably due to the nature of the iterative extraction process. MCR-ALS relies on variance within spectral data sets to extract pure component factors and as the ratio between the glycolic and lactic units during hydrolysis is constant throughout the experiment (*i.e.* the data is co-linear) the algorithm does not detect any variance. Consequently a single 'PLGA' pure component is generated.
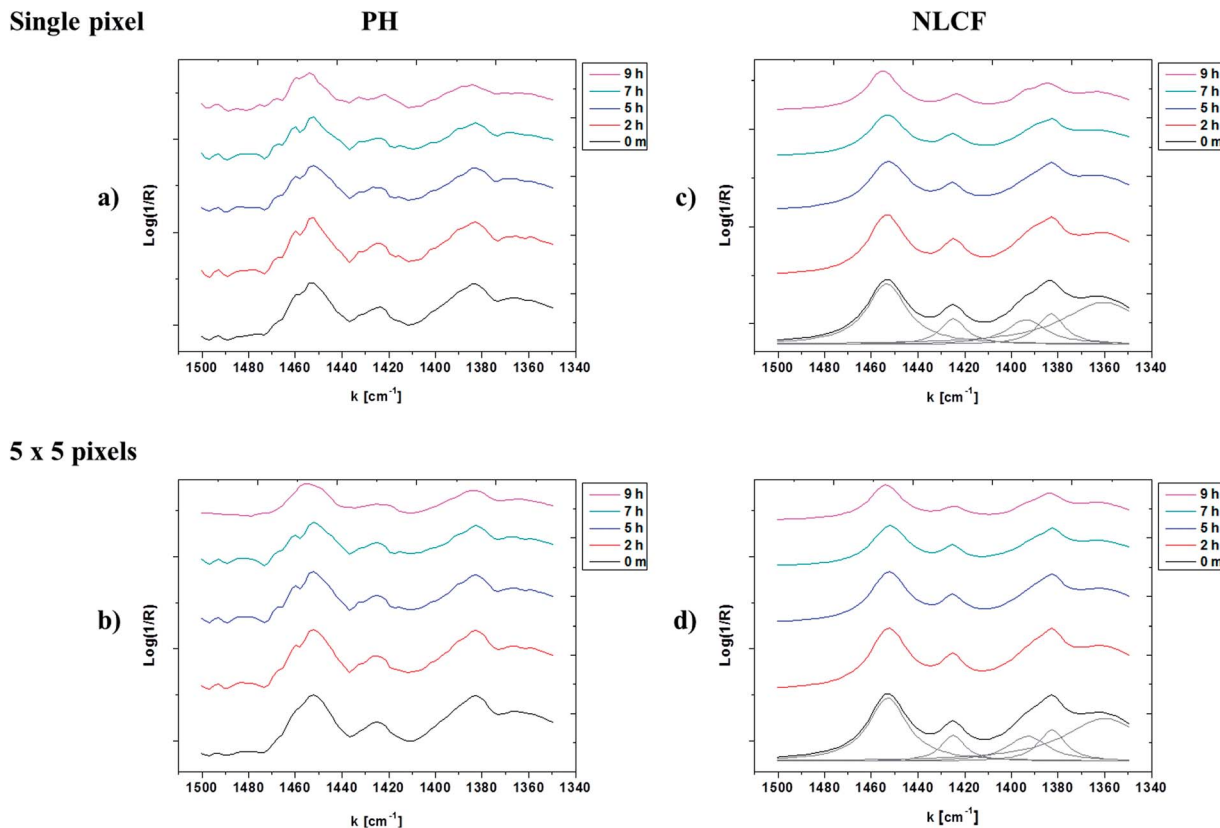
Fig. 8 Typical single pixel and averaged (over 5 × 5 pixels) spectra of pre-treated raw ((a) and (b)) and non-linear curve fitted ((c) and (d)) data. Spectra from bottom to top were obtained at $t = 0$, $t = 2$ h, $t = 5$ h, $t = 7$ h and $t = 9$ h, respectively.

Hydrolysis rate constants for the lactic units (k_L) and the glycolic units (k_G) were calculated using both the peak height data and the NLCF data from the logarithmic plot of peak intensity *versus* degradation time (see ESI data S7†) using the band ~1452 cm^{-1} for the lactic units and that at ~1424 cm^{-1} for the glycolic units, using the spectra shown in Fig. 8. First order kinetics as defined in eqn (10) and (11) were assumed;

$$\ln(I) = -k_L t + n \qquad (10)$$

for the lactic unit and,

$$\ln(I) = -k_G t + n \qquad (11)$$

for the glycolic unit.

Table 2 List of degradation rate constants (day^{-1}) calculated for triplicates of averaged 5 × 5 pixels and single pixel spectra using peak height values and curve fitted area values over the course of the 9 h hydrolysis experiment. Errors quoted are the standard deviation of 3 measurements taken from 3 different regions of the same particle

Method	5 × 5 pixels		Single pixel	
	k_L	k_G	k_L	k_G
Peak height	1.13 ± 0.2	1.41 ± 0.35	0.9 ± 0.53	1.53 ± 0.98
NLCF	1.47 ± 0.1	2.06 ± 0.13	1.29 ± 0.21	1.67 ± 0.34

Rate constants were calculated by selecting the spectrum (or extracted factor) at 3 random pixels within each image. For comparison, the same positions were used for each of the peak height, MCR-ALS and NLCF image analysis approaches and the mean of the three values are shown in Table 2.

Rate constants were also determined by binning the spectra/ factor score from 3 areas of 5 × 5 pixels from random regions within each image. Once more the same regions were used for each of the peak height, MCR-ALS and NLCF image analysis approaches and the calculated rate data (where possible) are shown in Table 2 and are the result of the mean of three values.

Tracy *et al.*[48] studied the degradation of poly(lactide-*co*-glycolide) microspheres *in vivo* and *in vitro* and determined degradation rate constants by measuring the polymer molecular weight as a function of time by gel-permeation chromatography. They found that the *in vivo* degradation rate was higher than *in vitro* degradation one. Their calculations of *in vivo* rate constant by GPC analysis for ester capped and uncapped (–COOH) PLGA50:50 microspheres were 0.033 ± 0.006 per day and 0.13 ± 0.05 respectively. Considering that the PLGA microparticle studied here was scCO$_2$ processed therefore very porous, and a calibration (*i.e.* %GA or %LA *versus* IR absorbance) was not considered as in ref. 47, due to having one polymer composition, the k values calculated are in reasonable agreement with each other and with the values determined by Tracy *et al.*[48] and, as one might anticipate, the error obtained when calculating rate constants by binning a number of spectra

is somewhat lower than that obtained from a single pixel. The errors are larger for the peak height derived calculations than those from the NLCF measurements. It is also clear that the ratio of the rate constants calculated for the lactic and glycolic groups is also comparable with that determined by Vey et al.;[47] we have determined the ratio of rate constants to be 1.2 (peak height binned pixels), 1.7 (peak height single pixels), 1.4 (NLCF binned pixels) and 1.3 (NLCF single pixels). Interestingly the error determined for the k calculations for the MCR-ALS processed images seemed to be independent of the number of pixels used to determine them. It is unclear if this finding is real or an anomaly of the pixels chosen to make the measurements.

Conclusions

A new algorithm for nonlinear curve fitting (NLCF) has been developed and applied to the analysis of mid-IR images of a single PLGA microparticle undergoing hydrolysis at 70 °C for the first time. The supervised NLCF approach has been shown to have several advantages over traditional peak height measurements and a commonly applied multivariate tool; MCR-ALS. Firstly the application of NLCF routines to such data has been shown to enhance the spatial resolution within a sample with (a) overlapping spectral signals and (b) containing interfaces with large discrepancies in the refractive index (i.e. air/polymer). Secondly it has been shown to improve S/N and sharpen features such as interfaces in processed images, due to its ability to discriminate between different species in a mixture, this is particularly pronounced when one compares this approach to standard peak height measurements. Thirdly as the approach does not appear to be greatly influenced by colinearity, unlike MCR-ALS, supervised NLCF can be used to extract chemical information from species changing at the same ratio during a kinetic process such as hydrolysis. Finally the high S/N at each pixel readily facilitates the calculation of rate constants from a single pixel with a low error when compared to traditional peak height approaches. All these advantages come at a significant time penalty; the NLCF algorithm described takes ~5 hours to extract information from a single mid-IR image containing 4096 spectra, this compares to ~2 seconds for peak height analysis and ~1 minute for MCR-ALS on the same image using the same PC.

With the help of fast developing computing hardware power, the supervised NLCF method developed here will be a useful IR imaging analysis tool providing high resolution images and quantitative analysis for many more cases particularly where hard modelling is the only option such as deconvoluting protein spectra when searching for changes in secondary structure.

Acknowledgements

References

1 J. M. Amigo, Anal. Bioanal. Chem., 2010, 398, 93–109.

2 S. Huotari, T. Pylkkanen, R. Verbeni, G. Monaco and K. Hamalainen, Nat. Mater., 2011, 10, 489–493.

3 G. Sciutto, P. Oliveri, S. Prati, M. Quaranta, S. Bersani and R. Mazzeo, Anal. Chim. Acta, 2012, 752, 30–38.

4 D. Zhang, P. Wang, M. N. Slipchenko, D. Ben-Amotz, A. M. Weiner and J. Cheng, Anal. Chem., 2013, 85, 98–106.

5 P. J. Williams, P. Geladi, T. J. Britz and M. Manley, Anal. Bioanal. Chem., 2012, 404, 1759–1769.

6 R. Bhargava, Appl. Spectrosc., 2012, 66, 1091–1120.

7 P. R. Griffiths and J. A. de Haseth, Fourier Transform Infrared Spectrometry, John Wiley & Sons Inc., Hoboken, New Jersey, 2nd edn, 2007.

8 P. Bassett, Drug Delivery Systems: Trends, Technologies and Market Opportunities, Drug & Market Development, Southborough, MA, USA, 2nd edn, 1999.

9 S. G. Kazarian and K. L. A. Chan, Biochim. Biophys. Acta, 2006, 1758, 858–867.

10 S. G. Kazarian and K. L. A. Chan, Appl. Spectrosc., 2010, 64, 135–152.

11 S. G. Kazarian and K. L. A. Chan, Analyst, 2013, 138, 1940–1951.

12 N. J. Harrick and F. K. duPre, Appl. Opt., 1966, 5, 1739.

13 F. M. Mirabella, J. Polym. Sci., Part B: Polym. Phys., 1983, 21, 2403.

14 G. Thomson and G. Poulter, US Pat., US20060261274 A1, 2006.

15 A. A. Gowena, F. Marinib, C. Esquerrea, C. O'Donnella, G. Downey and A. c. J. Burger, Anal. Chim. Acta, 2011, 705, 272–282.

16 B. Vajna, G. Patyi, Z. Nagy, A. Bodis, A. Farkas and G. Marosi, J. Raman Spectrosc., 2011, 42, 1977–1986.

17 M. Franssona, J. Johanssona, A. Sparéna and O. Svenssona, J. Chemom., 2010, 24, 674–680.

18 U. Edlund and A. Albertsson, Adv. Polym. Sci., 2002, 157, 67–112.

19 D. Lemoine, D. C. Francois, F. Kedzierewicz, V. Preat, M. Hoffman and P. Maincent, Biomaterials, 1996, 17, 2191–2197.

20 C. Wischke and S. P. Schwendeman, Int. J. Pharm., 2008, 364, 298–327.

21 F. Danhier, E. Ansorena, J. M. Silva, R. Coco, A. Le Breton and V. Préat, J. Controlled Release, 2012, 161, 505–522.

22 F. Jordan, A. Naylor, C. A. Kelly, S. M. Howdle, A. Lewis and L. Illum, J. Controlled Release, 2010, 141, 153–160.

23 R. A. Jain, Biomaterials, 2000, 21, 2475–2490.

24 M. J. Whitaker, J. Ho, O. R. Davies, G. Serhatkulu, S. Stolnik-Trenkic, S. M. Howdle and K. M. Skakesheff, J. Controlled Release, 2005, 101, 85–92.

25 N. J. Everall, I. M. Priestnall, F. Clarke, L. Jayes, G. Poulter, D. Coombs and M. W. George, Appl. Spectrosc., 2009, 63, 313–320.

26 K. L. A. Chan and S. G. Kazarian, Appl. Spectrosc., 2003, 57, 381–389.

27 B. O. Budevska, S. T. Sum and T. J. Jones, *Appl. Spectrosc.*, 2003, **57**, 124–131.

28 T. M. Hancewicz and J. H. Wang, *Chemom. Intell. Lab. Syst.*, 2005, **77**, 18–31.

29 J. M. Prats-Montalbán, A. de Juan and A. Ferrer, *Chemom. Intell. Lab. Syst.*, 2011, **107**, 1–23.

30 M. De Luca, S. Mas, G. Ioele, F. Oliverio, G. Ragno and R. Tauler, *Int. J. Pharm.*, 2010, **386**, 99–107.

31 A. de Juan and R. Tauler, *Crit. Rev. Anal. Chem.*, 2006, **36**, 163–176.

32 J. J. Andrew and T. M. Hancewicz, *Appl. Spectrosc.*, 1998, **52**, 797–807.

33 W. H. Lawton and E. A. Sylvestri, *Technometrics*, 1971, **13**, 617–633.

34 J. H. Wang, P. K. Hopke, T. M. Hancewicz and S. L. Zhang, *Anal. Chim. Acta*, 2003, **476**, 93–109.

35 S. Piquerasa, L. Duponchel, R. Tauler and A. de Juan, *Anal. Chim. Acta*, 2011, **705**, 182–192.

36 S. Piqueras, J. Burger, R. Tauler and A. de Juan, *Chemom. Intell. Lab. Syst.*, 2012, **117**, 169–182.

37 J. Kuligowski, G. Quintas, R. Tauler, B. Lendl and M. de la Guardia, *Anal. Chem.*, 2011, **83**, 4855–4862.

38 A. G. Michette and S. J. Pfauntsch, *J. Phys. D: Appl. Phys.*, 2000, **33**, 1186–1190.

39 L. Chen and M. Garland, *Appl. Spectrosc.*, 2003, **57**, 323–330.

40 R. Bhargava, S. Q. Wang and J. L. Koenig, *Appl. Spectrosc.*, 1998, **52**, 323–328.

41 H. Eskandari, S. E. Salcudean and R. Rohling, *IEEE Trans. on Ultrasonics, Ferroelectrics, and Frequency Control*, 2007, **54**, 1118–1130.

42 W. Xu, K. Chen, D. Liang and W. Chew, *Anal. Biochem.*, 2009, **387**, 42–53.

43 V. A. Solé, E. Papillon, M. Cotte, P. H. Walter and J. Susini, *Spectrochim. Acta, Part B*, 2007, **62**, 63–68.

44 M. Offroy, Y. Roggo, P. Milanfar and L. Duponchel, *Anal. Chim. Acta*, 2010, **674**, 220–226.

45 P. Lasch and D. Naumann, *Biochim. Biophys. Acta, Biomembr.*, 2006, **1758**, 814–829.

46 G. S. Bajwa, K. Hoebler, C. Sammon, P. Timmins and C. D. Melia, *J. Pharm. Sci.*, 2006, **95**, 2145–2157.

47 E. Vey, C. Rodger, J. Booth, M. Claybourn, A. F. Miller and A. Saiani, *Polym. Degrad. Stab.*, 2011, **96**, 1882–1889.

48 M. A. Tracy, K. L. Ward, L. Firouzabadian, Y. Wang, N. Dong, R. Qian and Y. Zhang, *Biomaterials*, 1999, **20**, 1057–1062.

49 G. Spenlehauer, M. Vert and J. P. Benoit, *Biomaterials*, 1989, **10**, 557–563.